

Oxidative and Internal Stress Effects of Dopants in Multilayer
 $\text{Yb}_2\text{Si}_2\text{O}_7$ Environmental Barrier Coatings

Thesis by
Benjamin Riley Herren

In Partial Fulfillment of the Requirements for the
Degree of
Doctor of Philosophy

Caltech

CALIFORNIA INSTITUTE OF TECHNOLOGY
Pasadena, California

2022
Defended 29 April, 2022

© 2022

Benjamin Riley Herren
ORCID: 0000-0002-6011-710X

All rights reserved

ACKNOWLEDGEMENTS

It is not possible to list everyone that enriched my life and my studies during my time as a graduate student, partly because that list is simply too long and partly because I wasn't taking notes for all of it. Still, with immense gratitude and appreciation I want to acknowledge and thank:

Professor Katherine Faber, for steady guidance and support; for asking and encouraging me to do things I didn't think I could do; for revising my disorganized thoughts and writing; for accounting for some of my stubbornness; and for thoughtfully building such a unique and special research group in which to do our work. Thank you for your support when life happened during my graduate studies, for patiently allowing someone without an academic background to develop one, and for experiencing some of those growing pains with me on the way. There are many times I wasn't sure there was a path forward, but you provided one and, sure enough, it worked out.

Professor Brent Fultz, Professor Guruswami Ravichandran, Dr. Kang Lee, Dr. Jon Almer, and Professor Bill Johnson, for being on my thesis and candidacy committees, for invaluable mentorship over the last several years, and for welcoming me into the academic and research communities.

Jon Almer and Kang Lee, for being knowledgeable and patient collaborators and for helping with all of my many questions. Your academic and personal mentorship has been invaluable.

Jon Almer, Andrew Chuang, Peter Kenesei, Jun-Sang Park, Roger Ranay, and Ali Mashayekhi, and the rest of Sector 1 and the APS, for making the beamline such an incredible place to visit and do research.

Matt Johnson, Neal Brodник, and Sara Gorske, for being in the trenches with me at the APS and being thoughtful sounding boards during some very long working hours.

The Faber Group, as it has (mostly) been during my time: Xiaomei Zeng, Putt Naviroj, Wei-Lin Tan, Neal Brodник, Noriaki Arai, Tai-Jung Kuo, Celia Chari, Chun-Wei Wu, Laura Quinn, Sara Gorske, Kevin Yu, Carl Keck, and Chris Long. Thank you for your help and guidance, for being incredible friends and researchers, for being earnest when it is easier to be cynical, and for making it so hard to consider working with anyone else.

Christy Jenstad, Jennifer Blankenship, Katie Pichotta, Angie Riley, and Tiffany Kimoto, for supporting me as a student and a fellow member of the department.

Matt Johnson, for encouragement, sound advice and steady friendship, and an honest perspective on life at some very important forks in the road.

Rebecca Gallivan, for being the best kind of friend a person could imagine, as well as a wonderful collaborator, and for keeping me on track with our work in the Caltech community.

The Caltech Y staff, including JJ, and the Outdoors Committee. Greg Fletcher for always looking for a way to help us make our adventures happen. Rebecca Gallivan, Kathryn Plant, Emily de Jong, Jimmy Ragan, Eitan Rapaport, Camille Bernal, Cullen Quine, and others, for co-planning and co-leading so many fun hikes and trips.

Claire Saunders, Camille Bernal, Stefan Haegli-Lohaus, Pedro Guzman, and Cullen Quine, for being curious scientists, helpful fellow researchers, and exciting neighbors to have in Keck.

Kathleen Kennedy, Jonathan Gross, and Shadow, for being supportive and caring and for balancing out some of the inevitably tricky things in life and graduate school.

Kevin Korner, for useful discussions and research help on math I don't understand.

Andrew Hoff, for being a curious and supportive friend, and for having a knack for understanding what I am thinking when I can't quite figure out how to say it.

Nate Hart, for helping me to visualize and create the custom induction furnace and enabling some of the most exciting research in this thesis.

Jim Barry, for helping me to think and feel more creatively in a time when I was so focused on analysis.

Christy Jenstad, Katie Pichotta, Matt Johnson, Mark Prator, and Gail Verderico, for our after-work discussions on research and life.

Christy Jenstad and Jennifer Blankenship, for being constant in your support and care, for looking out for me like family, and for helping me to grow as much as possible as a person.

The Hofmanns, Jenstads, and Blankenships, for providing a home away from home. The list here is long each of you has made my time better, as a researcher and even moreso as a person. If I could have done it otherwise, it certainly would have been a lot less fun.

My undergraduate advisors, Professor Mike Hurley, Professor Dave Estrada, Professor Harold Ackler, Professor Darryl Butt, and Jessica Economy, among the other faculty at Boise State University, for shepherding me through the early parts of my career in materials science and for encouraging me to take a bet on myself by pursuing graduate studies.

Conner Riebe and Nick London, for your support and inspiration over the last several years, your balanced perspective on life, and our long friendship. I look forward to being able to do things now.

Ryan Gelskey and the Gelskeys, for being my friends and family all these years.

Lee Coleman and Peter Huang, for trusting companionship and deep support of my mental and emotional health during graduate school.

My family, for whom this work has been a labor of love, for being so wonderfully supportive and providing a place I want to come home to. My Mom, Dad, Chelsea, Stephen, Finn, Forrest, and Baxter, and more.

I am also grateful for the funding and resources which made this work possible. The Stanback Innovation fund and Clinard Innovation Fund provided internal Caltech funding. The NASA Space Agreement Act (SAA) provided funding for this work at NASA Glenn, from which Kang Lee sent us the samples for the following studies. The Department of Energy and University of Chicago fund and manage the Advanced Photon Source at Argonne National Lab, where critical portions of this research were carried out using the unique capabilities of that synchrotron.

—Benjamin

ABSTRACT

One of the best approaches to improving the efficiency of turbine engines is to increase their operating temperatures. A revolutionary improvement toward this goal will be the replacement of structural metallic components with silicon-based ceramic-matrix composites (CMCs). However, corrosive chemistries in combustion engines necessitate chemical protection of the structural material. Environmental Barrier Coatings (EBCs) are designed for this purpose through thermomechanical and chemical compatibility with the system. High-temperature, humid oxidation of the EBC bondcoat, a silicon layer which adheres the topcoat to the substrate, remains a critical failure mode EBC systems.

This work studies the effects of chemical modifications on bondcoat oxidation during steam cycling in a current state-of-the-art EBC ($\text{Yb}_2\text{Si}_2\text{O}_7/\text{Si}$), and the implications for the durability of the system. Chemically modified EBCs have been shown to decrease oxide growth by more than 85 percent after 1000 hours of steam cycling. Post-exposure analyses are used to investigate the effects of chemistry on thermal oxide thickness and microstructure. Synchrotron X-ray scattering at the Advanced Photon Source, Argonne National Laboratory, is used to observe internal strains, connected to oxidation and chemistry through microstructure. Compared internal stresses, oxidation, and microstructure between baseline and modified EBCs promote the effectiveness of topcoat chemical modifications as they may apply to EBC durability. Microindentation, nanoindentation, and ongoing beam-bending experiments are also used to assess EBC interface toughness in a baseline EBC system. Additionally, a custom induction furnace has been designed and tested for in-situ steam cycling at the synchrotron. Traits facilitating the use of the custom furnace at the synchrotron make for convenient steam-cycling and other exposures in conventional laboratory settings, as well, with enhanced customizability and flexibility.

TABLE OF CONTENTS

Acknowledgements	iii
Abstract	vi
Table of Contents	vii
List of Illustrations	x
List of Tables	xvii
Chapter I: Introduction	1
1.1 Motivation	1
1.2 Objectives	2
1.3 Thesis organization	3
Chapter II: Background	4
2.1 Silicon-based ceramics for structural turbine applications	4
2.1.1 Fundamental model of silicon oxidation	6
2.1.2 Oxidation and volatility of silicon-based ceramics	11
2.2 Barrier coatings	14
2.2.1 Thermal barrier coatings (TBCs)	15
2.2.2 Environmental barrier coatings (EBCs)	17
2.2.3 Common processing methods for barrier coatings	19
2.3 Evolution of EBCs	20
2.3.1 Barium-strontium-aluminosilicate (BSAS) EBCs	21
2.3.2 Rare-earth silicate based EBCs	23
2.3.3 Rare earth availability and economics	23
2.3.4 Commonly investigated rare earth barrier coating systems	25
2.3.5 Ytterbium silicate-based EBCs	27
2.4 Failure in TBCs and EBCs	33
2.4.1 Failure mechanisms in TBCs	33
2.4.2 Failure mechanisms in EBCs	35
2.4.3 Bondcoat oxidation-based failure of TBC and EBC systems	36
2.5 Reducing oxidation in YbDS-based EBC systems	37
2.5.1 Modifications to silicon oxidation through chemistry	37
2.6 Steam cycling at NASA Glenn	40
2.7 Residual and internal stresses	42
2.7.1 Synchrotron-based wide angle X-ray scattering (WAXS)	44
2.8 X-ray computed tomography (XCT)	45
Chapter III: Oxidation and Microstructure of $\text{Yb}_2\text{Si}_2\text{O}_7$ -based EBC systems	47
3.1 Background	47
3.1.1 Deal and Grove model of silicon oxidation	47
3.2 Methods	48
3.2.1 Sample preparation	48
3.2.1.1 Multilayer coupon EBC-CMC samples	49

3.2.2	Imaging and chemical analysis	50
3.2.3	Transmission X-ray diffraction	50
3.3	Results	51
3.3.1	Microstructure in coupon-based samples	51
3.3.1.1	Baseline $\text{Yb}_2\text{Si}_2\text{O}_7$	51
3.3.1.2	Alumina-modified $\text{Yb}_2\text{Si}_2\text{O}_7$ (6A)	54
3.3.1.3	Mullite+YAG-modified $\text{Yb}_2\text{Si}_2\text{O}_7$ (M2Y)	60
3.3.1.4	Air exposure and topcoat thickness effects	63
3.4	Discussion	65
3.4.1	Microstructure and dopant effects	65
3.4.1.1	Baseline system	65
3.4.1.2	6A system	66
3.4.1.3	M2Y system	67
3.4.2	TGO growth	68
Chapter IV:	Biaxial Stresses in Ytterbium Disilicate-based EBC/CMC Systems . . .	72
4.1	Analytical modeling of internal stresses	73
4.1.1	Topcoat thickness effects	75
4.1.2	Oxide effects	76
4.2	Materials for <i>ex-situ</i> synchrotron studies	78
4.2.1	Coupon-based, multilayer EBC-CMC samples	78
4.2.2	$\text{Yb}_2\text{Si}_2\text{O}_7$ -based powders	79
4.3	Methods for <i>ex-situ</i> synchrotron studies	80
4.3.1	Internal stresses in thin films and coatings	80
4.3.2	X-ray penetration and absorption in ytterbium-based materials . . .	84
4.3.3	Interplanar spacings	86
4.3.4	Determination of strain-free (or stress-free) lattice parameters	88
4.4	Results and discussion	89
4.4.1	Effects of chemical modifications on $\text{Yb}_2\text{Si}_2\text{O}_7$ lattice parameters . . .	89
4.4.2	Chemistry effects on lattice parameters	91
4.4.3	Strain-free lattice parameters	94
4.4.4	Identification of the TGO with synchrotron diffraction	95
4.4.5	Equibiaxial internal stresses related to chemistry and exposure history	98
4.4.5.1	Effect of annealing on internal stresses	99
4.4.5.2	Stresses in the "annealed" condition	101
4.4.5.3	Stresses after steam cycling	103
4.4.5.4	Internal stresses from TGO growth and microstructure	106
Chapter V:	Interface Toughness Assessments in Ytterbium Disilicate-based EBC/CMC	
	Multilayer Systems	112
5.1	Fracture toughness evaluation of multilayer coatings	112
5.1.1	Cracking toward interfaces in bimaterial systems	112
5.1.2	Fracture toughness measurements with microindentation	115
5.1.3	Elastic-plastic measurements by microindentation	117
5.1.4	Toughness measurements with nanoindentation	119
5.1.5	Elastic-plastic measurements by nanoindentation	120
5.1.6	Single-edge notched beam (SENB) toughness	121

5.2	Methods	122
5.2.1	Sample preparation and imaging	122
5.2.2	Interface cracking	123
5.2.3	Microindentation	124
5.2.4	Nanoindentation	124
5.2.5	Single-edge notched beam (SENB) testing	125
5.3	Results and discussion	126
5.3.1	Microindentation cracking and toughness	126
5.3.2	Nanoindentation cracking and toughness	127
5.3.3	Single-edge notched beam (SENB) toughness	134
Chapter VI: Synchrotron-compatible <i>In-Situ</i> Heating Device		137
6.1	Design	138
6.2	Heating	139
6.3	Atmosphere control and incorporation of steam	141
6.4	Sample positioning and manipulation	143
6.5	Applications	143
6.5.1	Annealing	143
6.5.2	Steam cycling	144
6.5.3	High-temperature measurements at the APS	145
6.5.3.1	Heating and crystallization	145
6.5.3.2	Thermal expansion	147
6.6	Limitations and suggested improvements	151
Chapter VII: Conclusions and Suggestions for Future Work		154
7.1	Summary and conclusions	154
7.1.1	Baseline	154
7.1.2	Alumina-modified (6A)	155
7.1.3	Mullite+YAG-modified (M2Y)	157
7.2	Future work	159
7.2.1	Microstructure and oxidation	159
7.2.2	Synchrotron experiments	161
7.2.3	Interface toughness	162
7.2.4	Induction furnace and <i>in-situ</i> experiments	164
Bibliography		166

LIST OF ILLUSTRATIONS

<i>Number</i>	<i>Page</i>
2.1 Ratio of strength to weight (specific strength) for a range of structural materials. Note the much higher temperature capabilities of CMC materials compared to others. Reprinted from Schmidt et al. with publisher permission ¹⁹	5
2.2 Illustration of the oxidation process described by Deal and Grove, including relevant parameters and fluxes used in the derivation. Adapted from that publication ⁶	8
2.3 Oxide thickness versus time, as plotted by Deal and Grove ⁶ . The significant influence of temperature is visible in each plot. The order-of-magnitude difference of the time scales illustrates the 10x increased oxidation rate in humidity compared to dry O ₂ . Adapted and reprinted with publisher permission.	11
2.4 Specific weight gain of SiC samples in the oxidation studies of Opila ⁴² . Linear-parabolic behavior is observed, as is the significant influence of humidity on oxidation. Reprinted with publisher permission.	12
2.5 Deterioration of a SiC _f /SiC composite in high-temperature, high-pressure steam, before (left) and after (right) exposure. Reprinted from More et al. with publisher permission ⁴⁵	14
2.6 Generalized schematic of desirable barrier coating characteristics. Adapted from Lee ⁹	16
2.7 Turbine components coated in YSZ (left) and Gd ₂ Zr ₂ O ₇ (right), showing the enhanced damage resistance of the gadolinium-based coating. Reprinted with publisher permissions from Levi et al. ¹⁷	17
2.8 Schematic illustration of the plasma-spray technique ⁶¹	20
2.9 Upper section of a mullite EBC after steam cycling, with visibly deteriorated alumina layer where silica had volatilized out of mullite. Reprinted with publisher permission ⁹	21
2.10 BSAS-based multilayer coatings, prior to and after steam cycling. Micrographs are from different samples. Through-thickness cracking is evident in the mullite layer, as well as pores along the mullite-bondcoat interface. Reproduced with publisher permission ⁶⁶	22
2.11 Map of estimated rare earth element reserves, in tons, as listed in the USGS Mineral Commodities Survey, January 2021 ⁷²	24

2.12	Rare earth oxide production (mining) from 1960-2012. Compiled by the United States Geological Survey ⁷³	25
2.13	Volatilities of multiple rare earth silicates, as well as BSAS for comparison. Plot compiled by Fabian Stolzenburg using data originally plotted by Lee et al. ^{11,66}	28
2.14	Post-steam cycling microstructures of yttrium monosilicate (upper left), erbium monosilicate (upper right), ytterbium monosilicate (lower left), and lutetium monosilicate (lower right) based EBC systems. With steam cycling at 1400°C, yttrium monosilicate is almost entirely depleted after 46 hours and erbium monosilicate has developed a glassy layer and through-thickness cracking after 100 hours. Ytterbium and lutetium silicates, steam cycled for 300 hours at 1380°C, showed greater chemical stability, but developed through-thickness cracks. Adapted and reprinted from Lee et al. with publisher permission ⁶⁶	29
2.15	Yb ₂ O ₃ -SiO ₂ phase diagram, as reported in Costa et al. ⁷⁰ . Note the line compounds 1:1 and 1:2 which correspond to the monosilicate and disilicate, respectively, and the melting points of these compounds. Reprinted with publisher permission.	30
2.16	Ytterbium monosilicate sample, after high-temperature exposure to CMAS. The CMAS dissolved significant amounts of the monosilicate. Apatite crystals precipitated from the melt, as shown on the right using SEM and EDS maps as well as TEM selected area electron diffraction. Reprinted from Stolzenburg et al. with publisher permission ¹²	31
2.17	Ytterbium disilicate sample, after high-temperature exposure to CMAS. The well initially filled with CMAS was empty (filled with epoxy for imaging) post-exposure, with CMAS absorbed into the disilicate. Adapted and reprinted from Stolzenburg et al. with publisher permission ¹²	32
2.18	Summary of intrinsic (upper) and extrinsic (lower) failure mechanisms in a barrier coating system. The system illustrated is a columnar EB-PVD TBC. Reprinted from Levi et al. with publisher permission ¹⁷	34
2.19	Undulation in topcoat-oxide-bondcoat structure of multilayer coating system. Reprinted from Schlichting et al. with publisher permission ⁸⁹	36
2.20	Oxidation rates reported by Schlichting. Image adapted from that publication ¹⁴	39
2.21	Illustration of the steam cycling furnace used at NASA Glenn Research Center. Image courtesy of Kang N. Lee.	41
3.1	Overview of the EBC samples studied. Left: microstructure of the as-sprayed EBC layers and top of the substrate. Right: schematic of sample sections.	49

3.2	Microstructure of the baseline as-sprayed condition: (a) topcoat and (b) bondcoat.	51
3.3	Baseline annealed microstructure, in the topcoat (left) and near the topcoat/bondcoat interface.	52
3.4	Topcoat of the baseline 100-hour steam-cycled condition.	53
3.5	SEM micrographs of baseline topcoat/bondcoat interface in as-sprayed and steam-cycled (at NASA GRC) conditions. Red arrows indicate TGO cracking.	54
3.6	WAXS lineouts (normalized intensity vs. d -spacing) for the baseline composition after 1000 hours of steam cycling.	55
3.7	As-sprayed 6A topcoat microstructure, with topcoat (left) and interface (right) shown.	55
3.8	6A annealed microstructure, in the topcoat (left) and near the topcoat/bondcoat interface.	56
3.9	6A, steam cycled for 100 hours (a), 500 hours (b), and 1000 hours (c).	57
3.10	EDS map from the topcoat-bondcoat interface of the 6A 500-hour steam cycled sample.	58
3.11	Selected laboratory XRD patterns for the 6A topcoat.	58
3.12	WAXS lineouts for 6A after 1000 hours of steam cycling.	59
3.13	Microstructure of as-sprayed M2Y topcoat: topcoat (left) and topcoat-bondcoat interface (right).	60
3.14	M2Y annealed microstructure, in the topcoat (a) and near the topcoat/bondcoat interface (b).	61
3.15	Microstructure of M2Y after 100 (left) and 1000 (right) hours of steam cycling. The TGO and TGO cracks are indicated, as are pores/precipitates in the topcoat.	61
3.16	WAXS lineouts for M2Y after 1000 hours of steam cycling.	62
3.17	Baseline 500-hour air sample, with a thinner TGO than in the 500-hour steam-cycled sample.	63
3.18	TGO thicknesses for all compositions and topcoat thicknesses.	64
3.19	TGO thicknesses for all three compositions, showing parabolic behavior.	69
4.1	Predicted stresses in a $\text{Yb}_2\text{Si}_2\text{O}_7$ -based EBC/SiC system, with different topcoat thicknesses and a cooling temperature change of 1300°C	75
4.2	Predicted stresses in a $\text{Yb}_2\text{Si}_2\text{O}_7$ -based EBC/SiC system, with a $250\mu\text{m}$ topcoat and $\Delta T = 1000^\circ\text{C}$. The oxide, and the oxide thickness, have minimal effect prior to the cristobalite transformation.	76

4.3	Predicted stresses in a $\text{Yb}_2\text{Si}_2\text{O}_7$ -based EBC/SiC system, with a $250\mu\text{m}$ topcoat and $\Delta T = 1000^\circ\text{C}$. The oxide, and the oxide thickness, have minimal effect prior to the cristobalite transformation.	77
4.4	Schematic coordinate system for the d -vs- $\sin^2\psi$ method of computing internal stresses in films. Adapted from He ¹¹³	81
4.5	Schematic coordinate system for the d -vs- $\sin^2\psi$ method of computing internal stresses in films. Adapted from Stolzenburg ¹¹	82
4.6	Transmittance of X-rays through $\text{Yb}_2\text{Si}_2\text{O}_7$ over a range of discrete energy values. Curves are plotted for samples of 1.5mm and 2mm thicknesses using data and formulae from NIST ¹¹⁴	85
4.7	Representation of the WAXS setup used at Advanced Photon Source, Beamline 1-ID-E, on left. On the right, the positions (to scale) of all WAXS scans. . . .	86
4.8	Three-dimensional volume of the baseline 1000-hour steam-cycled sample, imaged with tomography and rendered to illustrate material surfaces and interface roughness.	87
4.9	Three-dimensional volume of the baseline as-sprayed sample collected by tomography and shown via 3D rendering, illustrating the macro-scale undulations which can complicate layer depths in WAXS configurations.	88
4.10	WAXS diffraction lineout for the 6A annealed powder. Phases are labeled for peaks above 2\AA d -spacing. The amorphous contribution is from the quartz capillary holding the powder.	91
4.11	The $\text{Yb}_2\text{Si}_2\text{O}_7$ crystal structure, modeled using Vesta software ¹¹⁷ . The crystal is oriented looking down the (a) a , (b) b , and (c) c axes, as well as an off-axis perspective (d).	92
4.12	Diffraction lineouts for the Baseline $\text{Yb}_2\text{Si}_2\text{O}_7$ powders, (a) after plasma-spray processing and (b) after annealing. Intensities are not scaled identically in the diffraction frames. Annealing at high temperature crystallizes the amorphous content in the disilicate, and remaining amorphous signal is from the quartz capillary.	95
4.13	Diffraction patterns of the $\text{Yb}_2\text{Si}_2\text{O}_7$ topcoat, cristobalite TGO, and silicon bondcoat, from bottom to top. The cristobalite TGO is typically not detected in individual diffraction frames in WAXS studies with taller X-ray beams. . .	96
4.14	Diffraction pattern collected using a $2\mu\text{m}$ -tall X-ray beam. These diffraction data were used to identify the topcoat and TGO phases and to fit strains in the TGO.	97

4.15	Internal biaxial stresses for the Baseline system, as-sprayed and annealed samples, as well as from the analytical model of Hsueh et al ¹⁰⁹ (straight lines). . .	99
4.16	Annealed stresses for Baseline, 6A, and M2Y samples, as well as the calculated result from the analytical model.	101
4.17	Stresses measured after 100 hours of steam cycling for all three compositions.	104
4.18	Stresses in 500-hour steam-cycled samples.	105
4.19	Biaxial stresses in the 1000-hour steam-cycled samples.	106
4.20	Internal stresses in Baseline composition multilayer samples, post-anneal and NASA Glenn steam-cycling.	107
4.21	SEM cross-section, after sectioning and polishing, of the Baseline 1000-hour steam-cycled sample, with oxide and damage indicated.	108
4.22	Representative tomography-generated slice, showing relevant features. No cracking is resolvable in the topcoat by tomography.	109
4.23	TGO in the 6A and M2Y systems after 1000 hours of steam cycling. Sharpness is enhanced to show very fine cracks.	109
4.24	Baseline internal stresses at 500 hours, with a NASA Glenn 500-hour air-cycled sample added.	110
4.25	Internal biaxial stresses for the 6A system, annealed and steam-cycled at NASA Glenn.	111
5.1	Schematics of a wedge-loaded crack impinging on an interface between materials. Except for the case of crack arrest, the crack will either penetrate into the neighboring material (left) or deflect along the interface (right). Adapted from Refs. [118] and [119].	113
5.2	Boundary curves for deflection or penetration (indicated) in bimaterial cracking, as adapted from Ref. [118].	114
5.3	Schematic of a Vickers indentation and radial cracks (left), as well as the subsurface half-penny crack configuration (right). Adapted from Anstis et al. ¹²² . . .	115
5.4	Vickers indentation in SiC using 196N load. Toughness measured from crack lengths was approximately $2.4\text{MPa}\sqrt{\text{m}}$	117
5.5	Schematics of a Vickers and Knoop indenter tips and well-formed impressions. Adapted from Ref. [124] and with publisher permission from Ref. [125]. . . .	118
5.6	Schematics of ideal Berkovich and Cube-Corner indenter tips. The more severe angle of the cube-corner tip is much more conducive to indentation cracking. Adapted from Ref. [129].	119
5.7	A Berkovich indenter impression made in $\text{Yb}_2\text{Si}_2\text{O}_7$	121

5.8	Geometry of the Single Edge Notched Beam (SENB) four-point bend test, with relevant features and dimensions labeled. The multi-color notch indicates a bi-material interface toughness test.	121
5.9	Ratio of energy release rates for deflected and penetrating cracks. The Dundurs' parameters for the materials in this work are indicated.	124
5.10	Results from microindentation cracking tests, showing extensive cracking and evidence of compaction in the $\text{Yb}_2\text{Si}_2\text{O}_7$ topcoat. Magnified images (lower) show crack deflection along the topcoat-bondcoat interface. Loads used were 9.8N (left) and 4.9N (right).	126
5.11	Cracks propagated to the topcoat-bondcoat interface from both sides in an as-sprayed baseline sample. Uncoated samples resulted in some surface charging.	128
5.12	Cracks impinging at the interface of the annealed sample. Crack penetration always accompanied very close indenter tip placements, multiple cracks interacting, or extensive chipping.	129
5.13	Cracks propagated to the topcoat-bondcoat interface after 100-hour, 500-hour, and 1000-hour steam cycling intervals.	129
5.14	A Cube-Corner indentation in the silicon bondcoat of the Baseline, 1000-hour steam-cycled sample. Indentation and crack measurements are shown on the right.	130
5.15	Two plots of the ratios of energy release rates for deflected and penetrating cracks, from He and Hutchinson ¹¹⁸ . The Dundurs' parameters for the EBC materials and TGO are indicated.	131
5.16	Internal stresses in the baseline system, from the annealed to 1000-hour steam-cycled conditions. Also shown in Chapter 4.	133
5.17	The SENB sample after failure.	135
6.1	Cross-section illustration of the custom induction furnace (not to scale), and the graphite susceptor with X-ray window.	138
6.2	Placement of the thermocouple using the tomography detector. Image width represents approximately 2mm.	140
6.3	Temperature vs. induction power for the induction furnace.	141
6.4	A baseline sample, annealed in flowing argon for 30 minutes using the custom induction furnace.	144
6.5	A baseline sample, steam cycled for 10 hours at Caltech using the custom induction furnace.	145
6.6	The custom induction furnace, in place and at high temperature (1000°C+) at the APS Beamline 1-ID.	146

6.7	WAXS patterns from the baseline powder: (a) before crystallization (991°C) and (b) after crystallization (1030°C). Remaining amorphous background is from the quartz capillary and furnace tubing. Axis values are pixels on the 2D detectors. Red pixels represent higher intensity.	147
6.8	WAXS fitting of the $\text{Yb}_2\text{Si}_2\text{O}_7$ (200) peak in the baseline (a and c) and 6A (b and d) powders. With baseline and 6A at 915-920°C (a and b), additional peak intensity distorts fitting in 6A (b). After crystallization and upon cooling to $\sim 910^\circ\text{C}$, both baseline and 6A peaks are readily fit as single peaks (c and d).	148
6.9	Normalized expansion vs. temperature for the baseline $\text{Yb}_2\text{Si}_2\text{O}_7$ powder. . .	149
6.10	Normalized expansion vs. temperature for the 6A and M2Y $\text{Yb}_2\text{Si}_2\text{O}_7$ -based powders.	150
6.11	Calculated stresses, based on the model by Hsueh et al. ¹⁰⁹ , with CTEs for (200) and (001) peaks.	152
6.12	WAXS pattern from the empty induction tube furnace. Amorphous background from fused quartz and crystalline peaks from α -cristobalite indicate some devitrification of the tubing after extensive use.	153
7.1	WAXS data collection on a cylindrical specimen. Figure reprinted from Siddiqui et al. ¹⁰⁰ with publisher permission.	161
7.2	Nano/micro-scale three-point bend setup. Figure reprinted from Tertuliano et al. ¹⁴⁵ with publisher permission.	164

LIST OF TABLES

<i>Number</i>	<i>Page</i>
2.1 Compiled properties of structural materials, including those discussed for turbine engines (highlighted).	6
2.2 Rare earth oxide prices, as listed online by Fisher Scientific in mid-2021. . . .	24
2.3 A brief list of residual stress measurement techniques, with relevant parameters. Adapted from Withers and Bhadeshia ⁹⁶	43
3.1 TGO thicknesses for all three compositions and conditions, with topcoat thicknesses of 250 μ m. Percent change values are compared to baseline values. . . .	69
4.1 Materials properties input to the analytical model for predicting biaxial stresses.	74
4.2 Lattice parameters of Yb ₂ Si ₂ O ₇ -based topcoat materials. Powder diffraction file (PDF) parameters and measured $d_0^{(021)}$ values for strain calculation are included for reference. Error analysis is discussed in subsection 4.1.1.	90
4.3 Materials in the multilayer structure, along with the peaks used for analysis, d_0 spacings, and related elastic properties.	98
5.1 Toughness values for the layers and topcoat/TGO interface in the baseline 1000-hour steam-cycled condition.	132
6.1 H ₂ O and O ₂ flow rates, from the work of Opila ⁷ (marked *) and this work. H ₂ O liquid and O ₂ flow rates determined the H ₂ O vapor and total flow rates.	142
6.2 Tabulated CTE data, from this work and that of Stolzenburg et al. ^{11,99} . Average (\sim bulk) values are from the three principal directions and do not include (021). R ² values marked * are only fit with two points.	151
7.1 Summarized results from this work.	159

Chapter 1

INTRODUCTION

1.1 Motivation

Gas-burning turbine engines play critical roles in aerospace transportation and electrical power generation, two areas where energy efficiency are receiving increasing attention. Thermodynamically, improvements to engine efficiency can be made by increasing the engine operating temperatures. Through the history of gas-burning turbine engines, metal alloys have been the most suitable structural materials. Although ever-increasing operating temperatures have led to the development stronger, high-temperature alloys, further increases in operating temperature require thermal protection of the alloys. Cooling of the alloy components permits higher combustion temperatures, but active systems sap efficiency from the system. Thermal barrier coatings (TBCs) have been developed extensively to provide a layer of low thermal conductivity between the engine environment and the alloy material. Active cooling and TBCs are incremental improvements which have progressively permitted higher alloy temperatures.

A revolutionary approach to high-temperature gas burning turbine engines is the use of ceramics as structural materials. In particular, silicon-based ceramics (SiC and Si_3N_4) have much higher melting temperatures than most alloys and are additionally less dense, reducing the weight of analogous components. The use of monolithic ceramic materials in turbine engines was estimated by Grondahl and Tsuchiya to improve combined cycle engine efficiency by 2-3%¹. A few years ago, in 2017, the United States commercial aviation industry consumed an estimated 720-860 TWh of energy from fuels²⁻⁵. Assuming efficiency gains of 2-3% are applied to the industry, implementation of ceramic structural materials could save an estimated 14.4-25.8 TWh of energy. Those energy savings equate to more than 10% of the solar energy consumed by the United States in that same year.

However, silicon-based ceramics are chemically vulnerable in the high-temperature combustion environment. Silica (SiO_2) develops as a native oxide on silicon in air and in water vapor, both of which are present in the combustion environment^{6,7}. Silicon oxidation rates increase with temperature, and at high temperatures the oxide additionally reacts with water vapor to form volatile silicon hydroxide. Combined oxidation and recession of the oxide by volatilization result in rapid recession of silicon-based ceramics in simulated combustion engine exposures⁸.

Environmental barrier coatings (EBCs) are under development to protect silicon-based ceramics from the harsh chemical environments experienced in gas-burning turbine engines. Yttria-stabilized zirconia (YSZ), mullite, and barium-strontium aluminosilicate (BSAS) coatings were early EBC candidate materials, but these coatings were limited by phase transformations, thermal mismatch, and silica volatility^{9–11}. Rare earth (RE) silicates have been identified and studied extensively as promising EBC materials due to their low silica volatility and high-temperature chemical stability. Ytterbium silicates, in particular ytterbium disilicate ($\text{Yb}_2\text{Si}_2\text{O}_7$) received attention for their favorable performance and economic viability. $\text{Yb}_2\text{Si}_2\text{O}_7$ has additionally been observed to perform well upon interaction with calcium-magnesium aluminosilicate (CMAS)^{12,13}. CMAS is a common molten glass contaminant in turbine engines, coming primarily from volcanic eruptions in aerospace applications and from sands and soils in stationary gas turbine operations. Considerations of layer bonding and thermal expansion compatibility have led to a common EBC design: a RE silicate EBC topcoat, a silicon bondcoat, and the SiC_f/SiC CMC substrate. Additional layers are sometimes added as diffusion barriers or thermal expansion gradients.

One major remaining challenge for current-generation EBCs is the oxidation of the silicon bondcoat, which occurs as the development of a thermally grown oxide (TGO) on the silicon surface. Silica TGOs introduce a new layer into the EBC/CMC system, disrupting thermal expansion compatibility and altering the adherence of the layers, both carefully chosen properties in designing EBCs. Dopant oxides have been shown to alter TGO growth rates in both amorphous silica/silicon and EBC/CMC systems^{14,15}. It is expected that TGO growth will affect internal stresses, through thermal mismatch, and have deleterious effects on layer bonding in EBC/CMC systems.

1.2 Objectives

There are four primary objectives of this work. The first is to assess microstructure and bondcoat TGO growth in doped $\text{Yb}_2\text{Si}_2\text{O}_7/\text{Si}$ EBC systems. Microstructure is explored as a function of heat treatment and steam cycling exposure for one unmodified and two modified $\text{Yb}_2\text{Si}_2\text{O}_7$ -based systems, where dopant effects are observed using microscopy and synchrotron X-ray transmission diffraction. TGO thickness, measured over time, allows for an assessment of growth rates and the effects of dopants on those rates.

The second objective is to use synchrotron diffraction techniques to measure internal strains (and hence internal stresses) in the multilayer EBC/CMC systems. Quantification of internal stress evolution along with TGO growth is necessary for understanding the role of TGO growth on the reliability of the EBC/CMC systems. Special care must also be taken to

ensure that dopant effects are taken into account when calculating strains, which necessitates an assessment of dopant effects on phases and lattice parameter changes.

The third objective is to assess interfacial fracture toughness in EBC/CMC systems, primarily that of the topcoat/bondcoat interface. TGO growth is expected to alter the toughness of the interface with the bondcoat and topcoat. Exploration of the interface toughness, using indentation techniques, provides for an estimation of interface toughness especially as it relates to layer toughnesses. Traditional, macro-scale interface toughness experiments are also used to address limitations of the indentation techniques.

The fourth objective is to develop a method by which to assess internal stresses and microstructure developments of EBC/CMCs *in-situ* during steam cycling at the synchrotron. Synchrotron measurements have been coupled with high temperature sample exposures previously, but water vapor has not been implemented in such experiments. A custom induction furnace is designed and developed which enables both steam cycling and synchrotron X-ray measurements, two capabilities which have not been combined before.

1.3 Thesis organization

This thesis is organized generally in the order of the objectives listed above. Chapter 2 provides necessary context and background for the materials problems at hand, as well as the inspiration and approach for minimizing TGO growth in EBC/CMC systems. Information on the techniques used to study and characterize materials in this work is also presented. Chapter 3 includes an assessment of microstructure and TGO growth in baseline and dopant-modified EBC/CMC systems as related to heat treatment, steam cycling, and chemistry. TGO growth rates and the effects of chemistry are also discussed. An analysis of internal strains and stresses in the baseline and modified EBC/CMC systems is presented in Chapter 4, preceded by the background for the techniques used. Additional analyses are included of the lattice parameter changes produced by dopant additions. Chapter 5 details mechanical analyses of interface toughness baseline EBC/CMC systems after steam cycling and TGO growth. This includes a new combination of indentation methods, as well as implementation of a bend testing method to address limitations of indentation analysis. Chapter 6 details the development of a custom induction furnace capable of *in-situ* steam cycling at the synchrotron. Multiple applications for the furnace are detailed, including separate steam cycling experiments and high-temperature synchrotron measurements. Chapter 7 summarizes the discoveries of this work and suggests future work in both EBC/CMC work and for the techniques used.

BACKGROUND

2.1 Silicon-based ceramics for structural turbine applications

For many years, metals and metal-based superalloys have been the standard and most feasible structural materials for turbine engine applications. Years of study and implementation of these materials have characterized their formability through component processing, their high fracture toughness, and their failure behavior. However, one major limitation of these structural materials is their melting point of approximately 1300°C, which prevents operation of the turbine engine at higher temperatures without intervention. Extensive materials research has been invested into increasing the operating temperatures of metallic and superalloy structural engine materials, resulting primarily in the development of thermal barrier coatings (TBCs) which protect the substrate structural material from higher engine temperatures. Advances in these coatings, which are primarily yttria-stabilized zirconia (YSZ) or rare earth zirconates, as well as improved cooling and/or improved engine designs has allowed for incremental increases in engine operating temperatures^{16,17}. To unlock a substantial increase in engine operating temperature, though, new structural materials or materials systems must be implemented in the place of metallic or superalloy-based components.

Ceramics possess many advantages over metals and alloys, particularly in high-temperature applications. Due to their very strong covalent and/or ionic chemical bonds, ceramics typically have much higher melting or sublimation temperatures than do metals. This allows ceramics to maintain their strength at temperatures much higher than the melting points of most metals, as illustrated in Fig. 2.1. Ceramics are typically less dense than metals, as well. Any weight that can be saved in the turbine engine will also improve efficiency, so lower density is advantageous.

Historically the strong covalent or ionic chemical bonding in ceramics has resulted in very strong materials which can survive at high temperatures yet can endure only small amounts of strain and plastic deformation. Strain to failure in many ceramics is less than 1%¹⁸. This behavior contrasts with that of metallic or alloy materials. Those materials inherit their fracture toughness from their less stiff (compared to covalent and ionic) metallic bonds which permit dislocation motion through the crystal structure and allow for extensive plastic deformation prior to crack extension. Toughness is resistance to crack extension, and sometimes can be conceptualized as the integral of strength and deformation (or stress and

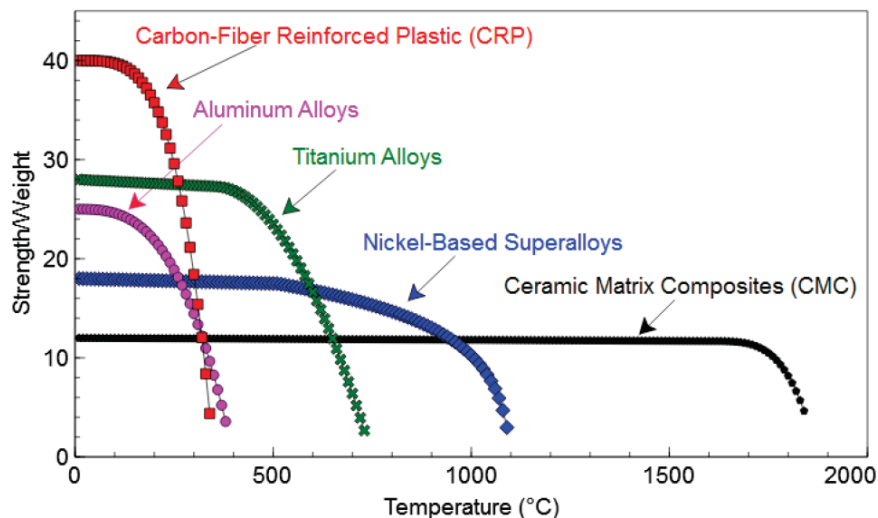


Figure 2.1: Ratio of strength to weight (specific strength) for a range of structural materials. Note the much higher temperature capabilities of CMC materials compared to others. Reprinted from Schmidt et al. with publisher permission¹⁹.

strain) prior to cracking, wherein very small strain tolerance greatly reduces the toughness of a material even in the case of high strength. Their infamous brittleness has prevented ceramics from being used in structural applications due to the need for structural materials to endure fatigue, high-temperature creep, and impacts—or at least due to the need for non-catastrophic failure as these processes take place.

To keep the desirable properties of ceramic materials and yet make a ceramic suitable for structural applications, ceramic matrix composites (CMCs) have been developed. In the case of this work, a composite silicon carbide fiber weave in a silicon carbide matrix (SiC_f/SiC) both keeps its very high strength and makes use of toughening mechanisms, primarily the deflection of cracks around the SiC fiber phase and pullout of the fibers from the surrounding matrix upon crack extension. Increasing the distance the cracks must travel, and changing their trajectory in mechanical loading conditions which are otherwise unchanged, necessarily increase the energy required to advance the cracks and thereby increases fracture toughness. Similarly, increasing the amount of energy needed to propagate a crack by forcing the pullout of a fiber phase from its surrounding matrix will improve the fracture toughness. This approach to toughening has increased the fracture toughness of SiC_f/SiC CMCs well past the point of most bulk ceramics, bringing them into competition with some traditional metals and into consideration for use as structural materials in turbine engines²⁰. Table 2.1 collects some of the key materials properties for a series of metals and ceramics, as well as ceramic-matrix composites^{19,21–23}. Compiled properties of several materials are arranged generally

Table 2.1: Compiled properties of structural materials, including those discussed for turbine engines (highlighted).

Material	Density (g/cm ³)	Fracture toughness (MPa√m)	T _{melt} (°C)	T _{sublime} (°C)
Aluminum alloy 2024-T3	2.77 ²⁴	44 ²⁴	502-638 ²⁵	–
Titanium alloy Ti-6Al-4V	4.43 ²⁴	44-66 ²⁴	1604-1660 ²⁶	–
4340 Steel °C	7.85 ²⁴	50-87.4 ²⁴	1427 ²⁷	–
718 Inconel (Ni-based superalloy)	8.92 ²³	66 ²³	1336 ²³	–
SiC/SiC composites	2.5 ²⁸	41.5 ²⁸	–	2300 ²²
Y ₂ O ₃ -doped Si ₃ N ₄	3.21 ²²	6-8 ²⁹	–	1900 ²²
Y ₂ O ₃ -stabilized ZrO ₂ (YSZ)	5.96 ³⁰	5-12 ^{31,24}	2681-2847 ³²	–
Al ₂ O ₃	3.98 ²⁴	2.5-5.9 ^{33,34}	2072 ³⁵	–
Bulk SiC	3.18	2.4	–	2300

by fracture toughness, including structural superalloy and ceramic materials intended for use in turbine engines (highlighted). Common structural alloys and ceramics are included for context and comparison.

Many key limitations of metal/alloy structural materials in turbine combustion engines are addressed by the development of silicon-based CMCs, in particular SiC_f/SiC CMC as mentioned above. While SiC_f/SiC surpasses the thermomechanical limitations of alloys, it is however vulnerable to the chemistry of the high-temperature combustion environment. As will be discussed in detail below, oxygen and water vapor—unavoidable in a combustion engine—present a challenge to SiC_f/SiC CMCs given their silicon content.

2.1.1 Fundamental model of silicon oxidation

Given the importance of oxidation as a failure pathway in EBC/CMC systems, it is necessary to understand some of the fundamental factors that influence oxide growth.

Deal and Grove, working for Fairchild Semiconductor in the 1960s, produced a keystone description of the oxidation of silicon. General relationships were described for the silicon oxidation process, and key descriptors including rate constants and possible inflection points between different regimes of oxidation were highlighted. Particular attention was paid to temperature, humidity, and partial pressure in the oxidizing environment⁶.

Primary aspects and outcomes of the Deal and Grove analysis will be covered to highlight the effects of oxidation conditions on oxide growth. The analysis considers three primary fluxes, as shown in Fig. 2.2. The flux F_1 of oxidants from the gas to the vicinity of the oxide surface is

$$F_1 = h(C^* - C_0) \quad (2.1)$$

where h is a gas-phase transport coefficient and represents a rate constant for flux at the gas-oxide interface. C^* is the equilibrium concentration of the oxidant in the oxide, and C_0 is the concentration of the oxidant at the outer surface of the oxide at any given time. C^* is related to the partial pressure of the oxidant in the gas through Henry's law:

$$C^* = Kp \quad (2.2)$$

where K is the gas solubility parameter from Henry's Law and p is the partial pressure of the oxidant. Next, the flux F_2 of oxidants through the oxide is

$$F_2 = D_{eff} \left(\frac{C_0 - C_i}{x_0} \right) \quad (2.3)$$

where D_{eff} is the effective diffusion coefficient, C_i is the concentration of the oxidant near the oxide-silicon interface, and x_0 is the thickness of the oxide layer. The fractional term, the concentration gradient of oxidants across the oxide, is frequently shortened to $-dC/dx$. The third flux is

$$F_3 = kC_i \quad (2.4)$$

where k is the rate constant associated with the silicon surface. In steady state oxidation conditions, all three fluxes are equal

$$F_1 = F_2 = F_3 = F. \quad (2.5)$$

Solving $F_1 = F_2$ and $F_2 = F_3$ with the assumption of diffusion-controlled oxidation and incorporating N_1 , the number of oxidant molecules incorporated into a unit volume of the oxide layer, gives the differential equation describing the rate of growth of the oxide:

$$\frac{dx_0}{dt} = \frac{F}{N_1} = \frac{kC^*/N_1}{1 + \frac{k}{h} + \frac{kx_0}{D_{eff}}}. \quad (2.6)$$

The general initial condition for the equation assumes that there is some pre-existing oxide layer with thickness x_i present before the oxidation step under study. This permits inclusion of previous oxidation steps and can account for initial oxide layers present due to electric fields (intrinsic and applied) and space charge effects. Accounting for an initial oxide layer thickness sets

$$x_0 = x_i \text{ at } t = 0. \quad (2.7)$$

The solution to this differential equation is

$$x_0^2 + Ax_0 = Bt + x_i^2 + Ax_i \quad (2.8)$$

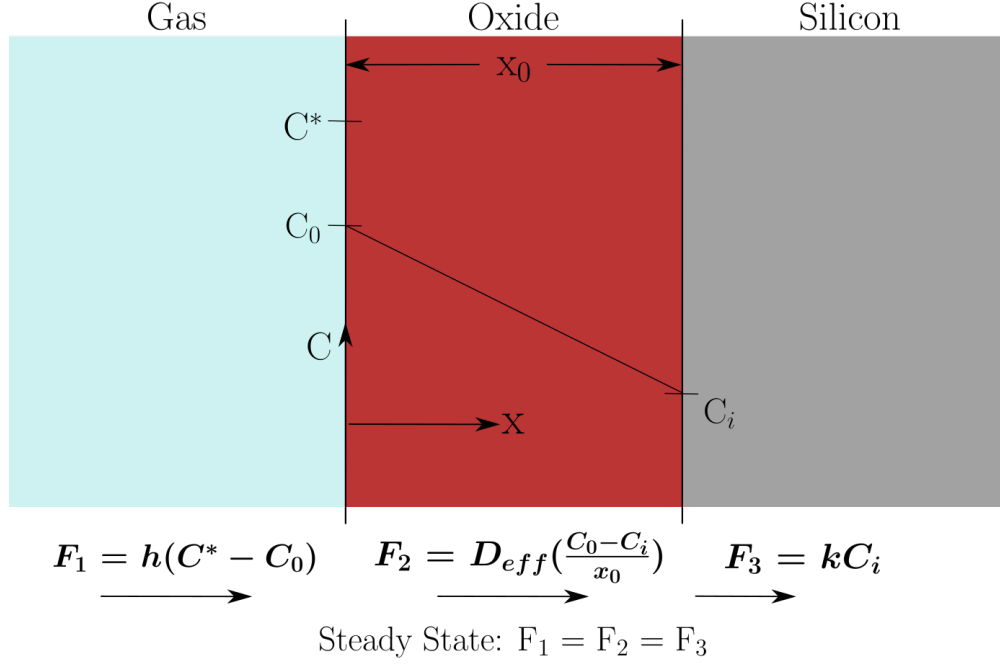


Figure 2.2: Illustration of the oxidation process described by Deal and Grove, including relevant parameters and fluxes used in the derivation. Adapted from that publication⁶.

or, upon rewriting,

$$x_0^2 + Ax_0 = B(t + \tau). \quad (2.9)$$

In this solution,

$$A \equiv 2D_{eff}(1/k + 1/h) \quad (2.10)$$

$$B \equiv 2D_{eff}C^*/N_1 \quad (2.11)$$

$$\tau \equiv (x_i^2 + Ax_i)/B. \quad (2.12)$$

Solving the re-written, quadratic solution to Eq. 2.5 results in

$$\frac{x_0}{A/2} = \left[1 + \frac{t + \tau}{A^2/4B}\right]^{\frac{1}{2}} - 1 \quad (2.13)$$

which is a general relationship for predicting the oxide thickness as a function of time. For short times, where $t \ll A^2/4B$,

$$\frac{x_0}{A/2} \cong \frac{1}{2} \left(\frac{t + \tau}{A^2/4B}\right) \quad (2.14)$$

or

$$x_0 \cong \frac{B}{A}(t + \tau) \quad (2.15)$$

where there is a linear relationship between time and oxide thickness. Thus, this extreme considers the linear oxidation regime. In this approximation, the coefficient

$$\frac{B}{A} = \frac{kh}{k+h} \left(\frac{C^*}{N_1} \right) \quad (2.16)$$

is the linear rate constant. Conversely, for long oxidation times where $t \gg A^2/4B$ and $t \gg \tau$,

$$\frac{x_0}{A/2} \cong \left[\frac{t}{A^2/4B} \right]^{1/2} \quad (2.17)$$

or

$$x_0^2 \cong Bt. \quad (2.18)$$

Here the correspondence is between time and the *square* of the oxide thickness. B is the parabolic rate constant, and this extreme is considered the parabolic oxidation regime.

The inflection point between linear and parabolic oxidation regimes can be described relative to the characteristic time of the oxidation process,

$$\frac{A^2}{4B} = \frac{D_{eff}N_1}{2C^*(1/k + 1/h)^2}, \quad (2.19)$$

or by the characteristic distance of the oxidation process

$$\frac{A}{2} = \frac{D_{eff}}{1/k + 1/h}. \quad (2.20)$$

The criterion for linear oxidation is satisfied when oxidation time is less than the characteristic time or the oxide thickness is less than the characteristic thickness. The criterion for parabolic oxidation is met when the oxidation time or oxide thickness are larger than the characteristic time and distance, respectively.

There is a useful expression which describes a combined linear-parabolic behavior in the oxidation of silicon, as well:

$$\frac{x}{A/2} = \left[1 + \frac{t}{A^2/4B} \right]^{1/2} - 1. \quad (2.21)$$

This expression holds when the oxidation conditions lie somewhere between entirely linear and entirely parabolic regimes. It is important to note that the distinctions between linear, parabolic, and linear-parabolic will reflect the oxidation conditions, as illustrated through the presence of the variables A and B in Eq. 2.20.

Deal and Grove's experiments, and their analysis of the experiments of others, showed a strong relationship between the parabolic rate constant and temperature. The exponential, Arrhenius-type dependence of silicon oxidation upon temperature allowed for the assessment

of activation energies for the diffusion of oxidants through the oxide layer. Arrhenius behavior is described generally by the equation:

$$k = Ae\left(\frac{-E_a}{RT}\right). \quad (2.22)$$

In this case, k is a generic rate constant, A is a pre-exponential term, E_a is the activation energy, R is the universal gas constant, and T is temperature in Kelvin. A logarithmic plot of the rate constant against the inverse of temperature yields the pre-exponential component and the activation energy, which are respectively the y-intercept and the negative of the slope if the plot is linear. Activation energies for oxidation in wet and dry oxidation experiments also corresponded to the activation energies of the diffusivities of oxygen and water through fused silica in temperature-dependent oxidation experiments. The dependence of silicon oxidation on temperature underscores the necessity of understanding oxidation in silicon-based engine materials to design for increased temperatures in the combustion environment.

The parabolic rate constant in experiments is much higher for wet-oxygen oxidation than for dry oxidation, yet the diffusivity of water is lower than that of oxygen in fused silica. However the flux of the oxidant, and therefore the parabolic rate constant B , is proportional to the equilibrium concentration of the oxidant C^* . The equilibrium concentration for water in fused silica is three orders of magnitude higher than that for oxygen. The difference in solubility of the oxidizing species overcomes the difference in diffusivity, and accounts for the enhanced oxidation rates of silicon in wet-oxygen conditions. Fig. 2.3 shows the oxide thickness vs. time plots of Deal and Grove, with dry oxidation on the left and humid oxidation on the right⁶. Notice that similar oxide thicknesses are reached approximately 10x faster in humid oxidation. Since water vapor bears critical influence on the oxidation rate of silicon, and water vapor is unavoidable in the combustion engine environment, it is critical to incorporate humidity into studies of the oxidation of silicon and silicon-based materials.

The parabolic rate constant was also shown to be proportional to the partial pressure of the oxidant in the gas. This finding is important in its own right, since it shows the positive correlation of partial pressure of the oxidant on the oxidation process. Additionally, assumptions made about the pressure dependence of the parabolic rate constant depended on Henry's Law, which in turn relies on the absence of dissociation of diffusing species at the oxide-atmosphere interface. Clear dependence of oxidation on oxidant partial pressure thus allowed Deal and Grove to infer that the diffusing species in dry oxidation is molecular oxygen, and that in wet oxidation it is undissociated water. Deal and Grove noted from earlier research by Jorgensen that the effect of electric fields on oxidation indicates the negatively charged superior O_2^- may be the diffusing species in dry oxidation^{6,36}.

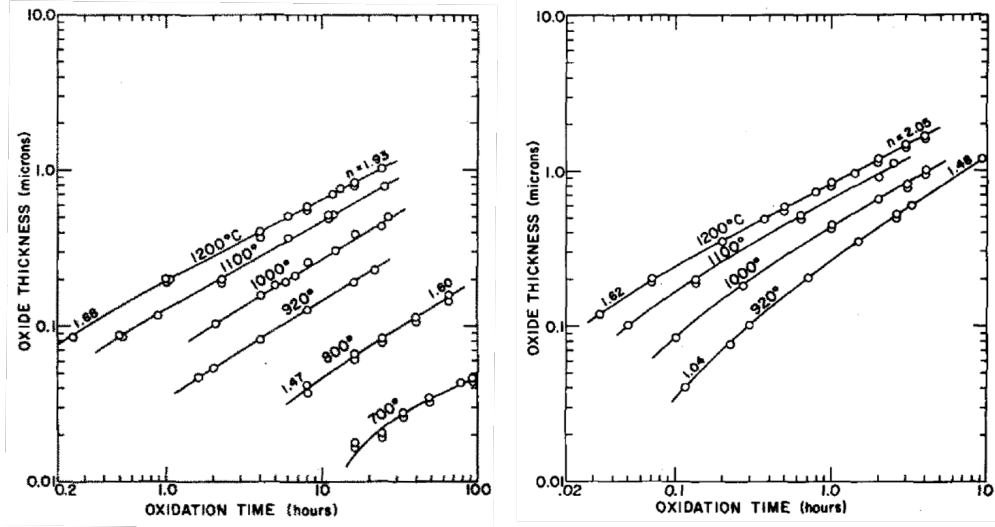


Figure 2.3: Oxide thickness versus time, as plotted by Deal and Grove⁶. The significant influence of temperature is visible in each plot. The order-of-magnitude difference of the time scales illustrates the 10x increased oxidation rate in humidity compared to dry O₂. Adapted and reprinted with publisher permission.

2.1.2 Oxidation and volatility of silicon-based ceramics

In the combustion engine environment, silicon oxidation, volatilization of the oxide, and overall material recession limit the use of silicon-based ceramics as structural materials. Prior to implementation of these new structural materials, it is necessary that these processes be understood and mitigated as much as is feasible. The framework of Deal and Grove is modified and applied to silicon-based ceramics. A description of volatilization expands on the model of oxidation to include further degradation in the combustion environment.

At temperatures above 800 or 900°C, oxidizing species in the combustion environment react with silicon in silicon-based ceramics to form silica (SiO₂), as noted in Eq. 2.22^{6,37}.



For pure silicon, Deal and Grove described the rate-limiting step for oxidation in humid environments as the diffusion of water vapor through the oxide layer to the oxide-silicon interface⁶. In the case of SiC, oxidation has been analyzed with several possible rate-limiting mechanisms proposed. It has been noted that oxidation of silicon carbide powders does in some ways mimic oxidation of silicon, and in fact several general details of oxidation hold true for both silicon and silicon carbide³⁸. Some other studies have focused on the outward diffusion of CO from SiC either as the rate-limiting step in itself or as a combined rate-limiting step along with the inward diffusion of oxygen^{39,40}. The crystallinity of the silica

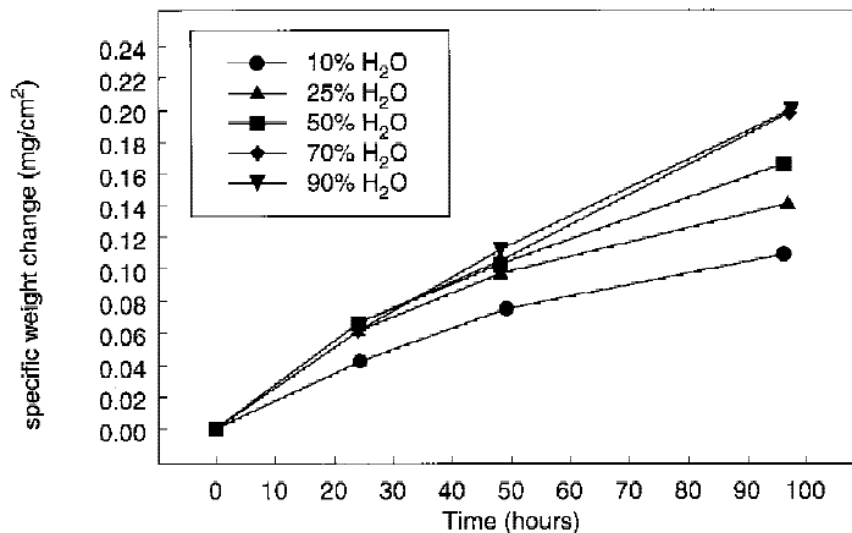


Figure 2.4: Specific weight gain of SiC samples in the oxidation studies of Opila⁴². Linear-parabolic behavior is observed, as is the significant influence of humidity on oxidation. Reprinted with publisher permission.

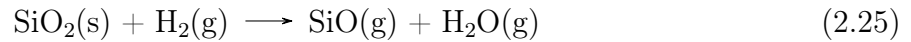
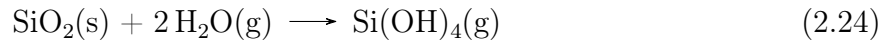
scale and possible dissociation of oxidizing species have been considered for their possible influence on oxidation rate, as well⁴¹.

Opila put forth a study describing the rate limiting mechanisms in the oxidation of SiC coupons as the inward diffusion of H₂O and the outward diffusion of OH⁻. These coupled mechanisms accounted for the unique power-law exponent derived in this and other wet-oxidation experiments⁷. Again in the case of silicon carbide oxidation, although the diffusivity of water in silica is 100 times lower than that of oxygen, the solubility of water is 1000 times higher than that of oxygen. Thus, the presence of water vapor in the oxidizing atmosphere was shown to increase oxidation of silicon carbide by approximately an order of magnitude. The large increase in oxide growth on silicon carbide with the presence of water vapor is shared with silicon as it was discussed by Deal and Grove^{6,7}.

Opila also made use of the linear-parabolic rate law for oxidation for intermediate oxidation times and temperatures, described in subsection 2.2.1 above. This expression models the oxidation at times or oxide thicknesses where both reaction rate (linear) and diffusion rate (parabolic) effects influence oxidation rate. At lower temperatures or short times, linear behavior holds while at higher temperatures or longer times, parabolic behavior holds^{6,7}. Fig. 2.4, from Opila's work⁴², shows the linear-parabolic curves of specific weight change during oxidation versus time for a series of relative humidities in the oxidizing environment, emphasizing the role of humidity in the oxidation of silicon carbide⁴².

A more recent review and experimental study by Wilson and Opila extended the work on oxidation of SiC to consider Hi-Nicalon SiC fibers⁴³. Linear and parabolic oxidation behaviors were observed and activation energies calculated much as can be done for silicon and bulk SiC⁴³. Studies of SiC oxidation have also considered ceramic-matrix composites, which can be vulnerable to excess oxidant ingress along the fiber tows in the composite. Additionally, the effect of impurities on oxidation in CMCs has been studied. Boron nitride, a common interphase material between SiC fibers and SiC matrix in ceramic-matrix composites, contributes boron at high temperatures which increases the initial oxidation rate dramatically⁴⁴.

The silicon oxide scale tends to be stable in moisture-free environments and unstable in humid conditions. As mentioned previously, humidity is unavoidable in the combustion environment, and so the silica scale will be unstable in the combustion engine. There are two main proposed degradation reactions leading to the volatilization and instability of the oxide scale. The first is that water vapor in the environment can react with the silica to form silicon hydroxide (Eq. 2.23). Alternatively, hydrogen gas in the environment could react with the silica scale to form gaseous silicon monoxide (Equation 2.24)^{7,42}.



At engine operating temperatures, these reaction products are volatile compounds which evaporate and deteriorate the oxide, reducing oxide thickness and, for thin oxides, possibly leaving bare silicon behind. Repeated cycles of silicon oxidation, formation of volatile compounds, and evaporation of those compounds lead to rapid material recession of silicon-based ceramics in engine steam cycling. The kinetics of this process have been described in the literature as paralinear, since the oxidation process is parabolic and the volatilization process is linear. Fig. 2.5 shows this deterioration in the case of SiC_f/SiC samples exposed in a high-temperature (1204°C), high pressure (10atm) rig⁸. In that study, there was volatilization of approximately 500 microns of the material and severe structural damage to another 500 microns. In addition to fundamental oxidation parameters from classical oxidation models^{42,45}, the authors attributed the dramatic recession in the high-pressure, air+15% H₂O atmosphere to a moving boundary of dense, vitreous silica which converted to porous cristobalite and allowed oxidation to proceed rapidly. Still, as mentioned above, the presence of water vapor at high temperatures accelerates the oxidation of silicon and volatilization of the oxide, supplying a critical component in the degradation process.

Operating conditions in the engine have large influence on the described degradation process. It is known that the oxide thickness, time to steady-state recession, and steady-state

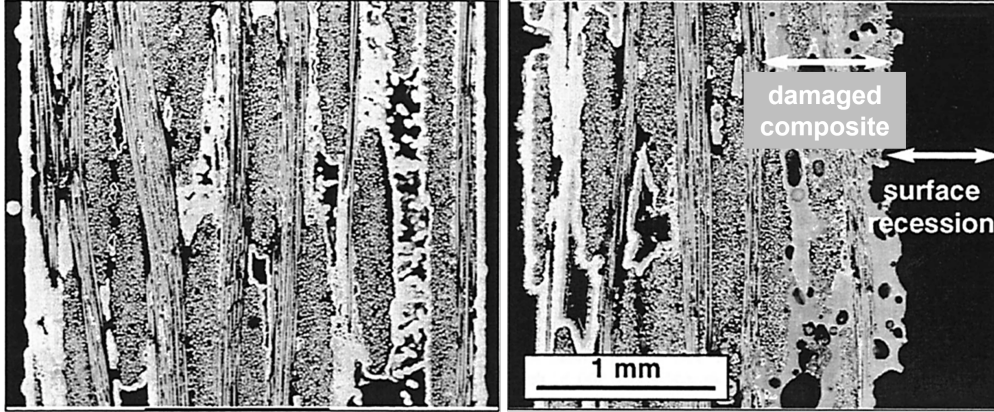


Figure 2.5: Deterioration of a SiC_f/SiC composite in high-temperature, high-pressure steam, before (left) and after (right) exposure. Reprinted from More et al. with publisher permission⁴⁵.

recession rate depend on engine conditions (gas flow velocity, temperature, partial pressure of water vapor, total pressure) and thermodynamic behaviors (enthalpies of oxidation and volatilization)⁴⁶. Generally, the Arrhenius-type behavior of the degradation chemistry underpins the exponential response of oxidation and volatilization to increased temperature. Recession rates also increase along with gas flow velocity and engine pressure, both of which may be used to improve engine efficiency⁴⁶.

The coupled problems of oxidation and volatilization for SiC_f/SiC structural materials necessitate the formulation of coating materials to protect the structural materials from the inherent chemistry of the combustion environment. While the vulnerabilities of silicon-based ceramics in combustion engines are not the same as those of metallic and superalloy materials, some progress in coating systems for the more traditional structural materials can be used to guide the development of coatings for silicon-based ceramics.

2.2 Barrier coatings

A barrier coating is a material layer applied to a substrate in order to protect the substrate from a deleterious condition or environment. These coatings are commonly applied to materials which are expected to survive in harsh or extreme environments. Thermal barrier coatings protect substrate materials from high temperatures, preserving the mechanical strengths of the structural substrates. Environmental barrier coatings, on the other hand, protect substrate materials from corrosive environments and harsh chemistries. Barrier coatings can serve other, and also combined, purposes, but the following explanations focus on the purposes and properties of thermal and environmental coatings.

2.2.1 Thermal barrier coatings (TBCs)

Thermal barrier coatings (TBCs) have been used for more than 45 years in metallic engine systems to protect the structural alloys from the high temperatures in the engine⁴⁷. Alloys are thermomechanically vulnerable to especially high temperature environments, such as the combustion engines in which they are in service. With increasing engine temperature, an unprotected alloy component will lose its structural stability. Thus, the primary goal of thermal barrier coatings is to allow for high surface temperatures at the coating-atmosphere interface while maintaining lower temperatures at the coating-substrate interface, making low thermal conductivity a critical and necessary property for TBC materials⁴⁷⁻⁴⁹. While environmental barrier coatings (EBCs) for ceramics are designed for different properties than TBCs, many of the basics of coating design as applied to TBCs carry over to understanding EBC efficacy⁹.

Aside from low thermal conductivity, effectively protecting alloy structural materials from high temperatures, TBC systems must possess good adhesion between the coating and substrate, good agreement in thermal expansion between the coating and substrate, and durability of the coating material in the engine environment. Good adhesion helps to maintain the layered TBC/substrate structure and prevent premature spallation of the TBC from the substrate. This is especially important because the coefficients of thermal expansion, or the relative expansion or contraction of a material with changes in temperature, of the TBC material(s) and the substrate alloy are not a perfect match. Due to changes in temperature, CTE mismatch produces stresses which are compressive in some layers and tensile in others, which can then lead to cracking and, some, spallation of the TBC. Durability of the TBC material in the engine environment is also critical because it ensures the phase stability of the TBC material even upon prolonged exposure to humidity and to inevitable contaminants in the turbine engine, including molten glasses such as calcium-magnesium aluminosilicates (CMAS). Fig. 2.6 is a generalized illustration of desired traits for both thermal and environmental barrier coatings.

Yttria-stabilized zirconia (YSZ) is a common TBC material which has been used on nickel-based superalloy components, with research into these TBCs dating back to 1976. YSZ is a popular TBC material because of its very low thermal conductivity of approximately $2.3\text{Wm}^{-1}\text{K}^{-1}$ ⁵⁰. This low thermal conductivity is attributed to phonon scattering off the concentrated oxygen vacancies in the YSZ structure, which greatly diminishes phonon transport and thus heat transfer through the crystalline YSZ layer.

The coefficient of thermal expansion of YSZ, approximately 11×10^{-6} , is not a perfect match for those of nickel superalloy substrates, which are typically around 14×10^{-6} . This mismatch

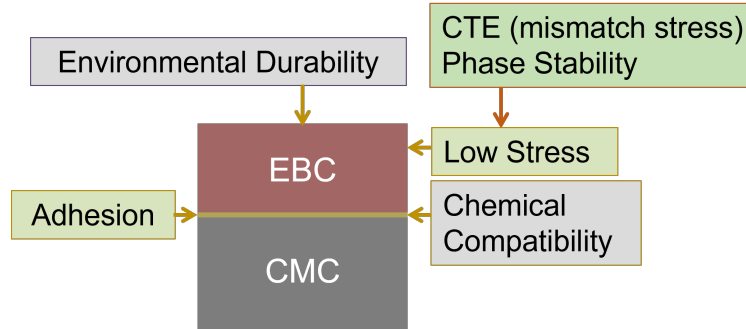


Figure 2.6: Generalized schematic of desirable barrier coating characteristics. Adapted from Lee⁹.

of approximately 3×10^{-6} can lead to quite large stresses, sometimes exceeding 700 MPa over temperature ranges of 1200°C. Despite the fact that this thermal expansion mismatch is not insignificant and can lead to high stresses in the YSZ topcoat layer, the CTE of YSZ is still quite large compared to CTE values for most other ceramic coating materials. This makes YSZ a very appealing material for TBC application⁵⁰.

A common TBC architecture includes two designed layers on top of the nickel-based superalloy structural substrate. The first deposited layer is a NiCrAlY bondcoat, designed to promote interlayer adhesion in the system and attach the topcoat to the structural material¹⁶. The second deposited layer is the YSZ topcoat, which interfaces on its top surface with the atmosphere and, originally, on its bottom surface with the bondcoat. A third layer is an unavoidable thermally grown oxide (TGO) that grows during use to thicknesses of 1-10 microns on the NiCrAlY bondcoat and sits at the interface between the topcoat and the bondcoat⁵¹. The growth of this layer is actually aided in part by the concentrated oxygen vacancies in YSZ (mentioned above), which facilitate the diffusion of oxygen through the topcoat⁵². The TGO is composed mainly of alumina, which is considered to be a relatively stable and benign oxide. While it is preferable not to grow a TGO in the system, alumina can provide some protection for the bondcoat from further oxidation due to its low oxygen permeability. The CTE of alumina is different from those of the surrounding layers, leading to large internal stresses, but its limited thickness and low permeability make it a preferable TGO compared to some others⁵³.

Certain YSZ TBC microstructures must be leveraged in order to permit the use of these coatings in extreme applications, such as those requiring especially high engine temperatures of 1500°C or higher¹⁷. In those applications, the microstructure resultant from the more traditional and economical plasma-spray processing technique does not always exhibit sufficient strain tolerance for the large internal strains and stresses developed over very

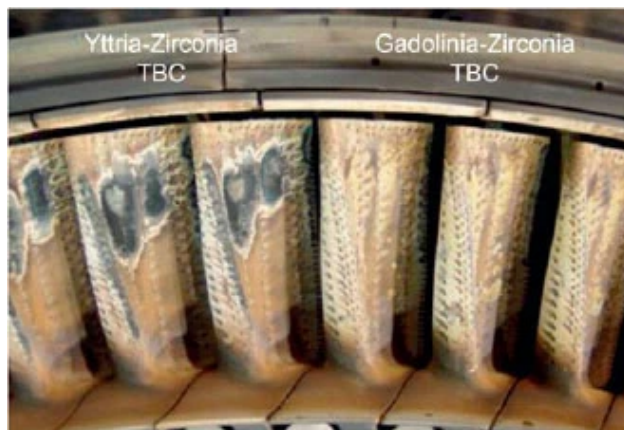


Figure 2.7: Turbine components coated in YSZ (left) and $\text{Gd}_2\text{Zr}_2\text{O}_7$ (right), showing the enhanced damage resistance of the gadolinium-based coating. Reprinted with publisher permissions from Levi et al.¹⁷.

large temperature excursions. Electron beam physical vapor deposition (EB-PVD), however, allows for materials to be deposited with very different, and in these cases dendritic, microstructures. With the primary dendrites in these structures oriented perpendicular to the superalloy surface in the materials, the topcoats can show much greater strain tolerance and improved lifetime duration. However, EB-PVD is much slower and more expensive than typical plasma-spray techniques, making it less desirable for high-volume or high-throughput production⁵⁴.

Other key developments have improved the favorable properties of YSZ-based TBC topcoat materials, including the incorporation of rare-earth zirconates. The addition of gadolinium zirconate ($\text{Gd}_2\text{Zr}_2\text{O}_7$) to YSZ, for example, has produced a TBC layer with even lower thermal conductivity than that of YSZ alone, along with better sintering resistance and, perhaps more importantly, resistance to penetration by the calcium-magnesium aluminosilicate (CMAS) engine contaminants¹⁷. A comparison between these two TBCs is shown in Fig. 2.7. Some recent works have considered the efficacies of certain environmental barrier coatings in providing heat protection for the substrate. Such materials, including unary, binary, or multi-component rare earth silicates, might function dually as TBCs and EBCs⁵⁵.

2.2.2 Environmental barrier coatings (EBCs)

Environmental barrier coatings (EBCs) are differentiated from thermal barrier coatings (TBCs) by the conditions from which they protect their substrates. TBCs are most often applied to metallic substrates, such as nickel-based superalloys, with the goal being to protect the alloy structural material from the intense heat of the engine and permit higher

operating temperatures. The heat protection provided by TBCs' low thermal conductivity maintains the structural stability of the alloy by preventing mechanical flow due to very high temperatures. Environmental barrier coatings (EBCs), on the other hand, are applied on ceramic matrix composite (CMC) substrates in order to protect them from the corrosive chemistries present in the turbine engine environment as discussed in previous sections⁵⁶. CMC materials are thermomechanically stable at much higher temperatures than alloys and will not mechanically flow at the NASA Roadmap temperature of interest for turbine substrate materials, which is 1315°C^{57,58}. Their vulnerability lies primarily in the corrosive combustion atmosphere, as well as in the high-temperature volatility of silica scales grown in that environment. Because of this, EBCs are chosen and designed not for their thermal conductivity properties but instead for their ability to protect silicon-based ceramics from corrosion in the turbine engine environment⁵⁶.

Many of the design principles and durability/failure considerations used in the research and implementation of TBCs apply to EBCs as well. EBCs need to bond well with the substrate, possess a good match of CTE between the EBC layers and the substrate, and be resilient to the engine atmosphere and contaminants⁹. The resilience of the topcoat in the engine environment is mainly determined by its stability, in terms of oxidation and volatility of silica species, in the humid, high-temperature conditions as well as its reactivity (or lack thereof) with common engine contaminants. At the goal temperatures laid out in the NASA roadmap⁵⁸ for turbine engine development, humidity in the engine atmosphere plays a large role in the volatility and degradation of silicate EBCs just as it does for silica TGO scales grown on silicon and silicon-based materials¹⁵. In terms of the oxidation of the bondcoat in CMC/EBC systems, the oxygen or oxidant permeability of the topcoat is another important property to consider in the material choice for this layer.

The most common structural ceramic intended for gas-burning turbine engines is a SiC_f/SiC CMC. In current-generation EBC systems, bonding between the EBC layer(s) and this substrate is greatly facilitated by a silicon bondcoat deposited on top of the CMC substrate. Sometimes, an intermediate diffusion layer is deposited between the bondcoat and topcoat in order to slow the diffusion of oxidants to the bondcoat or substrate⁵⁹. The uppermost layer is the topcoat, the composition and processing architecture of which has evolved over the course of EBC research and development. Current-generation CMC/EBC systems almost always consist of the designed topcoat and bondcoat layers applied to the CMC substrate, as in Ref.¹⁵. As with TBCs, there is also an unavoidable oxide layer that grows on the bondcoat in current CMC/EBC systems. Some stationary turbine engine components have been made from CMCs and used in commercial flights; however these materials require more research

and development prior to full implementation in engines⁶⁰. The next sections will describe the development of this current system over years of research into multiple generations of EBC systems.

2.2.3 Common processing methods for barrier coatings

Barrier coating materials can be processed by a variety of means, including sintering of powders, dip-coating, gel preparation, physical vapor deposition (including Electron Beam Physical Vapor Deposition, or EB-PVD), and, perhaps the most common method for barrier coating preparation, air plasma spray deposition. The accessible processing pathways for barrier coating materials keep the barrier low for their implementation, since plasma spray is among the most common coating processing methods and is among the least expensive. At the same time, multiple processing pathways permit flexible design of coating microstructure that can be limited by processing time and capital expenses rather than by technological limitation.

Some vapor deposition techniques, including chemical vapor deposition (CVD) and physical vapor deposition (PVD), are relatively slow deposition methods but can offer great control over coating microstructure. For example, electron beam physical vapor deposition (EB-PVD) can be used to produce highly tailored coating microstructures for increased strain tolerance and other favorable properties⁵⁴. However, in addition to increased processing time, the machinery and instrumentation required for vapor deposition techniques can be quite expensive and therefore lead to further increases in processing costs. While vapor deposition techniques have a role to play in the development and implementation of barrier coatings, the current relative costs of these methods are undesirable for mass implementation. Materials systems with barrier coatings deposited by vapor deposition are not studied in this work, and so these deposition techniques will not be covered in detail.

Plasma spray techniques, by contrast, are well-established, commercially available, and commonly used to deposit metallic or ceramic coatings onto substrates. Air plasma spray deposition refers to plasma spray processing in ambient atmospheric conditions. Alternative plasma spray techniques make use of vacuum chambers (Vacuum Pressure Spray, or VPS) or low pressure protective gases (Low Pressure Plasma Spray, or LPPS). Most plasma spray processing, including that used for producing multilayer EBC samples in this work, is of the air plasma spray type, and so here the technique will be referred to as plasma spray for brevity.

Plasma spray processing, which is illustrated in Fig. 2.8, is able to deposit refractory coating materials due to the extremely high temperatures reached by the powder particles as they

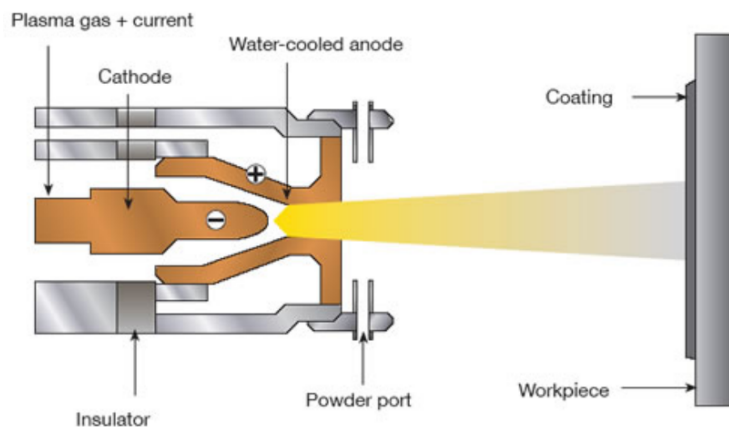


Figure 2.8: Schematic illustration of the plasma-spray technique⁶¹.

are fed through the plasma. The high velocities of the molten particles, rapid cooling (splat quenching) upon deposition, and relatively large amounts of material contained in each deposited particle make plasma spraying a fast deposition technique for ceramic and metal coatings. When rapid fabrication is desired, line-of-sight deposition can be manipulated to cover the intended substrate, and microstructural features such as pores and splat boundaries are acceptable or beneficial to a material system, plasma spray is often a favorable and relatively economical deposition technique.

2.3 Evolution of EBCs

Early EBCs were designed to protect silicon-based ceramics from molten salts in heat exchangers⁶². The volatility of silica in the topcoat and the amorphous character in the as-sprayed EBCs presented restrictions for early mullite EBC systems. As seen in Fig. 2.9, silica volatility in the mullite coating left behind a porous alumina layer. The issue of significant amorphous character in the as-sprayed coatings was mitigated by spraying the coatings onto a heated substrate⁶³, which allowed the coatings to crystallize at least in part. This solution has been implemented in EBC processing through subsequent generations.

Early attempts to use YSZ as a first-generation EBC were unsuccessful due to the large CTE of YSZ (sometimes as low as $7.5 \times 10^{-6} K^{-1}$, although frequently measured as high as $11 \times 10^{-6} K^{-1}$, depending on Y_2O_3 content and transformation toughening)⁵⁰ compared with the other ceramic layers in the CMC/EBC systems (typically between $4 \times 10^{-6} K^{-1}$ and $5 \times 10^{-6} K^{-1}$ for silicon-based ceramics)¹⁰. The large CTE of YSZ led to tensile stresses in the topcoat layer, which served as a source of through-thickness cracking. YSZ/mullite coatings were also attempted and performed fairly well⁶⁴, but through-thickness cracks developed in the mullite, permitting water vapor corrosion through the compromised diffusion barrier and

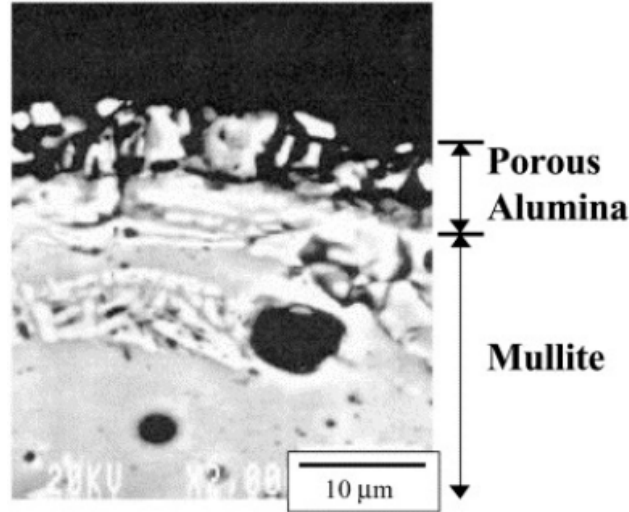


Figure 2.9: Upper section of a mullite EBC after steam cycling, with visibly deteriorated alumina layer where silica had volatilized out of mullite. Reprinted with publisher permission⁹.

leading to premature coating failure⁶⁵.

2.3.1 Barium-strontium-aluminosilicate (BSAS) EBCs

The standard, second-generation EBC system possessed a barium-strontium aluminosilicate (BSAS, $(1-x)\text{BaO} \cdot x\text{SrO} \cdot \text{Al}_2\text{O}_3 \cdot 2\text{SiO}_2$, $0 \leq x \leq 1$) topcoat. This topcoat was paired with a mullite diffusion layer and a silicon bondcoat. The benefits of this system were close matches in CTE as well as low silica volatility of the BSAS in the engine atmosphere⁹. As reported by Harder et al., the CTEs of the BSAS (celsian), mullite, silicon, and silicon carbide phases were $4.28 \times 10^{-6} \text{K}^{-1}$, $5.50 \times 10^{-6} \text{K}^{-1}$, $4.44 \times 10^{-6} \text{K}^{-1}$, and $5.06 \times 10^{-6} \text{K}^{-1}$, respectively⁵⁹.

Early second-generation studies by Lee assessed BSAS deposited directly onto the silicon bondcoat, which was adhered to the CMC substrate. In these systems, BSAS allowed oxygen permeation through the topcoat and rapid oxidation of the silicon bondcoat. The silica TGO then reacted with BSAS, forming a glass reaction product and bubbles at the topcoat/bondcoat interface, leading to rapid spallation¹⁰. A mullite layer was then added to serve as a diffusion barrier, to mixed success. While the mullite acted as a diffusion barrier while intact, a CTE mismatch between mullite and the SiC_f/SiC CMC led to large tensile stresses and through-thickness cracking in the mullite layer. With its role as a diffusion layer compromised, mullite permitted the transport of oxygen to the bondcoat, which again led to rapid oxidation, formation of bubbles at the interface, and spallation failure of the coating¹⁰.

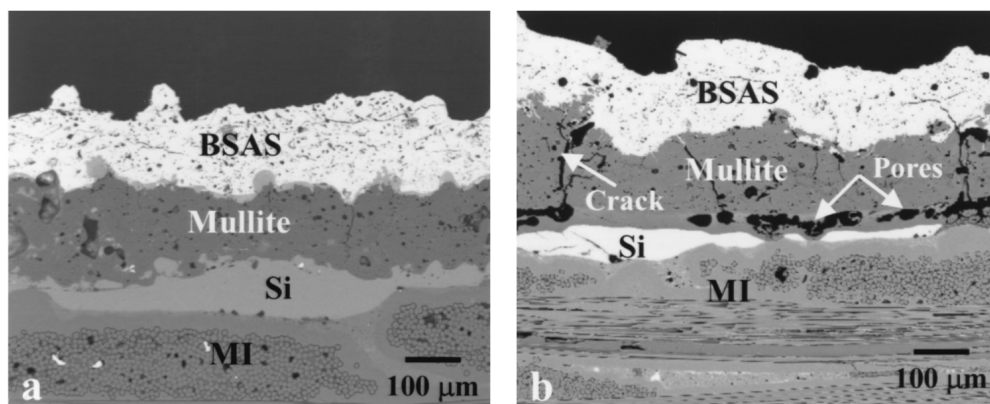


Figure 2.10: BSAS-based multilayer coatings, prior to and after steam cycling. Micrographs are from different samples. Through-thickness cracking is evident in the mullite layer, as well as pores along the mullite-bondcoat interface. Reproduced with publisher permission⁶⁶.

BSAS was then incorporated into the mullite to lower the CTE of the diffusion layer. The result was that most of the BSAS incorporated in the mullite was of the hexacelsian phase, which has the larger CTE of the two primary BSAS phases (hexacelsian CTE is $8.37 \times 10^{-6} K^{-1}$ and celsian CTE is $4.28 \times 10^{-6} K^{-1}$)⁵⁹. The use of BSAS in the diffusion layer still helped prevent cracking, but a low-temperature eutectic between BSAS and silica prevented the use of these materials above $1300^\circ C$ ^{10,67}.

Harder et al. studied phase transformations and stresses in BSAS EBC systems⁶⁸. The hexacelsian BSAS phase, which was metastable, was measured to be under tensile internal stresses and developed through-thickness cracks. Temperature cycling of the systems converted the hexacelsian phase to the celsian phase, which was predicted to be in compression⁵⁹. In fact, cracks present in the BSAS layers prior to the conversion from hexacelsian to celsian phase actually closed upon this transformation. However, the cracks present in the mullite did not close and the properties of the diffusion barrier remained compromised⁵⁹, as shown from a similar study in Fig. 2.10¹⁰.

Harder's *in-situ* WAXS studies at the Advanced Photon Source (APS) allowed stresses to be measured during heating and cooling cycles in the CMC/EBC systems. In those experiments, the stress-free celsian phase converted to the hexacelsian phase upon cooling, which developed stresses through the cooling profile. With significant cooling, there was a reduction in stresses associated with crack development in the coating. Compressive internal stresses developed during cooling in the intermediate SAS (strontium aluminosilicate) and mullite layer⁵⁹.

The hexacelsian to celsian phase transformation altered internal stresses significantly, and therefore needed to be better understood and potentially controlled. It was found that un-

melted seed crystals of the celsian phase greatly aided in the transformation of the BSAS from the hexacelsian to the celsian phase. This analysis showed that the presence of seed celsian-phase crystals in the BSAS layer aided in this transformation by lowering the activation energy barrier for the transformation. Such behavior showed that there were potentially significant benefits that could come from the imperfections in the plasma spray deposition of the layers^{59,69}. Ultimately, the low-temperature eutectic formed between BSAS and silica, mentioned above, proved to be insurmountable. Since CMC/EBC materials are intended for temperatures well in excess of 1300°C, studies moved instead on the next generation of EBC materials.

2.3.2 Rare-earth silicate based EBCs

A unique combination of properties that make rare earth silicates interesting and, in some cases, suitable for use as EBC materials in gas-burning turbine engine environments. In particular, the CTEs of most rare earth silicates are relatively close to the CTEs of the other materials in current-generation systems. The CTE of SiC (in the SiC_f/SiC CMC) is approximately $5.1 \times 10^{-6} K^{-1}$, and the CTE of silicon is approximately $4.4 \times 10^{-6} K^{-1}$. For comparison, the CTEs of rare earth silicates are typically in the range of $5-7 \times 10^{-6} K^{-1}$. As discussed previously, a relatively close match of CTEs helps to minimize the internal stresses developed upon cooling the multilayer systems from high temperature.

The melting points of rare earth silicates are often more than suitable for EBC use, as well, since they frequently exceed the goal operating temperatures in gas-burning engines by a few hundred degrees Celsius. Two commonly studied rare earth silicates, ytterbium monosilicate and ytterbium disilicate, are line compounds which have melting points at 1950°C and 1850°C, respectively (this can be seen below in Fig. 2.15, as well)⁷⁰. Since the goal temperature for surface-exposed materials (EBCs) as written in the NASA roadmap is 1482°C⁵⁸, these coatings will not melt in the turbine engine under intended operating conditions. These silicates are vulnerable to other interactions in the engine environment, as discussed below, but with respect to temperature alone their use is not precluded.

2.3.3 Rare earth availability and economics

Rare earth (RE) elements are important in both science and technology, beyond their usefulness as silicates in coating materials. Rare earth elements are used in the production of consumer electronics batteries, hybrid powertrain automotive batteries, and as phosphors, catalysts, and polishing compounds, to name a few things⁷¹. The rising importance of rare earth elements drives up demand for minerals from which these elements can be separated. Fig. 2.11 shows proven rare earth element reserves globally, as reported by the USGS Min-

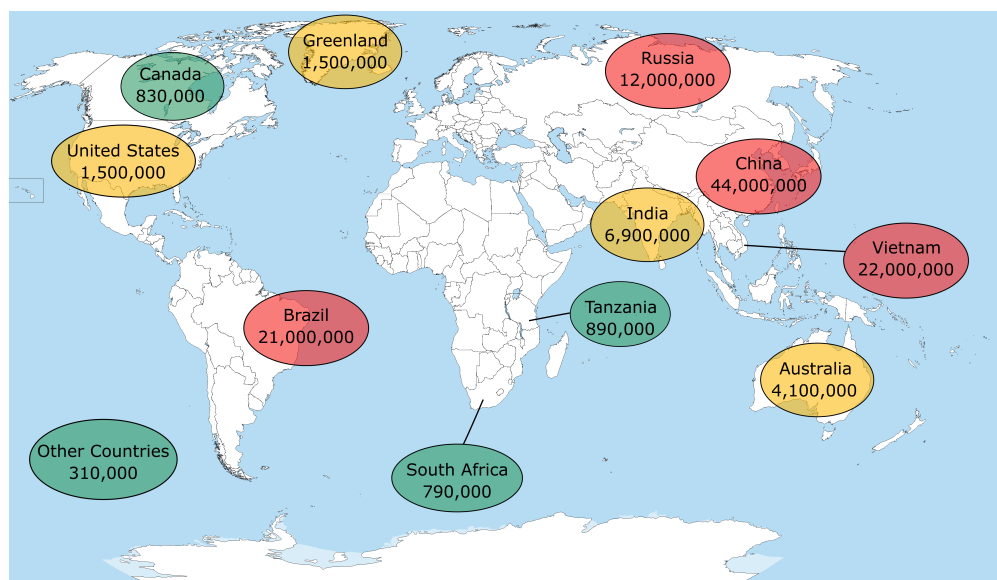


Figure 2.11: Map of estimated rare earth element reserves, in tons, as listed in the USGS Mineral Commodities Survey, January 2021⁷².

Table 2.2: Rare earth oxide prices, as listed online by Fisher Scientific in mid-2021.

RE Oxide	Dy ₂ O ₃	Er ₂ O ₃	Eu ₂ O ₃	Gd ₂ O ₃	La ₂ O ₃	Lu ₂ O ₃	Nd ₂ O ₃	Sc ₂ O ₃	Y ₂ O ₃	Yb ₂ O ₃
Price (\$/gram)	6.04	3.01	15.34	4.27	0.72	16.40	1.54	35.62	4.92	5.51

eral Commodities Survey in 2021⁷². Large reserves of rare earth-containing minerals exist in nations which are critical to international supply chains. China, in particular, both has a growing demand for technological materials and devices and possesses large stores of rare earth minerals.

Accessibility of rare earth-bearing minerals and ores is subject to geopolitical pressures, as well. In the case where a nation with large reserves decreases supply for any reason, such as was intentionally done in 2010⁷¹, prices of rare earth materials tend to increase dramatically. Given their importance as technological materials, the United States must maintain favorable trade and political relationships with nations that export rare earth materials. It is also notable that the United States possesses significant rare earth reserves, as well. Increased mining of rare earth minerals by the United States can help to stabilize the supply and price structure of rare earths for domestic use.

Fig. 2.12 shows rare earth production over time, as reported by the United States Geological Survey⁷³. Plots are cumulative. Rare earth oxide production has increased overall during this period of time. Note also that production peaked in the United States and most other countries in the mid-1980s, whereas production in China began in earnest at this time. China

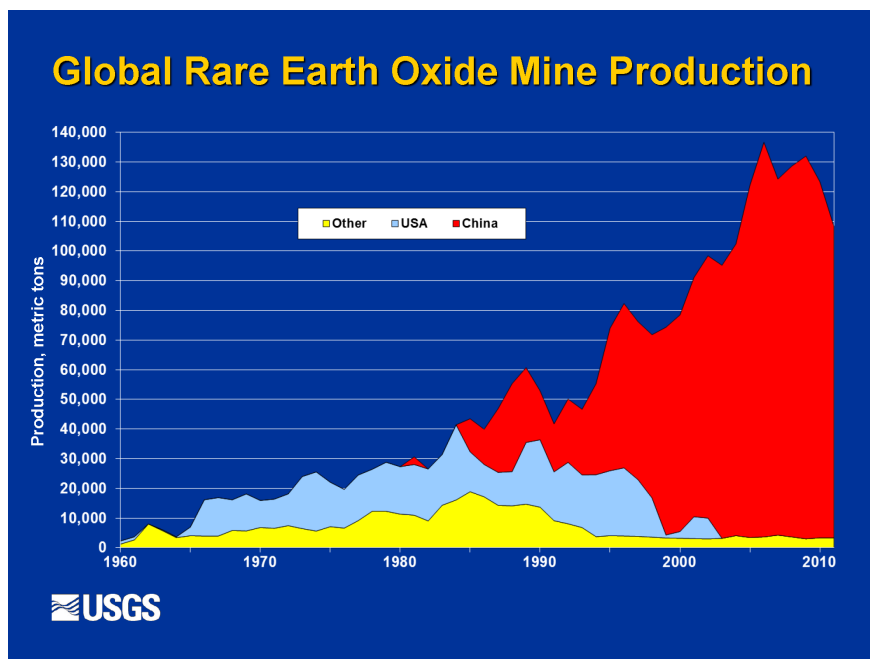


Figure 2.12: Rare earth oxide production (mining) from 1960-2012. Compiled by the United States Geological Survey⁷³.

is clearly the most dominant producer of rare earth oxides thus far in the 21st century.

The wide spread of prices shown in Table 2.2 for the rare earth oxides is in part due to the availability of minerals containing each kind of oxide and in part due to the relative ease or difficulty of separating a specific rare earth oxide from an ore or mineral. Some implications of the variance in prices will be discussed in section 2.3.5

2.3.4 Commonly investigated rare earth barrier coating systems

Silicates incorporating most rare earth elements have been investigated at least preliminarily in a range of literature, with some interesting and promising results. Recently, Ridley et al. investigated multiple rare earth silicates including those of scandium (Sc), yttrium (Y), neodymium (Nd), dysprosium (Dy), erbium (er), and ytterbium (Yb), along with four equimolar binary cation mixtures of these silicates and a five-cation equimolar mixture⁵⁵. It was shown that the CTEs of the equimolar binary cation mixtures followed a rule of mixtures between the CTEs of the two cation silicates. Additionally, the five-cation equimolar mixture was shown to have a rather low thermal conductivity. Multicomponent rare earth silicate systems might in this way be used to tune the CTEs of the layer as well as produce layers which can act dually as EBCs and TBCs. Ridley et al. also studied the efficacy of hafnon (HfSiO_4) as a candidate EBC material. While CTE match with the substrate was

quite good, silica depletion in high-velocity steam testing⁷⁴. High-velocity steam studies were also carried out by Ridley et al. to assess the stability of yttrium disilicate in that environment, with high silica volatilities carrying implications for the suitability of rare earth silicates depending on gas velocity⁷⁵.

Yttrium tantalate (YTaO_4) was studied by Lepple et al. to determine the phase stability and thermochemistry of that compound as a candidate coating material⁷⁶. YTaO_4 undergoes a phase transformation from monoclinic to tetragonal structures between 1400°C and 1500°C, with the kinetics highly dependent on measurement parameters. Interestingly, this transformation is not accompanied by a large volume change, which would have negative implications for the stress state of the compound in service as a coating. The high melting temperature, 2090°C, along with its thermochemical properties, raises interest in YTaO_4 and similar compounds as EBC candidates, likely in the next generation of coating materials⁷⁶.

Another form of rare earth-based systems which has been investigated extensively is the combination of rare earth coatings with CMAS contaminant deposits. Jackson et al. explored the interaction of CMAS deposits with columnar, bilayer $\text{Gd}_2\text{Zr}_2\text{O}_7/\text{Y}_2\text{O}_3\text{-ZrO}_2$ (GZO/YSZ) TBC coatings and propensity for cracking in thermal gradients⁷⁷. Interaction between CMAS and the columnar GZO topcoat formed a reaction zone stiffer than the columnar GZO, decreasing the effective toughness of that layer and mitigating the effectiveness of the columnar structure⁷⁷.

Holgate et al.⁷⁸ showed that, for common YSZ-CMAS combinations, the kinetics of dissolution of the silicate dominated the saturation of the CMAS melt rather than diffusional constraints. The diffusion of Y^{3+} into the melt was faster than that of Zr^{4+} and controlled saturation and the onset of apatite precipitation. It was noted that Y^{3+} can act as a proxy for some other rare earth ions, such as Yb^{3+} , expanding on the implications of this result. Additionally, the interaction kinetics were much more strongly influenced by the composition of the CMAS melt than by temperature in the range 1300-1400°C⁷⁸.

Summers et al. also showed that the Ca:Si ratio in CMAS deposits will drastically influence the recession of yttrium disilicate barrier coatings⁷⁹. CMAS compositions with high initial Ca:Si ratios react very strongly with the $\text{Y}_2\text{Si}_2\text{O}_7$, leading to significant recession of the coating and forming thick layers of apatite precipitates in a residual melt matrix. Ca:Si ratios below a threshold value, approximately 0.25, resulted in limited reaction zones although the coating and deposit still reacted quite readily. Since CMAS dissolves SiO_2 from the silicates to replace CaO, which precipitates in apatite crystals, high Ca:Si ratios in the CMAS indirectly fueled extensive dissolution of the disilicate coating⁷⁹.

Interactions between CMAS and ytterbium silicates were explored by Zhao et al.⁸⁰ using $C_{33}M_9A_{13}S_{45}$ (the amounts of each oxide denoted by subscripts), a composition explored previously in the literature^{12,81,82}. The monosilicate reacted quite strongly with the CMAS deposit, which dissolved the silicate and from which apatite crystals would precipitate. Eventually, extensive apatite precipitation near the deposit-silicate interface formed a dense layer which helped to slow further silicate recession. The disilicate, on the other hand, was more resistant to CMAS interaction. However, residual monosilicate in the disilicate layer reacted readily with CMAS. The irregular placement of the monosilicate within the disilicate served as reaction pathways for the CMAS interaction and precluded the formation of a dense layer of apatite crystals which could impede further recession⁸⁰. Reactions between CMAS and ytterbium silicates had been previously investigated by Stolzenburg et al.¹². The results of that study will be detailed further in the next section; briefly, there were numerous similar results between the works of Stolzenburg et al. and Zhao et al., and CMAS-monosilicate interactions were significantly more deleterious to the silicate than in the case of the CMAS-disilicate interactions¹².

2.3.5 Ytterbium silicate-based EBCs

Given that rare earth silicates are formed basically of units of rare earth oxides and silica, and the importance of the volatility of silica as discussed previously, volatility of EBC topcoat materials must also be considered. The volatility of some key rare earth silicates was studied by Lee in terms of specific weight loss in a 50% H_2O -balance O_2 environment at 1500 °C, with air flow rate set to 4.4cm/s and total pressure to 1 atmosphere⁶⁶. As can be seen in Fig. 2.13, $Yb_2Si_2O_7$, Yb_2SiO_5 , and Sc_2SiO_5 all performed comparably to or better than BSAS. Y_2SiO_5 even showed specific weight gain under these conditions but, in EBC systems which included a mullite diffusion layer directly under the topcoat, Y_2SiO_5 and mullite reacted to form a low-melting eutectic. No Y_2SiO_5 topcoat material remained after preliminary experiments in which this reaction took place, and so due to its reactivity this silicate was determined to be unsuitable for EBCs. A comparison of post-exposure micrographs can be seen in Fig. 2.14 for four rare earth silicates, illustrating the effects described here and of deleterious CTE differences in the multilayer systems.

Yb_2SiO_5 displayed the best stability of the silicates studied in the volatility experiment, showing almost no specific weight loss or gain over the duration of the exposure⁶⁶. $Yb_2Si_2O_7$ was more volatile than the monosilicate and was actually comparable in specific weight loss to BSAS. Specific weight loss in Sc_2SiO_5 fell between those of Yb_2SiO_5 and $Yb_2Si_2O_7$. The volatility of $Yb_2Si_2O_7$ was shown by Harder et al. to consist of the removal of SiO_2 from the disilicate near the free surface⁸³, leaving behind residual monosilicate (as could be expected

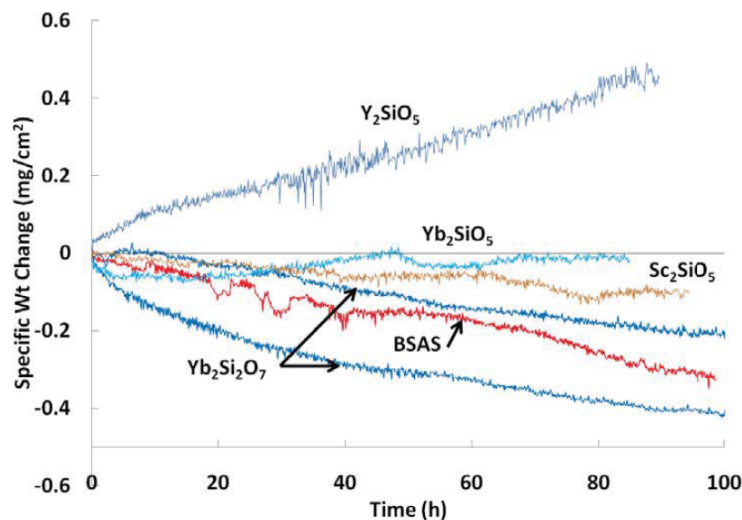


Figure 2.13: Volatilities of multiple rare earth silicates, as well as BSAS for comparison. Plot compiled by Fabian Stolzenburg using data originally plotted by Lee et al.^{11,66}.

from the phase diagram, Fig. 2.15). In 100% humidity at 1400°C, the remaining monosilicate did not form a dense layer and so the removal of SiO₂ was not impeded by a stable monosilicate atop the disilicate. However, this experiment incorporated much higher humidity than would be expected in the engine environment and, in cases where the monosilicate could form a denser top layer upon volatilization of the disilicate, the rate of progression of this conversion was calculated by Stolzenburg to be slow enough that recession would be limited to 50% of the topcoat's thickness after 25,000 hours¹¹. In industrial turbine applications, which place these materials in service for much longer duration than do aircraft applications, 25,000 hours of durability is frequently implemented as a design criterion⁸⁴.

Given that the volatilities of some of the viable rare earth silicates are comparable, economics necessarily played a role in the selection of promising EBC candidate materials. As shown in the previous section, the price of ytterbium is quite favorable compared to that of some other rare earth elements which are otherwise technically relevant. As seen in Table 2.2 above, as of mid-2021 the respective prices of ytterbium, scandium, and lutetium oxides at \$5.51 per gram, \$35.62 per gram, and \$16.40 per gram, respectively, guiding the selection toward ytterbium silicates for further study and potential use.

Comparison between the ytterbium silicates yielded details relevant to the choice of EBC topcoat material. Ytterbium disilicate (YbDS) possesses three key benefits over ytterbium monosilicate (YbMS) through these comparisons. The first of these is that the CTE of YbDS ($4.7 \times 10^{-6} K^{-1}$) is slightly smaller than that of the SiC_f/SiC CMC substrate ($5.1 \times 10^{-6} K^{-1}$), whereas the CTE of YbMS is slightly larger than that of the substrate ($5.6 \times 10^{-6} K^{-1}$). As

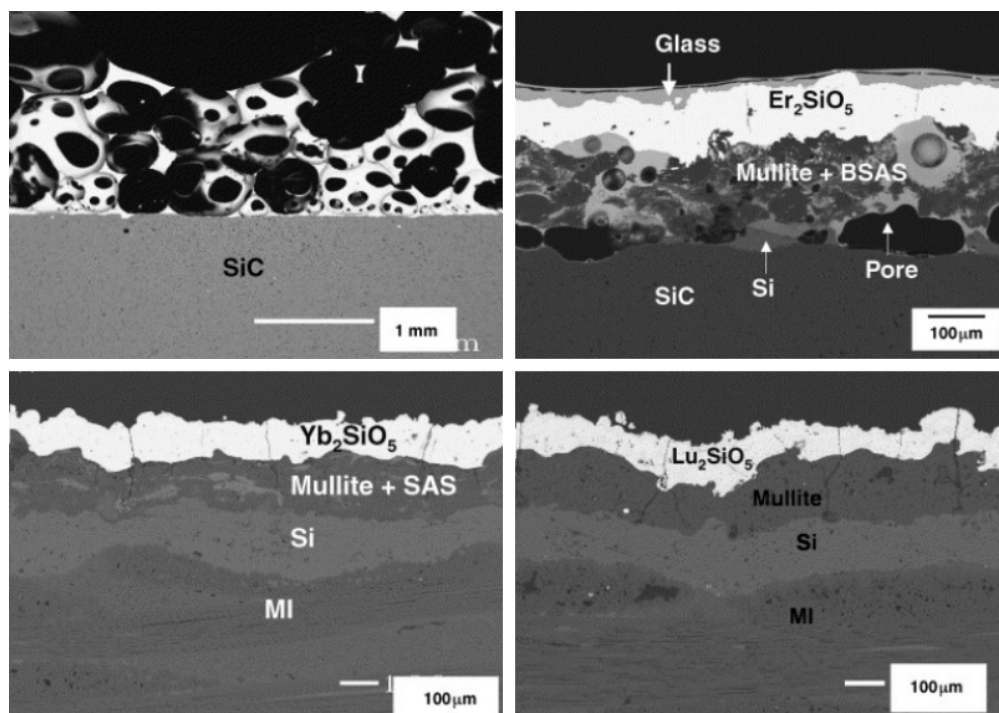


Figure 2.14: Post-steam cycling microstructures of yttrium monosilicate (upper left), erbium monosilicate (upper right), ytterbium monosilicate (lower left), and lutetium monosilicate (lower right) based EBC systems. With steam cycling at 1400°C, yttrium monosilicate is almost entirely depleted after 46 hours and erbium monosilicate has developed a glassy layer and through-thickness cracking after 100 hours. Ytterbium and lutetium silicates, steam cycled for 300 hours at 1380°C, showed greater chemical stability, but developed through-thickness cracks. Adapted and reprinted from Lee et al. with publisher permission⁶⁶.

mentioned previously, this is important because it serves as an indicator of the internal stresses that will develop in the multilayer system as the materials are heated and cooled repeatedly. The YbDS topcoat layer is likely to develop compressive stresses upon cooling from high temperatures, while the YbMS is likely to develop tensile stresses. This was confirmed by Stolzenburg et al.¹¹. The contribution of the tensile stresses in YbMS to the development of through-thickness cracks in the topcoat makes YbDS a more attractive option with respect to internal stresses.

The second primary advantage of YbDS over YbMS in EBC applications is the volume change in each material upon allomorphic phase transformation from the as-sprayed, partly amorphous condition to the crystalline condition upon heating to engine operating temperatures. As discussed by Stolzenburg¹¹, in YbMS there is a significant volume contraction due to densification of the amorphous content upon crystallization in the as-sprayed topcoats. Such a contraction would inevitably alter the internal stress profile of the topcoat layer.

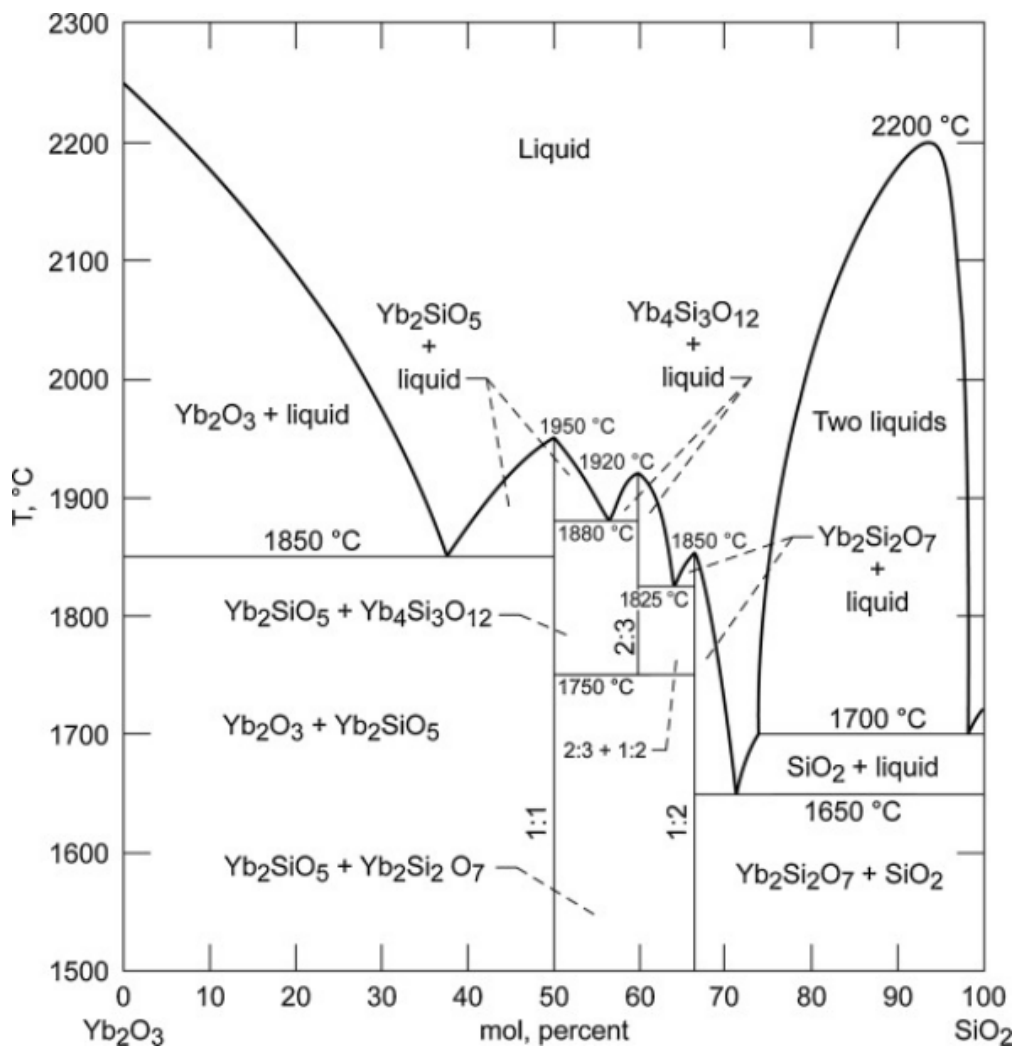


Figure 2.15: Yb_2O_3 - SiO_2 phase diagram, as reported in Costa et al.⁷⁰. Note the line compounds 1:1 and 1:2 which correspond to the monosilicate and disilicate, respectively, and the melting points of these compounds. Reprinted with publisher permission.

By contrast, there was no observable change in volume for the disilicate upon crystallization. This was the case for crystallization of both free-standing YbDS samples and YbDS as part of a multilayer EBC/CMC system. Lack of volume change upon devitrification is quite uncommon and provides a clear advantage for the implementation of YbDS rather than YbMS¹¹.

The third major advantage of the disilicate over the monosilicate is its lower reactivity with, and degradation by, engine contaminants such as CMAS (calcium-magnesium aluminosilicate). In Stolzenburg's investigations, the monosilicate was found to react very strongly with CMAS, rapidly decreasing in crystallinity upon high-temperature interaction with the contaminant¹¹. In addition to the degradation of YbMS crystallinity, there was dissolution

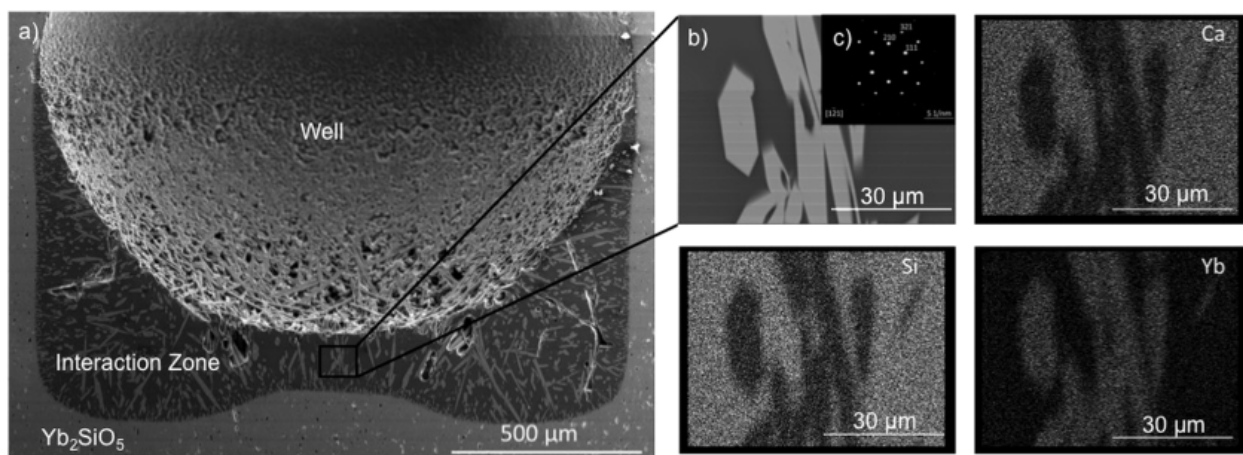


Figure 2.16: Ytterbium monosilicate sample, after high-temperature exposure to CMAS. The CMAS dissolved significant amounts of the monosilicate. Apatite crystals precipitated from the melt, as shown on the right using SEM and EDS maps as well as TEM selected area electron diffraction. Reprinted from Stolzenburg et al. with publisher permission¹².

of Yb into the CMAS and extensive formation of a needle-like, hexagonal $\text{CaYb}_4(\text{SiO}_4)_3\text{O}$ apatite phase in the Yb-enriched CMAS matrix, as shown in Fig. 2.16¹². The rapid, deleterious interaction between YbMS and CMAS precluded the use of the monosilicate as the EBC topcoat layer in applications where CMAS contamination is a major concern¹².

While ytterbium disilicate did interact with CMAS, the crystallinity of the disilicate decreased more slowly than did the crystallinity of the monosilicate, and final crystallinity of the disilicate after reaction studies was higher than that of the monosilicate. The disilicate also did not dissolve as the monosilicate did upon interaction with CMAS; rather the disilicate appeared to have absorbed the CMAS contaminant (Fig. 2.17¹²). The same $\text{CaYb}_4(\text{SiO}_4)_3\text{O}$ apatite phase was observed in disilicate samples post-CMAS reaction, but these precipitates were quite small and appeared in a YbDS matrix near the YbDS-CMAS interaction interface. This compared favorably to the collection of large, needle-like precipitates in a CMAS matrix that developed upon CMAS interaction with YbMS¹².

Another observation from Stolzenburg's YbDS-CMAS studies was that, in the case of incomplete interaction between the CMAS and YbDS topcoat, the CMAS contaminant acted as a distinct layer on top of the original multilayer structure. Although the CTE of CMAS ($6\text{-}8 \times 10^{-6} \text{K}^{-1}$) depends on composition and therefore can vary, it is generally larger than that of YbDS. When CMAS acts as an additional layer in the system as it cools, a tensile stress can develop in the CMAS layer. While this new internal stress could increase the compressive stress in the YbDS layer to satisfy force balance in the layers, in some cases the tensile stresses in CMAS were large enough to create through-cracking in the CMAS

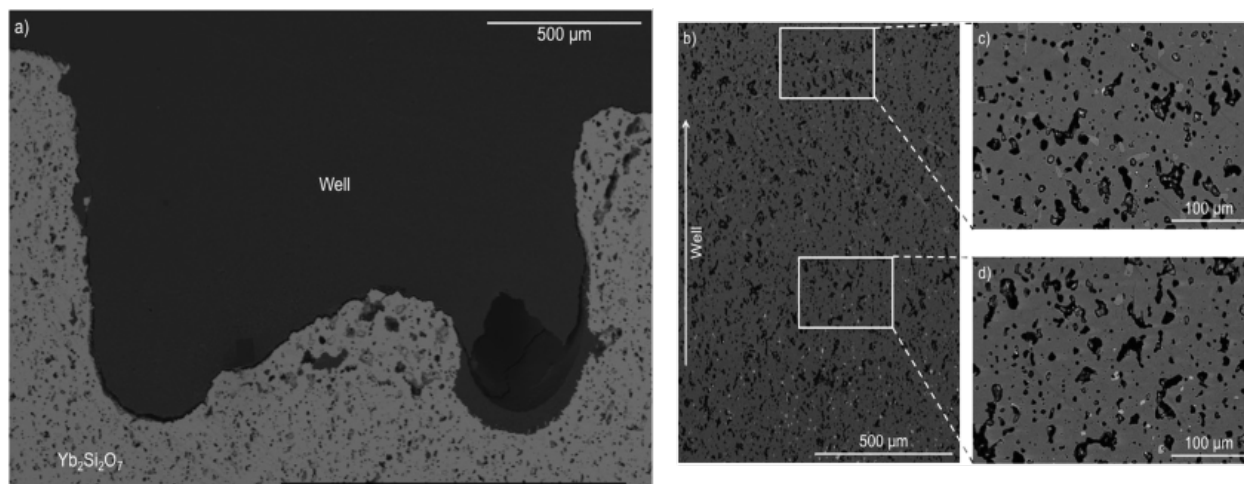


Figure 2.17: Ytterbium disilicate sample, after high-temperature exposure to CMAS. The well initially filled with CMAS was empty (filled with epoxy for imaging) post-exposure, with CMAS absorbed into the disilicate. Adapted and reprinted from Stolzenburg et al. with publisher permission¹².

that continued into and through the YbDS. While cracking is a concern in the YbDS-CMAS interaction, it was acknowledged that the CMAS loading used in Stolzenburg’s study was likely larger than what would be observed in the actual engine environment, meaning that these effects—while necessary to understand and thereby facilitated by the heavy CMAS loading—could be slightly exaggerated^{11,12}.

Compared to the monosilicate, ytterbium disilicate is more likely to develop compressive internal stresses due to its smaller CTE, it shows almost no volume contraction upon crystallization, and it is much more resistant to interaction with CMAS engine contaminants. These promising characteristics strongly motivate further research into YbDS as a prominent EBC topcoat material. Within the context of current-generation EBCs, one of the remaining major vulnerabilities for the multilayer EBC/CMC materials is oxidation of the bondcoat in the engine environment. This phenomenon will be discussed further in the next sections as it applies to ytterbium disilicate systems and explored throughout the remainder of this thesis.

As mentioned previously, the current generation of CMC/EBC systems include the substrate, a silicon bondcoat, and, given the context discussed above, a rare-earth silicate topcoat (ytterbium disilicate, for this study). A limitation that must be noted in the current generation of CMC/EBCs is the melting point of the silicon bondcoat, 1414°C, which is relatively low compared to those of the other layers. This allows for flow to occur at high temperatures, providing a mechanism for stress relief in the multilayer system. Silicon’s melting temper-

ature also presents a limitation because the NASA goal temperature for CMC substrates, 1315°C, is a significant portion of the melting temperature. While silicon will not melt at the substrate temperature, the goal temperature for EBC surfaces, 1482°C, exceeds the melting point of silicon⁸⁵. While current-generation CMC/EBC systems have successfully used silicon bondcoats, the melting point of the bondcoat is clearly an issue for next-generation systems with higher goal temperatures. This could be overcome by implementing directional cooling and imposing a temperature gradient in the system to keep the silicon below its melting point, however such measures would be costly and could reduce the efficiency of the engine by preventing its operation at higher temperatures. Next-generation bondcoat materials will need to surpass this melting point. While next-generation bondcoat materials are beyond the scope of this work, this is useful context for understanding the work at hand.

2.4 Failure in TBCs and EBCs

There are many failure mechanisms in common between TBCs and EBCs. Essentially, these break down into extrinsic and intrinsic failure modes of coating systems, as discussed in the following subsections. Discussions of TBC and EBC failure mechanisms are kept separate to distinguish specific failure mechanisms studied for EBC materials relevant to the present study. The shared nature of some of these mechanisms is indicated, and analysis for TBC systems is applied in many cases to EBCs due to the similarities of these systems and the failure mechanisms as explored in the scientific literature.

2.4.1 Failure mechanisms in TBCs

There are two general sources of failure in TBC systems, intrinsic and extrinsic, each of which are illustrated in Fig. 2.18 and detailed here. Extrinsic failure mechanisms include those which are factors unrelated to the properties of the constituent layer materials, such as erosion, impact from large debris in the engine, or contamination (commonly by molten aluminosilicates) and chemical reactions with engineered materials structures. Impact from large debris in the engine cannot necessarily be avoided, but damage can be mitigated by choosing materials of relatively high fracture toughness (as YSZ is, for a ceramic, although in EBC applications YSZ is not of the transformation-toughened variety¹⁷). Erosion necessitates materials of sufficiently high toughness, and interaction with engine contaminants such as calcium-magnesium aluminosilicate (CMAS) deposits can lead to phase transformations, delamination, and cavitation. These potential consequences require that the topcoat material have minimal interaction with the contaminants.

Intrinsic failure mechanisms, on the other hand, include those which are caused by the properties of the materials in use. These can include incompatible materials properties,

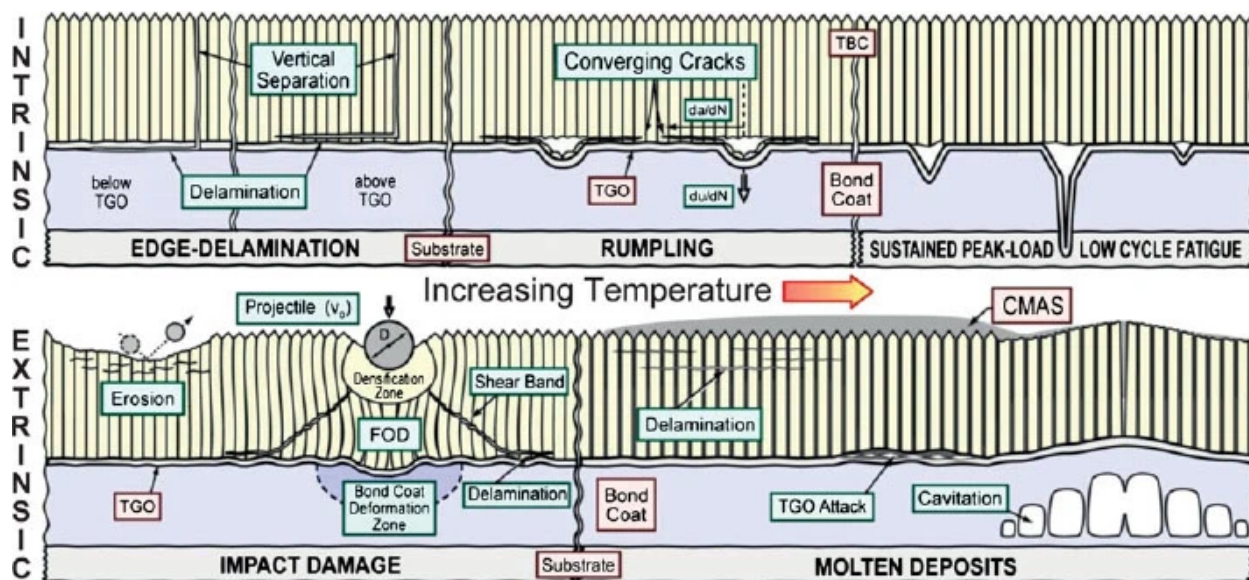


Figure 2.18: Summary of intrinsic (upper) and extrinsic (lower) failure mechanisms in a barrier coating system. The system illustrated is a columnar EB-PVD TBC. Reprinted from Levi et al. with publisher permission¹⁷.

such as mismatched coefficient of thermal expansion, poor bonding between material layers, and reactivity between layers leading to the formation of unpredictable or disadvantageous chemical products. The main driver for intrinsic failure mechanisms is mismatch between the CTEs of the layers in the system, including the TGO, and how the systems evolve due to CTE mismatch. Cracking can occur and propagate in multiple ways. Vertical separation and through-thickness cracking in the topcoat can lead to edge delamination along the layer interfaces, rumpling due to repeated temperature cycling can lead to convergent cracks along the layer interface, and increasingly high operating temperatures can lead to more rapid fatigue failure. In developing TBCs, it is important to choose materials and design structures which avoid intrinsic failure mechanisms while also accounting for likely sources of extrinsic failure mechanisms.

Growth of a TGO layer in a given TBC system can also have a significant deleterious effect on the longevity of the system. In fact, TGO growth serves as a major source of failure in both TBCs and EBCs. Since this phenomenon applies to both TBCs and EBCs and is a primary focus of this work, it will be discussed in more detail in a later section.

While TBCs and EBCs are not the same, they are highly analogous in certain respects including the failure mechanisms discussed here. The framework above for considering failure due to TGO growth in TBC systems is very useful when designing EBC systems and is of particular interest to the present work. Oxidation-based failures in EBC systems, discussed

below in section 2.3.4, must be well-understood in order to design appropriate coatings.

2.4.2 Failure mechanisms in EBCs

Many failure modes are shared between EBCs and TBCs due to some of the more general aspects of coating failure in brittle material systems. Intrinsic modes are concerned primarily with mismatches in CTE and other material properties, including interactions between the layers in the materials.

Extrinsic modes are again related to engine contaminants and large debris. Interactions between EBCs and engine contaminants can lead to changes in material properties, such as CTE, as well as degradation, delamination, and spallation of the EBC topcoat. In the case of EBCs, as with TBCs, oxidation is also a major extrinsic mode of failure due to the silicon bondcoat most commonly implemented in EBC systems. Oxidation of the bondcoat in EBC systems adds a new TGO layer with different properties, including CTE, compared to the other layers in the system. With increasing TGO growth, the bonding between the topcoat and the layer beneath it (silicon, being replaced with TGO) changes and diminishes. The oxidation process can produce intrinsic material incompatibilities into CMC/EBC systems which contribute to more rapid failure than would occur without TGO growth.

As discussed previously, the contaminant of primary concern is the same for EBCs as it is for TBCs: CMAS deposits⁸⁶. CMAS reacts with a wide variety of barrier coating materials^{81,82,87}. As with TBCs, in EBC systems interactions with CMAS can lead to the formation of new phases in the topcoat, thereby changing the material properties (primarily CTE) in that layer. This can lead to degradation, the formation of glassy reaction zones, delamination, and through-thickness cracking in the topcoat layer which are often sources of failure for the multilayer systems¹².

CMC/EBC systems need also to be designed with allomorphic phase transformations in mind, due to the potential for volume changes discussed above^{9,63}. These changes, as well as potential changes in material properties, can affect the interactions between the layers in the multilayer material system and can affect the match or mismatch of CTEs. Allomorphic phase transformations likely affect multiple layers of some CMC/EBC systems, such as in systems based on a BSAS EBC topcoat⁵⁷.

Match or mismatch of CTE between the layers is again significant for its contribution to intrinsic failure modes in the materials. Mismatch of CTE between the layers will result in compressive stresses in some layers and tensile in others. When CTE mismatches are large enough, the stresses can also be large enough to result in through-thickness cracking^{9,63}, which enhances the ingress of oxidants and other contaminants to the bondcoat layer. The

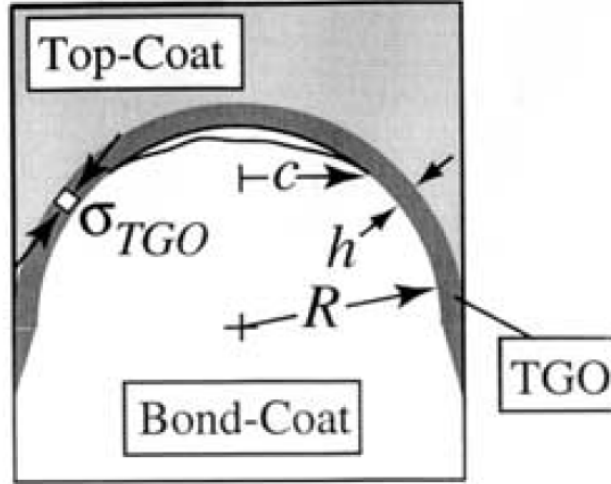


Figure 2.19: Undulation in topcoat-oxide-bondcoat structure of multilayer coating system. Reprinted from Schlichting et al. with publisher permission⁸⁹.

enhanced growth of TGO in the case of accelerated oxidant ingress leads to premature delamination and spallation of the topcoat.

2.4.3 Bondcoat oxidation-based failure of TBC and EBC systems

Many failures in TBC and EBC systems are caused by TGO growth at a readily oxidized layer^{15,88,89}. Thermal expansion mismatch between the topcoat and TGO at the topcoat/bondcoat interface is a critical issue as TGO growth progresses. This and other failure sources are well-described in the context of EB-PVD processed TBC topcoats (Fig. 2.18)¹⁷ and discussed in sections 2.4.1 and 2.4.2. Features of interest also apply to TBCs of non EB-PVD architecture, as well as to EBCs. Any, many, or all of these failure mechanisms can be in progress simultaneously¹⁷, and this description provides useful context for the many possible combined sources of failure. The likelihood of bondcoat oxidation in a coating system, as a direct source of failure or as one which combines with others to cause failure, motivates a closer look at the mechanical effects of bondcoat oxidation.

A fracture criterion for spallation of topcoats related to TGO growth and properties was established by Schlichting et al.⁸⁹. This criterion relates some of the key parameters shown in Fig. 2.19, including the radius of a given layer undulation, the thickness and internal stress present in the TGO, and the crack length in the material. A mathematical expression of this criterion is⁸⁹:

$$\frac{\pi R^2 E_{TGO} \Gamma}{2 B h^3 \sigma_{TGO}^2} \leq (1 - e^{-c/h}) \cos \frac{c}{R} + e^{-c/h} \frac{R}{2h} \sin \frac{c}{R}. \quad (2.26)$$

On the left-hand side of the inequality, R is the radius of undulation of the substrate sur-

face, E_{TGO} is the elastic constant of the TGO material, Γ is the fracture energy of the TGO/bondcoat interface, B is a constant, h is the thickness of the TGO layer, and σ_{TGO} is the stress in the TGO. On the right-hand side, repeated variables have the same meaning and c is the length of the crack as shown in Fig. 2.19. **The left-hand side represents the resistance to fracture, and the right-hand side represents the driving force for cracking.** We see that as TGO thickness increases, and/or internal stresses in the TGO increase, and/or the radii of the undulations decrease, the resistance to fracture decreases. The driving force for cracking also increases with crack size and TGO thickness, underscoring the need to minimize TGO growth⁸⁹.

Of particular importance are the exponents on the h and σ terms in the denominator of the fracture resistance term. The fracture resistance decreases as $\frac{1}{h^3}$ and $\frac{1}{\sigma^2}$, showing just how deleterious the effect is of TGO growth on the fracture and spallation resistance of the system. Furthermore, the strain energy in the TGO scales with the TGO thickness, meaning that an increase in TGO thickness results in an increase in TGO internal stress⁸⁹. TGO stresses even into the GPa range have been measured by Raman spectroscopy after short oxide growth times⁹⁰. **The critical effect of TGO growth on TBC and EBC systems necessitates coating design to account for and mitigate oxidation.**

2.5 Reducing oxidation in YbDS-based EBC systems

As detailed previously, oxidation is a critical issue for barrier coating systems on substrates. In current-generation EBC systems, the silicon bondcoat is especially vulnerable to accelerated oxidation due to the humidity in the combustion environment. It is well-known that temperature, time, and partial pressure of the oxidant, among other factors, are positively correlated with increased oxidation. However, as discussed earlier, increasing combustion engine efficiency requires increased temperatures and possibly increased pressures in the engine. Additionally, the turbine materials put into service are expected to survive extended durations of exposure (25,000 hours, for natural gas power generators)⁸⁴. Since the fundamental factors influencing silicon oxidation cannot be minimized and still allow for improvements in engine efficiency, alternative solutions must be devised for addressing the issue of silicon oxidation in current-generation EBCs.

2.5.1 Modifications to silicon oxidation through chemistry

Since the incorporation of silicon bondcoats into the second generation of EBC systems, NASA Glenn has focused on decreasing oxidation and oxide growth of these bondcoats in order to mitigate oxide/TGO-based failures and extend the systems' usable life times.

To reduce oxidation of the silicon bondcoat in current-generation EBC/CMC systems, work

by Schlichting has provided inspiration^{14,15}. In that work, Schlichting studied the effects of oxide additives in glassy silica coatings applied on single-crystal silicon substrates. The substrates were dip-coated in alcohol solutions, and coatings were converted by thermal decomposition in a furnace to produce binary $\text{Al}_2\text{O}_3/\text{SiO}_2$, $\text{TiO}_2/\text{SiO}_2$, $\text{B}_2\text{O}_3/\text{SiO}_2$, and $\text{Ge}_2\text{O}_3/\text{SiO}_2$ glassy coatings. Oxidation experiments, performed in oxygen for 20 hours in temperatures from 700°C to 1100°C, were used to study the effects of the oxide additives on oxidation rate and oxidant diffusion through the coating to the silicon substrate¹⁴. Results are adapted in Fig. 2.20¹⁴.

Oxidation rate and (converted by Schlichting) oxygen diffusion rate data in the experiment showed that the addition of Ge_2O_3 to the coatings increased these rates compared to the system with the baseline (pure SiO_2) control coating. Furthermore, oxidation and oxygen diffusion rates increased along with Ge_2O_3 mole percent in the coating. B_2O_3 increased the rates even further, and the same relationship of increased rates along with mole percent boron was observed. Glasses with additions of Al_2O_3 or TiO_2 showed oxidation and diffusion rates slightly increased from the baseline SiO_2 , or in some cases comparable to the control value¹⁴.

In two cases, the addition of 10 mole percent Al_2O_3 or 10 mole percent TiO_2 , there was a decreased activation energy for oxygen diffusion from 82 kJ/mol in pure silica to 62 kJ/mol in the modified coatings. At higher temperatures, the diffusion rate of oxygen through the modified coatings was actually lower than in the case of the baseline. This was due to the Arrhenius behavior of the diffusion, where decreased activation energy results in smaller temperature dependence¹⁴.

The effects of the additives on oxygen diffusion are attributed to structural changes in the glass network of silica. In the cases of boron and germanium, increased diffusion was explained by the example of large B_5O_6 rings. The presence of larger rings in the glassy structure provided a mechanism by which oxygen could diffuse through the larger ring openings more easily than in the pure silica glass. Aluminum, on the other hand, was known to occupy silicon sites in silica glasses, straining the silica glass structure. With enough alumina added, the structural strain could lead to crystallization of mullite and a decrease in oxygen diffusion. Schlichting further tested these relationships by producing a coating with 20 mole percent Al_2O_3 and 5 mole percent Na_2O . The alkali ions opened the glassy network ring structure and oxygen diffusion was dramatically increased¹⁴. Wang et al. studied the diffusion of oxygen tracer species in pure and Al-doped amorphous silica TGOs and found that the diffusion of oxygen was suppressed by the Al^{3+} impurities, attributing the difference to aluminum ions sitting in the interstitials of the network rings in the glassy structure⁹¹.

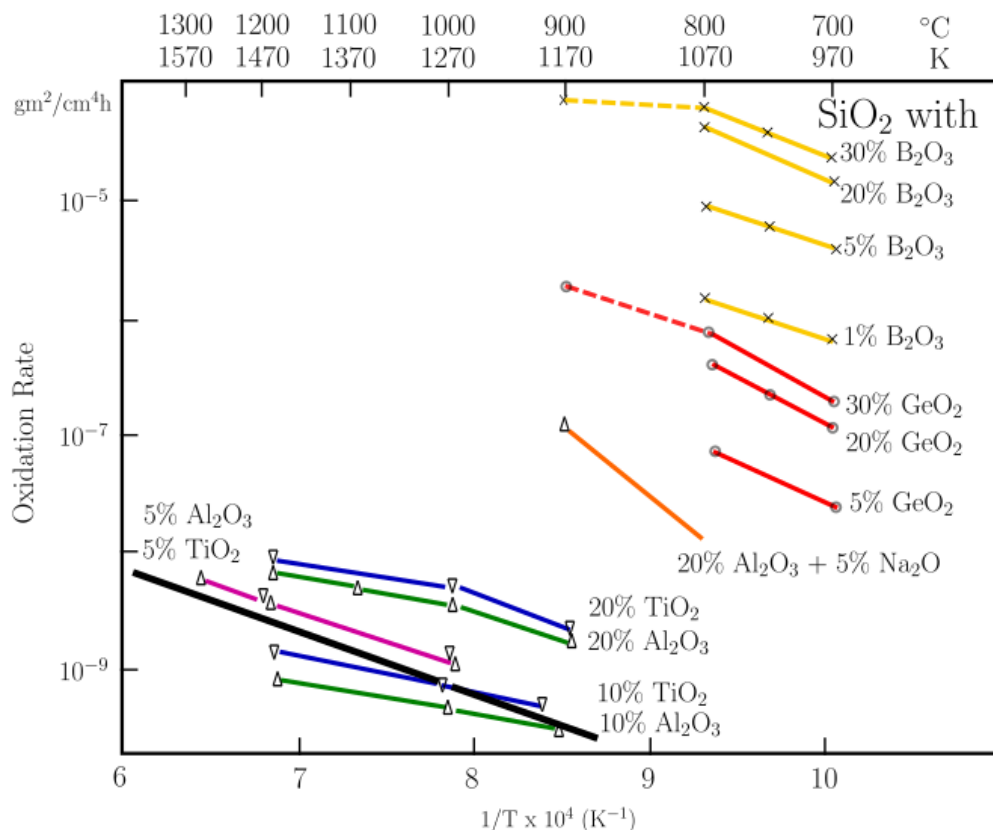


Figure 2.20: Oxidation rates reported by Schlichting. Image adapted from that publication¹⁴.

Using Schlichting's work as inspiration, Kang Lee at NASA Glenn Research Center investigated the effects of select oxide additives on the oxidation of Si bondcoats in CMC/EBC systems with the silicon bondcoat and a YbDS-based topcoat, which were deposited onto SiC_f/SiC CMC substrates¹⁵. Lee provided the SiC-based substrate materials (SiC_f/SiC or Hexoloy SiC), silicon, ytterbium disilicate powders, and oxide additive powders to a third party, air-plasma spray vendor for processing. The oxides were added to the precursor powders used to produce plasma-sprayed YbDS topcoat layers. These oxide additives included alumina (Al₂O₃), mullite (3 Al₂O₃ · 2 SiO₂ or 2Al₂O₃SiO₂), yttrium aluminum garnet (or YAG, Y₃Al₅O₁₂), and/or titania (TiO₂) in varying amounts to produce desired topcoat compositions¹⁵.

One early hypothesis was that the oxide additives could affect deposition or sintering and therefore the microstructures of the topcoat materials, thereby reducing oxidant diffusion through elimination of oxygen gas or water vapor diffusion pathways of cracks, pores, and/or splat boundaries. At the same time, or alternatively, the oxide additives could affect the atomic structure of the topcoat material through cation substitution or the formation of

secondary phases. The topcoat contains significant amorphous content upon plasma-spray deposition but crystallizes rapidly upon heating to 1316°C, which was the maximum intended temperature of the thermal cycling profiles in the study. Thus, changes in atomic structure would be in crystalline rather than amorphous materials, a departure from the work of Schlichting. Still, in the second outcome, atomic or molecular diffusion of oxidants would be inhibited through the material structure much as was studied in the Schlichting's earlier work. A third possible effect of doping the topcoat materials with oxide additives could be the incorporation of some dopant species into the growing thermal silicon oxide layer at the topcoat-bondcoat interface. Altering the composition of the silicon thermal oxide could in turn alter the further oxidation behavior of the silicon layer, much as was observed in the work of Schlichting^{14,15,92,93}.

The basics of Deal and Grove's analysis (discussed previously) can apply to EBC/CMC silicon bondcoat oxidation either by treating the topcoat as oxygen permeable and not rate-limiting, or by treating it as diffusion limiting with respect to oxidant species. In the first case, linear behavior would be observed at early oxidation stages and oxide growth would slow in a parabolic fashion with increasing thickness, corresponding to the third outcome described above. In the second case, later-stage—or parabolic—growth would be observed from the outset of an oxidation experiment, corresponding either of the first two outcomes above.

Oxide additives were included in small amounts in the YbDS precursor powders, with the intent being to prevent the formation of significant secondary phases and instead study the effects of small changes in chemistry. Significant secondary phases might present new issues in that they would likely possess significantly different materials properties than the YbDS intended for study, complicating any analysis. Secondary phases could also enhance or diminish the general effectiveness of the topcoat in the combustion engine environment, but in either case would likely obfuscate the effect of chemical changes on one primary topcoat phase. Incorporating small amounts of additives can thus limit the assessment to primarily YbDS topcoat materials. Limiting the effects in this way expands research into a promising topcoat material and might serve as a framework for considering similar changes to other topcoat materials¹⁵.

2.6 Steam cycling at NASA Glenn

Steam cycling is commonly used to test the suitability of materials intended for engine use by simulating the hot, humid combustion environment, and is useful for exposing CMC/EBC samples to humid oxidation and thermal cycling in the same experiment. This simulation

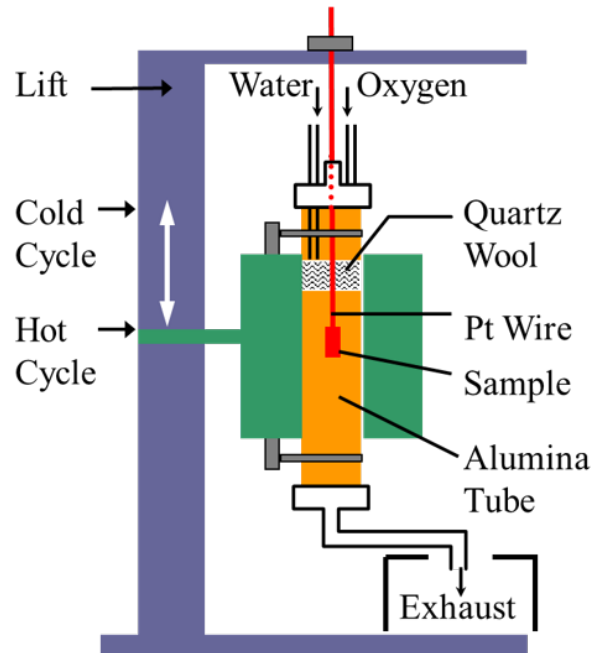


Figure 2.21: Illustration of the steam cycling furnace used at NASA Glenn Research Center. Image courtesy of Kang N. Lee.

permits the study of samples much smaller than the material structures required to construct a full engine prior to their implementation, which is advantageous when the materials used are expensive. Very generally, samples are placed into some kind of furnace which is fitted with the means to flow a gas of choice in the sample chamber. For steam cycling, the gas of choice naturally is humid air or humid oxygen. Temperature profile and humidity in steam cycling experiments are determined by those which will be imposed or necessary for the engine application.

At NASA Glenn, steam cycling experiments are performed in a setup illustrated in Fig. 2.21. The setup consists of a vertically oriented tube furnace with fittings on either end of the tube for flowing gases. The sample is suspended in the tube furnace by a platinum wire, allowing for separate and independent movements of the sample and furnace. A motorized hoist moves the tube furnace up and down around the sample, allowing for rapid temperature cycling of the sample between the hot and ‘cold’ sections of the furnace without subjecting the tube or furnace elements to thermal shock.

Two input ports are used for the atmosphere, one through which oxygen gas is flowed and the other through which liquid water is dripped into the tube using a peristaltic pump. The liquid water is caught by quartz wool installed inside the ‘cool’ (still several hundred degrees Celsius) section at the top of the tube, where it then evaporates to humidify the flowing gas.

The flow rates of oxygen and water are prescribed to set the humidity at elevated temperature in the furnace hot section, using the ideal gas law and accounting for temperature changes.

For current-generation EBCs testing, one steam cycle consisted of a one-hour dwell at 1316°C (2400°F), the set point and hot section temperature of the furnace, followed by a 20-minute dwell in the cooler section of the furnace, which was cooler than the hot section by several hundred degrees Celsius yet still hot enough to evaporate water. The atmosphere was 90 percent water vapor, balance oxygen (90% H₂O, bal. O₂), as determined by flow rates and prescribed for the 1316°C hot section of the furnace. This steam cycling setup has been used many times in previous NASA Glenn temperature and steam cycling studies^{10,15,94}.

2.7 Residual and internal stresses

Residual stresses are stresses which remain in a material after the original source of a stress is no longer applied. Sources of residual stress commonly include machining, surface treatments, thermal expansion mismatch, nonequilibrium cooling. The primary sources of stress in this work are thermal expansion mismatch, processing including rapid quenching, and chemical changes in the form of phase transformations. Internal stresses are stresses present in a material due to the material properties. Since the stresses under consideration arise from the properties of the materials studied, they are technically internal stresses. In the literature, stresses in environmental barrier coating systems are commonly referred to as either residual stresses or internal stresses.

Internal coating stresses are the combined effect of three stresses⁹⁴:

$$\sigma_c = \sigma_q + \sigma_{chem} + \sigma_t \quad (2.27)$$

Quenching stresses, σ_q , arise from rapid and non-equilibrium cooling that takes place during plasma-spray processing⁹⁵. Chemical stresses, σ_{chem} , are difficult to quantify and arise from sintering, oxidation, and phase changes in the materials⁹⁴. Thermal mismatch stresses, σ_t , result from thermal expansion mismatch between bonded materials. Thermal mismatch stresses can be calculated using the expression¹⁸:

$$\sigma_t = \frac{(\alpha_c - \alpha_s)(\Delta T)E_c}{(1 - \nu_c)}. \quad (2.28)$$

In this equation, α_c and α_s are the thermal expansion coefficients for the coating and substrate, respectively. ΔT is the change in temperature, in the same units as the CTE temperature. E_c and ν_c are the elastic modulus and Poisson's ratio, respectively, of the coating material.

Withers and Bhadeshia compiled a list of various stress measurement techniques, which are summarized in the adapted table below (Table 2.3)⁹⁶:

Table 2.3: A brief list of residual stress measurement techniques, with relevant parameters. Adapted from Withers and Bhadeshia⁹⁶.

Method	Penetration	Spatial resolution	Accuracy
Raman spectroscopy	$< 1\mu\text{m}$	$\sim < 1\mu\text{m}$	$\Delta\lambda \approx 0.1 \text{ cm}^{-1}$
Laboratory X-ray diffraction	$< 50\mu\text{m}$ (Al); $< 5\mu\text{m}$ (Ti)	1mm lateral 20 μm depth	$\pm 20\text{MPa}$
Synchrotron X-ray diffraction	50-150mm (Al)	20 μm laterally	$\pm 10 \mu\text{strain}$
Neutron diffraction	200mm (Al) 4mm (Ti)	500 μm	$\pm 50 \mu\text{strain}$
Magnetic (magnetic domains)	10mm	1mm	10%
Ultrasonics (elastic wave velocity)	$> 10\text{cm}$	5mm	10%
Hole drilling (shape distortion)	$\sim 1\text{-}2\text{x}$ hole dia.	50 μm depth	$\pm 50\text{MPa}$
Curvature (shape distortion)	0.1-0.5 of thickness	0.05 of thickness	Limited by min. measurable curvature

Several aspects of the internal stress measurements needed for multilayer CMC/EBC materials influence the choice of experiment. Spatial resolution should be fine enough for measurements smaller in size than the individual layers, in order to observe trends in stresses inside each layer. Since the thinnest layer in a given sample is often on the order of tens of microns, all techniques are eliminated except for Raman spectroscopy and X-ray diffraction. Next, measured stresses must represent the bulk of each layer, where surface effects introduced by sample preparation do not exist. Raman spectroscopy typically measures stresses at the surface or including a small volume of the subsurface. Likewise, X-ray diffraction experiments in reflection geometries measure only small depths into the sample surface. Sample machining required for these experiments rules out Raman spectroscopy and reflection diffraction, since measured stresses are unlikely to represent bulk stresses.

The remaining choice is to use transmission diffraction, where samples are thick enough along the X-ray beam such that measured stresses represent almost entirely the bulk with minimal surface machining effects. As indicated in Table 2.3, laboratory X-ray sources have minimal penetration into many materials. Since rare earth elements are very X-ray absorbing, samples for laboratory X-ray transmission would need to be so thin that surface effects would again dominate the measurements. This is also in part due to the relatively low photon flux provided by laboratory sources.

Internal stress measurements in multilayer CMC/EBC materials must be accomplished using transmission diffraction geometry with high spatial resolution. Sufficient photon flux is

critical for measuring samples of sufficient thickness on a reasonable timescale. As discussed in greater detail below, synchrotron X-ray diffraction is the only technique offering this combination of traits.

2.7.1 Synchrotron-based wide angle X-ray scattering (WAXS)

Synchrotron X-ray diffraction, more specifically Wide-Angle X-ray Scattering (WAXS), is the only non-destructive measurement technique with the resolution and flux necessary to measure strains in bulk materials like those in this work. Diffraction resolution is particularly important for ceramic materials because, as these are typically strong and brittle, relatively small strains can be related to very high stresses. The strain resolution from WAXS measurements depends on sample specifics, X-ray energies, and experimental setup; a careful WAXS experiment can achieve strain resolution of approximately 10 μ strain. This strain resolution produces a stress resolution of approximately 10 MPa for every 100 GPa of material hardness. Hardness of a few to several hundred GPa in most ceramic materials, and ceramic stresses typically of hundreds of MPa, make this resolution very favorable for the multilayer materials under consideration¹¹.

WAXS has been used on many prior occasions to measure and study strains and stresses in materials. To name a select few: Weyant et al. studied stresses and microstructure in tantalum oxide-based coatings on silicon nitride substrates, as well as YSZ coatings on NiCrAlY substrates^{95,97,98}; Harder et al. studied residual strains and phase transformations in BSAS coatings^{59,68}; Stolzenburg et al. studied residual strains, phase transformations, and engine contaminant effects in ytterbium silicates^{13,99}; and Siddiqui et al. studied strains and stresses in multilayer cylindrical thermal barrier coatings on metallic substrates¹⁰⁰. These studies were all performed at beamline 1-ID of the Advanced Photon Source (Argonne National Laboratory, Lemont IL).

The high photon fluxes at synchrotron sources are critical for providing sufficient diffraction from the materials, and they permit sample thicknesses much larger than could be used in transmission diffraction experiments in a typical laboratory setup. The sample thickness for adequate diffraction statistics depends strongly on composition: samples of lighter elements can be thicker than those of heavier elements for reasonable data collection. Since the materials in current-generation EBCs contain high concentrations of rare earth elements, which that strongly attenuate X-rays, the sample thickness along the photon beam is generally limited to a few millimeters for timely measurements and data collection. Stolzenburg et al. used rare earth silicate samples of 1.5-2mm thickness along the X-ray beam, which could be reasonably measured by WAXS¹³.

The multilayer configuration of the CMC/EBC systems further confirms the necessity of synchrotron facilities for X-ray diffraction. Because the layers in the as-deposited samples can be as small as tens of micrometers tall, with height being measured vertically and perpendicular to the beam path, it is necessary to have control over the X-ray beam dimensions in order to measure these relatively thin individual layers. Previous synchrotron WAXS studies on CMC/EBC systems have used beam heights of tens of microns in order to resolve strains well within individual layers^{13,59,68,97–99}. These beam sizes even permitted diffraction through each individual layer at several vertical positions, meaning that strains and stresses could be analyzed with some meaningful resolution with respect to the vertical dimension of the samples.

Data collection equipment at most synchrotron sources allows for experimental data to be collected over several days of a user visit. Some WAXS-capable beamlines also have the capability and facilities to incorporate sophisticated *in-situ* experimental setups, such as advanced sample fixturing and positioning, mechanical testing, and specialized heating, that cannot be coupled with X-ray measurement techniques in most laboratory facilities.

2.8 X-ray computed tomography (XCT)

X-ray Computed Tomography (XCT), also referred to in this work as tomography, is a technique used for analyzing microstructure in three-dimensional volumes of samples. This unlocks the visualization and analysis of a sample in three dimensions, in contrast to two-dimensional or short depth-of-field imaging methods. The overall and pixel sizes of the detector, as well as the size of the datasets produced (which can be many tens of gigabytes to more than one terabyte, for high-resolution images and small rotation step sizes), create an inverse relationship between resolution and size of analyzed sample volume. Sample size, data collection method, and experimental setup also influence resolution. Synchrotron XCT studies of EBC systems generally reach resolutions of approximately 1-2 μm per pixel, and have been used to great effect to identify features such as pores and cracks in three-dimensional samples, such as by Stolzenburg et al.¹³.

The tomography mode is determined by the distance from the sample to the detector. In absorption mode, which requires the detector to be in the near field (small sample-detector distance), differences in contrast are produced by differences in the absorption coefficients, and therefore electron densities, of the materials. Absorption mode is useful for more quantitative 3D analysis. In phase contrast mode, which uses a detector in the far field (larger sample-detector distance), differences in index of refraction produce image features. Phase contrast imaging is favorable for visualizing interfaces between dissimilar materials, cracks,

and crevices, and for maximizing contrast between phases of similar density. Near-field and far-field distances are defined by the samples and experimental setup. Generally, near field describes sample-detector distance of centimeters whereas far field describes a distance of tens of centimeters. Intermediate sample-detector distances provide a mix of absorption and phase contrast imaging. Due to the temperature sensitivity of CCD cameras typically used in tomography image collection, *in-situ* heating experiments can sometimes preclude the use of a near field setup.

Chapter 3

OXIDATION AND MICROSTRUCTURE OF YB₂SI₂O₇-BASED EBC SYSTEMS

Studies of oxidation and microstructure evolution in the Yb₂Si₂O₇-based EBC systems were performed on multilayer systems with a substrate, bondcoat, and topcoat. Coupon samples with flat ceramic-matrix composite (CMC) substrates coated on one large side, the most common configuration in literature studies, were used for consistency with previous studies. CMC samples were also readily available in flat geometries without special processing, and more closely mimicked the real-world application of the materials. Varying the topcoat thicknesses of coupon-based samples provided a means of cross-analyzing microstructure and oxidation.

Microstructure is explored first, to develop an overall impression of the samples. This includes microstructural features as they result from the chemistry in each Yb₂Si₂O₇-based system, including thermal oxide (TGO) growth, as well as the changes in these features with exposure to high-temperature and/or steam conditions. Microstructure observations are critical in the detailed discussion on the oxidation of the bondcoat in each EBC system.

3.1 Background

3.1.1 Deal and Grove model of silicon oxidation

In the Deal and Grove model of silicon oxidation (described in Section 2.1.1), the general relationship for oxidation is given by

$$\frac{x_0}{A/2} = \left[1 + \frac{t + \tau}{A^2/4B}\right]^{\frac{1}{2}} - 1 \quad (3.1)$$

where oxide thickness is related to time. The term A is defined:

$$A \equiv 2D_{eff}(1/k + 1/h) \quad (3.2)$$

where D_{eff} is the effective diffusivity of the oxidant in the oxide, h is a gas-phase transport coefficient, and k is a rate constant associated with the silicon surface. Next,

$$B \equiv 2D_{eff}C^*/N_1 \quad (3.3)$$

where C^* is the equilibrium concentration of the oxidant in the oxide, and N_1 is the number of oxidant molecules in a unit volume of the oxide layer. C^* is further defined:

$$C^* = Kp. \quad (3.4)$$

K is the gas solubility parameter from Henry's Law and p is the partial pressure of the oxidant in the gas. Lastly for the general relationship,

$$\tau \equiv (x_i^2 + Ax_i)/B. \quad (3.5)$$

For short times, where $t \ll A^2/4B$,

$$\frac{x_0}{A/2} \cong \frac{1}{2} \left(\frac{t + \tau}{A^2/4B} \right) \quad (3.6)$$

or

$$x_0 \cong \frac{B}{A}(t + \tau). \quad (3.7)$$

The relationship between oxide thickness and time is linear, thus, this is the linear rate regime. The coefficient

$$\frac{B}{A} = \frac{kh}{k+h} \left(\frac{C^*}{N_1} \right) \quad (3.8)$$

is the linear rate constant. For long oxidation times where $t \gg A^2/4B$ and $t \gg \tau$,

$$\frac{x_0}{A/2} \cong \left[\frac{t}{A^2/4B} \right]^{\frac{1}{2}} \quad (3.9)$$

or

$$x_0^2 \cong Bt. \quad (3.10)$$

In this case, the *square* of the oxide thickness is related to time, thus this is the parabolic rate regime. The two different rate regimes and the relationship between time and TGO thickness for each is important for understanding the oxidation behaviors in the multilayer systems.

3.2 Methods

3.2.1 Sample preparation

All multilayer samples of this work were air plasma-spray processed by a third party vendor contracted by Dr. Kang Lee at NASA Glenn Research Center. Baseline topcoats (called "baseline" in this work), composed of unmodified $\text{Yb}_2\text{Si}_2\text{O}_7$, were plasma sprayed using a pre-sintered mixture of Yb_2O_3 and SiO_2 powders. Alumina-modified topcoats ("6A") included 6 wt.% Al_2O_3 powders, added to the baseline $\text{Yb}_2\text{Si}_2\text{O}_7$ and spray-dried prior to plasma-spraying. Mullite-and-YAG-modified topcoat "M2Y" included 1.39 wt.% mullite and 2.33 wt.% YAG, incorporated in the same way as the alumina dopants in 6A. A second mullite-and-YAG-modified topcoat (also called "M5Y") included 1.39 wt.% mullite and 4.66 wt.% YAG.

After processing, CMC-substrate samples were sectioned for steam cycling at NASA Glenn; steam cycling experiments were performed using the rig described in Chapter 2 (Fig. 2.21).

Then, steam-cycled and other samples were received at Caltech from NASA Glenn for analysis. In some cases, a custom induction furnace at Caltech (described in Chapter 6) was used for additional analysis.

3.2.1.1 Multilayer coupon EBC-CMC samples

Multilayer EBC samples on flat CMC substrates were plasma-sprayed onto a chemical vapor infiltrated (CVI) SiC_f/SiC coupon of approximately 25mm length, 12.5mm width, and 3-3.5mm thickness. The silicon bondcoat was plasma-sprayed to a nominal thickness of $125\mu\text{m}$, then the $\text{Yb}_2\text{Si}_2\text{O}_7$ -based topcoat to a nominal thickness of $250\mu\text{m}$ for the primary samples studied. For studies measuring oxide growth in samples of varied topcoat thickness, the $\text{Yb}_2\text{Si}_2\text{O}_7$ -based layers were instead sprayed to nominal thicknesses of $125\mu\text{m}$ (5 mils) and $500\mu\text{m}$ (20 mils). As-processed sample dimensions for multilayer materials were approximately 25.4mm (1 inch) length, 12.7mm (1/2 inch) width, and 3.5-4mm height (this dimension being the combined thicknesses of the substrate and the coatings).

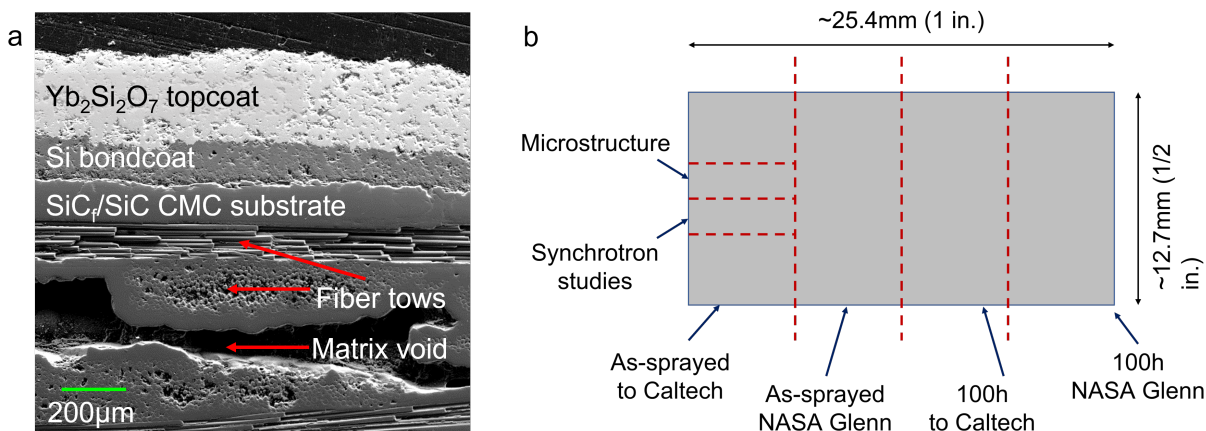


Figure 3.1: Overview of the EBC samples studied. Left: microstructure of the as-sprayed EBC layers and top of the substrate. Right: schematic of sample sections.

At NASA Glenn Research Center, one as-sprayed sample of each composition was sectioned in half lengthwise, with one half retained and the other steam-cycled for 100 hours in a custom steam-cycling rig at that facility. Another as-sprayed sample of each composition was steam cycled for 500 hours in the steam cycling rig and then sectioned in half lengthwise, with one half retained and the other steam cycled for another 500 hours (for a total of 1000 hours). Each of the 100-hour, 500-hour, and 1000-hour steam cycled samples was then cut in half (again lengthwise), with one half retained at NASA Glenn for analysis. Sectioning and allocations are illustrated in Fig. 3.1b. An as-sprayed sample, halves of steam-cycled

samples, and an additional sample exposed to air for 500 hours at high temperature were received at Caltech for analysis and synchrotron experiments. Samples of baseline, 6A, and M2Y composition, with $125\mu\text{m}$ and $500\mu\text{m}$ thick topcoats each of which were 500-hour and 1000-hour steam-cycled conditions, were also received at Caltech. Additionally, the custom induction furnace (mentioned above and described later) was used to anneal one sample of each composition at $1315\text{-}1320^\circ\text{C}$ in flowing argon. The short heating step was designed to crystallize the topcoat material and subject the multilayer system to uniform cooling from high temperature, with minimal changes in microstructure or TGO growth. In all cases of oxidized samples (steam cycling and air exposure), samples were sectioned as far from from the originally uncoated surfaces as possible. This minimized oxidant ingress through the sides of the samples and was intended to maximize the effects of the topcoat in oxidation behavior. The same sample geometries were used in the works of Harder⁵⁹ and Stolzenburg¹¹.

From the 6-7mm long, 12.5mm wide, and 3.5-4mm thick samples, samples of 1.5-2mm width were sectioned along the 12.5mm dimension for microscopy, synchrotron, and mechanical properties studies. This produced samples of 6-7mm length, 1.5-2mm width, and 3.5-4mm height. Samples for microscopy were cast in acrylic, ground and polished down to a $1\mu\text{m}$ diamond suspension, and carbon-coated for scanning electron microscopy.

3.2.2 Imaging and chemical analysis

Scanning electron microscopy (SEM) and energy-dispersive spectroscopy (EDS) were used for imaging and chemical analysis, respectively. To maximize contrast of microstructure in the samples, the accelerating voltage was set to 15kV. The $\text{Yb}_2\text{Si}_2\text{O}_7$ topcoats had very low electrical conductivity and were prone to surface charging by electrons in the SEM. This was addressed by applying two or three carbon coats and using carbon tape, adhered to each sample end. The working distance for imaging was also set to 7-8mm, which further reduced surface charging.

In backscattered electron imaging mode, very low-brightness and high-contrast imaging settings were used to distinguish features in the EBC topcoats. Mid-level brightness and lower contrast settings, in both backscattered and secondary electron modes, were used to image other layers and the substrate, as well as interfaces. For EDS, accelerating voltage was kept at 15kV and detectors collected X-rays for 30-45 seconds when scanning points and small regions to maximize signal.

3.2.3 Transmission X-ray diffraction

Synchrotron X-ray diffraction was used to collect diffraction patterns in the multilayer EBC materials at the Advanced Photon Source, Argonne National Laboratory. For microstructure

studies, a $2\mu\text{m}$ tall, $100\mu\text{m}$ wide photon beam was used to maximize the resolution with respect to the thickness of the oxide. Key differences between the transmission diffraction patterns and laboratory reflection X-ray diffraction patterns are the transmission geometry used and the high photon flux available at the Advanced Photon Source, which provide spatial resolution and X-ray reflections which could not be achieved using laboratory XRD sources. Transmission diffraction patterns were collected beginning at the top surface of the topcoat and successively through the depth of the topcoat, bondcoat, and part of the substrate. Patterns shown in microstructure analysis are from three locations, and are plotted as normalized and offset intensity against d-spacing. From the bottom up, the first patterns from the mid-height of the topcoat, the second from the topcoat-bondcoat interface, and the third from the bondcoat. Further details of WAXS experiments are discussed in Chapter 4.

3.3 Results

3.3.1 Microstructure in coupon-based samples

3.3.1.1 Baseline $\text{Yb}_2\text{Si}_2\text{O}_7$

In the as-sprayed condition (Fig. 3.2), the air-plasma spray process is evident in the microstructure. The roughness of layer interfaces and the top surface are the result of rapid splat-quenching in plasma-spraying. Splat boundaries, the interfaces between splat-quenched particles, are visible, as well as pores left from processing. Prior to heating, splat boundaries appear in the topcoat, oriented in-plane between successive splats and out-of-plane between neighboring splats.

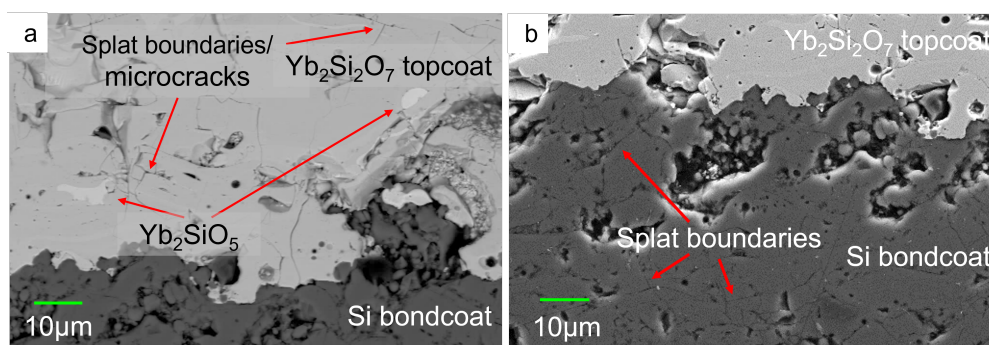


Figure 3.2: Microstructure of the baseline as-sprayed condition: (a) topcoat and (b) bondcoat.

As seen in the left-hand Fig. 3.2a, some splats in the as-sprayed topcoat appear brighter in SEM imaging due to the higher proportion of Yb. These splats are silica-poor from

processing, as also observed in Ref. [15]. Since the plasma-spray process incorporated pre-sintered Yb_2O_3 and SiO_2 powders in stoichiometric combination to form $\text{Yb}_2\text{Si}_2\text{O}_7$, the silica-poor particles likely formed by incomplete mixing or incomplete reaction of the precursor powders.

Splat boundaries can also be identified within the Si bondcoat (Fig. 3.2b). In this case, though, the boundaries are almost entirely comprised of small voids or very thin separations between splats. There is also no visible thermal oxide (TGO) at the topcoat/bondcoat interface in the as-sprayed condition, as expected.

In the substrate, fiber tows visible by SEM are of two primary orientations: into/out of the plane of the image and in-the-plane of both the image and the substrate layer (Fig. 3.2a). Woven tows are infiltrated with SiC matrix. Incomplete infiltration of the CMC with the SiC matrix also leads to voids in the CMC microstructure.

An annealed sample, which was heated to 1315-1320°C for 30 minutes in flowing argon, is shown in Fig. 3.3. In the topcoat (a), the residual Yb_2SiO_5 splats and some splat boundaries are still visible. The splat boundaries are still visible in the bondcoat, as well. In both layers, the splat boundaries are less prevalent than in the as-sprayed condition. There is no visible TGO at the interface of the topcoat and bondcoat (Fig. 3.3b).

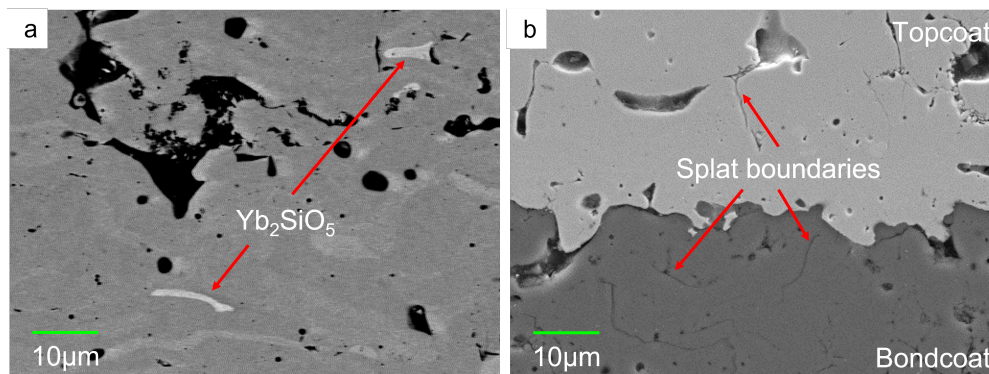


Figure 3.3: Baseline annealed microstructure, in the topcoat (left) and near the topcoat/bondcoat interface.

After 100 hours of steam cycling at 1316°C, small voids or separations between splats are no longer present as in the as-sprayed and annealed conditions. $\text{Yb}_2\text{Si}_2\text{O}_5$ -rich splats remain after steam cycling and, as seen in Fig. 3.4, even through 1000 hours of steam cycling. A TGO $4.4 \pm 1.9 \mu\text{m}$ thick (average \pm standard deviation) is present at the topcoat/bondcoat interface after 100 hours of steam cycling. Fig. 3.5 shows the development of the TGO from the as-sprayed condition through all steam-cycling exposures from the NASA Glenn

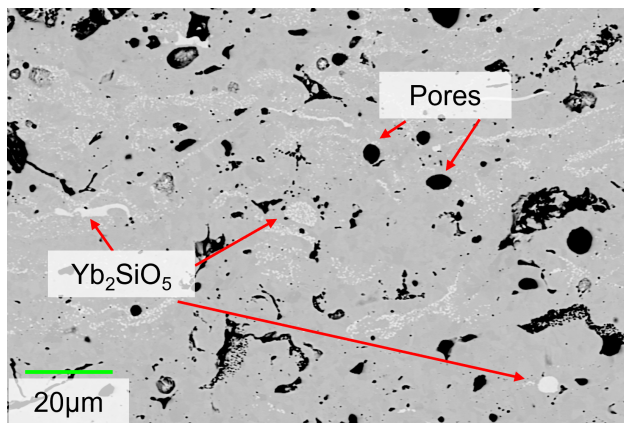


Figure 3.4: Topcoat of the baseline 100-hour steam-cycled condition.

rig. The TGO, identified in other literature sources as cristobalite by the extensive cracking and/or using Raman spectroscopy^{15,101}, shows some vertical cracking after 100 hours of steam cycling, attributed to the 4-5% volume contraction during the transformation from high-temperature β -cristobalite to low-temperature α -cristobalite. The cristobalite TGO and implications are explored further in the Discussion section.

After 500 hours of steam cycling, the TGO at the topcoat-bondcoat interface is $10.8 \pm 4.4 \mu\text{m}$, with noticeably more cracking compared to 100 hours, visible as out-of-plane cracks in the oxide as well as in-plane cracks and void formation near the interfaces of the TGO with the topcoat or bondcoat (Fig. 3.5c). The baseline topcoat and bondcoat after 1000 hours of steam cycling were similar again to those observed earlier in steam cycling. The TGO was thicker than in the 500-hour sample, at approximately $13.8 \pm 4.1 \mu\text{m}$, with significant out-of-plane cracking of the oxide and in-plane cracking and voids near the oxide-topcoat and oxide-bondcoat interfaces (Fig. 3.5d).

Fig. 3.6 shows synchrotron diffraction patterns which provide further detail on the phases present in the baseline system after 1000 hours of steam cycling. The topcoat pattern shows peaks primarily from $\text{Yb}_2\text{Si}_2\text{O}_7$. Two other phases are detected, one being small amounts of α -cristobalite, the low-temperature structure of the cristobalite SiO_2 polymorph, and the other being Yb_2SiO_5 . Multiple reflections are indicated in the figure for the α -cristobalite phase but, since there is overlap between several peaks from this phase and some from the disilicate phase, the peak near 4.05 \AA provides the primary evidence. It is not clear where the cristobalite is present within the topcoat, since there are no locations with obvious contrast differences indicating a lower-density phase or with particle/grain shapes very different from those of the Yb-silicate phases. However, the very low intensity of these peaks indicate that the phase is either comprised of many small particles or is not present in large amounts.

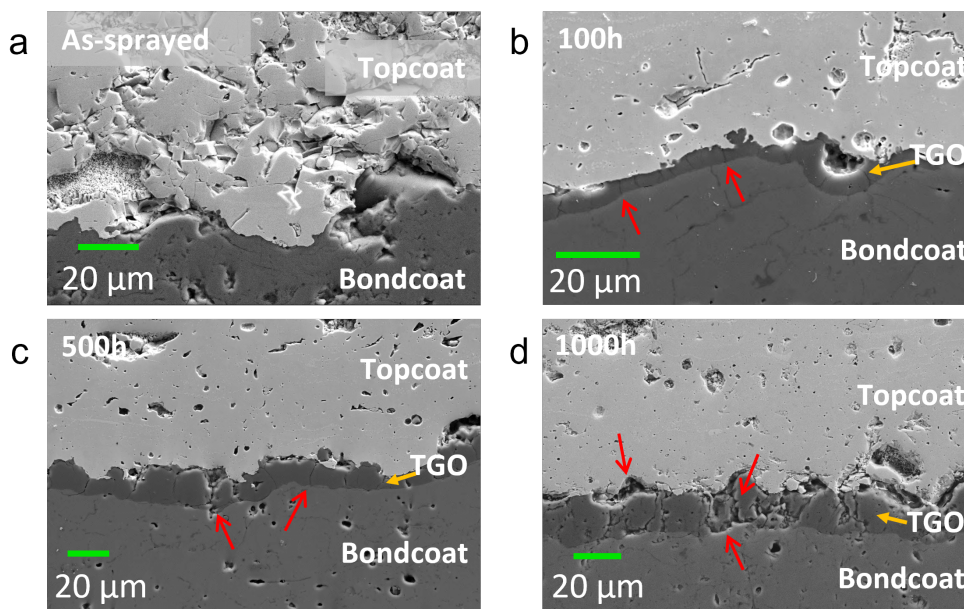


Figure 3.5: SEM micrographs of baseline topcoat/bondcoat interface in as-sprayed and steam-cycled (at NASA GRC) conditions. Red arrows indicate TGO cracking.

The TGO pattern shows low-intensity peaks from the $\text{Yb}_2\text{Si}_2\text{O}_7$ phase. Interface roughness on the order of the TGO thickness makes it difficult to isolate the TGO with transmission diffraction, and so both layers are included in the diffraction. For the same reason, the primary silicon peak appears in this pattern. The presence of an intense α -cristobalite peak confirms the crystallinity and phase of the TGO in the baseline system.

The bondcoat diffraction pattern shows primarily silicon, as expected. Small, trace peaks from the disilicate phase are present; this is again due to interface roughness and its effect on transmission diffraction sampling. Lastly, there is one peak near the location of the primary peak for α -cristobalite. This peak is at a slightly higher d-spacing value, however, and is closer to the location of a β -cristobalite peak.

3.3.1.2 Alumina-modified $\text{Yb}_2\text{Si}_2\text{O}_7$ (6A)

In the as-sprayed condition of the 6A system, splats of varying contrast are again visible in backscatter electron imaging, indicating composition differences. As in the case of the baseline system, the primary contrast difference within the topcoat distinguishes medium-grey splats (the majority of the splats), indicative of $\text{Yb}_2\text{Si}_2\text{O}_7$ in composition, from lighter-colored splats which are indicative of Yb_2SiO_5 . Both kinds of Yb-silicate splats are observed by EDS to possess aluminum, although the Yb_2SiO_5 splats possess less Al (~ 0.5 -1 wt.%) than the $\text{Yb}_2\text{Si}_2\text{O}_7$ splats (~ 1 -2 wt.%). However there are also some oval-shaped splats,

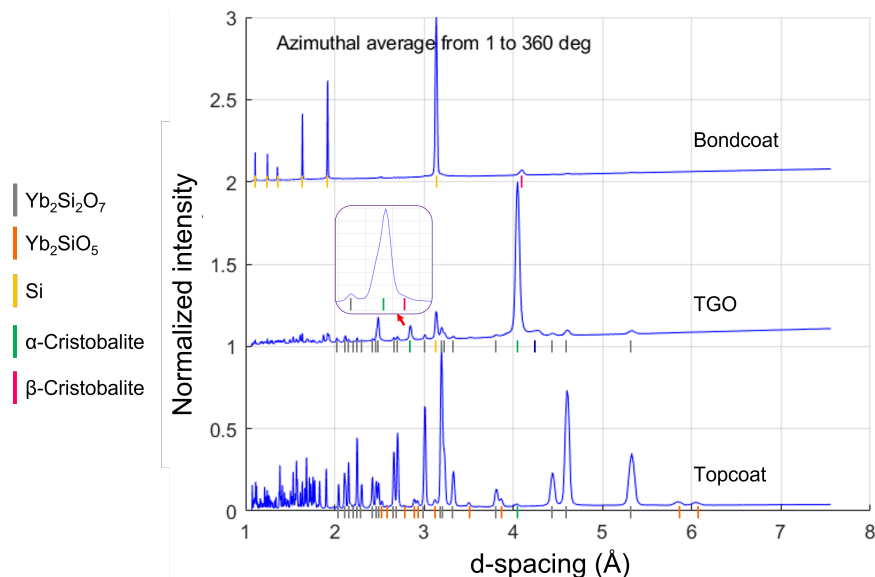


Figure 3.6: WAXS lineouts (normalized intensity vs. d -spacing) for the baseline composition after 1000 hours of steam cycling.

speckled with light and dark grains, present in the as-sprayed 6A topcoat. Measured with EDS, the lighter specks possess approximately (by wt.%) 20% O, 9% Si, 70% Yb, and no (or very little) Al. This is between the Yb_2SiO_5 and $\text{Yb}_2\text{Si}_2\text{O}_7$ compositions, indicating a slightly Yb-rich $\text{Yb}_2\text{Si}_2\text{O}_7$ composition. The darker specks possess approximately (by wt.%) 23% O, 5% Al, 8% Si, and 64% Yb; this indicates a $\text{Yb}_2\text{Si}_2\text{O}_7$ composition with Al_2O_3 added. The Al_2O_3 is segregated into the darker specks of the speckled splats, indicating incomplete mixing of the alumina dopants in some particles during plasma-spray processing.

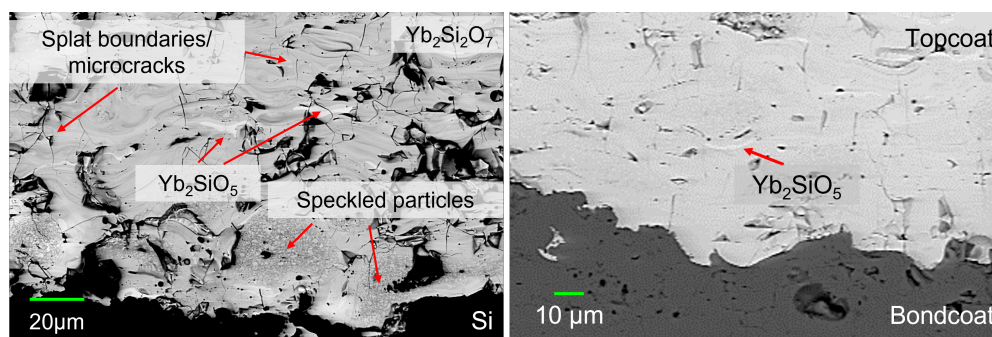


Figure 3.7: As-sprayed 6A topcoat microstructure, with topcoat (left) and interface (right) shown.

The annealed 6A sample is shown in Fig. 3.8. In the topcoat (Fig. 3.8a), Yb_2SiO_5 splats have broken up into fine particles, likely due to reaction with the dopants. There are also

pores and precipitates in the topcoat which were not present in the as-sprayed sample. Splat boundaries are still visible in the bondcoat, but less prevalent than in the as-sprayed condition (Fig. 3.8b). There is no visible TGO at the interface of the topcoat and bondcoat.

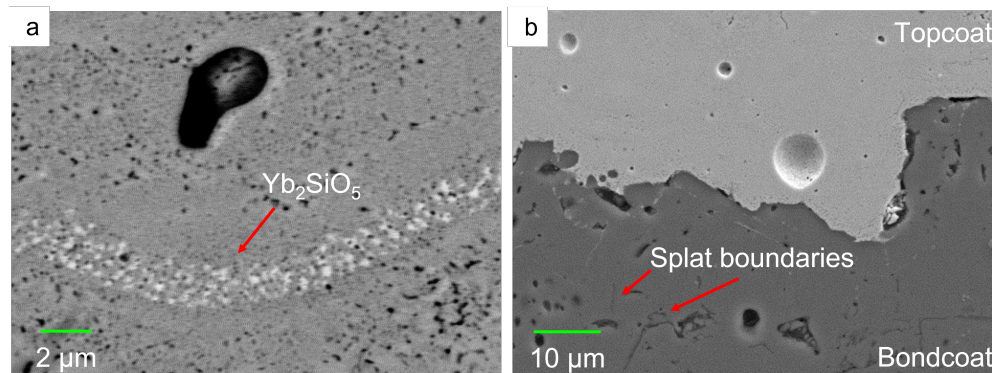


Figure 3.8: 6A annealed microstructure, in the topcoat (left) and near the topcoat/bondcoat interface.

After 100 hours of steam cycling, the contrast between monosilicate- and disilicate-rich splats from the as-sprayed and annealed conditions disappears—thus, the monosilicate-rich splats are assumed to no longer be present in 6A after steam cycling (Fig. 3.9a). This contrasts with the baseline, where the monosilicate was still evident after annealing and steam cycling. Extensive amounts of a second phase are also present in the 6A topcoat, appearing as precipitates which look needle-like in the two-dimensional image. The width of the needles is less than $1\ \mu\text{m}$, and so it is likely that EDS sampled some topcoat volume around the needle(s) in addition to the precipitates themselves. Given the size of the EDS probe in SEM with respect to the size and orientation of the needle-like precipitates, it was not possible to determine the composition of the precipitates using that method. Given the X-ray diffraction evidence for $\text{Yb}_3\text{Al}_5\text{O}_{12}$, the composition of the needles is likely close to the (approximately) 63 wt.% Yb, 9 wt.% Si, 7 wt.% Al, and 21 wt.% O measurement. The needle-like precipitates would then be either the $\text{Yb}_3\text{Al}_5\text{O}_{12}$ composition or that composition enriched with added silicon. The SEM and EDS spot sizes and resulting ambiguity over the volumes measured make characterization of the precipitates difficult.

A new, interfacial layer also develops between the topcoat and bondcoat of the 6A system after 100 hours of steam cycling. Measured with EDS, this layer contains approximately 31-32 wt.% Yb, 22-23 wt.% Si, 38-39 wt.% O, and 7-9 wt.% Al. As seen in Fig. 3.9a, there are also rounded grains near the interface of the topcoat and this interfacial layer. Some of these grains appear to be dense, with no visible pores or needles, while others appear

dense only near the grain-interfacial layer interface and include pores or precipitates away from the immediate vicinity of the interface. The composition of the grains oriented into the interface is approximately 65-66 wt.% Yb, 10-11 wt.% Si, and 24-25 wt.% O. No aluminum was detected by EDS in these grains near the interfacial layer. This composition is very close to stoichiometric $\text{Yb}_2\text{Si}_2\text{O}_7$. The TGO at the interface of the bondcoat and the interfacial layer, of the 100-hour steam-cycled sample is $0.42 \pm 0.09 \mu\text{m}$ thick.

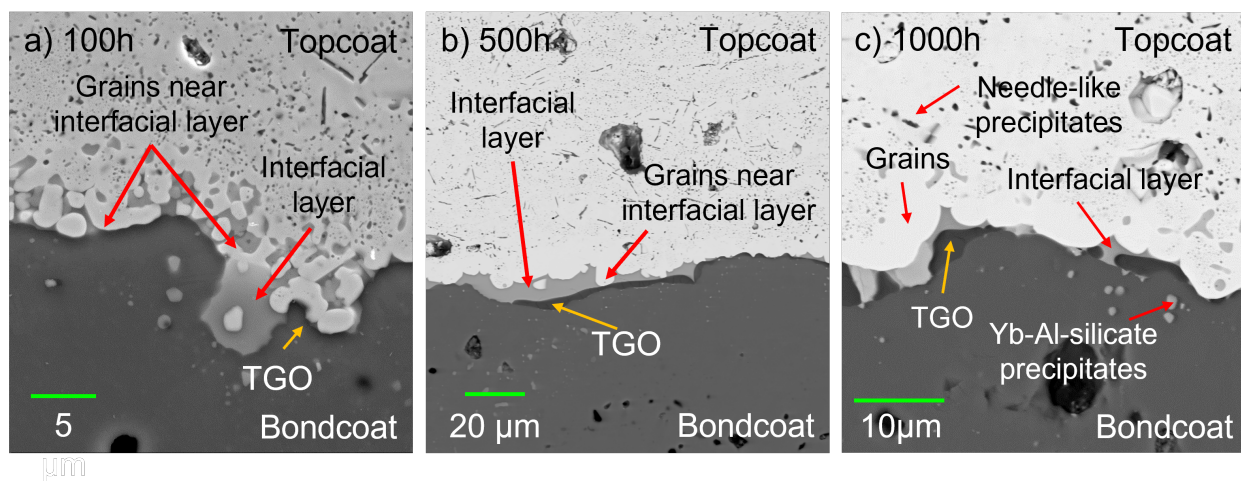


Figure 3.9: 6A, steam cycled for 100 hours (a), 500 hours (b), and 1000 hours (c).

After 500 hours of steam cycling, the 6A topcoat retains the same needle-like precipitates and small pores as observed after 100 hours of steam cycling (Fig. 3.9b). The grey interfacial layer between the topcoat and the TGO persists after 500 hours of steam cycling, as do rounded grains within and adjacent to the interfacial layer from the topcoat side. A secondary phase is present in the laboratory XRD pattern of the 500-hour steam-cycled sample which also appeared in the XRD pattern for the 100-hour steam-cycled topcoat (Fig. 3.11). The TGO after 500 hours of steam cycling is approximately $1.2 \pm 0.6 \mu\text{m}$.

An EDS map of the interface region of the 6A, 500-hour steam cycled sample shows the relative amounts of O, Al, Si, and Yb in the topcoat, interfacial layer, and bondcoat. The interfacial layer is lower in Yb than the topcoat and lower in Si than the bondcoat. There is more relative O present in the interfacial layer than in the topcoat or bondcoat. The Al $K\alpha_1$ and Yb $M\alpha$ spectral peaks overlap, making distinction between these elements difficult by EDS. The interfacial layer does not have the same composition as a silicon TGO and is relatively silicon-poor for a silicon TGO.

The laboratory XRD pattern (Fig. 3.11) of the topcoat after 500 hours of steam cycling shows $\text{Yb}_2\text{Si}_2\text{O}_7$ as well as peaks which correspond to a garnet structure, like yttrium aluminum

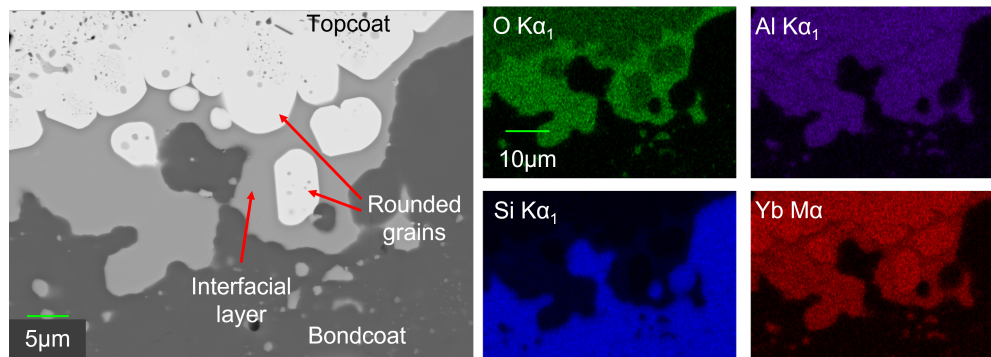


Figure 3.10: EDS map from the topcoat-bondcoat interface of the 6A 500-hour steam cycled sample.

garnet (YAG, $Y_3Al_5O_{12}$). Yttrium is not present in the 6A system, so this structure must be formed by ytterbium with aluminum and oxygen from the as-sprayed topcoat to form $Yb_3Al_5O_{12}$, a garnet structure with ytterbium, as also noted by Lee¹⁵. The $Yb_3Al_5O_{12}$ phase has similar interplanar spacings to those of the $Y_3Al_5O_{12}$ phase.

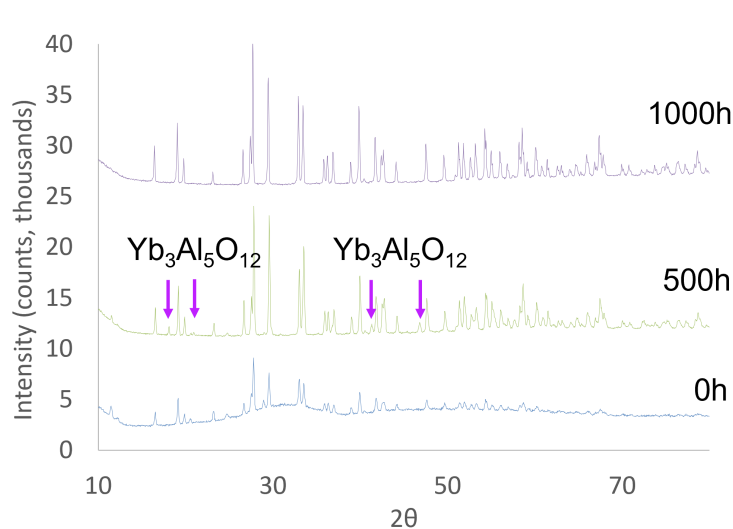


Figure 3.11: Selected laboratory XRD patterns for the 6A topcoat.

The 1000-hour steam-cycled, 6A topcoat retains many of the features observed in the 100-hour and 500-hour steam-cycled samples (Fig. 3.9c). The pores and needle-like precipitates are both still present in this topcoat. Interestingly, the laboratory XRD pattern for this sample does not show the presence of the secondary, ytterbium aluminum garnet phase seen in the laboratory XRD from the 100-hour and 500-hour samples. The TGO after 1000 hours of steam cycling is $2.1 \pm 1.6 \mu\text{m}$.

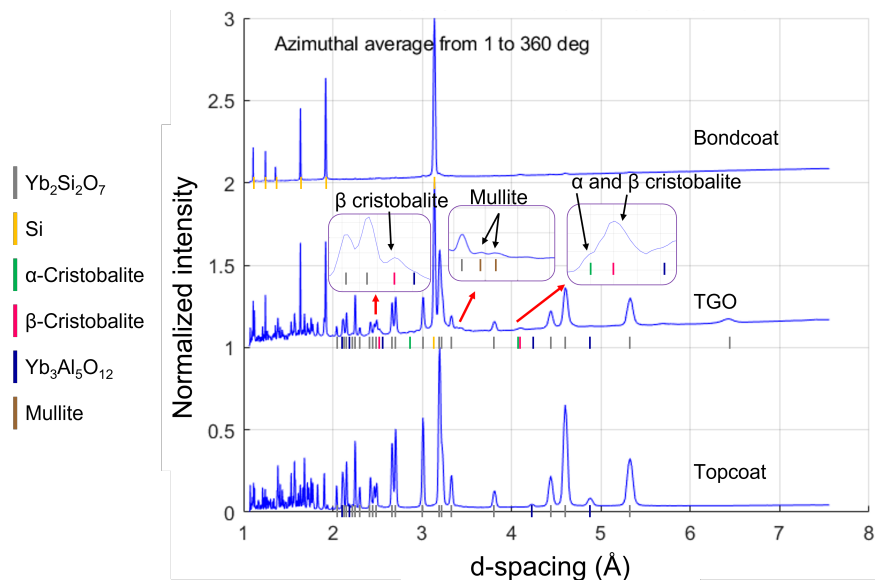


Figure 3.12: WAXS lineouts for 6A after 1000 hours of steam cycling.

Fig. 3.12 shows transmission X-ray diffraction patterns, plotted as normalized and offset intensity against d -spacing, for three locations in the 6A, 1000h steam-cycled sample. As with the baseline transmission WAXS patterns, these were collected at the synchrotron using a $2\mu\text{m}$ tall, $100\mu\text{m}$ wide photon beam, further details for which are discussed in Chapter 4. The improved spatial resolution and photon flux from synchrotron diffraction show a different picture than that observed in conventional laboratory diffraction.

The topcoat pattern is dominated by peaks for the $\text{Yb}_2\text{Si}_2\text{O}_7$ structure, and additionally includes some peaks for the ytterbium-based garnet structure. While the $\text{Yb}_3\text{Al}_5\text{O}_{12}$ phase is present in this topcoat, the low intensity of these peaks, compared to those of the $\text{Yb}_2\text{Si}_2\text{O}_7$ phase, likely explains why the garnet phase was not detected by laboratory XRD. Some α -cristobalite peak locations overlap with confirmed $\text{Yb}_2\text{Si}_2\text{O}_7$ and $\text{Yb}_3\text{Al}_5\text{O}_{12}$ peaks in the 6A, 1000-hour topcoat. Since it is unlikely that the cristobalite phase is actually present in the topcoat in significant amounts, and that phase is not confirmed, the cristobalite peaks are not labeled.

Due to TGO thickness and interface roughness, it was not possible to isolate the TGO at the topcoat-bondcoat interface in 6A for transmission diffraction. Thus, $\text{Yb}_2\text{Si}_2\text{O}_7$, TGO, and $\text{Yb}_3\text{Al}_5\text{O}_{12}$ peaks are all present. The TGO peaks include both the low-temperature, α -cristobalite tetragonal and the high-temperature, β -cristobalite cubic structures.

The bondcoat pattern shows the majority silicon phase. Trace peaks from the $\text{Yb}_2\text{Si}_2\text{O}_7$ structure are likely due to the interface roughness in the system. There are additionally peaks

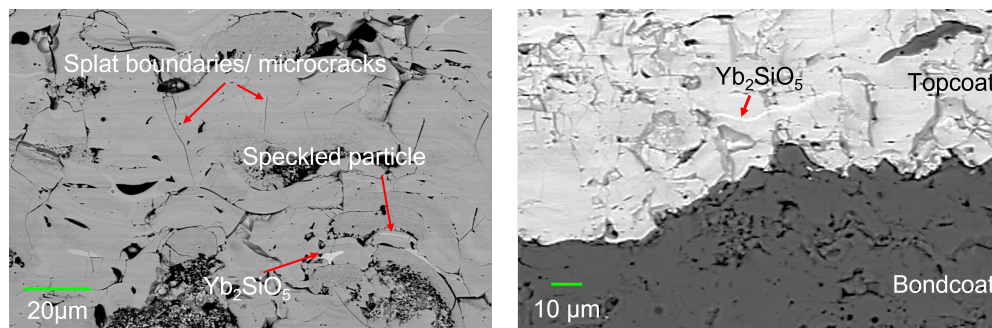


Figure 3.13: Microstructure of as-sprayed M2Y topcoat: topcoat (left) and topcoat-bondcoat interface (right).

present from mullite, indicating some reaction between alumina and silica (or aluminum and silicon-bearing oxides or silicates) in the vicinity of the TGO.

Like in the baseline composition, there is not a large difference in the microstructures of the alumina-modified topcoats between the 250 μm topcoat and the 125 μm and 500 μm topcoats. After 500 hours and 1000 hours of steam cycling, the distinction between disilicate-rich and monosilicate-rich particles disappeared in the topcoat thickness-varied samples as it did in the 250- μm topcoat samples. The secondary phase, appearing as needles or platelets in the topcoat, also exists in these topcoats as in the 250 μm thick topcoats. Near the topcoat-TGO interface, the rounded grains also exist in these samples.

3.3.1.3 Mullite+YAG-modified $\text{Yb}_2\text{Si}_2\text{O}_7$ (M2Y)

The microstructure of the as-sprayed, M2Y topcoat again resembles that of the baseline $\text{Yb}_2\text{Si}_2\text{O}_7$ topcoat. This includes the monosilicate splats and other features present in the as-sprayed baseline and 6A topcoats. As with the 6A composition, the chemical changes do not appear to significantly change the microstructure during the plasma spray process.

The annealed M2Y sample is shown in Fig. 3.14. In the topcoat (a), some residual Yb_2SiO_5 splats are visible as in the as-sprayed condition. Splat boundaries are visible in the topcoat and bondcoat, as well (Fig. 3.14 b). In both layers, the splat boundaries are less prevalent than in the as-sprayed condition, as noted in the baseline and 6A annealed samples. There is no visible TGO at the interface of the topcoat and bondcoat.

After 100 hours of steam cycling at 1316 $^\circ\text{C}$, the monosilicate splats are no longer visible in the topcoat (Fig. 3.15). In contrast to the 6A topcoat after the steam cycling, the M2Y possesses no needle-like or platelet-like secondary phases. Near the interface with the silicon bondcoat, the topcoat shows some similarities to the 6A system. While there is not an

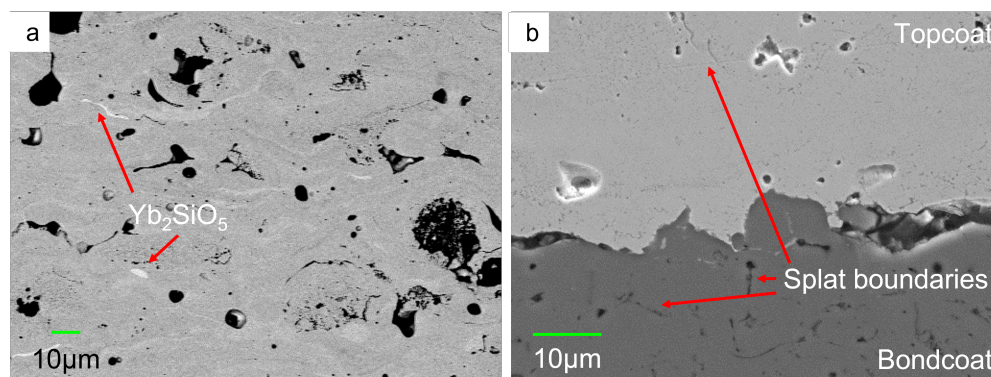


Figure 3.14: M2Y annealed microstructure, in the topcoat (a) and near the topcoat/bondcoat interface (b).

interfacial layer between the topcoat and the bondcoat, except for the TGO, there are what appear to be distinct grains protruding from the topcoat into the TGO. As in the 6A system, these grains appear denser than the topcoat directly above them. EDS scans indicate that these grains are very close to the $\text{Yb}_2\text{Si}_2\text{O}_7$ composition, as in the 6A system. In the case of M2Y, however, while there is no Al detected by EDS there is 1-2 wt.% Y in the interfacial area of the topcoat near the TGO. The TGO thickness after 100 hours of steam cycling is $0.86 \pm 0.3 \mu\text{m}$.

After 500 hours of steam cycling, the microstructure (not shown) does not change significantly compared to the 100-hour steam-cycled sample. TGO thickness in the 500-hour sample is $1.3 \pm 0.3 \mu\text{m}$. There is some oxide present in the bondcoat, likely inside pores and/or splat boundaries which oxidized similar to the baseline system in Fig. 3.17.

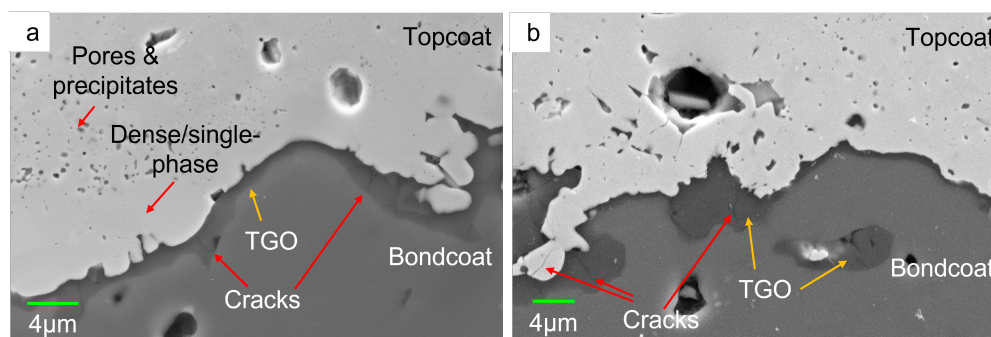


Figure 3.15: Microstructure of M2Y after 100 (left) and 1000 (right) hours of steam cycling. The TGO and TGO cracks are indicated, as are pores/precipitates in the topcoat.

The M2Y topcoat does not change significantly after 1000 hours of steam cycling, compared to the 100-hour and 500-hour conditions (Fig. 3.15b). The grains near the topcoat-oxide

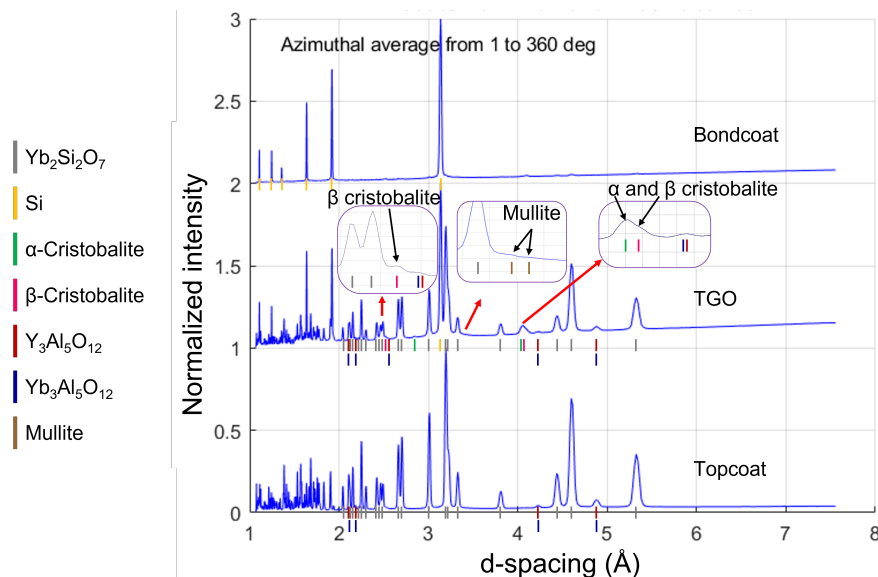


Figure 3.16: WAXS lineouts for M2Y after 1000 hours of steam cycling.

interface persist after 1000 hours of steam cycling, as does their apparent density near the interface with the TGO. TGO thickness in this condition is $1.7 \pm 0.8 \mu\text{m}$.

Fig. 3.16 shows transmission diffraction patterns, once again plotted as normalized and offset intensity against d -spacing, for three locations in the M2Y, 1000h steam-cycled sample. As with the baseline and 6A transmission WAXS patterns, these were collected at the synchrotron using a $2 \mu\text{m}$ tall, $100 \mu\text{m}$ wide photon beam.

As expected, the topcoat diffraction pattern shows primarily peaks from the $\text{Yb}_2\text{Si}_2\text{O}_7$ phase. There are additionally some minor peaks present from either (or both) the $\text{Y}_3\text{Al}_5\text{O}_{12}$ or the $\text{Yb}_3\text{Al}_5\text{O}_{12}$ garnet structures. Since both of these phases share a structure, and the crystal ionic radii of Y and Yb are 104pm and 100.8pm, respectively¹⁰², the peaks of these two garnet structures are not readily distinguishable. In contrast to the 6A 1000-hour transmission diffraction data, there is no evidence of either α or β cristobalite phases in the topcoat.

The diffraction pattern from the TGO, however, does confirm the presence of a crystalline TGO. As with the 6A TGO, there is evidence of the β -cristobalite phase in the TGO. Qualitatively, the presence of the β structure is not as strong in the 1000-hour, steam-cycled M2Y sample as it is in the 1000-hour, steam-cycled 6A sample. Similarly, there are small peaks present in the location of mullite peaks, as with the 6A TGO. The mullite peaks in M2Y are lower relative intensity than those in the 6A TGO, however. The bondcoat pattern, as in the cases of baseline and 6A, shows primarily silicon with trace peaks from the $\text{Yb}_2\text{Si}_2\text{O}_7$ and TGO phases. The interface roughness produces this effect, as previously.

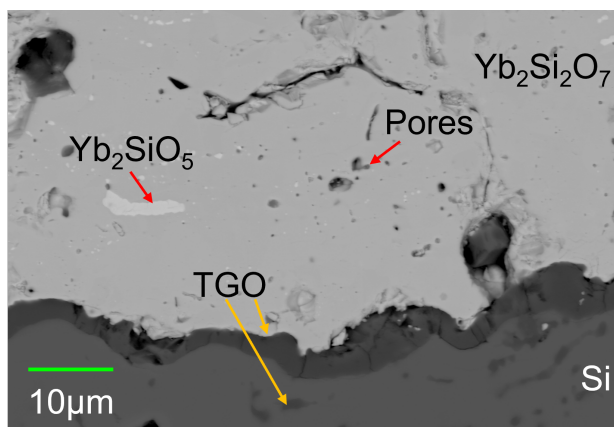


Figure 3.17: Baseline 500-hour air sample, with a thinner TGO than in the 500-hour steam-cycled sample.

3.3.1.4 Air exposure and topcoat thickness effects

A baseline sample exposed to high temperature in air for 500 hours provides a useful comparison to steam-cycled samples (Fig. 3.17). Many features are similar between this sample and steam-cycled samples, including the residual Yb_2SiO_5 particles, pores in the topcoat, and some cracking in the TGO. However, the TGO is thinner in this sample, at $2.3 \pm 0.7 \mu\text{m}$ compared to the 500-hour steam-cycled sample ($10.8 \pm 4.4 \mu\text{m}$).

Microstructure and TGO thicknesses were also observed for samples of different topcoat thickness in each of the baseline, 6A, and M2Y compositions. The microstructures of baseline samples with 125- μm and 500- μm topcoat thicknesses are similar those of the baseline sample with the 250 μm topcoat. TGO thicknesses in the 125- μm and 500- μm topcoat samples, measured by SEM, are approximately $10.1 \pm 3 \mu\text{m}$ and $10.3 \pm 4 \mu\text{m}$, respectively, after 500 hours of steam cycling. After 1000 hours of steam cycling, the respective TGO thicknesses of the 125- μm and 500- μm topcoat samples were $12.8 \pm 6 \mu\text{m}$ and $13.5 \pm 4.6 \mu\text{m}$.

The TGO thicknesses in the 6A, 125 μm -topcoat samples are $1.6 \pm 0.7 \mu\text{m}$ and $2.2 \pm 0.6 \mu\text{m}$ for the 500-hour and 1000-hour steam-cycled conditions, respectively. The TGO thicknesses in the samples with 125 μm and 250 μm topcoats are similar. By contrast, the 6A sample with a 500 μm topcoat has no TGO visible by SEM imaging, as noted by Lee et al.¹⁰³. The implications are discussed in the next section.

Similarly, the TGO thickness in the M2Y system does not seem to depend on the topcoat thickness. As in the M2Y samples with 250- μm thick topcoats, there is no evident Yb_2SiO_5 phase after steam cycling. There are also no visible secondary phases in SEM, and the rounded grains near the topcoat/TGO interface exist in these samples, as well as the higher

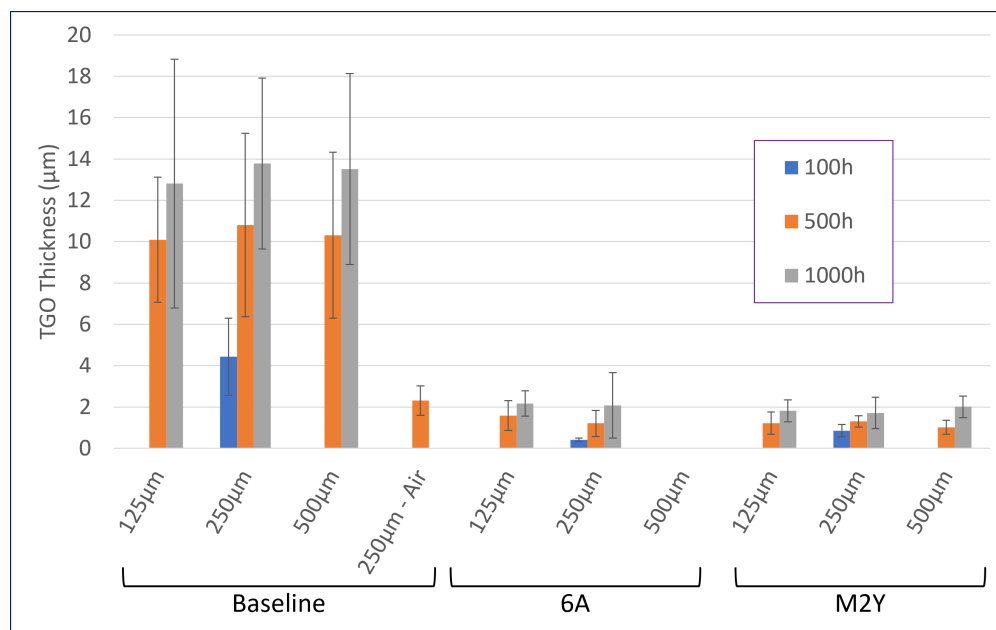


Figure 3.18: TGO thicknesses for all compositions and topcoat thicknesses.

evident density near the grain-layer interfaces. TGO thicknesses in 500-hour are $1.2 \pm 0.5 \mu\text{m}$ $1.0 \pm 0.3 \mu\text{m}$ in the $125 \mu\text{m}$ and $500 \mu\text{m}$ topcoat samples, respectively. TGO thicknesses in the 1000-hour steam-cycled samples are respectively $1.8 \pm 0.5 \mu\text{m}$ $2.0 \pm 0.5 \mu\text{m}$ for the $125 \mu\text{m}$ and $500 \mu\text{m}$ thick topcoats of this composition. Compared to the observations of M2Y samples with $250 \mu\text{m}$ thick topcoats, these values are again similar.

In the baseline and M2Y systems, the TGO thicknesses measured are similar between topcoat thicknesses for the steam-cycled conditions available (Fig. 3.18). This indicates that, in those two systems, the topcoat thickness does not have a significant effect on the TGO thickness and therefore on the oxidation behavior of the TGO. The rate-limiting layer in those systems should then be the TGO, through which the oxidants must diffuse in order to react with the bondcoat and form additional TGO. This is addressed further in the next section.

In the 6A system, TGO thicknesses were similar between the samples with $125 \mu\text{m}$ and $250 \mu\text{m}$ topcoats. However, there was no TGO present in the samples with the $500 \mu\text{m}$ thick topcoat even after 1000 hours of steam cycling. Similar observations for all three compositions were made by Lee et al.¹⁰³. As discussed further in the next section, in the case of the 6A composition it was additionally hypothesized by Lee et al. that the TGO growth phase takes place after significant dopant effects produce the intermediate layer observed¹⁰³. Given the similarity in TGO thicknesses of the 6A samples with $125 \mu\text{m}$ and $250 \mu\text{m}$ topcoats it is likely that, once TGO growth has commenced in this composition, the TGO thickness is

insensitive to topcoat thickness as it was in the baseline and M2Y compositions.

3.4 Discussion

3.4.1 Microstructure and dopant effects

3.4.1.1 Baseline system

In the literature, the TGO of EBC systems with a silicon bondcoat is indicated to be cristobalite (α -cristobalite at low temperatures and β -cristobalite at high temperatures). The α -cristobalite phase is typically identified by the cracking present in the TGO¹⁵, since there is a 4-5% volume change from the high-temperature β -cristobalite to the low-temperature α -cristobalite, which occurs at ~ 220 - 250°C ¹⁰⁴⁻¹⁰⁶. Such a large volume reduction is destructive to a material, as observed in the TGO of the baseline composition with increasing thickness. The α -cristobalite phase has also been identified in the literature using Raman spectroscopy, as in the work of Richards et al.¹⁰¹.

The transmission diffraction evidence presented in this chapter expands the work of Lee and Lee et al.^{15,103}, with respect to the coating systems studied, and on the identification of EBC TGO in the literature, by confirming that the TGO is α -cristobalite. This identification of the α -cristobalite TGO reinforces the explanation for TGO cracking, due to the large volume change associated with the transformation between the high-temperature and low-temperature cristobalite structures. Extensive steam exposure, thermal cycling, and the volume change with the β - and α - cristobalite structures are crucial for producing the thick TGO and are critically destructive to the TGO in the baseline system.

The cristobalite peak observed in transmission diffraction through the silicon bondcoat of the baseline 1000-hour steam-cycled sample deserves further attention. There is uncertainty as to whether the phase is α -cristobalite or β -cristobalite due to small diffraction intensity, which tends to increase error in d-spacing measurements by WAXS. If the peak is from the β -cristobalite phase, then it could be that this phase is located closer to the bondcoat due to the growth of silica TGO. New TGO is created at the TGO-silicon interface by oxidants migrating through the TGO and sits at the top surface of the silicon. It was shown by Breneman and Halloran, using differential scanning calorimetry to study transformation temperature hysteresis, that the energy barrier for the cristobalite transformation decreases with increasing cycles¹⁰⁶. This was associated with twinning and microcracking in the cristobalite, which enabled the transformation by reducing the associated stresses. In the present work, it is likely that small diffraction peaks near the TGO/silicon interface represent β -cristobalite stabilized as a continuous layer bonded to the silicon bondcoat and therefore may experience strain stabilization. Thicker TGO (such as the remainder of the TGO layer in this system),

by comparison, crack and lack stabilizing forces supplied by the silicon substrate. This stabilization mechanism is not confirmed in the present work, but rather may contribute to the explanation for the presence of the peak from the high-temperature cristobalite phase.

3.4.1.2 6A system

In the 6A system, the differences in topcoat microstructure compared to the baseline system are attributed to the influence of the dopants in the system. It was suggested by Lee that the monosilicate particles react with the Al_2O_3 dopant to form the precipitate particles¹⁵. This is not unreasonable, since the precipitates were shown to have significant amounts of Al, along with Yb, Si, and O. This would also account for the disappearance of the Yb_2SiO_5 phase in the 6A topcoat, when it persisted in the baseline topcoat. As noted in Fig. 3.8, the microstructure of the Yb_2SiO_5 splats visibly change even after 30 minutes at $\sim 1300^\circ\text{C}$, indicating that the reaction(s) causing the monosilicate to disappear occurs rapidly.

The development of the interfacial layer between the topcoat and bondcoat of the 6A system is attributed to the influence of dopants in the system. The higher silicon content in this layer, compared to the topcoat, indicates that prolonged steam cycling exposure leads to the reaction of the topcoat with silicon from the bondcoat and formation of the secondary phase in this microstructure¹⁵. A similar layer was observed in the work of Richards et al., in which the Yb_2SiO_5 topcoat and mullite diffusion layer reacted to form a layer with 51.4-54 wt.% Yb, 7.7-13.8 wt.% Al, 10.6-14.6 wt.% Si, and 23.7-24.2 wt.% O. As mentioned previously, in the present work the composition of the interfacial layer is approximately 31-32 wt.% Yb, 7-9 wt.% Al, 22-23 wt.% Si, and 38-39 wt.% O. Compared to the interfacial layer in the work of Richards et al., with the Yb-monosilicate topcoat, the lower Yb and Al content and the relatively higher Si and O content in the interfacial layer of the present work are likely the result of the Yb-disilicate. Since there is no detailed phase diagram for the Yb_2O_3 - Al_2O_3 - SiO_2 ternary system, it is unclear if these are two compositions within the same phase field or different phases. Richards et al. indicated that, due to the ranges of concentration of each element in the layer, the phase likely had a wide phase field¹⁰⁷.

Although the $\text{Yb}_3\text{Al}_5\text{O}_{12}$ phase disappears from the laboratory XRD patterns between 500 and 1000 hours of steam cycling, it is present in the high-flux, high-resolution synchrotron diffraction data of the 1000-hour steam cycled sample. This indicates that the amount of the garnet phase has decreased in the topcoat below the detectable limit of the laboratory XRD between those two steam cycling intervals but has not disappeared entirely. This change between 500 and 1000 hours of steam cycling is likely due to the migration of the highly mobile precipitate particles through the TGO and bondcoat, which progressively removes

Yb-Al-silicate material from the topcoat. The precipitates observed in the bondcoat do not match the composition of the Yb-based garnet; however the reaction of the ytterbium aluminum garnet phase with the silicon bondcoat is hypothesized to produce the Yb-Al-silicate phase which has not yet been identified¹⁰³. Lee also noted, from separate laboratory XRD data, that the garnet phase has likely not disappeared entirely from the topcoat or sample, but that it remains in quantities below the detection of the laboratory XRD¹⁵; that observation is confirmed here. Lee et al. later hypothesized that the precipitates in the topcoat of 6A migrate toward the TGO and bondcoat, reacting there to form the silicate intermediate layer¹⁰³. Precipitates from this layer were observed to migrate further toward the bondcoat in the work of Lee and Lee et al.^{15,103}. The interfacial layer was hypothesized by Lee et al. to form the TGO present in the 6A system after long steam-cycling times¹⁰³. This behavior was discussed in terms of an "incubation" period, during which the intermediate layer is formed and the dopant chemical effects influence the microstructure prior to significant TGO growth¹⁰³. The lack of precipitates in the grains near to the intermediate layer and the TGO, observed here and in the work of Lee et al.¹⁰³, support that hypothesis.

For the TGO in 6A, it has been shown in the literature that the β -cristobalite phase can be stabilized by the occupation of interstitial sites by large cations (Na, Ca, Cu, Sr in the literature, primarily) and charge-balancing Al^{3+} substitutions on Si^{4+} sites¹⁰⁵. Yb cation radii (both ionic and crystal ionic, from the work of Shannon¹⁰²) are similar to those of the so-called "stuffing cations" used in the literature to stabilize the β -cristobalite structure. Thus, the addition of Al in the 6A system and presence (observed with EDS) of Al and Yb in the TGO support the evidence of the β -cristobalite structure. This result refutes the hypothesis of earlier work, where it was hypothesized that the oxide was amorphous in the 6A system¹⁵. Furthermore, since the transition from β - to α -cristobalite is accompanied by a 4-5% volume contraction, the stabilization of some β -cristobalite helps to explain the lack of cracking in the 6A TGO compared to the baseline TGO. The additional presence of mullite peaks in the TGO of the 6A 1000-hour sample is in agreement with the work of Lee et al., who identified mullite in the TGO of M2Y using TEM. Mullite, a combination of alumina and silica, could readily form with alumina added to the 6A topcoat and ample silica in the TGO.

3.4.1.3 M2Y system

The microstructure of the M2Y system is also influenced by the topcoat dopants, although not as extensively as 6A. One shared feature was the much smaller TGO in the dopant-modified systems than in the baseline system. In the work of Lee et al., it was noted

that the "incubation" phase of dopant activity in the 6A system likely occurred in other modified, $\text{Yb}_2\text{Si}_2\text{O}_7$ -based EBC systems (including M2Y) but over shorter time scales - likely completing prior to the 100-hour steam-cycling interval. The microstructure of the topcoats and the rounded grains near the topcoat/TGO interface in 6A are evidence for this behavior, and the similar observations in M2Y support analogous behavior in the second modified system. In the present work, the similar chemistry observed with EDS, and especially with transmission diffraction in the TGO of 6A and M2Y, (accounting for differences in WAXS intensity) further support the belief that there is a shared multi-step incubation of dopant effects prior to TGO growth due to the chemistry in M2Y as also noted in 6A. Further investigations with shorter steam-cycling times could be used for confirmation.

As with the TGO of the 6A system, the observation of β -cristobalite peaks with transmission diffraction for M2Y is supported by the literature on the stabilization of the β -cristobalite structure. As in the 6A system, this would be accomplished in the TGO of the M2Y system by the incorporation of "stuffing atoms" (ions), such as Yb or Y, into β -cristobalite interstitial sites, accompanied by charge-balancing substitutions of Al^{3+} ions onto Si^{4+} sites. High-resolution TEM would be needed to confirm this hypothesis in both the 6A and M2Y systems.

The 6A topcoat chemistry possesses significantly more Al_2O_3 from dopant additions than does the M2Y chemistry. If one assumes that the amount of alumina dopant addition correlates to the amount of alumina, or aluminum cations, as well as rare earth ions, which are incorporated into the TGO, then it follows that more β -cristobalite should be stabilized in the 6A system than in the M2Y system. With TEM and EDS of the TGO of an M2Y sample on a CVI CMC substrate, Lee et al. observed crystalline TGO grains with amorphous TGO grain boundaries and aluminum-rich precipitates¹⁰³. The EDS spectra of the aluminum-rich precipitates in that work resembled that of mullite. The aluminum-rich, needle-like particles observed by TEM in the TGO in the work of Lee et al.¹⁰³ were not observed by SEM in the present work. However, the transmission WAXS data presented here for the M2Y TGO show peaks from the mullite phase with low relative intensity, which were also present in the 6A TGO. The mullite peaks were lower relative intensity in the M2Y TGO than in the 6A TGO most likely due to the lower concentration of alumina or alumina-containing species (mullite, as added in dopant form) in the M2Y system. The present work confirms the crystallinity of the TGO with transmission X-ray diffraction, with evidence of β -cristobalite.

3.4.2 TGO growth

Comparison between the three compositions helps to assess the effectiveness of the dopant modifications on TGO growth. The TGO thicknesses are plotted in Fig. 3.19. All compo-

sitions demonstrate parabolic growth of their respective TGOs. It is also evident by direct comparison that the TGO thicknesses are drastically reduced in the 6A and M2Y systems.

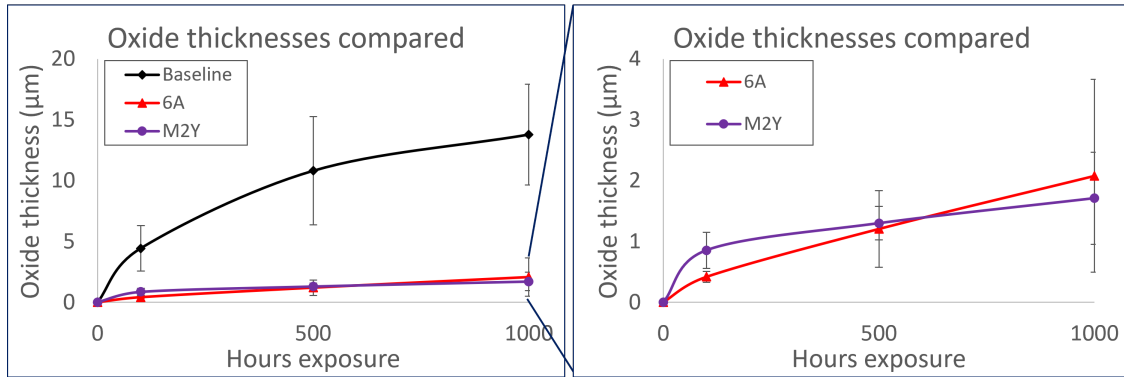


Figure 3.19: TGO thicknesses for all three compositions, showing parabolic behavior.

With parabolic behavior observed, the square of TGO thickness is then used to calculate the parabolic rate using Eq. 3.10. The TGO thicknesses and parabolic growth rates in samples of all three compositions, for samples with $250\mu\text{m}$ topcoats, are shown in Table 3.1. Additionally, percent changes of the TGO thickness compared to baseline are shown, as well as the parabolic TGO growth rates as established.

The TGO thickness values are reduced by more than 80% after each steam cycling interval in the 6A and M2Y compositions, both compared to the baseline. Additionally the parabolic rate reductions in the 6A and M2Y systems, compared to the baseline system, are both greater than 95%. Based on measurement error, it can be said conservatively that the parabolic rate reduced by at least 80% in dopant-modified EBCs, as was seen with the TGO thickness.

Table 3.1: TGO thicknesses for all three compositions and conditions, with topcoat thicknesses of $250\mu\text{m}$. Percent change values are compared to baseline values.

	Baseline		6A		M2Y	
	x (μm)	Δ	x (μm)	Δ	x (μm)	Δ
TGO Thickness						
As-sprayed	0	–	0	–	0	–
100h steam	4.4 ± 1.9	–	0.42 ± 0.09	-90%	0.86 ± 0.3	-81%
500h steam	10.8 ± 4.4	–	1.2 ± 0.6	-89%	1.3 ± 0.3	-88%
1000h steam	13.8 ± 4.1	–	2.1 ± 1.6	-88%	1.7 ± 0.8	-88%
500h air	2.3 ± 0.7	–	–	–	–	–
Parabolic rate	$\mu\text{m}^2/\text{hr}$	Δ	$\mu\text{m}^2/\text{hr}$	Δ	$\mu\text{m}^2/\text{hr}$	Δ
Steam cycled	0.1932	–	0.0043	-98%	0.0027	-99%

Using extrapolated values for the parabolic rate from the work of Deal and Grove⁶, Lee estimated that the presence of the EBC topcoat reduced the parabolic rate by a factor of 5.4¹⁵. However, the TGO in the work of Deal and Grove was described simply as being "the oxide" and was not confirmed to be cristobalite as observed in the baseline system of the work by Lee (by observations of TGO cracking)¹⁵, by Lee et al. (with TEM and selected-area electron diffraction)¹⁰³, and in the present work with transmission X-ray diffraction. In the study of Rodriguez-Viejo et al., tracer oxygen species were used to study the diffusion of bulk oxygen in vitreous silica and polycrystalline β -cristobalite in the temperature range 1240-1500°C¹⁰⁸. It was observed in that work that the diffusivity of oxygen in vitreous silica is five times higher than in polycrystalline β -cristobalite. It is unclear what the difference is in the diffusivity of water between vitreous silica and β -cristobalite. If there is a similar effect for water to that observed for oxygen, then the difference in parabolic rate observed by Lee et al. could be due to the diffusivity, related to the difference in the molecular structure of the TGO, and not due only to the presence of the $\text{Yb}_2\text{Si}_2\text{O}_7$ EBC topcoat. Similarly, the solubility of water molecules in β -cristobalite is not known for comparison with vitreous silica or "the oxide" in the work of Deal and Grove. The work of Wang et al. focused on the diffusion of tracer oxygen species in unmodified and Al-doped, amorphous silica TGOs⁹¹. It was found that Al impurities decreased the diffusion of O in the glassy structure⁹¹. This change was attributed to occupation of interstitial sites in the rings of the glassy network by Al^{3+} ions, which inhibited migration of the oxygen⁹¹. The identical mechanism is not expected in a crystalline TGO due to structural differences, but lattice site occupation or interstitial occupation by Al^{3+} ions does still appear to inhibit migration of oxidants in the system of the present work.

Given the TGO-controlled oxidation of the systems at hand, the difference in parabolic oxidation rate between the baseline and dopant-modified systems can be used to compare the permeabilities of the TGOs to oxidative species using Eq. 3.3. Permeability is the product of diffusivity and solubility (or equilibrium concentration) for the oxidative species (D_{eff} and C^* , respectively, in the model of Deal and Grove). This comparison assumes that the number of oxidant molecules in a unit volume of oxide, N_1 , is approximately constant.

The permeabilities of the TGOs are seen to be significantly different between the baseline and dopant-modified EBCs. The reduction in parabolic rate for the 6A and M2Y systems can be attributed to two causes. The β -cristobalite observed in the 6A and M2Y TGOs, stabilized by Yb and Al impurities in the TGO, could prevent cracking in the TGO that would normally occur during cooling through the transformation from β -cristobalite to α -cristobalite. If cracks in the TGO serve as oxidant diffusion pathways, then fewer cracks should slow oxidant

diffusion. However, although they are less prevalent than in the baseline, some cracks are still observed in the modified TGOs and so the effect of β -cristobalite on cracking may not have a dominant influence on TGO growth. It is not clear how the polymorph of cristobalite affects the diffusivity and/or equilibrium concentration of water vapor, and so the influence of β -cristobalite on oxidation in an un-cracked layer is unknown.

Other features of the TGO microstructure could have a strong influence on the diffusion of oxidants through the TGO. As mentioned previously, alumina-rich particles observed by Lee et al. in the TGO of M2Y samples were measured by EDS to be similar in composition to mullite¹⁰³. In the present work, transmission diffraction data confirmed the presence of mullite in the TGOs of both the 6A and M2Y systems. Mullite has been used in EBCs to act as a diffusion barrier to slow the migration of oxidative species^{10,11}. The presence of mullite in the TGOs should then reduce the parabolic growth rate, noted in Table 3.1.

Better quantification of the oxidation behaviors in the baseline EBC system would provide greater insight into the above results and could be accomplished in two different experiments. First, studies of TGO growth on silicon substrates, with a cristobalite TGO, would elucidate the parabolic TGO growth rate with an oxide which is specifically cristobalite. This study would clarify the effect of the baseline topcoat on the parabolic rate. A similar study while varying the partial pressure of water vapor would then establish the effective diffusivity, D_{eff} , of the water vapor in the cristobalite. Substitution of Eq. 3.4 into 3.3 shows that, when C^* , K , and N_1 are constant, a plot of parabolic rate B against partial pressure allows for evaluation of D_{eff} . With D_{eff} available, C^* can then be calculated for a given oxidant partial pressure.

Similar experiments would elucidate the effects of dopants on the permeability of the TGOs in the doped systems, and the related parabolic rate, as influenced by both the topcoat and the TGO phase. If the topcoat does not affect the bondcoat oxidation behaviors, or if the modified topcoats affect the rate in the same way as seen in the baseline topcoat, then varying the oxidant partial pressure as described above would clarify D_{eff} and C^* for each modified system. The topcoats could influence the parabolic rate differently than in the baseline system, though, by altering the partial pressure of the oxidant at the topcoat/bondcoat interface. In that case experiments designed either to separate the topcoat from the multilayer system or to mimic the TGO in a model system for oxidation study, would allow for characterization of D_{eff} and C^* .

Chapter 4

BIAXIAL STRESSES IN YTTERBIUM DISILICATE-BASED EBC/CMC SYSTEMS

Internal strains and stresses are assessed for the baseline and chemically modified multilayer EBC/CMC systems of this work. An analytical model is introduced for estimating the internal stresses developed in an idealized multilayer system which undergoes a uniform temperature cooling ramp. Experimental measurements are discussed, beginning with sample configurations and preparation. Next, a conceptual framework is described for determining internal stresses in films using X-ray diffraction. Experimental conditions are established for optimizing X-ray experiments to be used on the materials under consideration. Experimental methods are then discussed for taking interplanar spacing measurements, determining strain-free/stress-free lattice parameters, and measuring crystallographic elastic properties for stress calculations. The effects of chemical modifications on crystal structure in topcoat materials are discussed, as well as features observed using an especially small diffraction beam size. Finally, measured internal biaxial stresses are analyzed with respect to conditions of time, temperature, and atmosphere for each sample composition. Comparisons between compositions for each sample condition are also made to better interrogate the experimental matrix of sample treatments. The importance of material processing is emphasized, and microstructural developments are implicated in the development of internal stresses with steam cycling exposure.

Revisiting the inspiration for the use of dopants in the $\text{Yb}_2\text{Si}_2\text{O}_7$ -based EBC topcoats confirms that, as in the work of Schlichting, the addition of oxide dopants to the system reduced the TGO growth in the system. In the present work, the TGO growth was reduced by more than 80%, when compared both as TGO thickness and as TGO parabolic growth rate. As the TGO in the case of the multilayer EBCs was shown to be crystalline, primarily cristobalite (α or β structure, depending on temperature), the oxidation mechanism is expected to be different than in the work of Schlichting. However, similarities such as the presence of mullite in the TGO of this work and that of Schlichting are likely to account for some amount of TGO growth reduction. As discussed above, additional work is required to assess the impact of the EBC topcoats on the parabolic rate as well as the influence of the TGO crystal structure (α -cristobalite and β -cristobalite) and additional phases (e.g., mullite).

4.1 Analytical modeling of internal stresses

To interpret the internal stresses measured after thermal cycling of these multilayer systems, it is useful to predict the internal stresses in a simplified system. Internal stresses in certain multilayer material systems can be modeled using the closed-form solution of Hsueh et al¹⁰⁹. This model assumes that layers are flat, well-bonded, and isotropic. The properties required for the model are the elastic modulus, Poisson's ratio, and coefficient of thermal expansion of the materials and the thicknesses of the layers. Then, the change in temperature of the system can be used to estimate the internal stresses developed through the cooling temperature change.

In this model, for a multilayer system there are considered to be $n + 1$ layers present: n coating layers and the substrate. The n coating layers each have individual thickness t_i , and the substrate thickness is t_s . Index i tracks the layer number, beginning with layer 1 which interfaces with the substrate and continuing to the uppermost layer n . The coordinate system is defined to have $z = 0$ at the interface of the substrate and layer 1, the free surface of the substrate at $z = -t_s$, and the free surface of layer n at $z = h_n$. Then, the relationship between h_i and t_i is

$$h_i = \sum_{j=1}^i t_j \quad (i = 1 \text{ to } n). \quad (4.1)$$

The model assumes that the interfaces remain bonded during temperature changes. For a temperature change ΔT , the different CTEs of the substrate and each layer (α_s and all α_i , respectively) will cause bending in the system. The total strain can be separated into uniform and bending components, and the in-plane biaxial stress distributions in the substrate and layers, σ_s and σ_i , are

$$\sigma_s = E'_s \left(c + \frac{z - t_b}{r} - \alpha_s \Delta T \right) \quad (\text{for } -t_s \leq z \leq 0) \quad (4.2)$$

$$\sigma_i = E'_s \left(c + \frac{z - t_b}{r} - \alpha_i \Delta T \right) \quad (\text{for } -i = 1 \text{ to } n). \quad (4.3)$$

$E' = \frac{E}{1-\nu}$ is the biaxial modulus, E is the Young's modulus, ν is Poisson's ratio, and c is the uniform strain component. The position of the bending axis at which the bending strain component is zero is $z = t_b$, and r is the radius of curvature of the system.

Hsueh et al's. expressions for stresses are based on the thin-plate theory, where pure bending is taken into account and the effect of shear deformation is neglected¹⁰⁹. Additionally, the transverse section of the multilayer system begins and remains plane and normal to the bending axis.

The forces resulting from the uniform and bending strain components are zero, and the total bending moment from the stresses in Eqns. 4.2 and 4.3 is also defined to be zero¹⁰⁹. These boundary conditions, rooted in physical force and moment balances, allow for derivation of c , t_b , and r :

$$c = \frac{(E'_s t_s \alpha_s + \sum_{i=1}^n E'_i t_i \alpha_i) \Delta T}{E'_s t_s + \sum_{i=1}^n E'_i t_i} \quad (4.4)$$

$$t_b = \frac{-E'_s t_s^2 + \sum_{i=1}^n E'_i t_i (2h_{i-1} + t_i)}{2(E'_s t_s + \sum_{i=1}^n E'_i t_i)} \quad (4.5)$$

$$\frac{1}{r} = \frac{3[E'_s(c - \alpha_s \Delta T)t_s^2 - \sum_{i=1}^n E'_i t_i (c - \alpha_i \Delta T)(2h_{i-1} + t_i)]}{E'_s t_s^2 (2t_s + 3t_b) + \sum_{i=1}^n E'_i t_i [6h_{i-1}^2 + 6h_{i-1} t_i + 2t_i^2 - 3t_b(2h_{i-1} + t_i)]}. \quad (4.6)$$

The stresses in the substrate (σ_s) and each layer (σ_i) are functions of z . When there is one layer ($i = 1$), h_{i-1} (h_0 in this case) is equal to zero. The solutions presented by Hsueh et al. are considered to be exact for positions remote from the free edges of the system. In the systems of this study, the SiC_f/SiC CMC substrate is modeled as a bulk SiC substrate. The silicon bondcoat is modeled as layer $i = 1$, the topcoat is layer n , and n is equal to 2 or more depending on the absence or presence of an oxide or other additional layer(s) between the bondcoat and topcoat. With the analytical model at hand, the materials properties (Table 4.1) of the constituents in the multilayer system of this work can be used to compute stresses.

Table 4.1: Materials properties input to the analytical model for predicting biaxial stresses.

Material	CTE (x10 ⁻⁶)	E (GPa)	ν	Thickness (mm)
Silicon carbide (SiC) ⁵⁹	5.1	420	0.17	3
Silicon (Si) ^{59,110}	4.4	163	0.22	0.125
β -Cristobalite ^{101,104,111} (TGO)	3.1	70	-0.044	0, 0.005 0.010, 0.020
Yb ₂ Si ₂ O ₇ ¹¹	4.7	205	0.33	0.125, 0.250, 0.500

As seen in Table 4.1, silicon carbide has the largest CTE of the materials in the engineered multilayer system, silicon has the smallest, and Yb₂Si₂O₇ is between those two. It was observed in Chapter 3 that the TGO in the baseline system, and at least part of the TGO in 6A and M2Y, is α -cristobalite. However, α -cristobalite is the low-temperature polymorph of cristobalite, while high-temperature ($\sim 250^\circ\text{C}+$) β -cristobalite is stable for most of the heating and cooling temperature range. A range of CTE values are reported in the literature for β -cristobalite^{101,104}. The CTE used here follows the work of Richards et al., who

modeled a similar system using the CTE value in Table 4.1. Elastic properties similar to those calculated in the work of Pabst et al. are used here as well¹¹¹, representing "dense isotropic polycrystalline aggregates" of the silica polymorphs studied. Since β -cristobalite is the high-temperature form of cristobalite and persists for the majority of the heating and cooling temperature range in engine cycling, properties for this phase were prioritized for the majority of the ΔT of the steam cycling, and the transformation to α -cristobalite is handled separately to assess the effects and implications of the transformation.

4.1.1 Topcoat thickness effects

Results of the closed-form solution are seen in Fig. 4.1 for three coating thicknesses, with each system cooled by 1300°C ($\Delta T = 1300^\circ\text{C}$). The solution shows compressive internal stresses in the $250\text{-}\mu\text{m}$ $\text{Yb}_2\text{Si}_2\text{O}_7$ -based topcoat of approximately 120MPa and in the $125\text{-}\mu\text{m}$ Si bondcoat of approximately 160MPa . Computed stresses in the SiC substrate are tensile, beginning at approximately 70MPa and decreasing through the thickness measured experimentally in this work.

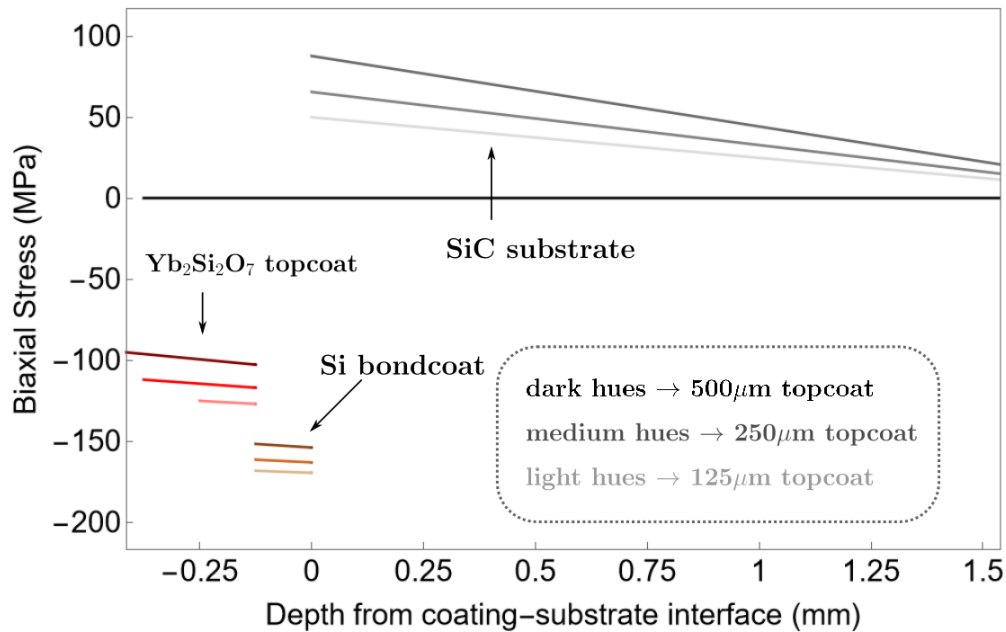


Figure 4.1: Predicted stresses in a $\text{Yb}_2\text{Si}_2\text{O}_7$ -based EBC/SiC system, with different topcoat thicknesses and a cooling temperature change of 1300°C .

Altering the topcoat thickness, using the values shown on the plot, changes the computed coating stresses by less than 20MPa from those of the $250\text{-}\mu\text{m}$ topcoat case, comparable to (or sometimes smaller than) the error expected in the experimental measurements. Due to the difference in all layers being less than $\sim 30\text{MPa}$ (the largest difference being in the

substrate near the interface), biaxial stress measurements were not taken for samples with $125\mu\text{m}$ and $500\mu\text{m}$ -thick topcoats.

4.1.2 Oxide effects

The influence of oxide thickness on biaxial internal stresses was also analyzed using the closed-form solution. Previous reports in the literature indicate, from evidence of cracking and using Raman spectroscopy, that the oxide is the cristobalite polymorph of SiO_2 ^{15,101}. The β cubic form of cristobalite is the high-temperature form, and this phase should persist over most of the temperature range of engine operation ($\approx 250\text{-}1300^\circ\text{C}$). Literature sources show a range of CTE values for this phase. However, the value 3.1×10^{-6} was used by Richards et al. for β -cristobalite when considering the effect of TGO growth and delamination in EBC systems¹⁰¹, so that value was used here as well. A cooling temperature $\Delta T = 1000^\circ\text{C}$ was used, to model the cooling from high-temperature to approximately the transformation temperature from β -cristobalite to α -cristobalite. Plotting oxide thicknesses of $0\mu\text{m}$ (no oxide), $5\mu\text{m}$, $10\mu\text{m}$, and $20\mu\text{m}$ shows the role of oxide growth on stresses, with a range of thicknesses encompassing those observed in the baseline EBC/CMC system in the steam cycling times studied (up to $\sim 14\mu\text{m}$ after 1000 hours steam cycling) (Chapter 3 and Ref. [15]).

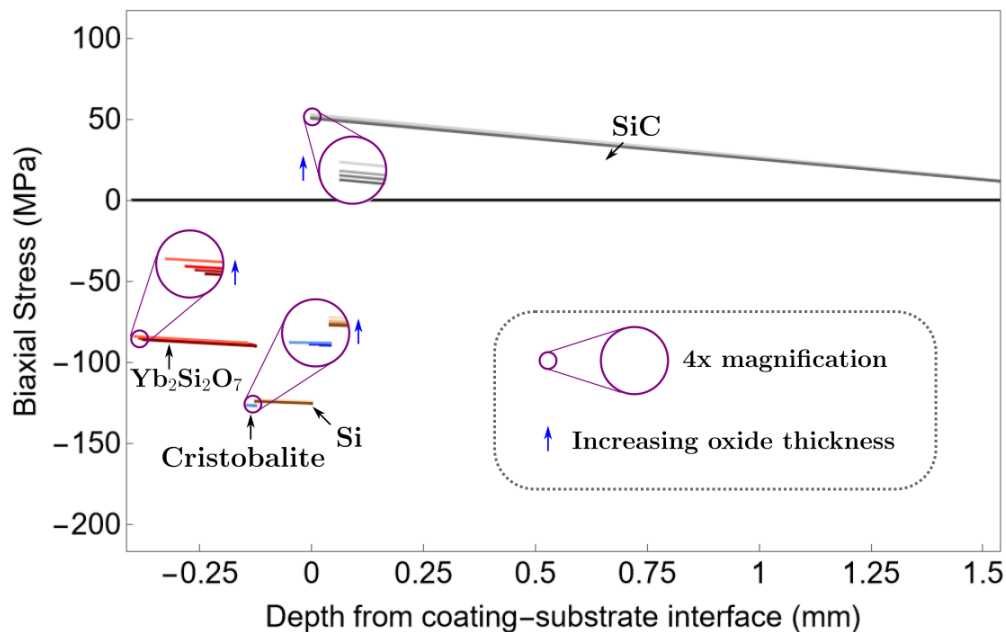


Figure 4.2: Predicted stresses in a $\text{Yb}_2\text{Si}_2\text{O}_7$ -based EBC/SiC system, with a $250\mu\text{m}$ topcoat and $\Delta T = 1000^\circ\text{C}$. The oxide, and the oxide thickness, have minimal effect prior to the cristobalite transformation.

It can be seen from Fig. 4.2 that the presence of the oxide changes the stresses in the surrounding layers by less than 5MPa. Additionally, increasing the oxide thickness even to $20\mu\text{m}$ changes the stresses of the coating layers by less than 10MPa. In fact, the TGO stresses themselves also change by only 5-10MPa with increasing TGO thickness. This is shown using the magnified regions of the stress curves, where the divergence between conditions is largest.

Next, the transformation from β -cristobalite to α -cristobalite was modeled by converting the volume change associated with this transformation into a linear change and treating that as a CTE. A conservative estimate of 4% volume change was divided by 3 to give $\sim 1.33\%$ change, which was entered into the model as a CTE of 1.33×10^{-2} . The transformation takes place over approximately 20°C of cooling, so $\Delta T = 20$. The ending strains and radius of bending curvature, from the previous step incorporating β -cristobalite, were used as starting points, in addition to the ending stresses in each layer and the substrate. With the additional step designed to approximate the cristobalite transformation, the stress evolution shows non-physical results (Fig. 4.3).

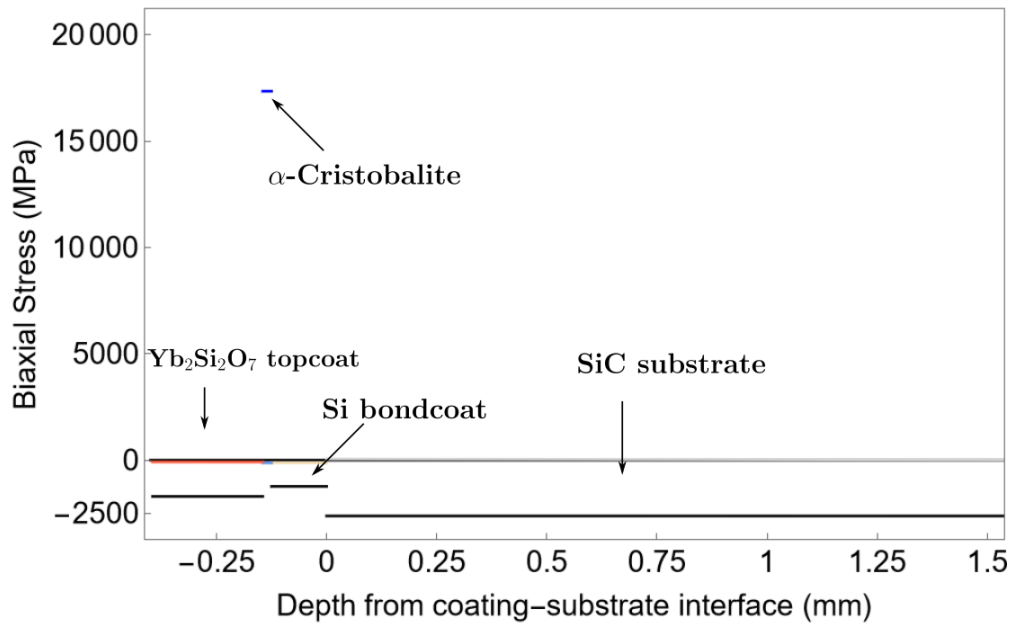


Figure 4.3: Predicted stresses in a $\text{Yb}_2\text{Si}_2\text{O}_7$ -based EBC/SiC system, with a $250\mu\text{m}$ topcoat and $\Delta T = 1000^\circ\text{C}$. The oxide, and the oxide thickness, have minimal effect prior to the cristobalite transformation.

As seen in the figure, through the cristobalite transformation tensile stresses more than 15GPa develop in the α -cristobalite and compressive stresses multiple gigapascals in magnitude develop in the coatings and the substrate. None of these stress magnitudes should be sustained by the materials in the system, and so this step instead illustrates the reason for

cracking in the TGO rather than a realistic picture of internal stresses in the system after the cristobalite transformation. Extensive cracking, as was observed in Chapter 3 through microscopy of the TGO, served to relieve TGO stresses, particularly in the baseline system.

The overall behavior of the cristobalite phases is more complex than what can be factored into the analytical model due to the phase transformation. The displacive transition from the high-temperature, β -cubic form of cristobalite to the low-temperature, α -tetragonal form (or vice-versa) starting at approximately 220-250°C at ambient pressure is accompanied by a four to five percent volume change^{104,107}. This large volume change influences the stresses in the oxide and the surrounding layers in ways which for which this model cannot truly account, since the stresses shown could not be sustained by any material in the system and cracking would necessarily develop as a stress relief mechanism. As the TGO develops significant cracking due to the multi-gigapascal tensile internal stresses from the phase transformation and volume change, as has been observed in similar systems in the literature¹⁰⁷, the assumptions of the analytical model—particularly that layers are continuous and homogeneous—no longer hold and the real stress curves should deviate from the model. However, despite these limitations, the model does successfully underscore the need for stress relief in the system due especially to the cristobalite transformation.

Additionally, the calculations prior to the incorporation of the cristobalite transformation provide the relative magnitude that we might expect of internal stresses in the multilayer EBC/substrate system. It is important to note that the actual air plasma-sprayed materials possess porosity and layer interfaces and surfaces of significant roughness, and so layers are not completely flat and homogeneous. Additionally, although the layers should have large numbers of crystalline grains comprising an isotropic layer, the crystal structures of the materials themselves, particularly of monoclinic $\text{Yb}_2\text{Si}_2\text{O}_7$, may give rise to anisotropic elastic properties. Lastly, challenges to the assumption that the layers are well-bonded would diminish the effectiveness of the model's predictive capabilities. In most sample conditions, the assumptions of the model are maintained sufficiently well for the modeled internal stresses to be realistic. Cases where the assumptions are not maintained will be discussed as they arise.

4.2 Materials for *ex-situ* synchrotron studies

4.2.1 Coupon-based, multilayer EBC-CMC samples

Samples used in synchrotron studies were taken from the same multilayer samples used in microstructure and mechanical properties studies, provided by Kang Lee at NASA Glenn Research Center. The three compositions of multilayer samples studied at the synchrotron

were baseline (nominally 100 wt.% $\text{Yb}_2\text{Si}_2\text{O}_7$), 6A (alumina-modified: 6 wt.% alumina, bal. $\text{Yb}_2\text{Si}_2\text{O}_7$), and M2Y (1.39 wt.% mullite, 2.33 wt.% YAG, bal. $\text{Yb}_2\text{Si}_2\text{O}_7$). As described in Chapter 3, samples were sectioned into a size usable in microstructure/oxidation, synchrotron, and mechanical properties studies.

For synchrotron studies, samples of approximately 6-7mm width, 1.5-2mm depth, and 3.5-4mm height (combined layer thicknesses) were sectioned from the samples received from NASA Glenn using a variable-speed abrasive saw (Buehler IsoMet 5000) and a diamond-impregnated blade (Buehler IsoMet Diamond Wafering Blade). Some samples were subjected to short-term heating and/or oxidation studies to assess the effects crystallization of the coating layers or of steam cycling at times below 100h. Particularly, as-sprayed samples were heated to 1300°C for one hour in flowing argon to crystallize the topcoats and impose a uniform thermal history on the samples.

X-ray tomography datasets were collected at the synchrotron, with the multilayer samples rotated around the longest axis of the samples (parallel to the coating layers). Rotation step sizes were 0.2 to 0.5 degrees, and total rotational range was 360 degrees. Multiple volumes were collected to image from the topcoat down through the substrate. Image reconstructions were performed by beamline scientists at Beamline 1-ID at the APS.

4.2.2 $\text{Yb}_2\text{Si}_2\text{O}_7$ -based powders

Powders of EBC topcoat material were prepared from $\text{Yb}_2\text{Si}_2\text{O}_7$ -based layers, which were plasma-sprayed to approximately four millimeters thickness on graphite substrates by a third-party vendor. Powder samples of baseline, 6A, and M2Y composition were prepared, as well as an additional composition called M5Y, which was modified by additional YAG compared to M2Y (M5Y is 1.39 wt.% mullite, 4.66 wt.% YAG, bal. $\text{Yb}_2\text{Si}_2\text{O}_7$).

Sections of topcoat material were cut from the main sample using a Buehler IsoMet 5000 and then removed from the graphite substrate. A metal file was then used to abrade small powder particles from the free-standing topcoat sample. The size of the powder was assumed to be sufficiently small that internal strains were relieved. Powder particles were then collected into vials for *ex-situ* and *in-situ* synchrotron measurements and heat treatments. For each composition, some amount of the powders was loaded into capillary vials and heated in air using the induction furnace described in Chapter 6 to 1315-1320°C for 30 minutes to crystallize the amorphous content.

4.3 Methods for *ex-situ* synchrotron studies

4.3.1 Internal stresses in thin films and coatings

Thermal mismatch strains are inevitable in coatings and thin films which have different lattice parameters and/or thermal expansion coefficients than their substrates. For decades, researchers have considered the strains that develop in coatings and substrates due to thermal mismatch and have applied elasticity theory in their descriptions. Additionally, it is not feasible experimentally to measure strains in coating systems with an externally applied strain gage or similar device. A necessary solution for strain measurements in films is to use the crystallographic planes as strain gages and to measure the interplanar spacing values with diffraction techniques. An early model, by Vook and Witt, used elasticity theory to detail thermal mismatch strains in thin films. The Vook and Witt model made a series of critical assumptions about the strain states in these films¹¹²:

1. "The film was firmly attached to the substrate" (or the coating was well-bonded to the substrate):

2. "The thermal expansion of the film and substrate were isotropic in the plane of the substrate":

$$\varepsilon_{11} = \varepsilon_{22} = \varepsilon_{||} \quad (4.7)$$

3. "The stress on the film in a direction normal to the plane of the film was zero":

$$\sigma_{13} = 0 \quad (4.8)$$

4. "The shear strain in the plane of the film was zero":

$$\sigma_{12} = 0 \quad (4.9)$$

In their treatment, Vook and Witt described the use of laboratory X-ray diffraction, in a reflection geometry, to calculate lattice spacings and strains in the films by measuring diffraction from planes parallel to the film-substrate interface¹¹². This experimental geometry measures in-plane interplanar spacing values directly. However, it requires extensive sample manipulation to measure in-plane spacings in multiple directions relative to the sample and it precludes the measurement of out-of-plane spacings which can more fully inform the understanding of the strain tensor for a given system and condition.

Further development of these early ideas, and of the capabilities of experimental X-ray diffraction, have led to more sophisticated techniques for describing and measuring strains and calculating stresses in films and coatings. A common method for converting strains into stresses for coatings layers is the d vs $\sin^2\psi$ technique¹¹³. In this technique, interplanar

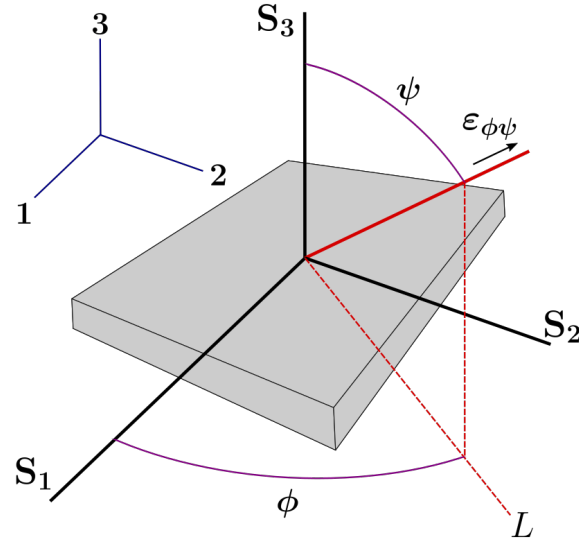


Figure 4.4: Schematic coordinate system for the d -vs- $\sin^2\psi$ method of computing internal stresses in films. Adapted from He¹¹³.

spacing d is measured relative to the combined in-plane (ϕ) and out-of-plane (ψ) directions, as shown in Fig. 4.4.

If the third assumption of Vook and Witt is true, and the stress out-of-plane in the film is zero, then the equibiaxial in-plane stress can be calculated by:

$$\frac{d_{\phi\psi} - d_0}{d_0} = \frac{1 + \nu}{E} \sigma_{\phi} \sin^2\psi - \frac{\nu}{E} (\sigma_{11} + \sigma_{22}). \quad (4.10)$$

Here, $d_{\phi\psi}$ is the interplanar spacing measured at the specific in-plane and out-of-plane directions (respectively), d_0 is the unstressed interplanar spacing, E is the elastic modulus, and ν is Poisson's ratio for the material comprising the layer.

It is advantageous to perform diffraction experiments in a transmission (through-thickness) geometry and using a 2-D detector for these measurements. This experimental setup can diffract over a wide range of ψ angles and multiple ϕ angles at once, generally eliminating the need for sample rotation and making the experimental measurement much more efficient and effective. This simplicity allows for faster *ex-situ* measurements and permits coupling with more sophisticated *in-situ* experiments.

In this diffraction setup, the Debye cones will produce Debye rings on the 2D detector, the radii of which are inversely proportional to the spacings of the diffracting planes. The azimuthal angle η around the diffraction ring will correspond to the orientation of the strain relative to the sample layers, thus corresponding also to ψ . When a flat sample is oriented

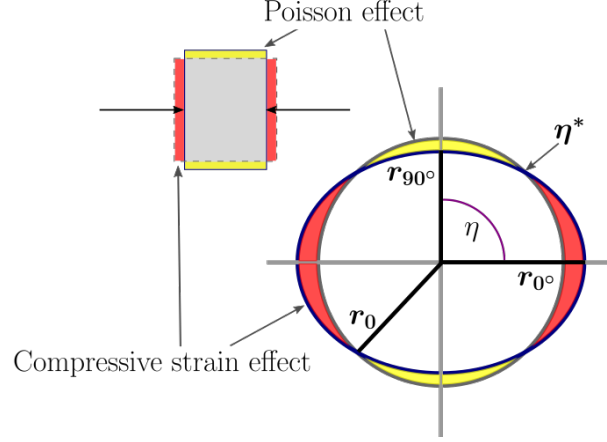


Figure 4.5: Schematic coordinate system for the d -vs- $\sin^2\psi$ method of computing internal stresses in films. Adapted from Stolzenburg¹¹.

with the coating-substrate interface parallel to the horizontal angles 0° and 180° on the detector, diffractions ring spots at these two angles correspond to in-plane d -spacing measurements while the angles $\eta = 90^\circ$ and 270° correspond to out-of-plane d -spacing values.

When a layer has a compressive in-plane strain, decreased d -spacing values will increase the diffracted ring radius at $\eta = 0^\circ$ and 180° , and vice-versa for tensile in-plane strains. Due to the Poisson effect, the d -spacings will be increased and ring radii decreased out-of-plane, at $\eta = 90^\circ$ and 270° , for a compressive in-plane strain (again vice-versa for a tensile in-plane strain). These effects are visually depicted in Fig. 4.5. Uniform d -spacing effects due to potential hydrostatic strains are not included in this conceptualization.

Strain can be calculated from the deformation of the diffraction rings at any azimuth using the relationship:

$$\varepsilon_\eta = \frac{r_0 - r_\eta}{r_0} = \frac{d_\eta - d_0}{d_0} \quad (4.11)$$

where r_0 and d_0 are the respective ring radius and interplanar spacing for the strain-free condition. For planar multilayer systems oriented as in Fig 4.7, in-plane strains are associated with azimuths 0° and 180° , and out-of-plane strains are associated with 90° and 270° . The equations of He¹¹³ are used to develop a strain tensor, $\varepsilon_{\theta\omega\psi\phi}^{hkl}$, which can in turn be used to convert strains measured by diffraction into stresses. In the sample coordinate system given, $S_1S_2S_3$, in Fig. 4.4 above, $\varepsilon_{\theta\omega\psi\phi}^{hkl}$ can be described with unit vector H_{hkl} :

$$H_{hkl} = \begin{pmatrix} h_1 \\ h_2 \\ h_3 \end{pmatrix} \quad (4.12)$$

where h_1 , h_2 , and h_3 are:

$$\begin{aligned} h_1 &= \sin\theta(\sin\phi\sin\psi\sin\omega + \cos\phi\cos\omega) + \cos\theta\cos\gamma\sin\phi\cos\psi \\ &\quad - \cos\theta\sin\gamma(\sin\phi\sin\psi\cos\omega - \cos\phi\sin\omega) \\ h_2 &= \sin\theta(\sin\phi\sin\psi\sin\omega - \cos\phi\cos\omega) - \cos\theta\cos\gamma\cos\phi\cos\psi \\ &\quad + \cos\theta\sin\gamma(\cos\phi\sin\psi\cos\omega - \sin\phi\sin\omega) \end{aligned} \quad (4.13)$$

$$h_3 = \sin\theta\cos\phi\sin\omega - \cos\theta\sin\gamma\cos\psi\cos\omega - \cos\theta\cos\gamma\sin\psi.$$

Strain measurement using X-ray diffraction can then be expressed by the following equation:

$$f_{11}\varepsilon_{11} + f_{12}\varepsilon_{12} + f_{22}\varepsilon_{22} + f_{13}\varepsilon_{13} + f_{23}\varepsilon_{23} + f_{33}\varepsilon_{33} = \ln\frac{\sin\theta_0}{\sin\theta} \quad (4.14)$$

where, in the sample coordinates S_1 , S_2 , and S_3 , ε_{ij} are the strain tensor components and f_{ij} are the strain coefficients:

$$f_{ij} = \begin{cases} h_{ij}^2 & \text{if } i = j \\ 2h_i h_j & \text{if } i \neq j. \end{cases} \quad (4.15)$$

With the assumptions of the Vook and Witt model for the equibiaxial coating ($\varepsilon_{11} = \varepsilon_{22}$, $\varepsilon_{13} = \varepsilon_{23} = 0$) reintroduced, the stresses can be calculated from the simplified equations:

$$\sigma_{ij} = \left(\frac{E}{1 + \nu} \right) \varepsilon_{ij} + \frac{\nu E}{(1 - 2\nu)(1 + \nu)} \delta_{ij} \varepsilon_{kk} \quad (4.16)$$

$$\delta_{ij} = \begin{cases} 1 & \text{if } i = j \\ 0 & \text{if } i \neq j. \end{cases} \quad (4.17)$$

Use of in-plane and out-of-plane d -spacing measurements (and therefore strains) simplifies the δ_{ij} dependency, giving:

$$\sigma_{11} = \sigma_{22} = \left(\frac{E}{1 + \nu_{hkl}} \right) \varepsilon_{11}^{hkl} + \frac{\nu_{hkl} E_{hkl}}{(1 - 2\nu_{hkl})(1 + \nu_{hkl})} (2\varepsilon_{11}^{hkl} + \varepsilon_{33}^{hkl}). \quad (4.18)$$

It should be noted for the diffraction experiments that, for each material of positive Poisson's ratio, there is also a strain-free angle η^* where the radius of the elliptical diffraction ring is undeformed and does not depend on the strain state. At this angle, $d = d_0$ is also true regardless of sample condition such as temperature, applied load, etc. This condition permits the measurement of d_0 under applied load or across ranges of temperature to compute strains or thermal expansion, even in the presence of internal stress effects at other azimuthal angles.

The elastic modulus and Poisson's ratio were previously measured by Stolzenburg et al. using *in-situ* loading experiments with WAXS measurements^{11,99}. In short, compression loading of bulk $\text{Yb}_2\text{Si}_2\text{O}_7$ bars coupled with WAXS measurement allowed for the relation of measured d -spacing to applied stress. WAXS data collected over a range of applied loads provided for the calculation of elastic modulus and Poisson's ratio. The direct relationship of applied load and d -spacing, established as a trend over several loads, was used for elastic modulus calculation.

Poisson's ratio was calculated, also in the work of Stolzenburg et al.^{11,99}, by assessing the strain-free angle η^* of the diffraction patterns (all measurements were conducted at nominally the same temperature). The angle η^* is related to Poisson's ratio through the equation:

$$\nu_{hkl} = \frac{\sin^2 \eta_{uniaxial}^*}{1 - \sin^2 \eta_{uniaxial}^*}. \quad (4.19)$$

Here, ν_{hkl} is the crystallographic Poisson's ratio and $\eta_{uniaxial}^*$ is the stress-free azimuthal angle in a uniaxial loading experiment.

4.3.2 X-ray penetration and absorption in ytterbium-based materials

Synchrotron studies of the materials in this work took place at Beamline 1-ID at the Advanced Photon Source (APS) at Argonne National Laboratory. This beamline provides high-energy (up to 100keV) X-rays for experiments. A superconducting undulator was used to provide high-flux photon radiation, approximately 6×10^{12} X-rays/second at 80keV photon energy. With the use of a silicon (111) Laue monochromator, the X-ray beam could be made highly monochromatic, with a resolution ($\frac{\Delta E}{E}$) of 1.3×10^{-3} . For photons of nominal energy 59keV, this resolution equates to a spread in photon energies of approximately 77eV. Experiments were tuned to maximize the benefits of such a high-resolution, high-flux photon source for diffraction experiments, particularly for the highly photon-absorbing rare-earth elements.

To optimize the signal-to-noise ratio of diffraction peak intensities, the X-ray energy chosen for diffraction had to account for the absorption of X-rays by the materials and where absorption edges exist with respect to photon energy. Ytterbium in particular is a heavy element, so a poor choice of photon energy could dramatically reduce the intensity of the Debye rings in the diffraction patterns. Absorption of the X-rays can be assessed by the mass attenuation coefficient for the compound, which is calculated using¹¹⁴:

$$\left(\frac{\mu}{\rho}\right)_{compound} = \sum w_i \left(\frac{\mu}{\rho}\right)_i \quad (4.20)$$

where w_i and $(\frac{\mu}{\rho})_i$ are the weight and mass attenuation coefficient, respectively, of the i^{th} element in the compound. Transmission is then calculated using the mass attenuation coefficient of the compound and other relevant features¹¹⁴:

$$T = \frac{I}{I_0} = \exp \left[- \left(\frac{\mu}{\rho} \right) x \right]. \quad (4.21)$$

Here, T is the transmittance, I and I_0 are the transmitted and incident intensities (respectively), and x is the mass thickness of the sample (in $\frac{g}{cm^2}$). The mass thickness is the product of the thickness, in cm, and the density, in $\frac{g}{cm^3}$. For the compound $Yb_2Si_2O_7$, transmittance is plotted against photon energy from 15 to 100keV for sample thicknesses of 1.5mm and 2mm (Fig. 4.6). The highest transmittance in this energy range occurs just below the absorption edge of 61.3keV, where transmission drops sharply as the photons contribute to excitations in the material rather than being diffracted. At the absorption edge, the transmittance through a 1.5mm-thick sample of $Yb_2Si_2O_7$ falls to 1.84×10^{-4} ; for the 2mm-thick sample the transmittance falls to 1.05×10^{-5} . For this work, a photon energy of 59.39 keV (set using a thulium filter) was used to maximize diffraction through the material.

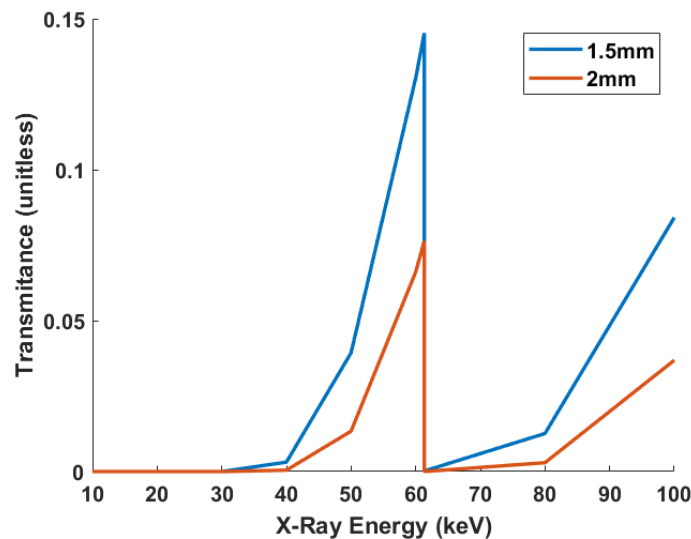


Figure 4.6: Transmittance of X-rays through $Yb_2Si_2O_7$ over a range of discrete energy values. Curves are plotted for samples of 1.5mm and 2mm thicknesses using data and formulae from NIST¹¹⁴.

The other main elements in these compounds and in the multilayer systems, Si, O, Al, and C, do not have absorption edges in the same high-energy photon range as Yb. These elements are also significantly lighter and have lower electron densities than Yb, therefore absorbing much less strongly than Yb. Yttrium is added to M2Y in such a small amount that it was assumed to contribute minimally to the absorption of photons.

4.3.3 Interplanar spacings

At Beamline 1-ID at the APS, amorphous silicon detectors of size 2048×2048 pixels² were used to record images of the diffraction Debye rings. Sample-detector distances were set at 1400-1500mm to include as many peaks of interest as possible for each material on one detector at sufficient resolution. Since WAXS was not coupled simultaneously with other techniques (such as Small-Angle X-ray Scattering, or SAXS, in previous works^{11,13}), a single-detector setup was used for all WAXS experiments. Any permitted reflection in the crystal system detected by the experimental setup (and fitted with the beamline's custom MATLAB script) could be used to compute strains using the strain-free spacing values. The setup is illustrated in Fig. 4.7. Peaks for which elastic properties were also known were then chosen for stress analysis.

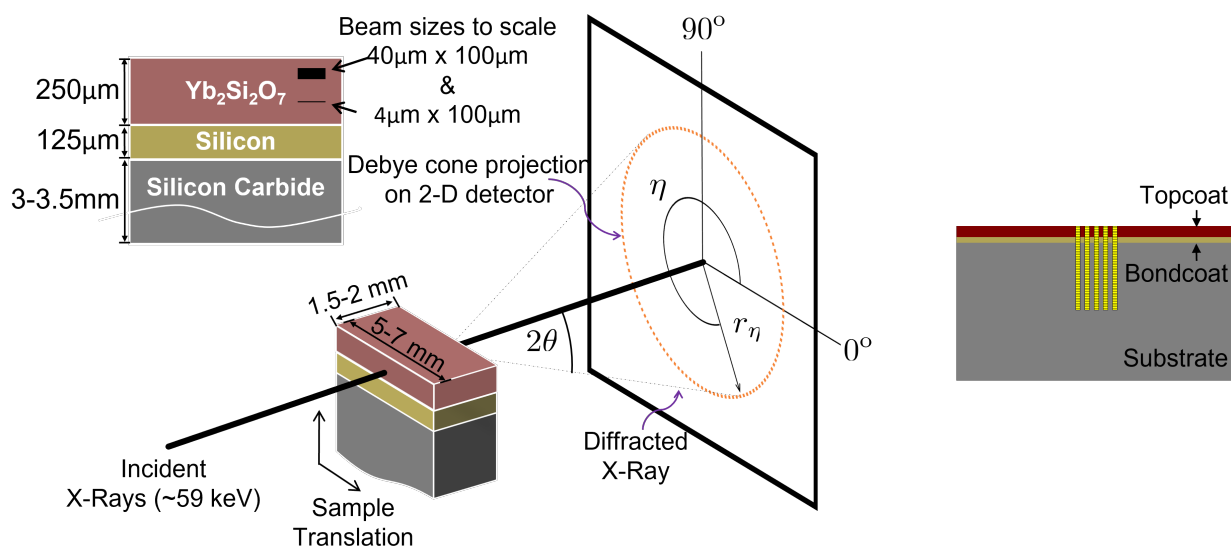


Figure 4.7: Representation of the WAXS setup used at Advanced Photon Source, Beamline 1-ID-E, on left. On the right, the positions (to scale) of all WAXS scans.

Stress error in diffraction measurements decreases with the number of grains contributing to diffraction¹¹⁵. Crystallites in as-sprayed coatings are estimated to be on the order of hundreds of nanometers in size for plasma-sprayed materials¹¹⁶. A diffraction volume on the order of $10^6 \mu\text{m}^3$ should include more than 10,000 grains, resulting in stress errors under 30MPa for most stiff materials^{11,115}.

The beam size could be made as small as $\sim 2 \mu\text{m}$ or as large as hundreds of microns or even millimeters along either edge (width or height) using beam knives and Si refractive lenses. For multilayer materials, the beam height can be set for vertical resolution well within each deposited layer and beam width can be set so the diffraction volumes include a large

number of grains. In the present work, an X-ray beam of height $40\mu\text{m}$ and width $100\mu\text{m}$ was used for stress measurements. Fig. 4.8 shows a tomographic 3D volume of the baseline, 1000-hour steam-cycled sample, where the volume properties have been tuned to mute the intensities of the materials. Fig. 4.8a shows the sample with the perspective centered in the middle of the topcoat, and Fig. 4.8b has the perspective centered on the topcoat-bondcoat interface. Effectively, the features which are visible are external and internal material surfaces, including layer edges, pores, and the fibers in the CMC substrate. The roughness of the interface seen here, on the order of several microns, illustrates the challenges of collecting WAXS data from a single layer near its interface with the next layer.

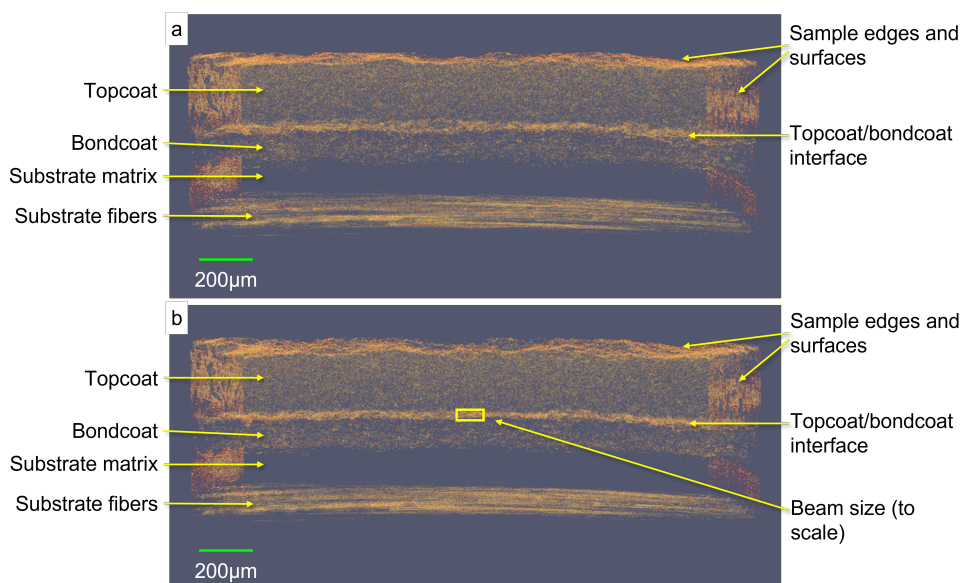


Figure 4.8: Three-dimensional volume of the baseline 1000-hour steam-cycled sample, imaged with tomography and rendered to illustrate material surfaces and interface roughness.

There are features of interest on a larger scale, as well, which can affect the configuration of a series of WAXS measurements. Fig. 4.9 shows another tomographic volume including a topcoat, bondcoat, and substrate, this time of the as-sprayed baseline system, shown at two different tilting angles around the horizontal axis of the page. The surface undulations of the substrate result in very similar undulations in the bondcoat and topcoat. When the undulations are on the order of tens of microns, the layers appear "lengthened" in stress-vs-depth curves (shown later).

For samples of thickness ranging from 1.5mm to 2mm, the $40\mu\text{m}$ beam size resulted in a diffraction volume of $6\text{-}8 \times 10^6 \mu\text{m}^3$, satisfying the volume criterion discussed above. Samples were translated vertically with respect to the beam and by a distance equal to the beam

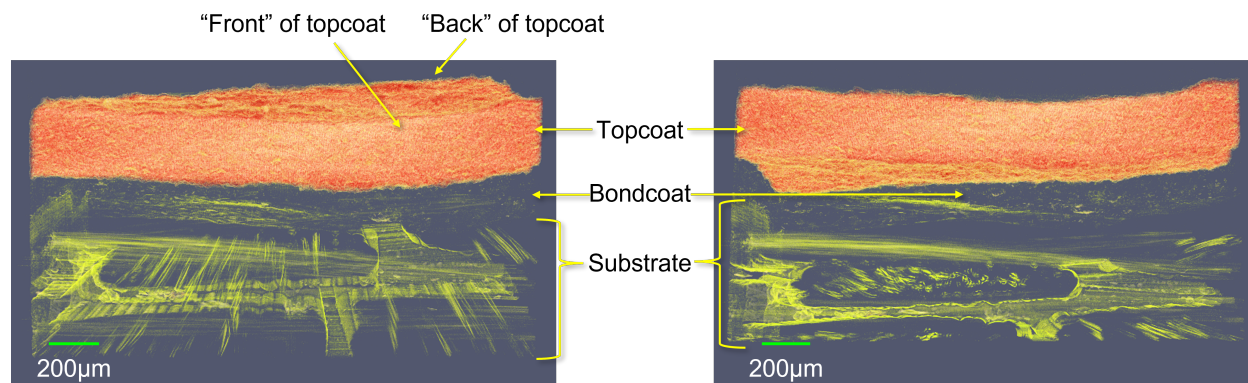


Figure 4.9: Three-dimensional volume of the baseline as-sprayed sample collected by tomography and shown via 3D rendering, illustrating the macro-scale undulations which can complicate layer depths in WAXS configurations.

height, resulting in a series of patterns collected from the topcoat down into the substrate. Five such columns of diffraction measurements, spaced $100\mu\text{m}$ apart horizontally and centered at the middle of the sample width, were collected. Computed stresses for a given depth were averaged across all five horizontal positions. With the $40\mu\text{m}\times 100\mu\text{m}$ beam, measuring 5 columns of strains to $1600\text{--}2000\mu\text{m}$ depth, as measured from the free surface of the topcoat, took approximately 2 hours per sample.

A shorter beam, still $100\mu\text{m}$ wide but instead approximately $2\mu\text{m}$ tall, was used to more carefully detect crystalline layers present in the samples. This fine spatial resolution came at the expense of sampling statistics and therefore to the exclusion of $2\mu\text{m}$ -resolved stress calculations. When the diffraction volumes were insufficient, averaging across several vertical positions could be used to improve diffraction statistics. The short-focus measurements took less time but made use of a "fast-sweep" data collection mode which compiled many frames into one file and required subsequent separation.

Powder samples were measured in quartz capillaries of 1-1.5mm inner diameter with a beam of size $200\mu\text{m}\times 200\mu\text{m}$. Sample size and beam size gave diffracted volumes of approximately $4\text{--}6\times 10^8\mu\text{m}^3$, neglecting surface curvature from the cylindrical capillaries.

4.3.4 Determination of strain-free (or stress-free) lattice parameters

The stress-free powders prepared for synchrotron studies were measured in the WAXS setup. Since spatial strain/stress resolution was not a concern for these samples, a beam of size $200\mu\text{m}\times 200\mu\text{m}$ was used to ensure diffraction from a large number of grains. Diffraction patterns were collected with the samples in their orientation as-mounted in the beamline, as well as at a 180-degree rotation. The average of these two values ensured that the sample-

detector distance could be corrected for eccentricities in mounting position, and additionally ensured that the effective sample-detector distance was the same for the multilayer samples and the powder samples. Analysis of these diffraction data was similar to that for the multilayer stress measurements. For the loose powders, however, d -spacing values were collected for the maximum number of peaks which could be reliably fit. Each peak and the corresponding d -spacing were then analyzed by the following for the monoclinic system.

$$\frac{1}{d^2} = \frac{h^2}{(a^2 \sin^2 \beta)} + \frac{k^2}{b^2} + \frac{l^2}{(c^2 \sin^2 \beta)} - \frac{2hl \cos \beta}{ac \sin^2 \beta}. \quad (4.22)$$

Using a custom MATLAB optimization code, repeated calculation of the lattice parameters using all well-fit peaks at once minimized the error across the large number of solutions. Fitting such a large number of peaks effectively over-constrained the system and provided a reliable set of lattice parameters for each powder. This method was also useful in that it helped to mitigate common measurement error associated with peaks of either small diffraction ring radius (large d -spacing) or single-index (e.g. the (100) peak).

Then, the resulting lattice parameters could be used to compute the d_0 spacings needed for strain calculations. These measurements and calculations were performed for both as-sprayed and annealed powders to measure the effects of the plasma-spray process and crystallization during early high-temperature cycling on the crystal structure on the disilicate-based powders.

4.4 Results and discussion

4.4.1 Effects of chemical modifications on $\text{Yb}_2\text{Si}_2\text{O}_7$ lattice parameters

The lattice parameters calculated from the stress-free powder WAXS measurements and subsequent fitting are reported in Table 4.1. For additional reference, lattice parameters of pure $\text{Yb}_2\text{Si}_2\text{O}_7$ reported in a PDF database are included. As mentioned previously, the compositions are referred to as baseline, 6A, and M2Y for the unmodified, alumina-modified, and mullite-and-YAG-modified materials, respectively. M5Y, a second mullite-and-YAG modified disilicate, added twice as much YAG by weight as did the M2Y composition.

The baseline annealed powder was measured twice at 0 degrees of rotation and twice at 180 degrees, and the differences in the d -spacings at each rotation were used to assess error in the measurements. At 0 degrees of rotation, the largest difference was approximately $2 \times 10^{-4} \text{ \AA}$. At 180 degrees of rotation, the largest difference was approximately $7 \times 10^{-5} \text{ \AA}$. With each pair of 0 and 180-degree measurements averaged (to correct for sample-detector distance), the largest difference between the averages was also approximately $7 \times 10^{-5} \text{ \AA}$. For the baseline system, differences mostly on the order of 10^{-5} \AA produced no change in the lattice parameters

Table 4.2: Lattice parameters of $\text{Yb}_2\text{Si}_2\text{O}_7$ -based topcoat materials. Powder diffraction file (PDF) parameters and measured $d_0^{(021)}$ values for strain calculation are included for reference. Error analysis is discussed in subsection 4.1.1.

Composition	Condition	a(Å)	b(Å)	c(Å)	β (°)	Vol. (Å ³)	$d_0^{(021)}$ (Å)
PDF	N/A	6.802	8.875	4.703	102.12	277.58	3.193080
Baseline	As-sprayed	6.7973	8.8666	4.7027	102.011	277.22	3.19247
	Annealed	6.7963	8.8661	4.7008	101.99	277.08	3.19145
6A	As-sprayed	6.7916	8.8620	4.7047	102.018	276.96	3.19216
	Annealed	6.8101	8.8642	4.7008	101.989	277.58	3.1911
M2Y	As-sprayed	6.7929	8.8628	4.7054	102.038	277.06	3.19254
	Annealed	6.7962	8.8681	4.7030	102.005	277.25	3.19245
M5Y	As-Sprayed	6.7934	8.8691	4.7066	102.034	277.52	3.19365
	Annealed	6.7999	8.8714	4.7031	101.995	277.35	3.19316

calculated by the method discussed above except for a 0.0003° decrease in the angle β . This change only altered the d_0 values computed for the monoclinic system on the order of 10^{-6} Å or less, which is below the resolution of the synchrotron WAXS measurement.

A conservative error of 1×10^{-4} Å (rounded up from the largest difference between averaged values) can be applied to the lattice parameter and d_0 values in Table 4.2. Where differences are observed in these values, they are typically on the order of 10^{-3} or greater. This confirms that the changes in lattice parameters are substantial, resulting from the effects of the dopants, and are not simply due to instrument effects in the synchrotron measurements. Differences on the order of the error, 10^{-4} Å, are considered too small to warrant detailed discussion of dopant placement and lattice parameter effects.

In the as-sprayed condition and compared to the baseline system, a decrease in lattice parameters a (approximately 0.08% for 6A and 0.06% for M2Y) and in b (approximately 0.05% for 6A and 0.04% for M2Y) and an increase in c from the baseline system to both modified systems (0.04% in 6A and 0.06% in M2Y) were observed. The angle β is smaller in the 6A system than in the baseline, whereas it is larger in the M2Y system. The unit cell volumes of the modified topcoat materials are also smaller than that of the Baseline system in this condition.

In the annealed condition, there was actually a higher value of a in the 6A powder than in the baseline (increase of approximately 0.2%), while in M2Y this parameter was smaller than for the baseline (decrease of 0.001%). Lattice parameter b shows the inverse: a smaller value in 6A and a larger value in M2Y, both compared to baseline, each by approximately 0.2%. Parameter c was the same for the baseline and 6A systems, while M2Y had a 0.04% larger value. The angle β was similar between baseline and 6A annealed samples, while it

was larger for the M2Y sample. Unit cell volumes of the three annealed powders were within 0.5 \AA^3 .

After annealing, the baseline parameters all decreased as the unit cell contracted. In 6A, both a and b increased while c and β decreased; unit cell volume increased in this case. M2Y behaved similarly to 6A, with decreases in c and β and increases in a , b , and unit cell volume.

4.4.2 Chemistry effects on lattice parameters

There is evidence, from high-resolution synchrotron diffraction, that the chemical additions to the $\text{Yb}_2\text{Si}_2\text{O}_7$ topcoats form secondary phases in the topcoats, as shown in Chapter 3. As an example, Fig. 4.10 shows diffraction lineouts for the annealed powder of 6A composition, prepared from free-standing topcoat material. During annealing, the powders crystallize and, in this case, form small amounts of a ytterbium aluminum garnet ($\text{Yb}_3\text{Al}_5\text{O}_{12}$) phase.

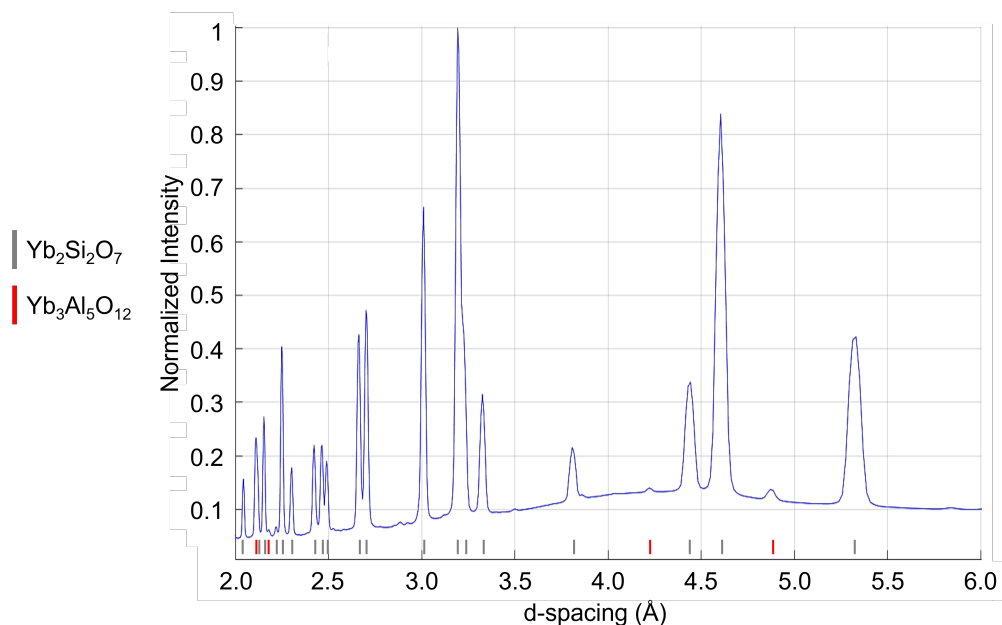


Figure 4.10: WAXS diffraction lineout for the 6A annealed powder. Phases are labeled for peaks above 2 \AA d -spacing. The amorphous contribution is from the quartz capillary holding the powder.

Although the topcoat materials do not remain single-phase, the majority still belongs to the $\text{Yb}_2\text{Si}_2\text{O}_7$ phase. Thus, changes to the $\text{Yb}_2\text{Si}_2\text{O}_7$ lattice parameters must be considered in the context of the chemical modifications to the topcoats. The chemical changes are treated here in terms of atomic, or rather ionic, substitutional and interstitial sites in the monoclinic disilicate crystal structure. The following crystal structure model (Fig. 4.11)

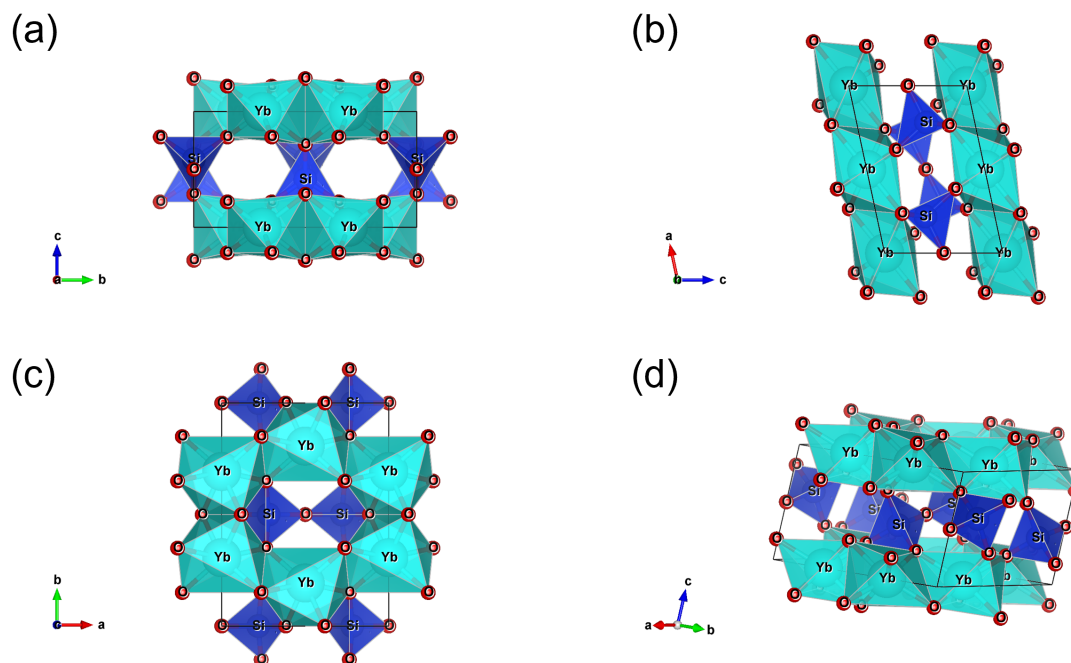


Figure 4.11: The $\text{Yb}_2\text{Si}_2\text{O}_7$ crystal structure, modeled using Vesta software¹¹⁷. The crystal is oriented looking down the (a) a , (b) b , and (c) c axes, as well as an off-axis perspective (d).

is used to discuss the possible implications for the lattice parameters due to the chemical modifications.

In the 6A powder, there was a measured increase in the a parameter and a decrease in b , compared to the baseline $\text{Yb}_2\text{Si}_2\text{O}_7$, in the annealed condition for each composition. Nominally, the only change to the topcoat chemistry in the 6A composition is the incorporation of alumina into the $\text{Yb}_2\text{Si}_2\text{O}_7$. Given that the crystal ionic radii of Al^{3+} , Si^{4+} , O^{2-} , and Yb^{3+} are (respectively) 67.5pm, 54pm, 126pm, and 100.8pm¹⁰², it is likely from an ionic radius perspective (minimizing strain in the lattice) that an Al^{3+} ion would sit on a Si^{4+} site. From Ref. [18], substitution of an Al^{3+} ion on another cation site (in this case, Si^{4+}) typically takes one of two forms in non-clay materials. The aluminum ion can occupy the site of a silicon ion and be accompanied by an alkali or alkaline earth ion which occupies an expanded interstitial site. In this case, the expansion of an interstitial site to accommodate an alkali or alkaline cation should increase at least one linear lattice parameter without a related decrease in another. Alternatively, an anion (O^{2-}) site can be left vacant in order to satisfy charge balance in the structure. The second mechanism allows for the increase in size of the cation site and the decrease of one anion site due to the oxygen vacancy.

In 6A, since there was an increase in a and a decrease in b , it is likely that the second mechanism is at play in the cation lattice site substitutions. When viewing the monoclinic crystal structure of $\text{Yb}_2\text{Si}_2\text{O}_7$ down the c axis (Fig. 4.11), there are visibly more Si^{4+} ions oriented along the b -axis than along the a -axis. If an Al^{3+} ion had an equal probability of occupying any Si^{4+} site in the structure, then an even distribution of cation substitutions should have a relatively more pronounced effect in the a parameter than in the b parameter. Also, if the assumption that the cation substitution is accompanied by an anion vacancy is correct, then the arrangement of the SiO_4 tetrahedra might explain the contraction of the b -axis length. Each such tetrahedron has one Si-O bond extending primarily along a , one primarily along c with some small orientation along a , and two primarily along b . The result, a large number of oxygen anions in the b direction of the crystal, would result in a more likely contraction in b than in the other linear parameters in the case of evenly dispersed charge-balanced defects. Lattice parameter c was nearly unchanged in 6A compared to the baseline. This could be due to the orientation along the a and b axes of most bonds in the structure. In this case, the dilation of silicon cation sites and contraction of oxygen anion sites in charge-balanced substitutions may mostly cancel one another out. The formation of $\text{Yb}_3\text{Al}_5\text{O}_{12}$ in the 6A topcoat is facilitated either by reaction between the Al_2O_3 dopants and the Yb_2SiO_5 left over from plasma-spray processing, in which case the disilicate parameters would be unaffected, or by the formation of Yb vacancies in the disilicate and accompanying charge-balancing modifications. In the second case, there would likely be a contraction of all linear lattice parameters in the unit cell, although the combined or compared contributions of these changes and those of substitutional impurities on the overall WAXS measurement are not quantified.

For the M2Y and M5Y compositions, there are obviously two chemical modifications to take into account when considering atomic/ionic incorporation of the dopants into the main disilicate structure. The first, the inclusion of mullite, should have a similar effect to that of alumina since mullite is composed of units of SiO_2 and Al_2O_3 . The second, the incorporation of YAG, should itself make two different contributions. One is by the incorporation of more Al^{3+} cations in the crystal structure, again with the same considerations as before. The second is by the incorporation of Y^{3+} ions into the crystal structure. Y^{3+} ions have the same valency as the Yb^{3+} ions in the disilicate, and the crystal ionic radius of Y^{3+} , 104pm, is close to that of Yb^{3+} , 100.8pm. There is also a commonly studied $\text{Y}_2\text{Si}_2\text{O}_7$ disilicate, reinforcing this preference of the Y^{3+} substitutions for the cation site in this structure.

With a higher number of Yb^{3+} ions arranged along the a axis than in the b and c axes in the disilicate crystal structure, an even distribution of Y^{3+} substitutional cations into Yb^{3+} sites

should have a relatively more pronounced effect on expanding the b and c parameters than on the a parameter. Additionally, the excess oxygen anions provided by the relatively oxygen-rich YAG could occupy interstitial sites, most likely similar to the sites seen at approximately $(\frac{1}{2}, \frac{1}{4}, \frac{1}{2})$ and $(\frac{1}{2}, \frac{3}{4}, \frac{1}{2})$. If the oxygen anions instead occupy vacant anion sites in the crystal structure, particularly in tetrahedra where Al^{3+} occupies the Si^{4+} site, then the occupation of interstitial sites by cations would be necessary to avoid charge imbalance. In either case, the presence of excess oxygen likely contributes to preventing the contraction of the b parameter in the structure, in contrast to the observations from the alumina-modified crystal structure. Relatively less aluminum in the M2Y composition, compared to that in the 6A composition, may also explain the lack of significant change in the a parameter of the M2Y composition.

In the M5Y composition, the a , b , and c lattice parameters are all increased compared to those of the Baseline composition. In comparison to the M2Y composition, where the difference is twice the amount of YAG added (by weight) in M5Y, both a and b increased while c stayed mostly the same. This may be explained by again examining the crystal structure. Given the length of the c parameter in the disilicate structure, and the relatively low number of rare-earth cations in that dimension, it is possible that the effect of Y^{3+} substitutions in Yb^{3+} sites in dilating the c parameter saturates at relatively low additions of YAG to the disilicate. By contrast, the a direction, which contains more rare earth cation sites, may show the effects of further Y^{3+} cation substitutions into the structure. The increase in b from M2Y to M5Y should be accounted for by the additional Y^{3+} and Al^{3+} cations, as well as the additional oxygen anions, by the same mechanisms described above.

4.4.3 Strain-free lattice parameters

The lattice parameter changes in the annealed powders were measured after heating the powders above 1300°C in quartz capillaries for 30 minutes each. The as-sprayed powders possessed a significant amount of amorphous material as shown in Fig. 4.12. Filing the as-sprayed topcoat material to very small particle sizes was intended to relieve any processing-related stresses. This may have been the case for the most part, given the very small differences in lattice parameters between the as-sprayed and annealed baseline powders. The larger differences in lattice parameters between the as-sprayed and annealed conditions for the 6A and M2Y powders are hypothesized to reflect both a small amount of stress relief and also the behavior of the modified topcoat chemistry. This is not unreasonable, since the plasma-spray precursors consist of all necessary constituent oxides, which were not chemically mixed prior to rapid melting and deposition. The oxide additions to the $\text{Yb}_2\text{Si}_2\text{O}_7$ base material could be expected to alter the lattice parameters with meaningful time at high temperature.

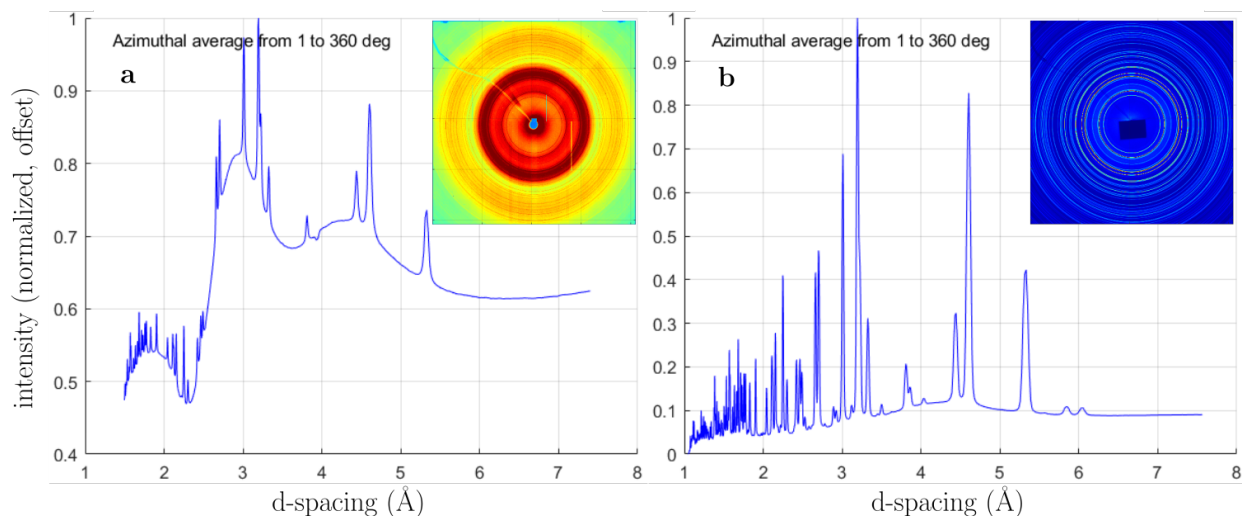


Figure 4.12: Diffraction lineouts for the Baseline $\text{Yb}_2\text{Si}_2\text{O}_7$ powders, (a) after plasma-spray processing and (b) after annealing. Intensities are not scaled identically in the diffraction frames. Annealing at high temperature crystallizes the amorphous content in the disilicate, and remaining amorphous signal is from the quartz capillary.

Ideally, this process could be repeated for topcoat powders after each temperature and steam cycling exposure time to fine-tune the accuracy of each measurement and to observe any trends over longer exposure times. However, the powders measured were from large samples sprayed to high thickness on graphite substrates for convenient preparation. Steam-cycled multilayer samples had much thinner topcoats and there was less of each sample to analyze, precluding stress-free powder measurements for each individual topcoat condition. Steam cycling of powders would not fully mimic the complexity of steam cycling in the multilayer system, so strain-free measurements of the steam-cycled topcoats were not realistic.

The changes between lattice parameters are generally small, and it would be tempting to consider all of the topcoat materials to be the same as the baseline for the purposes of computing strains. However, the materials studied presently are ceramics with high elastic moduli. Changes in strain on the order of the differences between the lattice parameters can result in significant changes to the computed biaxial stresses in the topcoat layers. Therefore, it was critical to assess the changes to the lattice parameters to understand chemical changes and to accurately measure strains and stresses.

4.4.4 Identification of the TGO with synchrotron diffraction

As mentioned previously, WAXS diffraction patterns were collected beginning just above the top surface of the topcoat and progressing into the depth of the EBC/CMC system. Diffraction lineouts from these patterns, either in raw form (intensity versus radius from

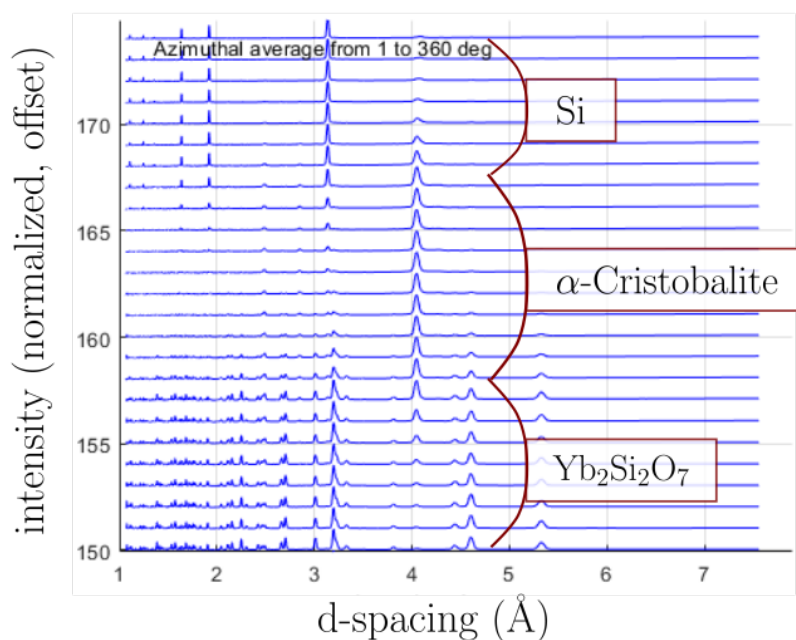


Figure 4.13: Diffraction patterns of the $\text{Yb}_2\text{Si}_2\text{O}_7$ topcoat, cristobalite TGO, and silicon bondcoat, from bottom to top. The cristobalite TGO is typically not detected in individual diffraction frames in WAXS studies with taller X-ray beams.

center of detector) or after a "caking" process to convert to d-spacing (thus lineouts of intensity versus d-spacing), were useful for determining the range of frames, and hence distance, over which to fit each material in the multilayer system. With a $40\mu\text{m}$ -tall beam, the diffraction peaks observed are primarily from majority phases. While minority phases can be observed with WAXS, it is only with the shorter X-ray beam in this case that the oxide could be observed as the main phase in a given diffraction pattern.

However, frames collected using the short-focus beam, which had a vertical height of slightly less than $2\mu\text{m}$, allowed for much better spatial resolution, and therefore increased oxide phase sensitivity in scans of TGO-majority volumes, than what is observed in measurements with the $40\mu\text{m}$ -tall beam. The thickest oxide layer measured in the samples of this study, approximately $14\mu\text{m}$ thick, grew in the 1000-hour steam cycled sample of Baseline topcoat composition. With the $40\mu\text{m}$ -tall beam, getting diffraction signal from only the TGO is impractical due to the large interface roughness of the layers (on the order of 10 to $20\mu\text{m}$). The vertical position of the beam is also determined as an incremental distance below the top of the topcoat; thus with variances in layer thickness and roughness there is a low chance of centering the beam on the oxide. With $2\mu\text{m}$ beam height, however, lineouts produced

during WAXS analysis showed the presence of a crystalline oxide between the topcoat and the bondcoat (Fig. 4.13), as expected from microscopy studies (Chapter 3) and noted in other literature studies¹⁰⁷.

As demonstrated in Fig. 4.13, based on the peaks present the TGO in the baseline system is the α -cristobalite polymorph of SiO_2 . As discussed in Chapter 3, the same method was used to observe both α -cristobalite and β -cristobalite in the 6A and M2Y multilayer samples after steam cycling. Without transmission diffraction capabilities, one would likely have to use a method such as TEM to characterize the oxide layer in this way. Observation of the EBC/CMC oxide layer using synchrotron WAXS diffraction, confirmation of its crystalline character, and the positive identification of the cristobalite phase are unique contributions of this work.

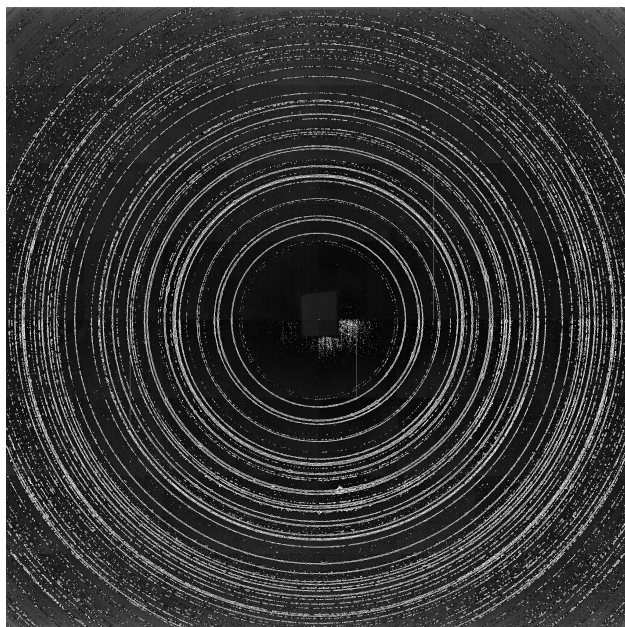


Figure 4.14: Diffraction pattern collected using a $2\mu\text{m}$ -tall X-ray beam. These diffraction data were used to identify the topcoat and TGO phases and to fit strains in the TGO.

Diffraction data from the short-focus beam measurements were used to assess strains in the α -cristobalite TGO of the baseline system after 1000 hours of steam cycling. An example diffraction pattern from this sample is shown in Fig. 4.14, where topcoat and TGO peaks are visible but not labeled. Measured from the highest-intensity peak, the (001) reflection, horizontal (in-plane) strains were approximately 0.001-0.0015 (0.1 to 0.15%) and vertical (out-of-plane) strains were 0 to 0.0005 (0 to 0.05%). These tensile strains reinforce and confirm the stress arguments made using the transmission diffraction data in Chapter 3 as well as the analytical model in this chapter, where the transformation and volume contraction

from β -cristobalite to α -cristobalite should produce large tensile stresses in the TGO. The cracking prevalent in the TGO of the baseline system, especially after 1000 hours of steam cycling, should provide stress relief in the layer; however, there is still measurable strain in the TGO which has not been relieved.

4.4.5 Equibiaxial internal stresses related to chemistry and exposure history

With the d_0 values reported above from the stress-free powders, in-plane and out-of-plane strains were assessed for the materials in the multilayer system. As also mentioned above, elastic properties were measured and/or calculated previously by Stolzenburg et al. for $\text{Yb}_2\text{Si}_2\text{O}_7$, Si, and SiC¹¹. The elastic properties are summarized in Table 4.3. The elastic properties of the chemically modified $\text{Yb}_2\text{Si}_2\text{O}_7$ were assumed to be sufficiently close to those of the baseline composition measured previously that the same values were used for those calculations.

Table 4.3: Materials in the multilayer structure, along with the peaks used for analysis, d_0 spacings, and related elastic properties.

Material	Reflection (hkl)	d_0 (Å)	Elastic modulus (GPa)	Poisson's ratio
$\text{Yb}_2\text{Si}_2\text{O}_7$	(021)	see Table 4.2	205.6 ¹¹	0.33 ¹¹
Si	(220)	1.9198	169	0.18
SiC _f /SiC	(220)	~ 1.54 (see text)	420 ⁵⁹	0.17 ⁵⁹

With all of the relevant strains and elastic properties at hand, biaxial stresses were computed using Eq. 4.18. Stresses in as-sprayed and annealed samples are shown with standard deviation error bars. For clarity, co-plotted stresses of annealed and steam cycled conditions do not include error bars and are linearized where the data points fall within ~30 MPa of the linearized value. Data points near surfaces and interfaces, which are prone to error due to low diffraction intensity, are also omitted in some places for clarity. The results are discussed in relation to exposure history and microstructure.

It should be noted that the effects of porosity and temperature on the elastic moduli of the materials are not accounted for in this analysis. This is the case for the modeled stresses, for which bulk changes or reduction of modulus with temperature are not incorporated. Additionally the changes in modulus due to porosity and temperature were not measured experimentally for the diffraction-based experimental stress analyses, although the moduli used for $\text{Yb}_2\text{Si}_2\text{O}_7$ were measured from free-standing, plasma-sprayed samples by Stolzenburg previously¹¹.

4.4.5.1 Effect of annealing on internal stresses

Biaxial internal stresses for the as-sprayed and annealed multilayer samples of baseline composition are shown in Fig. 4.15. In the as-sprayed topcoat, biaxial stresses are compressive and range from nearly -200MPa near the free surface to approximately 0MPa near the interface with the bondcoat. In the as-sprayed bondcoat the stresses are also compressive, ranging again from approximately -175MPa to -25MPa. In the SiC_f/SiC substrate the internal biaxial stresses are a mixture of tensile and compressive, oscillating as seen in Fig. 4.15. These biaxial stress oscillations in the substrate are the result of the microstructure of the composite, as was observed and described in the work of Stolzenburg et al.^{11,99}. The SiC fiber tows alternate in direction within the composite, and the differing stresses in the fiber tows and in the matrix produce the characteristic, oscillating and semi-periodic stress profile shown. The stresses in the substrate of the as-sprayed sample, oscillating around 0MPa, most likely result from unknown thermal gradients during the plasma-spray process, where the substrate is kept cooler than the sprayed coatings and therefore should develop a smaller stress than if it was kept at a higher deposition temperature.

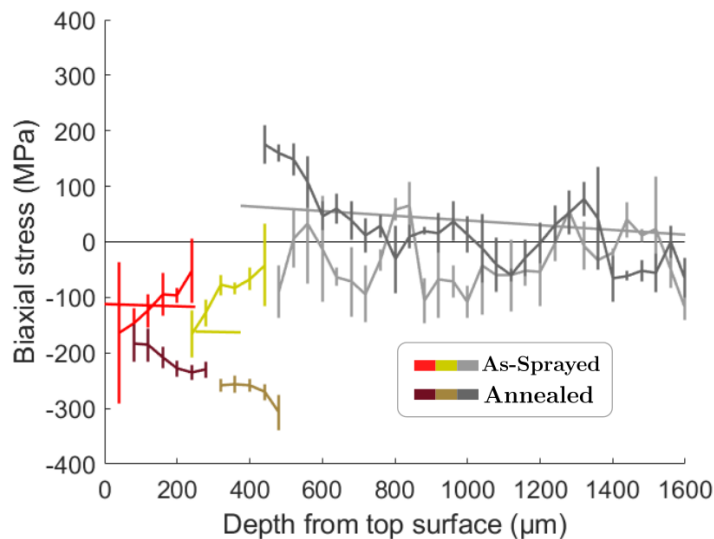


Figure 4.15: Internal biaxial stresses for the Baseline system, as-sprayed and annealed samples, as well as from the analytical model of Hsueh et al¹⁰⁹ (straight lines).

The annealed sample shows an increase in magnitude and (relative to as-sprayed) depth-wise consistency of compressive stresses throughout the topcoat, averaging between -180 and -235 MPa away from the free surface. Bondcoat compressive stresses also increase and "flatten out" throughout the layer, averaging between -260 and -320 MPa. Increased tensile stress in

the substrate is observed through most of the measured depth, reaching approximately 175 MPa near the interface with the bondcoat and decreasing away from the coatings.

The error bars in Fig. 4.15 represent the standard deviations of the average values and are larger in the topcoat and substrate of the as-sprayed sample. For the topcoat, this is attributed to the significant amorphous content in the layer, which reduces the signal-to-noise ratio of the diffraction peaks in the WAXS experiment and likely results in a different internal stress profile than a fully crystalline layer. The non-uniform temperature profile and cooling conditions present in the plasma spray process may contribute to variances of the internal stresses in the topcoat, although this contribution is not quantified here. In all compositions the standard deviations of the stresses in the topcoat decrease significantly after annealing, likely due to crystallization of the topcoat and imposition of relatively uniform temperatures and heating/cooling profiles in the steam cycling setup.

The differences in the stress profiles between the as-sprayed condition and the annealed condition might be attributed to three primary effects: the amorphous material left over from the topcoat from plasma-spray processing, the temperature history of the multilayer system, and interface bonding between the layers and substrate in the system. Since the as-sprayed system had not been heated to a high temperature for any significant time, there was still extensive amorphous $\text{Yb}_2\text{Si}_2\text{O}_7$ content in the topcoat (as seen in Fig. 4.12). The amorphous content could have retained quenching or other thermal stresses which could not be accounted for in the models used here. Additionally, the strains and elastic properties of $\text{Yb}_2\text{Si}_2\text{O}_7$ were calculated using crystalline WAXS reflections as described earlier, and so these values may not apply to amorphous $\text{Yb}_2\text{Si}_2\text{O}_7$.

Splat-quenching of very hot materials onto on a mildly heated substrate should also effect the internal stress profiles of the as-sprayed samples compared to those of the temperature-cycled samples. Primarily, rapid cooling of the deposited coating materials would produce very different stresses in those layers than would be seen in the substrate, which only cools to room temperature after deposition is completed. Thus, the stresses in the coating layers likely show the combined effects of quenching and then cooling from the substrate temperature, whereas the substrate stresses should show mostly cooling from the substrate hold temperature. There would also be temperature-stress implications due to local heating and cooling of the substrate surface during early deposition, as well as some heating effects to some depth beneath any splat-quenched particles as deposition progressed. However, these phenomena would be the focus of a study dedicated to fully characterizing the plasma-spray process and quenching effects rather than the study at hand, and so they are not deconvolved here.

4.4.5.2 Stresses in the "annealed" condition

There is a useful comparison to be made between the stresses and stress profiles of the three compositions. As discussed above, the similarities in the stresses between these samples in the as-sprayed and annealed conditions indicate that plasma-spray processing has a strong influence over the as-sprayed stresses. Additionally, the uniform heating and cooling of the entire multilayer system is critical for predictably producing the compressive coating stresses desired for promoting the longevity of the EBC coatings as shown in the analytical model presented. It should be noted, though, that the analytical model implemented in this work is not used to design turbine engines but rather is used to understand simplified engine behavior. From a design perspective, the effects of thermal history on internal stresses, as observed in the evolution from as-sprayed to annealed conditions, indicate that alternative or more sophisticated heating and cooling profiles can result in different stress profiles than those observed here.

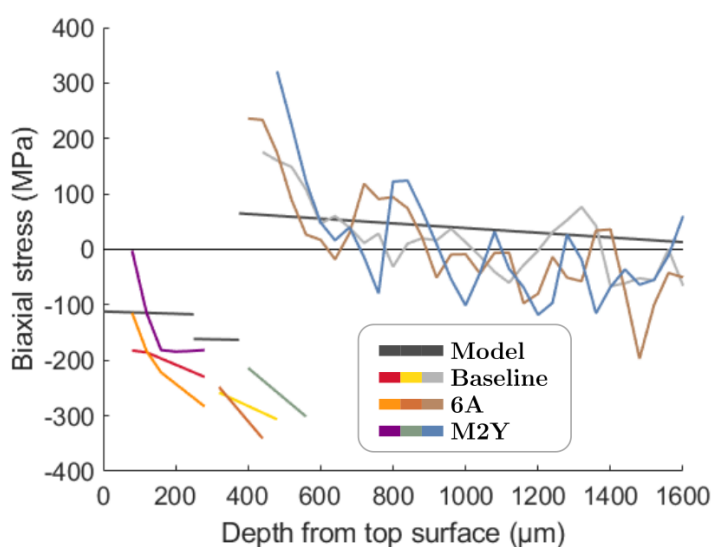


Figure 4.16: Annealed stresses for Baseline, 6A, and M2Y samples, as well as the calculated result from the analytical model.

Fig. 4.16 shows the stresses in the annealed multilayer samples of all three topcoat compositions, as well as the stresses calculated using the analytical model (straight, mostly horizontal lines). The irregular stress profile of the M2Y topcoat is attributed to surface undulations of the substrate, by which large height differences can appear between nearby areas in the coating materials. Low diffraction intensities in some frames result in strain errors which can produce larger or smaller stresses than the bulk of the layer. Layer undulations which

serve to "spread out" interfaces vertically are also the reason why measured layers are not perfectly in line with the model based on nominal layer thicknesses.

Despite those differences, the stress profiles of the three annealed samples are similar. All three have compressive stresses near -200-250MPa in the topcoat and -200-300MPa in the bondcoat. Tensile stresses are highest in the substrate and decline away from the coating layers, with the characteristic cyclic stresses expected due to the CMC microstructure. Measured stresses are similar in profile to modeled stresses, including the higher compressive stresses in the bondcoat compared to the topcoat. However, the measured bondcoat stresses increase in compressive value more so than the modeled bondcoat stresses. The high tensile stresses in the substrate near the bondcoat help to explain the high compressive bondcoat stresses near the same interface, since increases in each will offset one another and satisfy force balance requirements. This effect is most likely due to microstructure: the pores and voids in the CMC microstructure may result in a somewhat discontinuous substrate further away from the interface with the bondcoat. If this is the case, then the tensile stresses expected from the model would be borne unevenly by the CMC substrate material by effectively reducing the thickness of the substrate material which is supporting the thermal mismatch stress.

The coating stresses are also higher in magnitude in the annealed samples compared to the modeled stresses. In the work of Stolzenburg, the stresses measured in the diffusion barrier (mullite) and bondcoat (silicon) layers of multilayer EBCs with $\text{Yb}_2\text{Si}_2\text{O}_7$ topcoats were much smaller in magnitude than predicted using a similar model¹¹. This was attributed to microstructure, as it was noted that those layers varied in thickness and the layers were even absent in some locations, reducing their ability to sustain biaxial stresses¹¹. The coatings in the present work have relatively consistent thickness (despite surface and interface roughness and the effect of substrate surface undulations), resulting in significant biaxial stresses not observed in the previous work.

The coefficient of thermal expansion for the materials has a strong influence on stresses calculated using the analytical model. The CTEs of all $\text{Yb}_2\text{Si}_2\text{O}_7$, Si, and SiC have been reported with differing values in the literature^{13,101}, although the order of largest CTE to smallest CTE in the system remains across most sources. For example, the CTE values in the study of Richards et al.¹⁰¹ are 4.1×10^{-6} in both coatings and 4.7×10^{-6} in the substrate. The variation in CTEs in the literature, and the influence of changes to CTE on modeled stresses, serve as a potential source of inconsistency between modeled and measured stresses, if indeed the values used do not perfectly reflect those of the real system.

The analytical model also shows a dependence of the bending component of the strain,

t_b on the square of the thickness of the substrate. Given the microstructure of the real SiC_f/SiC CMC, the thickness which effectively supports stresses due to thermal mismatch between coating and substrate may not be the thickness of the CMC itself. Additionally, one aspect of the analytical model is that shear deformations are neglected, which may be a non-negligible feature of the real EBC/CMC materials in this study. Since these assumptions are used to develop the model, it is unclear what the effect would be on the model if they are not entirely applicable. Single-valued elastic and thermal expansion properties are used in the model for this work, which likely accounts for some difference between calculated and measured values. With respect to the CTE in particular, the value for bulk SiC is used in the model whereas the CTE of SiC_f/SiC CMC may be somewhat different and even highly anisotropic depending on the arrangement of matrix and fiber tows in the composite, as well as pores and voids in the matrix.

Finally, surface undulations of the substrate could increase the measured compressive stresses as an artifact of the measurement geometry. The Poisson effect created by in-plane biaxial stresses is most pronounced in the out-of-plane direction. Undulations and/or tilts could result in vertical d -spacing measurements which are not entirely out-of-plane, resulting in a measured value reflecting a diminished portion of the Poisson effect (Fig. 4.5). As can be seen in Eq. 4.18, out-of-plane strains (ε_{33}) which are not as tensile as those experiencing maximum Poisson effect will result in larger measured compressive stresses when ε_{11} is negative. Diffraction through thinner samples, taken from sections with flat interfaces, may show the significance of this effect, but machining stresses will start to dominate over thermal stresses as samples are made thinner and thinner. Significant undulations were not observed in all samples, and so this effect—however large or small it is—would not apply equally across every measurement.

4.4.5.3 Stresses after steam cycling

After 100 hours of steam cycling, the stress profiles of the baseline, 6A, and M2Y compositions were similar in many ways (Fig. 4.17). Topcoat stresses were -85-100 MPa, -25-75 MPa, and -150-200 MPa in baseline, 6A, and M2Y, respectively. Bondcoat stresses were -175-225 MPa compressive in baseline and M2Y, and slightly higher at -225-275 MPa in 6A. Substrate stresses in the baseline were mostly within 50-150 MPa tensile, with a few areas in the baseline higher near 225 MPa. M2Y substrate stresses were mostly within 0-200 MPa tensile, except for some compressive stresses far from the coatings. In all three compositions, tensile substrate stresses were highest near the substrate-bondcoat interface, as expected from the analytical model, and decreased with further depth into the substrate.

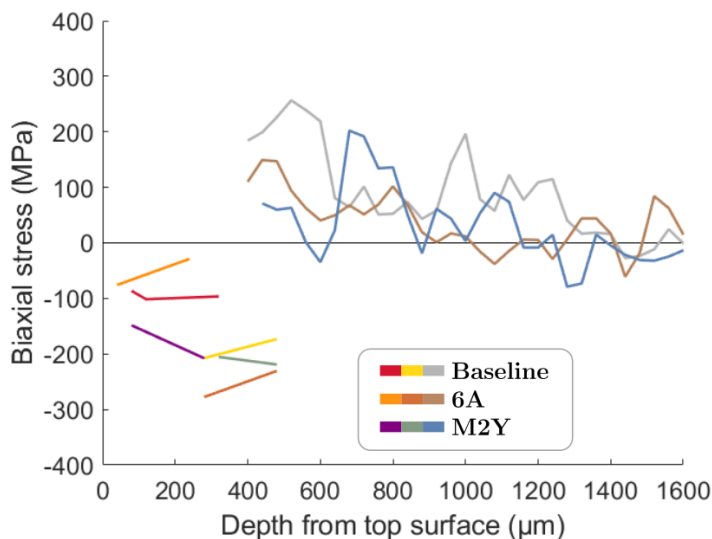


Figure 4.17: Stresses measured after 100 hours of steam cycling for all three compositions.

After 500 hours, the stress profiles of the three compositions are the most different from one another to this point, with compressive stresses near 0 MPa for the baseline and 6A topcoats and near -225-275 MPa for the M2Y topcoat (Fig. 4.18). Bondcoat stresses remained compressive in all samples of this condition, mostly between -150 and -250 MPa. Substrate stresses were also similar to one another again at this steam cycling condition, ranging from 0 to 200 MPa tensile stress near the bondcoat before tapering to a low-stress state away from that interface.

The notable difference between these three stress profiles is in the change between the 100-hour and 500-hour steam cycling histories for each composition. In the M2Y sample, the compressive stresses in the coating layers were mostly unchanged, or within approximately one standard deviation, of those in the 100-hour condition. In the baseline and 6A compositions, however, there was a notable drop of approximately 100 MPa in the compressive stress of the topcoat layer.

With 1000 hours of steam cycling, an even larger difference arises between the stress profiles of the compositions (Fig. 4.19). The baseline topcoat stresses increased significantly to 85-200 MPa *tensile*, the first significant tensile stress in this coating. Topcoat stresses in 6A are approximately -100 MPa compressive, returning from nearly stress-free at 500 hours to having compressive stress after 1000 hours. M2Y topcoat stresses are -175-225 MPa compressive, mostly unchanged from earlier steam cycling conditions. The bondcoat stresses are all compressive, with baseline ranging from -100-150 MPa and 6A and M2Y both near -200 MPa. Substrate stresses in the baseline and 6A samples are mostly 0 to 200 MPa from

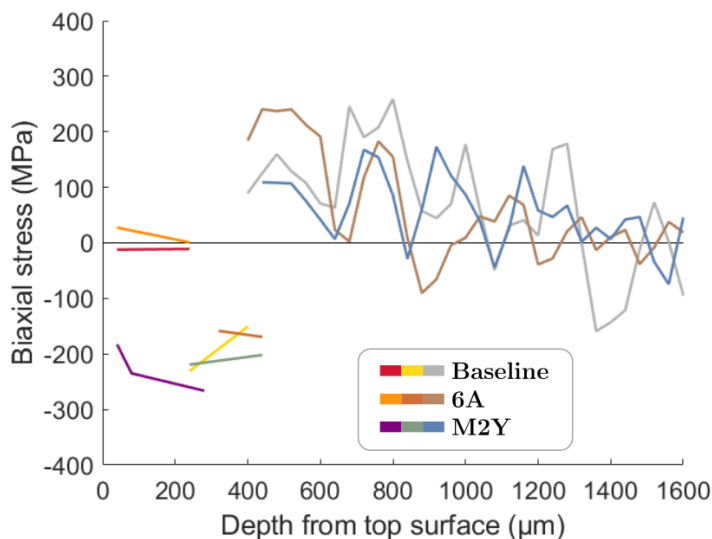


Figure 4.18: Stresses in 500-hour steam-cycled samples.

near the coatings to several hundred microns away from the interface. After short jumps of ~ 200 MPa (compressive in baseline, tensile in 6A), the stresses in these substrates mostly oscillated around 0 MPa. M2Y substrate stresses were larger than those of baseline and 6A, mostly 150-350 MPa tensile before decreasing away from the coatings. These large stresses could be explained by the state of the substrate after 1000 hours of steam cycling, where large voids were present in the matrix of the CMC. With less material present to satisfy force balance in the multilayer system, the material that is present would develop larger stresses to balance the compressive stresses in the coatings. While this alone may not entirely explain an increase in substrate stresses with no counterpart in coating stresses, differences in microstructure between different substrate coupons can introduce strong variability in stress profiles. For example, differences in the relative amount of fiber and matrix phases, as well as in the relative arrangement of the fibers, would likely have an impact on the measured stresses that are difficult to account for using WAXS alone.

Similarities in stresses between the three compositions after 100 hours of steam cycling would indicate without more perspective that the three coating systems are equivalently durable. However, the change in stresses from the 100-hour to 500-hour steam cycled conditions is rather different between the baseline and 6A compositions and the M2Y composition. The differences in stress state between the compositions accompany significant differences in sample microstructure, as discussed below.

Comparisons between the three compositions after 1000 hours of steam cycling show the most clear divergence in stress profiles and indicate a clear difference in the evolution of the

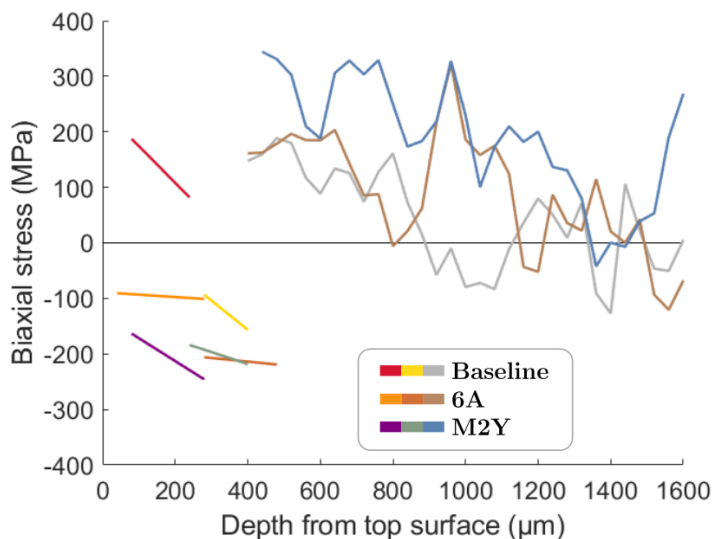


Figure 4.19: Biaxial stresses in the 1000-hour steam-cycled samples.

multilayer systems. From 500 hours to 1000 hours of steam cycling, the topcoat internal stresses become tensile in the baseline system and become or remain compressive in the modified systems. The contrast provided between the stresses in the baseline and modified samples strongly indicate that the modified systems have improved durability with respect to internal stresses in high-temperature, humid environments.

4.4.5.4 Internal stresses from TGO growth and microstructure

Direct comparison of internal stresses and microstructure in the baseline system, with specific comparisons, reinforces the connection between TGO thickness and internal stresses. Biaxial internal stresses are plotted for the baseline composition, in the annealed and 100-, 500-, and 1000-hour steam-cycled conditions, in Fig 4.20. As mentioned above, the topcoat stresses in particular evolve from approximately -200 MPa compressive in the annealed state to 85-200 MPa tensile after 1000 hours of steam cycling.

In all compositions, the oxide thickness should be zero or negligible in the as-sprayed and annealed conditions. In the baseline system, through steam cycling exposures the oxide thickness progressed from $\sim 4.4\mu\text{m}$ after 100 hours, to $\sim 10.8\mu\text{m}$ after 500 hours, to $\sim 13.8\mu\text{m}$ after 1000 hours. As observed in Chapter 3, the TGO in the baseline system is α -cristobalite, which is the low-temperature polymorph of cristobalite. As discussed previously, β -cristobalite was used in analytical stress modeling because that phase is stable through the majority of the temperatures traversed in steam cycling. The transformation from high-temperature β -cristobalite to low-temperature α -cristobalite, which takes place at approximately 250°C , is

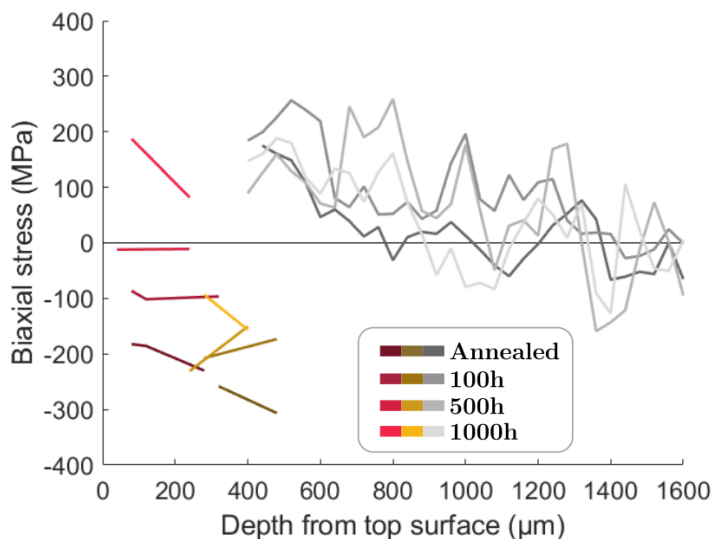


Figure 4.20: Internal stresses in Baseline composition multilayer samples, post-anneal and NASA Glenn steam-cycling.

accompanied by a volume contraction of 4-5%. With the TGO constrained in the multilayer system by the other layers, significant damage to the TGO is inevitable with such a volume contraction. As a result, vertical cracks appear in the TGO as do cracks between the TGO and neighboring layers. Parts of this oxide and damage are shown in Fig. 4.21. While the 1000-hour sample did not show spallation of the topcoat, it possessed the thickest and most damaged oxide and oxide-layer interface of all Baseline samples. The TGO cracking which results is critical for interpreting the internal stress measurements, as the damage in the TGO serves to relieve stresses in the nearby layers^{13,101}. Figure 4.22 shows a representative, two-dimensional "slice" of tomography data with no resolvable cracking in the topcoat. As discussed previously, the tensile strains in the TGO of the baseline system after 1000 hours of steam cycling serve to confirm the tensile stress state of the TGO, which has cracked in multiple places, as well as reinforce the mechanism for stress relief in the multilayer system. In terms of the analytical model of Hsueh¹⁰⁹, increased cracking also increasingly breaks with the assumption of intact layers and bonded interfaces.

The TGO thicknesses in 6A and M2Y after 1000 hours of steam cycling are approximately $2.1\mu\text{m}$ and $1.7\mu\text{m}$, respectively (Fig. 4.23). As discussed in Chapter 3, the TGOs in the modified systems are not single-phase α -cristobalite but contain some amount of β -cristobalite. Stabilized β -cristobalite does not undergo the volume contraction associated with the transformation between polymorphs. Decreased TGO thickness and amount of TGO volume contraction minimize the effects of TGO growth on internal stresses through steam cycling.

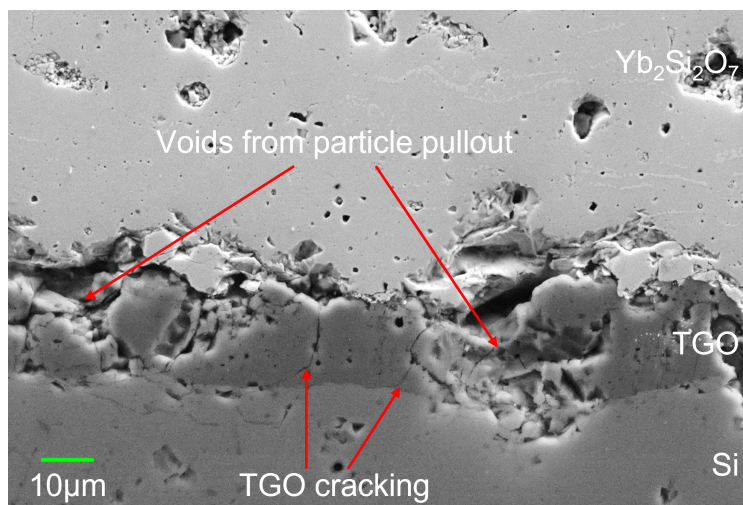


Figure 4.21: SEM cross-section, after sectioning and polishing, of the Baseline 1000-hour steam-cycled sample, with oxide and damage indicated.

A baseline sample which was thermally cycled in air for 500 hours, where the TGO thickness was approximately $2\mu\text{m}$ ¹⁵ was also measured by WAXS for comparison with the steam-cycled sample. Notably, the topcoat and bondcoat both retained significant compressive stresses: approximately -200 to -225 MPa for the topcoat and -250 MPa for the bondcoat (Fig. 4.24). The substrate stresses oscillated from approximately zero to 200 MPa for several hundred microns closest to the bondcoat prior to leveling out to oscillate around zero MPa away from the coatings. The internal stress states of the materials in this sample partially confirm the hypothesis that TGO thickness and transformation-induced cracking, combined, result in the stresses developed through steam cycling.

The development of tensile stresses in the baseline topcoat after 1000 hours of steam cycling could be due to the influence of the temperature-based CTE and phase transformations in the TGO. Additionally, in areas of the TGO with significant cracking, progressive oxidation of the silicon bondcoat could grow more oxide between cracks in the existing oxide. If this is the case, and assuming that the existing oxide is well-bonded to the topcoat when horizontal cracking is not present, then the introduction of additional material into vertical cracks could contribute to tensile stresses in the topcoat as the oxide layer "expands" by growth of new TGO into the cracks of existing TGO.

Although extensive cracking was not observed in the topcoat of the 1000-hour steam-cycled sample, the progression from a compressive stress state, to a nearly stress-free state, to a tensile stress state in the topcoat over a relatively short time (compared to the service life of the turbine engines) indicates that the stress development in the topcoat would contribute

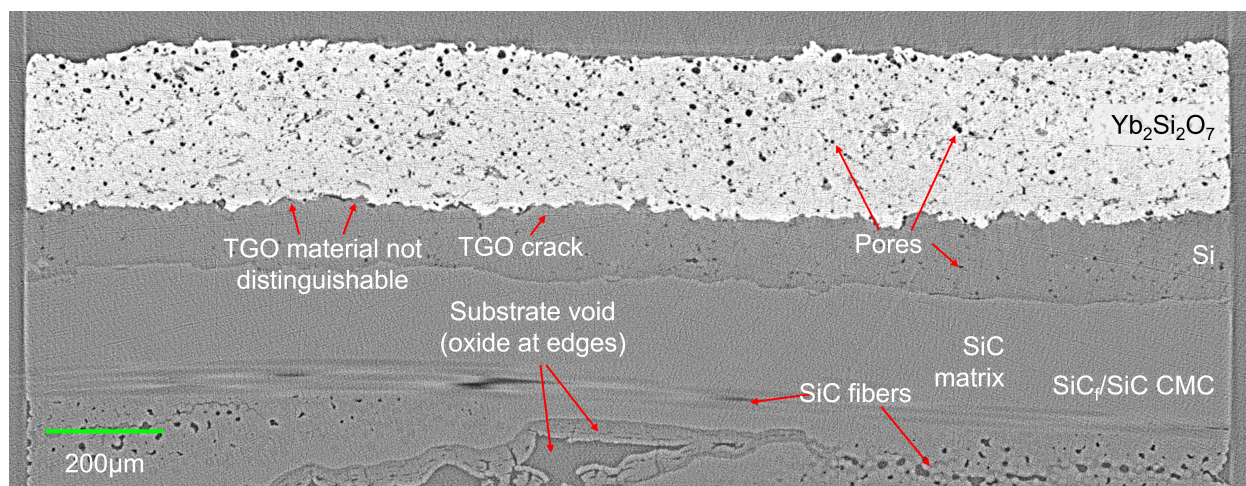


Figure 4.22: Representative tomography-generated slice, showing relevant features. No cracking is resolvable in the topcoat by tomography.

increasingly to cracking over time. Given that the goal time for a component to be in operation is at least 20,000 usable hours, observations of microstructure and internal biaxial stress in the multilayer materials indicate that oxidation poses a serious threat to the Baseline $\text{Yb}_2\text{Si}_2\text{O}_7$ -based EBC/CMC system.

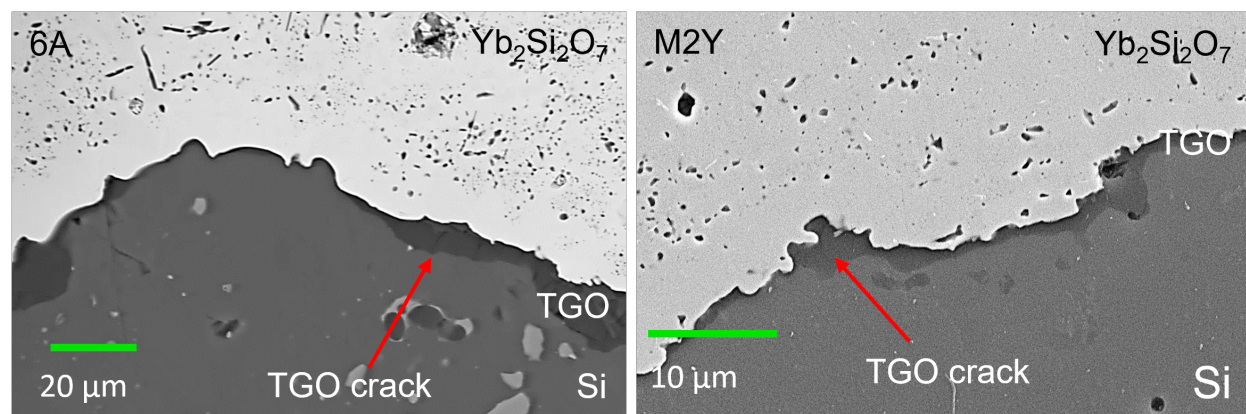


Figure 4.23: TGO in the 6A and M2Y systems after 1000 hours of steam cycling. Sharpness is enhanced to show very fine cracks.

Internal stress evolution in the 6A system is related to microstructure and chemistry, but not directly to TGO growth as in the baseline system (Fig. 4.25). In the 6A system, the change in topcoat stresses from 100 to 1000 hours of steam cycling is likely due to topcoat chemistry. As noted in Chapter 3, the minority phases such as $\text{Yb}_3\text{Al}_5\text{O}_{12}$ present in the 6A topcoats were observed by laboratory X-ray diffraction to disappear (within laboratory XRD

resolution) from 500 to 1000 hours of steam cycling. Although it was shown using WAXS that the Yb-based YAG phase was still present, the obvious change observed in laboratory XRD indicates chemical changes in the chemistry of the 6A topcoat over the steam cycling durations explored. The additional layer which appeared between the topcoat and bondcoat, most evident in the 100-hour and 500-hour steam-cycled conditions, also indicates chemical changes in the system. Migration of particles from the topcoat into the bondcoat of the 6A system, along with the additional interlayer and the observations from diffraction data, indicate temporary dopant effects in the system.

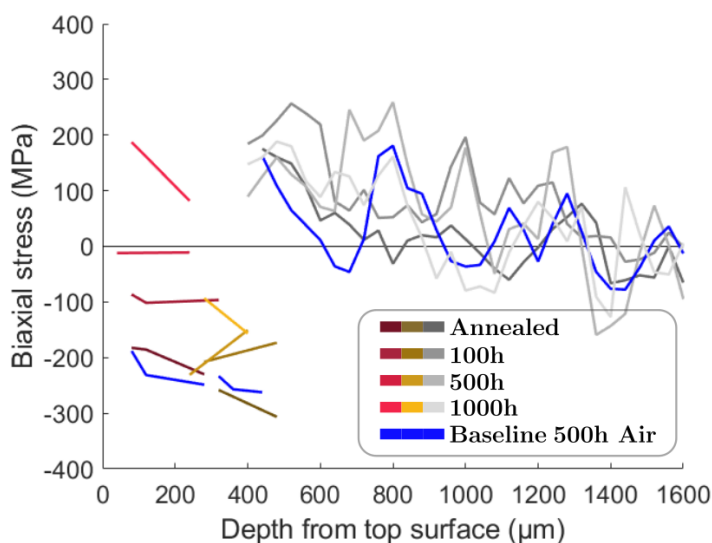


Figure 4.24: Baseline internal stresses at 500 hours, with a NASA Glenn 500-hour air-cycled sample added.

Temporary dopant effects have multiple implications for the 6A system. The additional layer developed between the topcoat and bondcoat could change internal stresses by relieving them through the formation of this layer, especially if the layer has low viscosity at steam-cycling temperatures, or by placing an additional layer of unknown mechanical properties in the system. The additional layer was not present in 6A after 1000 hours of steam cycling, which may indicate stabilization of topcoat chemistry with increasing exposure.

The dopant effects noted also likely influenced internal stresses by altering the lattice parameters over the steam cycling times studied, and therefore the relevant d_0 values for strain calculation. Since steam-cycled samples were relatively precious, d_0 measurements could not be taken for sample conditions other than as-sprayed and annealed, and so the effects of the chemical modifications are not quantified for steam-cycled conditions. Given the small oxide thicknesses in all alumina-modified samples, the stresses in the bondcoat and substrate, and

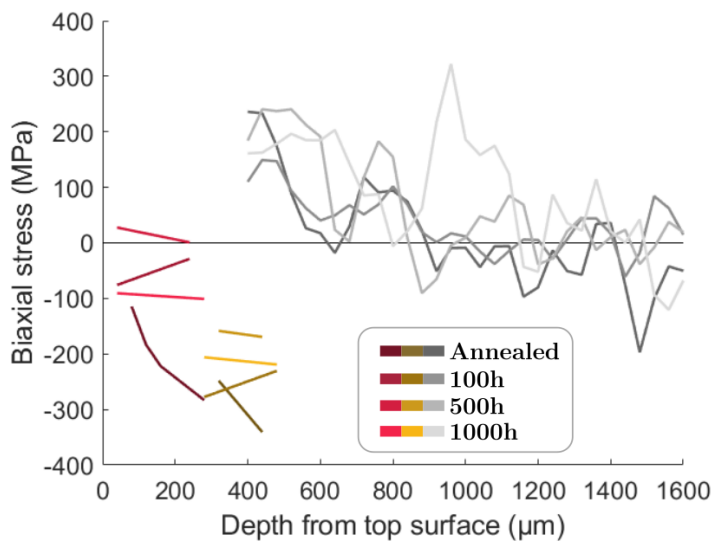


Figure 4.25: Internal biaxial stresses for the 6A system, annealed and steam-cycled at NASA Glenn.

the disappearance of the additional layer between the topcoat and bondcoat, it is likely that the coating stresses measured in 6A are at least somewhat compressive after extensive steam cycling as measured (Fig. 4.25) and predicted in the analytical model (Fig. 4.2).

INTERFACE TOUGHNESS ASSESSMENTS IN YTTERBIUM DISILICATE-BASED EBC/CMC MULTILAYER SYSTEMS

As mentioned in Chapter 2, spallation of the topcoat in multilayer EBC/CMC systems can occur by various mechanisms and lead to failure of the system. Therefore, in this study it is important to consider the likelihood that the coating layer will become detached from the substrate, particularly at the interface between the topcoat and the bondcoat or, with progressive oxidation, the topcoat and the oxide. This is accomplished by measurement of the interface toughness and assessment of the toughness of the interface as compared to the toughnesses of the layers on either side of it. Questions about the interface toughness involve the role of the oxide, and whether the toughness depends on the oxide thickness or simply the presence of the oxide as it replaces silicon at the interface. Additionally, the role of the plasma-spray process and thermal history on cracking behavior in these materials is assessed, since the crystallinity of the materials as well as interface bonding and internal stresses are all likely to have an effect.

5.1 Fracture toughness evaluation of multilayer coatings

5.1.1 Cracking toward interfaces in bimaterial systems

He and Hutchinson analyzed the effects of elastic mismatch and crack impingement angle on crack propagation at interfaces in biomaterials¹¹⁸. That work focused on the likelihood that a crack propagating from one material will deflect along an interface or penetrate through into the neighboring material. For the analysis to be valid, the length a of the continuing crack (after impingement) must be short relative to the length l of the crack prior to impingement. The elastic mismatch between the materials is described by Dundurs' parameter α :

$$\alpha = \frac{\mu_1(1 - \nu_2) - \mu_2(1 - \nu_1)}{\mu_1(1 - \nu_2) + \mu_2(1 - \nu_1)} \quad (5.1)$$

where μ is the shear modulus and ν is Poisson's ratio, each for material 1 or 2, as shown in Fig. 5.1. The parameter α is also commonly expressed as $\alpha = (\bar{E}_1 - \bar{E}_2)/(\bar{E}_1 + \bar{E}_2)$, where \bar{E} is the plane strain modulus $\bar{E} = E/(1 - \nu^2)$.

Through comparison of the relevant energy release rates of the materials and the interface, a relationship was determined for predicting the deflection of a crack at an interface:

$$G_{IC}/G_C < G_d/G_p. \quad (5.2)$$

Here, G_{IC} is the toughness of the interface, G_C is the Mode I toughness of Material I (the material opposite the interface from the wedge-loaded crack origin), G_d is the energy release rate of the deflected crack, and G_p is the energy release rate of the penetrating crack. Part of the analysis by He and Hutchinson considered the impingement of the crack at the interface at an oblique angle ω , helping to generalize the understanding of the crack impingement behavior¹¹⁸.

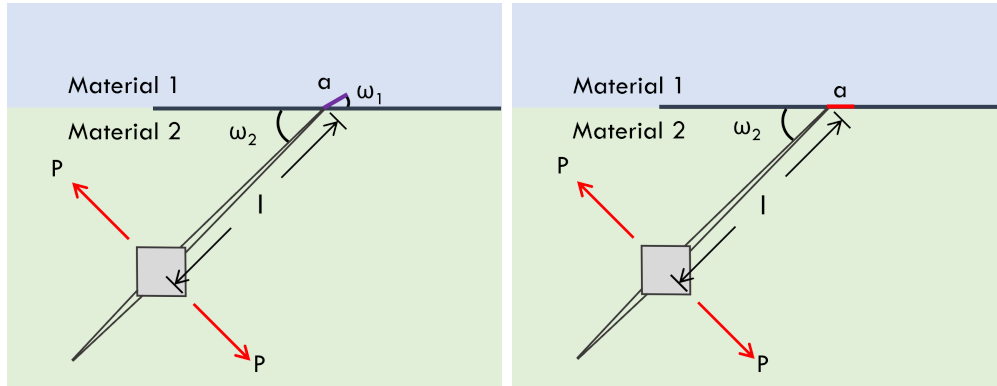


Figure 5.1: Schematics of a wedge-loaded crack impinging on an interface between materials. Except for the case of crack arrest, the crack will either penetrate into the neighboring material (left) or deflect along the interface (right). Adapted from Refs. [118] and [119].

For the wedge-loaded crack penetrating the interface, the stress intensity factor is:

$$K_I + iK_{II} = c(\alpha, \omega_1, \omega_2, \frac{a}{l}) \frac{P}{\sqrt{l}}. \quad (5.3)$$

Here, c is a complex-valued function of Dundurs' parameter α , ω_1 is the angle the deflected crack makes with the interface, ω_2 is the angle the impinging crack makes with the interface, and a is the deflected crack length, l is the impinging crack length, and P is the wedge load. Impinging crack length is measured as the distance from the wedge load to the interface. For the penetrating crack, the energy release rate is then:

$$G_p = \frac{(1 - \nu_1)}{2\mu_1} |c|^2 \frac{P^2}{l}. \quad (5.4)$$

For a given a/l ratio, the maximum of G_p with respect to ω_1 is G_p^{max} . The stress intensity of the deflected crack case is:

$$K_1 + iK_2 = d\left(\alpha, \omega_2, \frac{a}{l}\right) \frac{P}{\sqrt{l}}. \quad (5.5)$$

The complex-valued function d does not depend on ω_1 because that angle is zero. The energy release rate in the deflected-crack case is:

$$G_d = \left[\frac{(1 - \nu_1)}{\mu_1} + \frac{(1 - \nu_2)}{\mu_2} \right] (K_1^2 + K_2^2) / (4 \cosh^2 \pi \varepsilon) \quad (5.6)$$

where $K_1^2 + K_2^2 = |d|^2 P^2 / l$ and $\varepsilon = 0$. The ratio of the energy release rates is then:

$$G_d / G_p^{max} = \frac{|d|^2}{(1 - \alpha) |c|^2}. \quad (5.7)$$

This extension of the analysis also established an approach to alter the likelihood of deflecting a crack along the interface by controlling the crack approach angle. In Fig. 5.2 are a series of curves plotted as the ratio of G_d and G_p^{max} against the Dundurs' parameter α . The authors produced this plot for $a/l = 0.1$. The lower the energy release rate of a deflected crack relative to that of a penetrating crack, the higher the likelihood of the crack deflecting along the interface. For any value of α , it can also be seen that lower impingement angles increase the likelihood of crack deflection. Similarly, for any impingement angle it is seen that the likelihood of crack deflection increases with elastic mismatch between the materials, as described by the Dundurs parameter α .

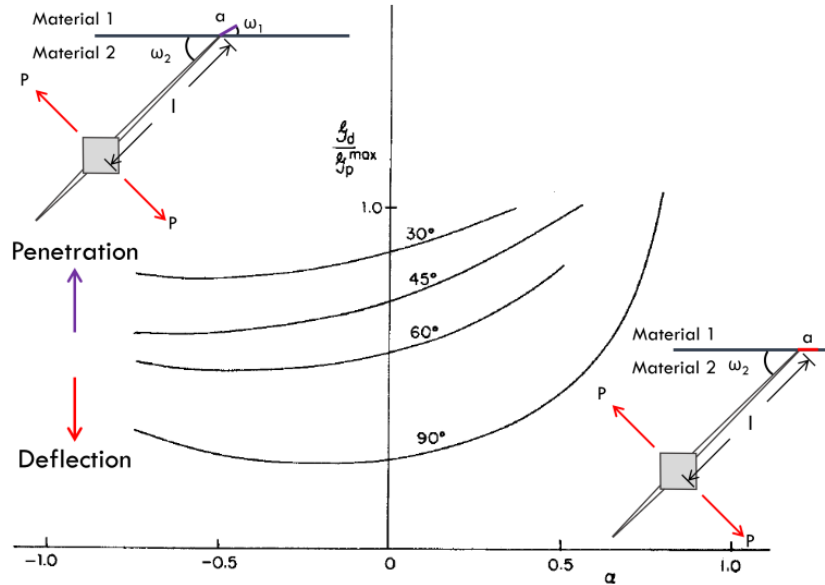


Figure 5.2: Boundary curves for deflection or penetration (indicated) in bimaterial cracking, as adapted from Ref. [118].

Bhattacharya et al. showed that a microindenter can successfully apply the wedge load described in the formalism of He et al.¹¹⁹. He, Evans, and Hutchinson then showed internal

stresses to have a large influence on the tendency of the crack to propagate in either layer of the bimaterial or to deflect along the interface¹²⁰. They showed that, as the internal stresses increase in magnitude, the role of these stresses can dominate over the ratio of energy release rates for the deflected crack and penetrating crack¹²⁰. Compressive, in-plane internal stresses can provide crack-closing forces which allow for stable crack growth or even prevent the growth of cracks in the out-of-plane direction, while tensile in-plane internal stresses can provide crack-opening forces and contribute to unstable crack growth. This result is relevant in the multilayer EBC/CMC systems studied here, as significant in-plane internal stresses were predicted and measured (Chapter 4). The assessment of interface toughness using the method of He et al. requires toughness values for each material in the bimaterial system, which can be measured by microindentation and nanoindentation using the appropriate adaptations.

5.1.2 Fracture toughness measurements with microindentation

Palmqvist established the important relationships governing the effects of fracture toughness on the observed indentation impression and cracking¹²¹. Later, Anstis et al. applied modern fracture mechanics to the relationship between indentation cracking and fracture toughness¹²². In that work, the cracks from a Vickers microindenter tip were assumed to take the half-penny shape beneath the surface of the material (Fig. 5.3)¹²².

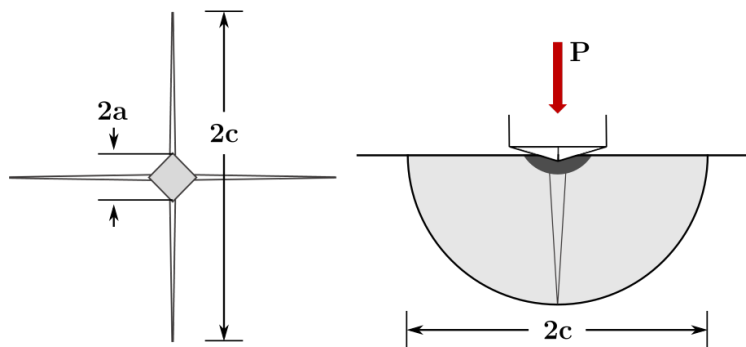


Figure 5.3: Schematic of a Vickers indentation and radial cracks (left), as well as the subsurface half-penny crack configuration (right). Adapted from Anstis et al.¹²².

When a Vickers tip is used to create cracks, one can measure the load P , the length a of the impression corners from the center, and the length c of the cracks from the center. The hardness H is related to the applied load, the deformed area, and a constant related to indenter geometry:

$$H = \frac{P}{\alpha_0 a^2}. \quad (5.8)$$

In this equation, α_0 is a numerical constant. When H is related to the mean contact pressure (which is load-invariant) and a is taken as the distance from the center to the corner of the impression, $\alpha_0 = 2^{122}$.

The development by Anstis et al. of fracture toughness from Vickers indentation considered the effect of "lateral" cracks, which spread outward from the indentation-deformed zone and may interact with the radial crack system¹²². In severely loaded systems the lateral cracks can curve upward and propagate sufficiently to reach the sample surface and cause chipping. Since chipping ruins the impression for both elastic-plastic and fracture analyses, indentation cracking experiments use loads below the chipping threshold for the material¹²².

The elastic-plastic field of the sharp Vickers indenter contributes elastic (reversible) and plastic (residual, or irreversible) components to the driving force for indentation cracking¹²². At the indentation surface, the elastic component was determined to be compressive and the plastic component tensile¹²³. Importantly, Anstis et al. noted the elastic component provides a restraining force against crack growth which is removed with the indenter tip, meaning that the radial cracks grow to their final lengths as the tip is removed (neglecting environmental effects)¹²². Thus, the plastic or residual field component is mostly responsible for the final penny-like crack configuration. The driving force for cracking can be expressed through the residual stress intensity factor

$$K_r = \frac{\chi_r}{Pc^{3/2}} \quad (5.9)$$

where χ_r is a constant, which depends on the square root of the ratio of the Young's modulus to hardness:

$$\chi_r = \xi_V^R \left(\frac{E}{H} \right)^{1/2}. \quad (5.10)$$

Here, ξ_V^R is a constant for radial cracks produced by Vickers indentation, and is material-independent. Since ξ_V^R goes as $\left(\frac{E}{H} \right)^{1/2}$, it is evident that ceramics of higher modulus relative to hardness (or "softer" ceramics) develop higher crack driving forces under like conditions¹²².

When the crack system reaches equilibrium, $c = c_0$ and $K_r = K_C^{122}$. On substitution:

$$K_C = \xi_V^R \left(\frac{E}{H} \right)^{1/2} \left(\frac{P}{c_0^{3/2}} \right). \quad (5.11)$$

Anstis et al. rearranged this expression to solve for ξ_V^R and, using known toughness values for "well-behaved" ceramic materials, calibrated $\xi_V^R = 0.016 \pm 0.004^{122}$.

Anstis et al. cautioned that above analysis of indentation cracking and the crack driving force assumes that the cracks behave in a "regular" manner throughout the process, including

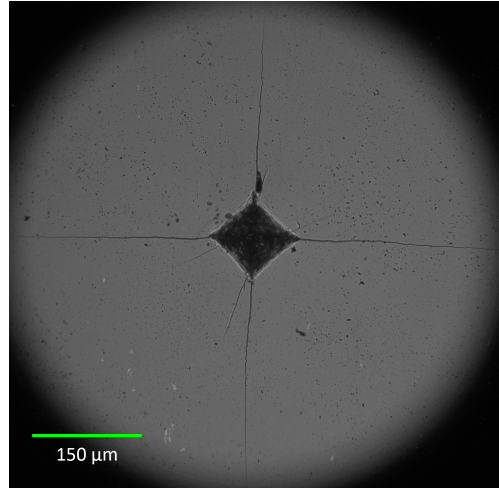


Figure 5.4: Vickers indentation in SiC using 196N load. Toughness measured from crack lengths was approximately $2.4\text{MPa}\sqrt{\text{m}}$.

deformation at constant volume under indentation and cracking¹²². Materials with low H/E ("soft") and those with open network structures (such as anomalous silicate glasses and porous solids) frequently pile-up around the indentation pattern or densify under the indentation, respectively. Both pile-up and densification are energy-dissipative processes, confounding the analysis of stress intensity and cracking behavior.

Lastly, material microstructure will greatly influence the results of microindentation cracking tests¹²². In dense materials, small grains and highly polycrystalline arrangement mean that indentation probes bulk polycrystalline effects, including the influence of grain boundaries, etc. Conversely, indentation probes monocrystalline properties when the grains are larger than the indentation and/or indentation-produced cracks¹²². When pores and bi-material interfaces are present such microstructural features are likely to affect the mechanical responses of the materials to microindentation loading, such that indentations at smaller scales are necessary.

5.1.3 Elastic-plastic measurements by microindentation

Hardness and Young's modulus measurements, or at least knowledge of these properties, are crucial for assessing fracture toughness in materials using indentation methods. Indentation hardness is the ability of a material to withstand plastic deformation in the area under the indenter, and is more specifically defined as the force required to produce a plastically deformed area. Indentation methods have been used historically to measure hardness of many materials. Experimentally, both the load force and the deformed area are measured to determine hardness.

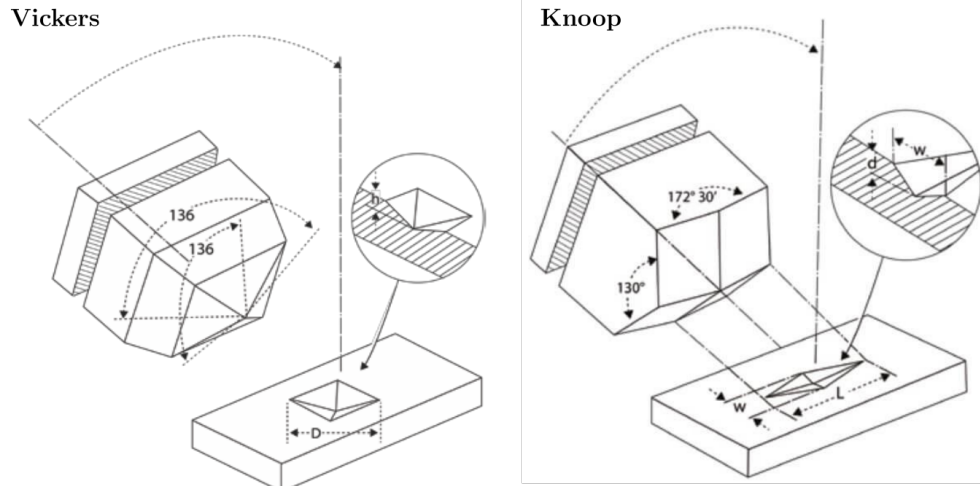


Figure 5.5: Schematics of a Vickers and Knoop indenter tips and well-formed impressions. Adapted from Ref. [124] and with publisher permission from Ref. [125].

Methods have also been developed to measure the elastic modulus of a material with indentation. That value was not readily available for bulk plasma-sprayed $\text{Yb}_2\text{Si}_2\text{O}_7$ with the processing and microstructure of the samples in this study. Vicker's indenter tips could be used to measure hardness and modulus, but the experimental conditions require that no cracking take place. Under those conditions electron microscopy must be used to ensure the absence of cracking and to measure the small indentations produced at low loads.

The work of Marshall et al. showed that a Knoop microindenter tip, which is diamond-shaped with one diagonal much longer than the other, can be used to assess the ratio of hardness to modulus even if cracking is present¹²⁶. In that work, Marshall et al. suggested that the length of the shorter diagonal contracts due to elastic effects upon unloading, whereas the length of the longer diagonal is mostly or entirely unaffected¹²⁶. The ratio of the long diagonal length to the short diagonal length, a/b , is 7.11 for a Knoop tip. The diagonals left by the indentation, a' (long; L in Fig. 5.5) and b' (short; w in Fig. 5.5), and the ratio b'/a' , indicates the hardness to modulus ratio H/E :

$$b'/a' \approx b'/a = b/a - \alpha H/E. \quad (5.12)$$

In data-fitting for several brittle materials, Marshall et al. showed that $\alpha = 0.45$ ¹²⁶. These experimental tools for measuring elastic-plastic behavior by microindentation can be used to collect the relevant information to assess fracture toughness using microindentation.

5.1.4 Toughness measurements with nanoindentation

When used for exploring elastic-plastic behavior, nanoindentation experiments frequently use either flat-tipped ("flat-punch"), spherical, or shallow pyramidal indenter tips. The pyramidal Berkovich tip comes to a somewhat shallow point which is not prone to generating significant cracking. A cube-corner tip, by contrast, comes to a point at a more severe angle which is more suited to creating significant cracks in brittle materials, as shown in literature studies^{127,128}. The angles of these tips, presented as the angle between a face and the center axis of the tip, are 65.3° and 35.3° for the Berkovich and Cube-Corner, respectively.

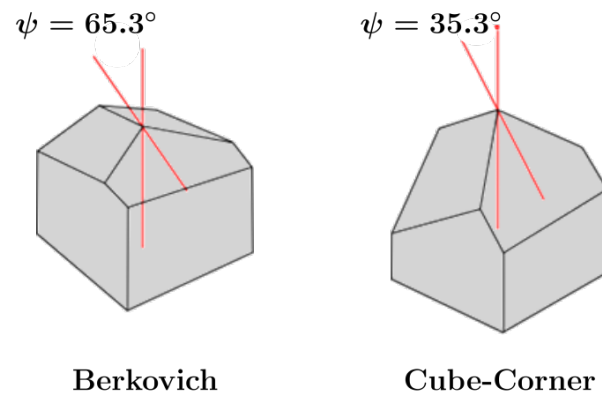


Figure 5.6: Schematics of ideal Berkovich and Cube-Corner indenter tips. The more severe angle of the cube-corner tip is much more conducive to indentation cracking. Adapted from Ref. [129].

Nanoindentation, using a cube-corner tip, and the interpretive framework for assessing toughness using the observables described in microindentation allows for measurement of fracture toughness of a wide range of materials, including those comprising multilayer systems.

The analytical framework of Anstis et al. was adapted for nanoindentation by Harding, Oliver, and Pharr¹³⁰. That work verified the same dependence of the critical stress intensity factor on modulus, hardness, load, and crack length as described in Eq. 5.11, but replacing ξ_R^V with the coefficient α . Efforts to define this coefficient have yet to settle whether the tip geometry, elastic-plastic properties of the sample, some combination of these, or still other properties have the most influence over its value¹³¹⁻¹³³. Curve-fitting to toughnesses of real materials and geometry-based, maximum values have also been used to estimate functions for the coefficient^{127,128}. The work of Lee et al.¹³¹ considered the coefficient by Anstis et al.¹²², as well as the indentation strain, and calculated $\alpha = 0.015 - 0.018$ for a Berkovich tip indenting materials of Poisson's ratio $\nu = 0.3$. This value agreed well with the coefficient value, 0.016 ± 0.004 , obtained by Anstis et al. Lee et al. further demonstrated an increase

in α with decreasing Poisson's ratio values, from 0.3 to 0. Additionally, α was shown to increase with indenter "sharpness," as represented by the angle, ψ , where a smaller angle describes a sharper indenter tip. (Note that sharpness in this context does not refer to the condition of the indenter head, which can blunt with extensive experimental use.) Another expression was given for the coefficient based solely on the geometry of the tip¹³¹:

$$\alpha^{LEM} = 0.03 \cot(\psi)^{2/3}. \quad (5.13)$$

The term α^{LEM} represents the coefficient from the Lawn-Evans-Marshall formulation, which was adapted in the work of Lee et al. and shown to serve effectively as an asymptotic upper bound for the values of α , in the absence of elastic-plastic material effects¹³¹. For a cube-corner tip $\psi = 35^\circ$, which gives a value $\alpha = 0.038$ ^{131,133}.

Laugier put forth an alternative relationship for indentation toughness, assuming the creation of Palmqvist-type cracks in indentation cracking experiments, which is presented here for comparison¹³⁴:

$$K_{IC} = k^p \left(\frac{a}{c-a} \right)^{\frac{1}{2}} \left(\frac{E}{H} \right)^{\frac{2}{3}} \frac{P}{c^{3/2}}. \quad (5.14)$$

The empirical constant, k^p , adapted by Laugier¹³⁴ from the half-penny crack configuration to the Palmqvist configuration, was then translated by Cuadrado et al. for the cube-corner tip and found to be $k^p = 0.057 \pm 0.002$ ¹³⁵. In that work, Cuadrado et al. also showed that materials of low toughness tend to develop quarter-penny cracks under cube-corner nanoindentation¹³⁵. Lee et al. also discussed the development of crack configurations, noting that for c/a (crack length to indent size) ratios of 2-2.5 the penny-like cracks should fully form¹³¹.

5.1.5 Elastic-plastic measurements by nanoindentation

Nanoindenters require instrumentation to measure both load and displacement through each loading experiment. The collection of load and displacement affords a measure of both hardness and stiffness. This has been explored extensively in the literature, perhaps most definitively by Oliver and Pharr¹³⁶, most often with a Berkovich nanoindenter tip (Fig 5.6), a three-sided pyramidal diamond indenter which produces an impression like that seen in Fig. 5.7.

From Oliver and Pharr, elastic modulus in nanoindentation can be computed using initial unloading stiffness¹³⁶. The reduced modulus is:

$$E_r = \frac{\sqrt{\pi}}{2} \frac{S}{\sqrt{A}} \quad (5.15)$$

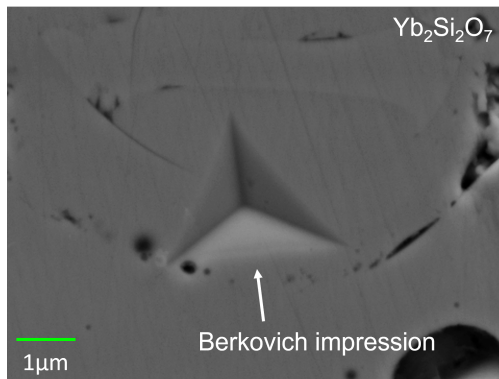


Figure 5.7: A Berkovich indenter impression made in $\text{Yb}_2\text{Si}_2\text{O}_7$.

where area A is determined using an area function specific to each nanoindenter tip and S is the maximum stiffness at unloading. The reduced modulus accounts for the modulus of both the sample and the indenter, in the case of non-rigid indenters, by relating

$$\frac{1}{E_r} = \frac{(1 - \nu^2)}{E} + \frac{(1 - \nu_i^2)}{E_i}. \quad (5.16)$$

E and ν are the Young's modulus and Poisson's ratio (respectively) for the sample, and E_i and ν_i are the Young's modulus and Poisson's ratio for the indenter.

5.1.6 Single-edge notched beam (SENB) toughness

Four-point bend tests have been used to measure the fracture toughness of a material on the macro-scale, and have additionally been implemented to test interface toughness in layered materials^{137,138}. As seen in Fig. 5.8, a beam of known dimensions is mounted in a four-point bending fixture, with a notch oriented on the tensile-stressed side of the beam.

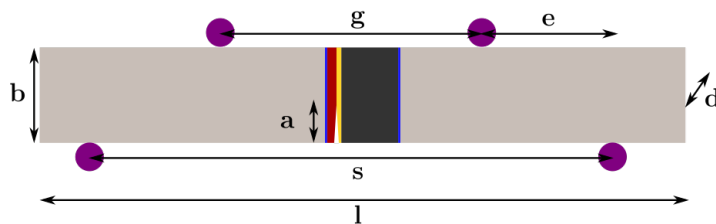


Figure 5.8: Geometry of the Single Edge Notched Beam (SENB) four-point bend test, with relevant features and dimensions labeled. The multi-color notch indicates a bi-material interface toughness test.

In this setup, g is the distance of the inner span, s is the distance of the outer span, l is the sample length, b is the sample height, d is the sample "depth" (into the plane of the page),

and a is the length of the precrack notch. For this test, geometric constraints are placed on the dimensions of the sample beams to ensure the validity of the result:

$$\frac{g}{b} > 2 \quad \frac{s}{b} \geq 2 \quad l \geq 4.2b \quad 2 \leq \frac{b}{d} \leq 8 \quad 0 < \frac{a}{b} < 0.6.$$

With the failure load measured for a sample, the stress intensity factor can be calculated:

$$K_I = \frac{3Pe\sqrt{a}}{db^2} \left[1.99 - 2.47 \left(\frac{a}{b} \right) + 12.97 \left(\frac{a}{b} \right)^2 - 23.17 \left(\frac{a}{b} \right)^3 + 24.80 \left(\frac{a}{b} \right)^4 \right]. \quad (5.17)$$

Use of this relationship allows for a direct assessment of fracture toughness using the setup described.

5.2 Methods

5.2.1 Sample preparation and imaging

Samples used in studies of indentation and fracture toughness experiments were taken from the same multilayer samples used in microstructure and internal stress studies, which were received at Caltech from Kang Lee at NASA Glenn Research Center. As discussed previously, samples were sectioned into a size usable in microstructure/oxidation, synchrotron, and mechanical properties studies. Since the goal was to characterize interface toughness as it evolves with steam cycling and TGO growth, and the strongest dependence of TGO growth on steam cycling was observed in the baseline system, baseline samples were used for interface toughness analysis.

To summarize, samples of approximately 6-7mm width, 1.5-2mm depth, and 3.5-4mm height (combined layer thicknesses) were sectioned from the samples received from NASA Glenn using a Buehler IsoMet 5000 saw and a diamond-impregnated blade (Buehler IsoMet Diamond Wafering Blade). For indentation testing, samples were then cast in acrylic and ground and polished down to a 1 μ m diamond suspension. An annealed sample was also prepared by heating an as-sprayed sample to 1300°C for 20 hours in air in a box furnace, with ramp rates of 5°C per minute to the maximum temperature. Air exposure at high temperature did produce a thin oxide on the bondcoat, but the long soak was used to ensure full crystallization of the topcoat. This sample was then cast in acrylic, then ground and polished down to a 1 μ m diamond suspension.

Optical microscopy was used to find (micro- and nano-) indentation sites and for preliminary assessments post-indentation. Measurements of indentation areas and cracks were taken using SEM. When samples were finished with indentation experiments, they were carbon-coated and imaged as described in Chapter 2. Samples which needed to be analyzed

by SEM and then continue with indentation experiments, imaging was carried out with low accelerating voltages (5 or 10kV) and small apertures to minimize surface charging by electrons.

For single-edge notched-beam (SENB) tests, multilayer samples were sectioned and sandwiched between two long, rectangular beams of aluminum nitride. JB Weld steel-reinforced epoxy was used to adhere the aluminum nitride bars to the top and bottom surfaces of the multilayer EBC/Hexoloy samples. These samples were sectioned into beams satisfying the dimensional requirements for the test. A notch was created at the interface of the topcoat and the neighboring layer using diamond paste and a thread to abrade material from the interface region.

5.2.2 Interface cracking

The Dundurs parameter α for the bimaterial formed of $\text{Yb}_2\text{Si}_2\text{O}_7$ and silicon is $\pm \sim 0.1$, depending on the material into which the indentation is applied, and so it was unlikely that there would be significantly different cracking behavior based on which side of the interface is used to propagate the indentation crack. Still, indentations were used for cracking in both the Si layer (propagating toward $\text{Yb}_2\text{Si}_2\text{O}_7$) and the $\text{Yb}_2\text{Si}_2\text{O}_7$ layer (propagating toward Si). Given the small thickness of the TGO relative to the size of the indenter impressions, indentations were applied in the $\text{Yb}_2\text{Si}_2\text{O}_7$ topcoat to propagate cracks toward the TGO (discussed further below). The Dundurs parameter for the bimaterial system formed by the $\text{Yb}_2\text{Si}_2\text{O}_7$ topcoat interfacing the TGO is approximately -0.5.

The Dundurs' parameters α for each bimaterial arrangement are indicated by red bars in Fig. 5.9. The largest "elastic mismatch," described through this parameter, is between $\text{Yb}_2\text{Si}_2\text{O}_7$ and α -cristobalite; $\text{Yb}_2\text{Si}_2\text{O}_7$ and silicon are fairly well matched in this regard. The plot serves as a map which shows boundary curves separating the conditions favoring deflection (below each curve) and penetration (above each curve). With more oblique impingement angle, the chances of deflection increase; a 90° (or normal) impingement angle at the interface maximizes the likelihood of penetration.

Fracture toughness values measured experimentally in this work are expressed as critical stress intensities. For plane-strain conditions, the energy release rate can be calculated from the critical stress intensity:

$$G_C = \frac{K_{IC}^2(1 - \nu^2)}{E} \quad (5.18)$$

where the energy release rate is G_C and the stress intensity factor (reported above) is K_{IC} .

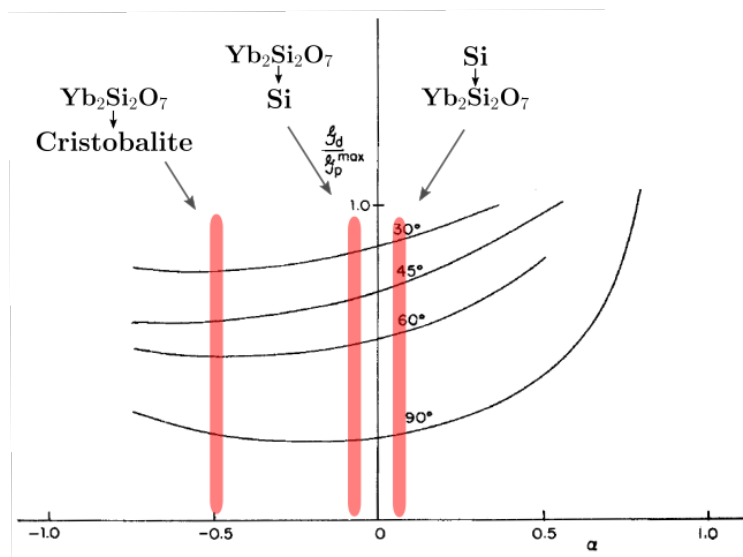


Figure 5.9: Ratio of energy release rates for deflected and penetrating cracks. The Dundurs' parameters for the materials in this work are indicated.

5.2.3 Microindentation

Drawing on the early work of He et al.¹¹⁸ and the validating study of Bhattacharya et al.¹¹⁹, microindentation was used in the present work to determine if the size scale of the indentation and cracking produced were suitable for the EBC system at hand. Indentations were made with loads of 4.9N and 9.8N to generate sufficient cracking to reach the interface from the indentation in the topcoat. However, issues with the microindentations interacting with EBC microstructure, as well as with the size of microindentation impressions, necessitated a different method for testing at smaller size scales. The results from microindentation testing are discussed more specifically below.

5.2.4 Nanoindentation

Several features of the EBC/CMC samples complicated the use of microindentation for toughness of layers and interfaces. Pores in the coatings could collapse upon microindentation loading, obfuscating the results of those tests. The roughness of the interfaces in the plasma-sprayed samples was also non-negligible compared to the microindentation size. Finally, the low number of samples, and the large microindentation patterns produced, created a scarcity in samples to be addressed for any large number of measurements. Thus, nanoindentation was utilized to effectively address microstructural concerns. The smaller nanoindentation tip and the much-smaller nanoindentation impression (both compared to microindentation) addressed the limitations of microindentation in the interface toughness assessments. The use of nanoindentation in the interface cracking method described is a departure from the

work of Bhattacharya et al. and other methods following the work of He and Hutchinson. To the author's knowledge, this is the first time that nanoindentation has been applied to assess interfaces EBC systems in the way of He et al.¹¹⁸ and Bhattacharya et al.¹¹⁹.

A cube-corner tip was necessary to create cracks and assess toughness in this work. A cube-corner tip was located at the University of California, Irvine, and was made accessible for these experiments. Toughness measurements in the topcoat and bondcoat layers used load-controlled methods. It was found that loads of 24.5mN generally produced adequate cracking in the materials, with smaller loads causing errors in the experiment software and larger loads (49mN and higher) tending to produce chipping. This load value was also chosen for consistency, because larger load values which could still produce valid toughness measurements in $\text{Yb}_2\text{Si}_2\text{O}_7$ were generally too destructive (e.g., caused excessive chipping) in silicon.

Additionally, the ambiguity around the precise value of the coefficient α in nanoindentation toughness measurements was simplified for this work. Since there is not a set method for determining α for a given material-and-tip combination, the value $\alpha = 0.038$ was used. This represents the coefficient as related to the cube-corner tip geometry, and ignores materials properties (which are the points of ambiguity in other analyses). Toughness values calculated with $\alpha = 0.038$ serve as upper bounds for the materials measured. For elastic-plastic measurements, the maximum load point and the next two points on unloading were used to compute the unloading stiffness, S , as the slope of the curve through these points. Hardness was computed as the maximum load divided by the contact area, with the second term assessed using the area function for the Berkovich tip used.

5.2.5 Single-edge notched beam (SENB) testing

An as-sprayed, baseline sample consisting of a $\text{Yb}_2\text{Si}_2\text{O}_7$ topcoat and Si bondcoat adhered to a Hexoloy SiC substrate was annealed at 1300°C in flowing argon using the custom furnace described in Chapter 6. This sample was then prepared for single-edge notched beam (SENB) testing by attaching a bar of aluminum nitride to the top of the topcoat and the bottom of the substrate using a strong epoxy (JB Weld). A bend beam satisfying the dimensional criteria for the SENB test was machined from the sample using a Buehler IsoMet 5000 and diamond-embedded saw blade. A notch was cut into the topcoat/bondcoat interface in two steps. First, a diamond scribe was used to create a shallow groove at the interface to guide a sharper implement for cutting. Then, the corner of a steel razor blade was used to make a sharper and deeper notch at the interface. The sample cross-section dimensions (as in Fig. 5.8) were $b = 6.75\text{mm}$ and $d = 3.18\text{mm}$; the notch length a was $180\mu\text{m}$. The sample was

then broken using the four-point bend test setup on a mechanical testing instrument (Instron 5900-series MTS). Outer and inner spans for the applied load (s and g , respectively) were set to 40mm and 20mm. Interface toughness was tested by placing the interface and notch parallel to the loading direction, as shown in Fig. 5.8.

5.3 Results and discussion

5.3.1 Microindentation cracking and toughness

Microindentation cracking tests were performed first to investigate the usefulness of the technique for assessing interface toughness. As seen in Fig. 5.10, loads of 4.9N and 9.8N were sufficient to produce cracking in the as-sprayed $\text{Yb}_2\text{Si}_2\text{O}_7$ topcoat. In the case of the 4.9N load (right-hand side indentation of Fig. 5.10), a long crack extends from the bottom of the four-point impression toward the interface with the bondcoat. Upon reaching the interface, the crack deflects along the interface rather than penetrate the bondcoat.

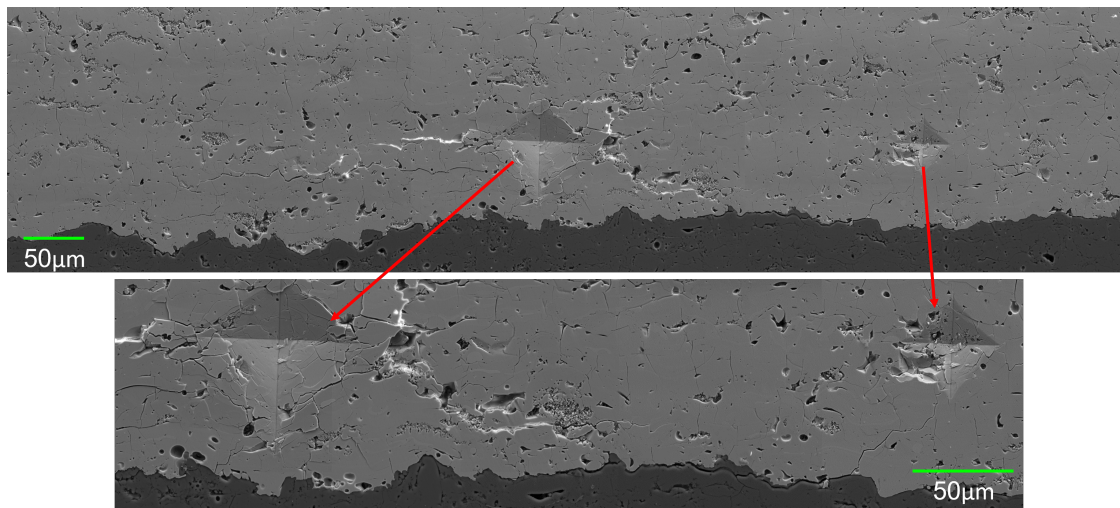


Figure 5.10: Results from microindentation cracking tests, showing extensive cracking and evidence of compaction in the $\text{Yb}_2\text{Si}_2\text{O}_7$ topcoat. Magnified images (lower) show crack deflection along the topcoat-bondcoat interface. Loads used were 9.8N (left) and 4.9N (right).

The 9.8N load, produced more extensive cracking than the 4.9N load. It is desirable to produce cracks of sufficient length to reach the interface from a distance, so the elastic-plastic zone from the impression does not influence the interface. However, the length of the cracks from the other impression corners occupy valuable sample space and further increase the distance required between neighboring impressions. Additionally, the visual evidence of topcoat compaction beneath the indenter tip, seen as a series of small cracks around the impression, indicates that the cracking observed is not the only method of energy dissipation in the experiment. For example, pore collapse and/or chipping (in the amorphous content

of the as-sprayed EBC) is seen in the right-hand impression (4.9N). Indentation toughness measurements should probe the material and not the combined material and microstructure, to the extent that this is possible. Toughness measurements with the responses shown from microindentation are inaccurate, and so the layer toughnesses could not be assessed using microindentation for interface toughness comparison.

Lastly, the impression from the 4.9N load was nearly $50\mu\text{m}$ across the diagonal of the indentation. Given the limited layer thicknesses, the even more limited amount of interface available for testing, and particularly the small number of steam-cycled samples available, such impressions would exhaust the usable sample space rapidly.

Based upon results in Chapter 4, it is likely that the EBC/CMC samples of any post-anneal condition would behave differently than the as-sprayed samples, with respect to cracking and interface behavior. However, the sizes of the impressions from Vickers microindentation seen in Fig. 5.10 still preclude further work with microindentation in the EBCs in this work. Since the elastic/plastic properties and fracture toughness of each layer were needed for interface toughness assessment, it was necessary to use nanoindentation to probe these properties on a smaller size scale to avoid microstructural complications and be economical with sample testing.

5.3.2 Nanoindentation cracking and toughness

Fig. 5.11 is representative of the nanoindentation tests propagating cracks into the topcoat-bondcoat interface of the as-sprayed condition. In all instances, and with the cracks propagated from topcoat to bondcoat and bondcoat to topcoat, the cracks deflected along the interface. This was true for all angles of crack impingement, as well, indicating that even favorable geometries (crack impingement normal to the interface) were insufficient to promote crack penetration. The implications for interface toughness are discussed below.

In the annealed condition, crack deflection and penetration both are observed. In contrast to the as-sprayed condition, however, penetration is achieved in the annealed sample mostly in cases where the indenter tip was placed very close (within $\sim 2\mu\text{m}$) to the interface. Since the size of the plastic field around an indentation is larger than the indentation itself, it is problematic to have the indenter so close to the interface when analyzing toughness, either directly or comparatively as in the case of the interface cracking method. Additionally, crack penetration is observed in cases where two or more cracks intersect at or near the interface, or in cases where there is excessive chipping around the indentation close to the interface.

In the 100-hour and 500-hour steam-cycled conditions, there is TGO of significant thickness between the topcoat and bondcoat which is not present in the as-sprayed condition. In both

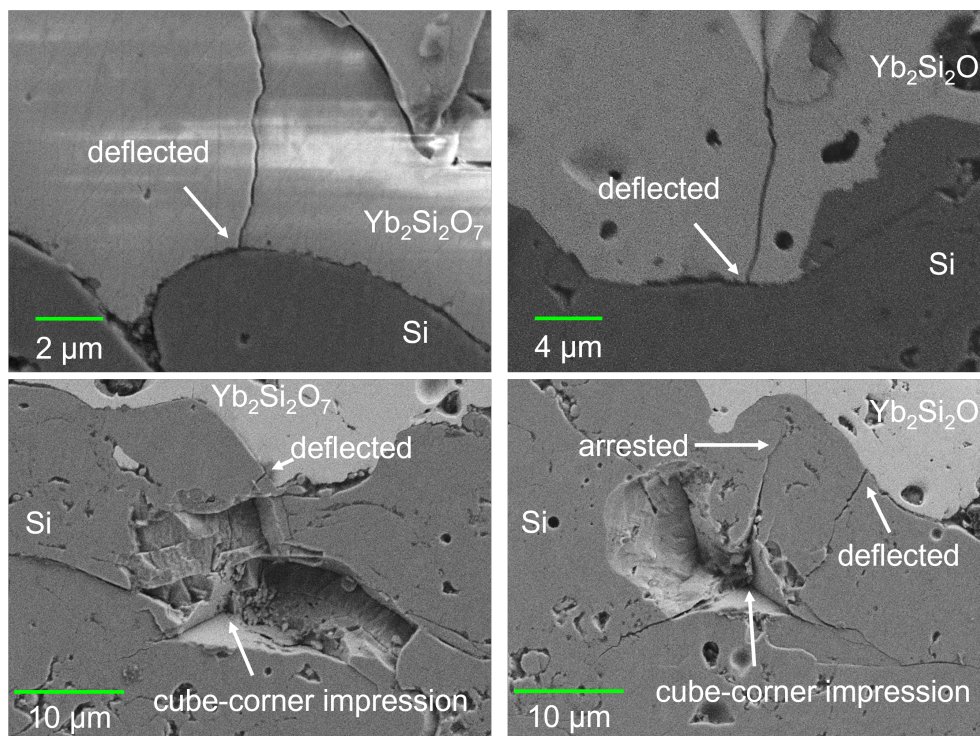


Figure 5.11: Cracks propagated to the topcoat-bondcoat interface from both sides in an as-sprayed baseline sample. Uncoated samples resulted in some surface charging.

100-hour and 500-hour steam-cycled samples there is also an evident preference for crack deflection, as the cracks again deflected along the interface, this time between the topcoat and the TGO (Fig. 5.13). In some cases, cracks did propagate into or through the oxide layer. However, these events followed a short deflection along the interface prior to penetration. Despite eventual penetration, such events are still classified as crack deflection^{119,122}.

Similar interface cracking behavior to that of the 100-hour and 500-hour steam-cycled samples was observed in the 1000-hour sample (Fig. 5.13). In all cases of propagating a crack to the interface between the topcoat and the TGO, the crack deflected along the interface rather than penetrate into the neighboring layer. As in the other steam-cycled samples, the toughness of the topcoat-TGO interface was low enough that crack deflection was preferred. Additionally, the TGO layers of the 1000-hour steam-cycled samples were heavily cracked in many areas and, in some places, at the interfaces of the oxide with its neighboring layers.

With the interface cracking observed, toughness measurements within the layers on either side of the interfaces were necessary to analyze interface toughness. Amorphous content and quenching stresses in the layers in the as-sprayed samples prevent accurate assessment of material toughnesses for this condition. The topcoats are prone to extensive chipping under

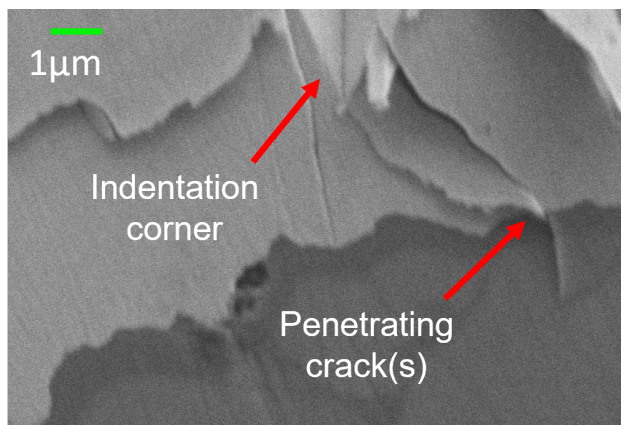


Figure 5.12: Cracks impinging at the interface of the annealed sample. Crack penetration always accompanied very close indenter tip placements, multiple cracks interacting, or extensive chipping.

a $\sim 25\text{mN}$ load using a cube-corner tip. While a small number of impressions produced cracks usable for toughness measurement, a large proportion of the impression sites were too damaged for reliable crack measurements (seen in the bondcoat, Fig 5.11). At lower loads the instrumentation would experience software errors and the measurement would fail.

For the annealed condition, the interface cracking behavior observed complicated analysis of the crack-interface interactions sufficiently that the interface cracking model no longer applied for the results obtained. For this reason, indentation toughness measurements were not made within each layer of the annealed sample. Additional annealed samples were then prepared for the single edge notch beam test described previously.

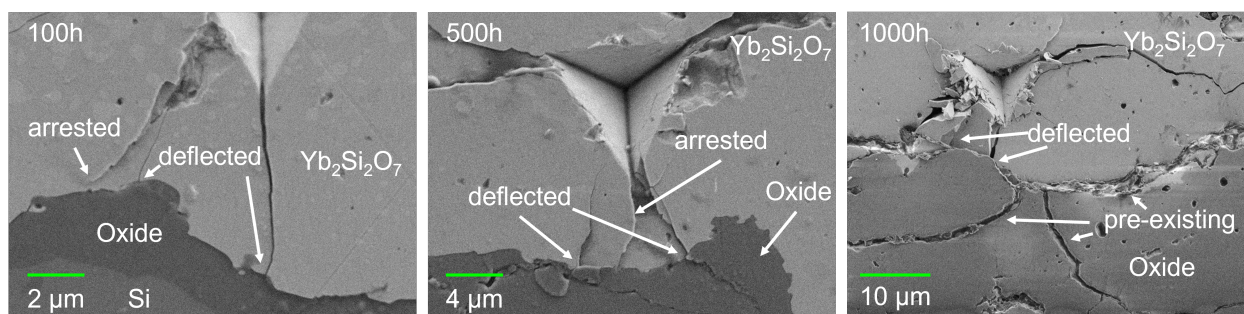


Figure 5.13: Cracks propagated to the topcoat-bondcoat interface after 100-hour, 500-hour, and 1000-hour steam cycling intervals.

After steam cycling, both the topcoat and the bondcoat show different nanoindentation cracking behavior than in the as-sprayed condition. While cracking and chipping occur at some indentation sites in these layers, they are much less prevalent than in the as-sprayed

samples. However, due to the size of the nanoindentation impression ($5\text{-}10\mu\text{m}$) in the TGO, the 1000-hour steam-cycled condition is the only sample with sufficient TGO thickness for toughness measurement in that layer. Indentation cracking in these materials demonstrates $c/a > 2$ for the materials studied (Fig. 5.14), and so the penny-like subsurface crack configuration is assumed and used for toughness analysis (thus, the toughness equation of Laugier et al. is not used). Toughness values in the coatings of the 1000-hour steam-cycled sample, as well as for the topcoat/TGO interface, are reported in Table 5.1).

Since all impingement angles in the present work result in crack deflection, the interpretation simplifies and the curve for 90° impingement is used to provide an upper bound on the interface toughness. The right-hand plot considers a crack impinging at an interface with a 90° angle and no wedge load applied. Note that the "singly deflected crack" curve is actually the same as the 90° curve re-plotted by He et al. on the left¹¹⁸. As seen for the Dundurs' parameters in this work, the ratio G_d/G_p for which deflection is always favored at a 90° impingement angle is approximately $1/4$ (the curve for the singly deflected crack does not deviate much through this range of Dundurs' parameter values).

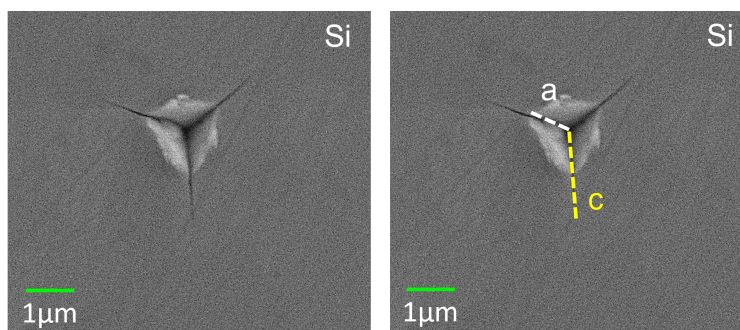


Figure 5.14: A Cube-Corner indentation in the silicon bondcoat of the Baseline, 1000-hour steam-cycled sample. Indentation and crack measurements are shown on the right.

The toughness of the cristobalite TGO, expressed as energy release rate rather than critical stress intensity, is used to estimate the interface toughness value. The average measured value of K_{IC} of each material is used to compute G_C for those materials. Then the plot of He and Hutchinson is used to compute the maximum interface toughness, using the toughness of the α -cristobalite TGO, both in terms of energy release rate. The maximum interface toughness values are presented, with the actual values likely lower than the maximum by some amount.

The cracking behavior and toughness values in the as-sprayed condition are influenced by the plasma-spray process and the microstructure and thermal history it imposes on the samples. Prior to heat treatment, the as-sprayed topcoat layer possesses a large amount of amorphous

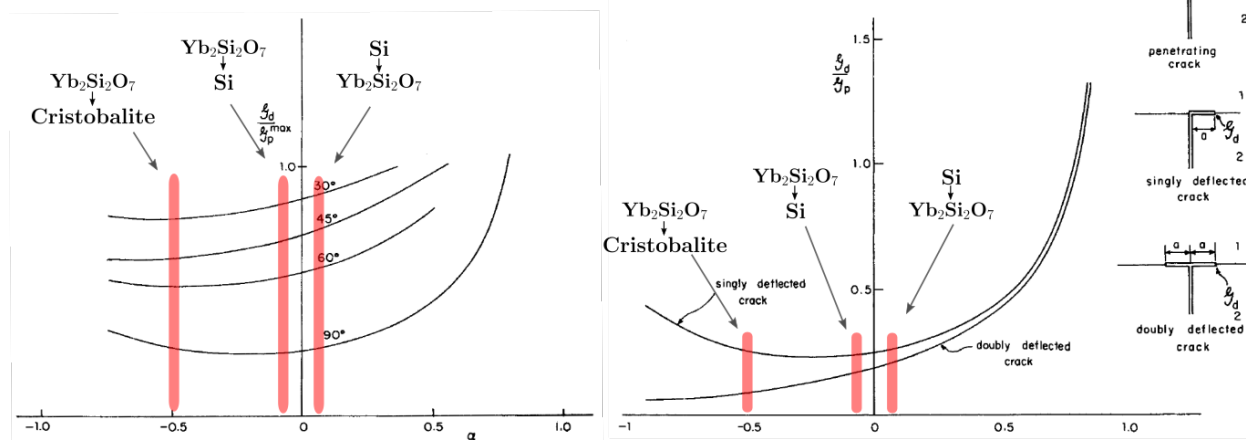


Figure 5.15: Two plots of the ratios of energy release rates for deflected and penetrating cracks, from He and Hutchinson¹¹⁸. The Dundurs' parameters for the EBC materials and TGO are indicated.

Yb₂Si₂O₇ content. The toughness of the amorphous material would likely be lower than the equivalent crystalline. As discussed in Chapter 4, the diffraction methods used to measure stresses cannot be applied to the amorphous material and so stresses in the amorphous material are unknown. In as-sprayed silicon, the thermal history is similarly unknown due to the complexity of the plasma-spray process. While there is no amorphous content measured in the as-sprayed silicon, the unknown thermal history and lack of annealing step means that there could be quenching stresses which contribute to the cracking and chipping behavior observed (example in Fig. 5.11).

After steam cycling, the difference in cracking between steam-cycled and as-sprayed topcoats is partly attributed to the crystallization of the disilicate, which is completely crystalline after all steam cycling durations studies. In both the topcoat and bondcoat, the quenching of annealing stresses also changes the cracking and toughness behaviors. The toughness values are affected strongly by the coefficient in Equation 5.11. The choice of 0.038 for this coefficient leads to slightly different toughness values than in the literature (Si is higher here, for example). The low toughness of the oxide in the 1000-hour steam-cycled condition could be due to several factors, including the (still) relatively small layer thickness, where indentations are necessarily placed near interfaces: in these experiments impressions of 5-10 μm size were made in oxides of approximately 14 μm thickness. Indentations should be far from interfaces and surfaces. Application of nanoindentation to the samples of this work pushes the limits of the method. However, the results taken quantities relative to one another are still usable for understanding the comparative fracture toughness values in the system.

Table 5.1: Toughness values for the layers and topcoat/TGO interface in the baseline 1000-hour steam-cycled condition.

Material (layer)	Thickness (μm ; approx.)	Toughness ($\text{MPa}\sqrt{\text{m}}$)	Toughness (J/m^2)
$\text{Yb}_2\text{Si}_2\text{O}_7$ (topcoat)	250	1.4 ± 0.28	9.06
Silicon (bondcoat)	125	1.2 ± 0.18	8.14
α -cristobalite (TGO)	13.8	0.9 ± 0.17	12.07
Interface: $\text{Yb}_2\text{Si}_2\text{O}_7/\text{TGO}$	–	0.45 (max.)	3.02 (max.)

Observed crack deflections in the baseline system varied with microstructure and internal stresses. There is no oxide present in the as-sprayed condition which was detectable by SEM. By contrast, there is an oxide present in all three of the steam-cycled samples. This difference is mentioned explicitly because, due to the presence of the oxide, testing in the as-sprayed and steam-cycled samples probes the fracture toughness of interfaces between different combinations of materials. Crack deflection along the topcoat/bondcoat or topcoat/TGO interface is observed for all sample conditions, even in cases where the impinging crack orientation should optimize that condition for penetration (or, crack impingement is normal to the interface). In the as-sprayed condition, the plasma-spray process and the thermal history of the materials obfuscate the condition of the interface. It is likely that the interface changes soon after exposure to high temperatures given the annealing and crystallization that take place within the coating layers.

In the steam-cycled conditions, the topcoat-oxide interface toughness is lower than the toughnesses of the topcoat and the TGO. Additionally, as noted previously, the TGO developed significant cracking with progressive growth. For example, after 500 hours of steam cycling some vertical cracking is noted in the TGO. After 1000 hours, vertical cracking increases and cracking also develops along the interfaces of the TGO with the bondcoat and the topcoat. Given the three-dimensional nature of the layer and interface roughness in the plasma-sprayed EBC/CMC materials, interface cracking adjacent to the oxide was difficult to observe prior to indentation experiments. The crack-impingement tests across the array of steam-cycled samples were useful, because they demonstrate that the topcoat/bondcoat interface is the least tough constituent in the multilayer system, even in a relatively undamaged condition (low steam-cycling times, minimal or no cracking observed).

Another consideration in interpreting these results is the error associated with indentation toughness measurements. For example, the toughness of bulk $\text{Yb}_2\text{Si}_2\text{O}_7$ has been measured in one case to be nearly $2\text{MPa}\sqrt{\text{m}}$, while four-point bend testing of an air plasma-sprayed $\text{Yb}_2\text{Si}_2\text{O}_7$ coating produced toughness slightly less than half of that of the bulk¹³⁹. Nanoin-

dentation was used in the present work to address microstructural issues, such as porosity, known to be up to 25% in plasma-sprayed materials¹¹, which could affect toughness measurements¹³⁹. However, the indentation toughness values presented in this work are likely most valuable in a comparative sense, rather than an absolute sense.

With respect to internal stresses, as was discussed previously there was a changing stress state in the topcoat of the Baseline EBC/CMC system. In the annealed condition, compressive stresses were measured by WAXS in the EBC coating layers (Fig. 5.16). In the 100-hour steam-cycled sample, significant compressive stresses persist through the depths of both coating layers. In both cases the compressive in-plane, biaxial internal stresses likely serve to provide crack-closing forces. In-plane, crack-closing forces would increase the resistance to cracking in the coating layers, making crack deflection along the interface even more likely.

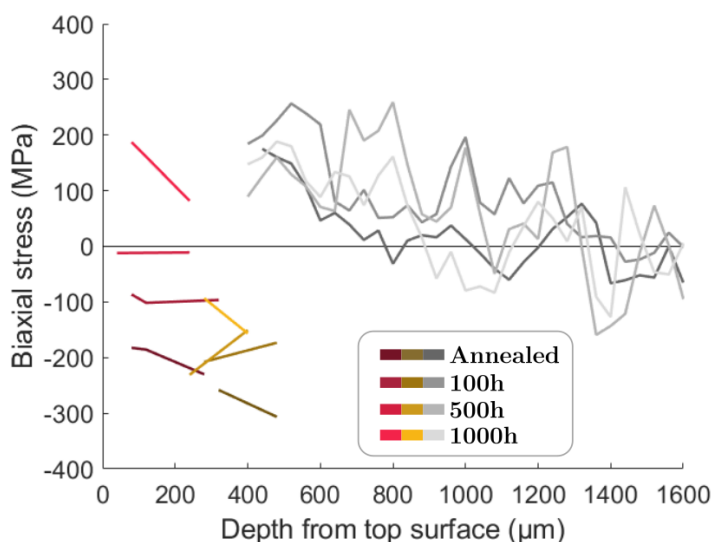


Figure 5.16: Internal stresses in the baseline system, from the annealed to 1000-hour steam-cycled conditions. Also shown in Chapter 4.

In the 500-hour and 1000-hour steam cycled samples, the topcoat was measured by WAXS to have a nearly stress-free state and a tensile stress state, respectively. As observed and discussed in Chapter 4 using the analytical model for internal stresses, the TGO develops tensile internal stresses due to the $\sim 5\%$ volume contraction of the oxide during the phase transformation from β -cristobalite to α -cristobalite, resulting in significant cracking of the TGO. For the 500-hour steam-cycled sample, the low-stress state of the topcoat likely has minimal influence over crack propagation in that layer; tensile stresses in the oxide would then contribute crack opening forces. There would be a similar situation in the 1000-hour steam-cycled sample, except that the tensile stresses in the topcoat could have provided

crack-opening forces in the topcoat. This could serve to lower the measured toughness, in addition to the effects of microstructure and testing method discussed above.

The 500-hour and 1000-hour steam-cycled samples, with layer thicknesses in the 1000-hour sample conducive to nanoindentation toughness measurements, provide a useful way to assess the behavior of cracks impinging at the topcoat/TGO interface due to their evolving internal stress states. The increased likelihood of crack penetration, from internal stress arguments, underscores the prevalence of the cracks to deflect along interfaces as being associated with low interface toughness (500-hour sample with stress-free topcoat) rather than being due in large part to internal stresses and their contributions to cracking behavior (1000-hour sample with tensile-stressed topcoat).

There are also geometrical effects not accounted for in the analysis of cracking near and toward interfaces in this work. Local stresses in the vicinity of high-curvature interfaces likely contribute to differing stress states which influence cracking in the materials. Evans et al. showed that, in compressively strained TGOs of TBC systems, the "rumpling" behavior of the TGO to minimize stresses produces tensile stresses in the topcoat and bondcoat in the vicinity of high-curvature "rumped" areas⁸⁸. The current system was shown previously to develop tensile strains in the TGO. Whether the roughness of the interface in the $\text{Yb}_2\text{Si}_2\text{O}_7$ -based systems of the current study result solely from plasma-spray processing or also from thermal cycling of the TGO (as in Evans et al.), there is some likelihood that tensile strains in the TGO result in compressive strains in the surrounding layers in the high-curvature areas near the TGO. This is the opposite case to that presented by Evans et al.⁸⁸, but is only inverted by the thermal mismatches between the layers and highlights the complexities of the indentation technique as it is applied to this engineered material system. The analysis of He and Hutchinson¹¹⁸, although later expanded to include internal stresses¹²⁰, does not incorporate angled crack impingement, internal stresses, and local geometric variations due to interface roughness. Full consideration of all these effects requires intensive solid mechanics analyses and is beyond the scope of the present work.

5.3.3 Single-edge notched beam (SENB) toughness

The SENB beam specimen failed at the epoxy interfaces first, with no damage to the multilayer ceramic. With the sample re-fabricated, in the last test it failed at the interface between the bondcoat and the substrate, rather than between the topcoat and the bondcoat as intended. SEM imaging of the failed specimen shows the groove created by the diamond scribe (Fig. 5.17), as well as the notch to guide the crack growth. Some cracking developed in the $\text{Yb}_2\text{Si}_2\text{O}_7$ topcoat (Fig. 5.17b); this surface experienced some electron charging during

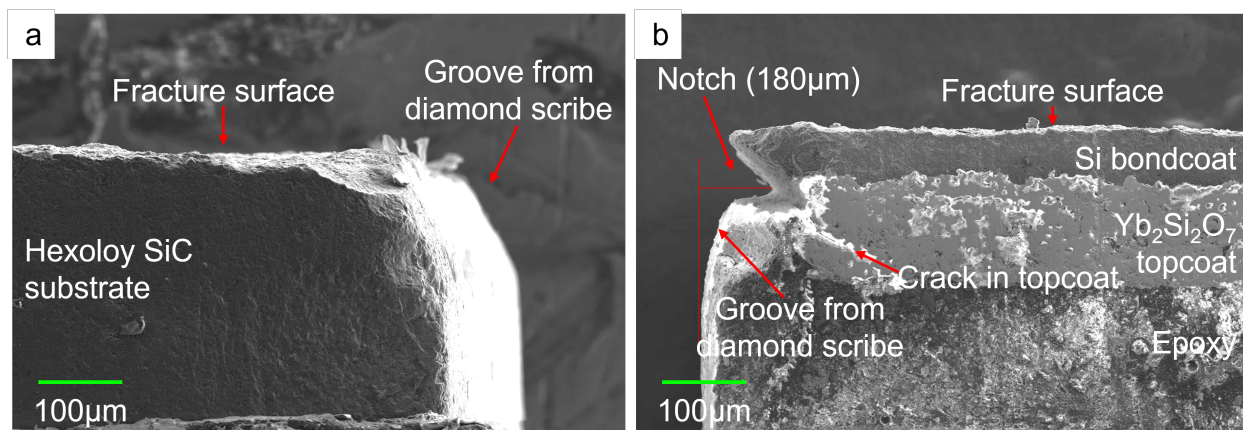


Figure 5.17: The SENB sample after failure.

imaging. Notably, the bondcoat layer appears well-adhered to the topcoat and there is little or no bondcoat attached to the substrate after failure. There are also imperfections

The highest load of failure for the sample was 127.5N. If the topcoat-bondcoat interface had failed, the toughness would be $0.69\text{MPa}\sqrt{\text{m}}$. Since the sample failed at different interfaces, this toughness value is instead taken as a lower bound for the interface toughness. There also are some chips in the material near to the topcoat-bondcoat interface but along the edge of the sample. These chips most likely served to nucleate cracks at the bondcoat-substrate interface. However, given the size of the imperfections compared to the size of the notch, one would expect the notch to nucleate the crack leading to failure. Additionally, there is some imprecision in placing the notch at the topcoat-bondcoat interface. This is due to the roughness of the interface, which is impossible to arrange perfectly in the SENB geometry, and also to the cutting tool used to create the notch. While the steel razor blades used did successfully make a notch in these materials, the thicknesses of the EBC layers compared to the thickness of the razor blade makes for imperfect notch placement. The tip of the notch in the beam is close to the topcoat-bondcoat interface, but there is some inaccuracy which may complicate the result by leading to the topcoat cracking observed. Difficulties in machining SENB specimens prevented additional testing, but refinement of sample fabrication would likely mitigate the effects of imperfections due to edge flaws and notch placement.

The result of the SENB test confirmed the hypothesis motivating this part of the present work, which was that the interface toughness of the EBC would change with the presence of the TGO between the topcoat and bondcoat. Using nanoindentation, the upper bound of the topcoat-TGO interface toughness of the 1000-hour, steam-cycled baseline sample is estimated at $0.45\text{MPa}\sqrt{\text{m}}$. From the SENB experiment, the lower bound of the topcoat-

bondcoat interface toughness in an annealed sample (no TGO) is estimated at $0.69\text{MPa}\sqrt{\text{m}}$. From these upper and lower bounds it is apparent that the interface toughness not only changes but also decreases with TGO growth.

SYNCHROTRON-COMPATIBLE *IN-SITU* HEATING DEVICE

It has been shown, in this work and in the literature, that high-temperature steam exposure and steam cycling both have critical influence on oxidation and failure of EBC systems^{15,101}. Previous synchrotron work on EBCs and TBCs (thermal barrier coatings) has been used to assess internal stresses and microstructure in multilayer EBC/CMC systems of various composition and steam cycling condition. For example, Stolzenburg et al. assessed stresses and microstructure in Yb-silicate/Mullite/Si EBCs as they related to the stoichiometry of the silicate (monosilicate and disilicate), heat treatments in air, and interactions with molten salt contaminants commonly found in turbine engines^{12,99}. Those studies coupled synchrotron measurements with high temperatures or mechanical compression testing¹¹, but did not include steam exposure or cycling.

In the present work, however, the relationship studied is between oxidation (TGO growth) and the resulting internal stresses and microstructural changes. Samples with various dopants and after multiple steam cycling intervals have been measured *ex-situ* to understand the influence of early heating and oxidation, but it is not clear exactly how internal stresses develop *in-situ* with temperature and steam exposure, especially at early exposure times. Additionally, the high-temperature behavior of the TGO, in particular, could be critical for understanding further TGO growth. For example, if the TGO at high temperature is β -cristobalite, then the cracking observed in the α -cristobalite TGO (at room temperature) upon transformation to the low-temperature polymorph could imply much about oxidant pathways in the TGO. Direct, *in-situ* observation of that behavior or any other in the process of TGO growth and stress development aid in understanding stresses overall.

Since silicon oxidation in this work depends critically on the incorporation of water vapor in the heating environment, there is a desire for a device which enables high-temperature steam exposure and/or steam cycling during synchrotron measurements. However, there is no evidence in the literature of high temperatures and water vapor being combined in synchrotron studies. Thus, a significant aim of the present work has been to develop an apparatus which combines these features and is compatible with the synchrotron beamline. Generally, the requirements for the device were that it incorporate a heating mechanism capable of reaching the same temperatures experienced in steam cycling (1316°C, for current-generation EBCs), that it permit the incorporation of steam in the sample exposure, and

that it be compatible with sample positioning and X-ray measurements at the synchrotron beamline.

6.1 Design

A custom induction furnace was designed for incorporating steam cycling into the synchrotron beamline, which is illustrated as a cross-section in Fig. 6.1. Essentially, this design builds upon a jacketed quartz tubing. The inner tube forms the sample chamber for the furnace, where samples are exposed to high temperature and flowing gas(es). The jacketed section, between the inner and outer tubes, contains a graphite cylinder which acts as a heating element. With the furnace placed into an induction coil, the graphite acts as the induction susceptor and heats based on the induction power supplied. The graphite is suspended from the bottom of the outer tube by approximately 10mm using quartz shelves into the jacketed space.

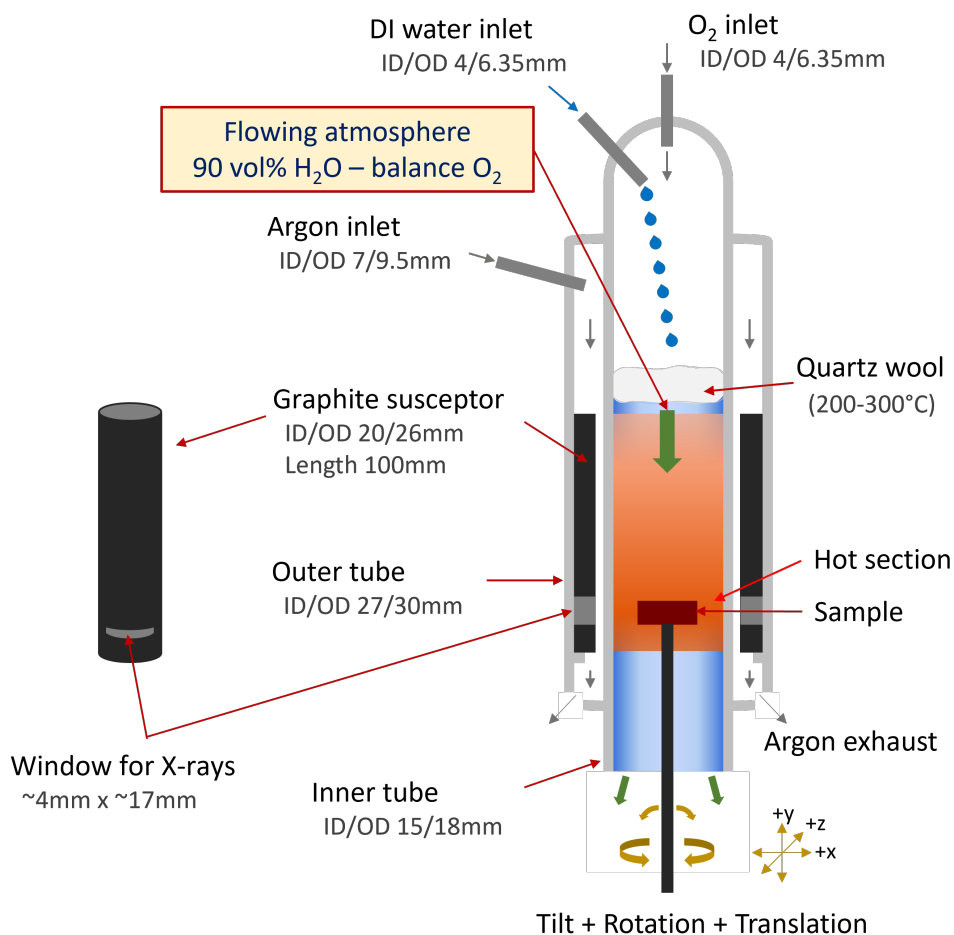


Figure 6.1: Cross-section illustration of the custom induction furnace (not to scale), and the graphite susceptor with X-ray window.

In addition to the basic design of the furnace, there are inlets placed which allow for fluid flow into the inner (sample chamber) and outer (jacketed) sections. The two inlets into the inner tube, each 6.35mm outer diameter (OD) and 4mm inner diameter (ID), can be used to introduce water and oxygen into this section at varying rates to achieve different partial pressures of water vapor, as in Refs. [7, 10]. These inlet ports can also be used to flow different gases through the sample chamber, such as argon. The inlet port into the jacketed section, which is 9.5mm OD and 7mm ID, allows for an inert gas (primarily argon, in testing) to flow past the graphite susceptor and out through three exhaust ports around the bottom of the outer tube, keeping the graphite from oxidizing in air, which occurs rapidly at high temperatures. The graphite susceptor additionally has "windows" machined through both sides of the cylinder to minimize the materials through which the X-ray beam must pass during synchrotron measurements, leaving just the sample and the quartz tubing in the beam path. This custom furnace design is essentially a smaller version of a more traditional tube furnace, with much improved portability and possibility of orientations (vertical, horizontal, off-axis, etc.).

6.2 Heating

Induction heating allows for flexibility in the design of the induction coil and the workpiece (susceptor), which is critical for the placement of the custom furnace in the synchrotron beamline. The complexity and positioning of the instruments at the beamline require a heating source to occupy minimal space. For example, even if there were not issues of material choice, X-ray transmissibility, etc., the size of the tube furnaces used for steam exposure in Refs. [7, 10] would preclude their implementation in the X-ray beamline.

As tested and used at the Advanced Photon Source (APS) and Caltech, a helical coil provided adequate induction heating of the workpiece. With the heating setup designed in such a way, the induction coil used is approximately 35-40mm OD. In most of the testing of the furnace, a coil of approximately 40mm height was used and centered vertically around the graphite X-ray window. With the current design, the cylindrical geometry of the graphite and helical coil produces a heating source which is relatively uniform across the sample chamber at any vertical (as depicted in Fig. 6.1) position. In the hot section, temperatures well in excess of 1300°C are achievable. In fact, when using graphite as a workpiece the temperature is limited primarily by the quartz glassware, which softens and melts at a lower temperature than graphite. Quartz typically begins to soften between 1600°C and 1700°C, and graphite melts well in excess of 3000°C. Induction coils of varying height are used to heat shorter or taller hot sections in the furnace.

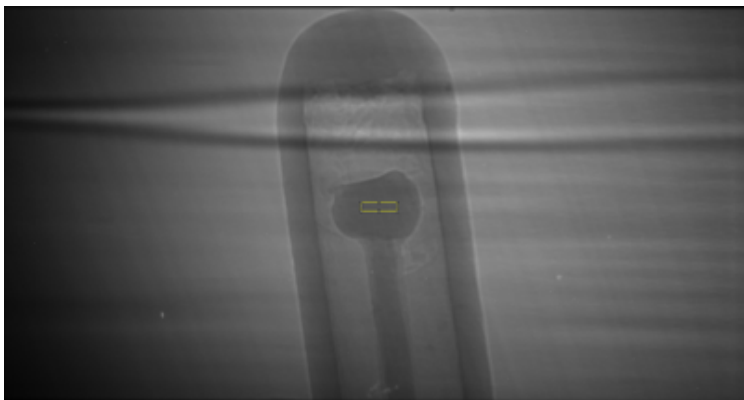


Figure 6.2: Placement of the thermocouple using the tomography detector. Image width represents approximately 2mm.

At the APS, a tomography detector was used to carefully center the induction coil vertically around the graphite window (Fig. 6.2), and to place a type-R thermocouple into the (horizontal and vertical) center of the X-ray window for temperature measurements and calibration. A modern induction workhead was used at Beamline 1 of the APS (Ambrell EASYHEAT 2.4kW; Ambrell Corporation; Rochester, NY), which has several different electrical taps to set the induction parameters. The voltage applied and the induction frequency, current, and power are observable parameters from the induction workhead. The induction power produces a reliable temperature value in the furnace hot section regardless of tap setting over the temperatures measured during calibration (approximately 400-1350°C). The difference is shown in Fig. 6.3. The induction system at Caltech, a combined power supply and workhead (Lepel Mr. Solid State) has a simpler set of induction settings, which consist of increasing voltage to change temperature. The specific settings are not detailed here, but the setup could be used to exceed 1350°C as with the APS beamline induction setup.

The use of graphite allows rapid heating and cooling of the workpiece, up to several hundred degrees Celsius per minute. Graphite is also a beneficial material choice for the workpiece for logistical reasons due to costs, ease of machining, and the low mass density of the material. Three to four graphite workpieces of the size and geometry depicted in Fig. 6.1 can be made from a single block which is relatively inexpensive to purchase. Graphite is readily machined into the cylindrical shape used in this furnace. Lastly, denser workpiece materials would be heavier in the tubing setup, and with sufficient motion could break the quartz tubing during transportation and manipulation of the setup.

With respect to the heating method, one benefit of the jacketed tubing design (inlet at the top, exhaust at the bottom) and the mass of argon (heavier than oxygen and nitrogen

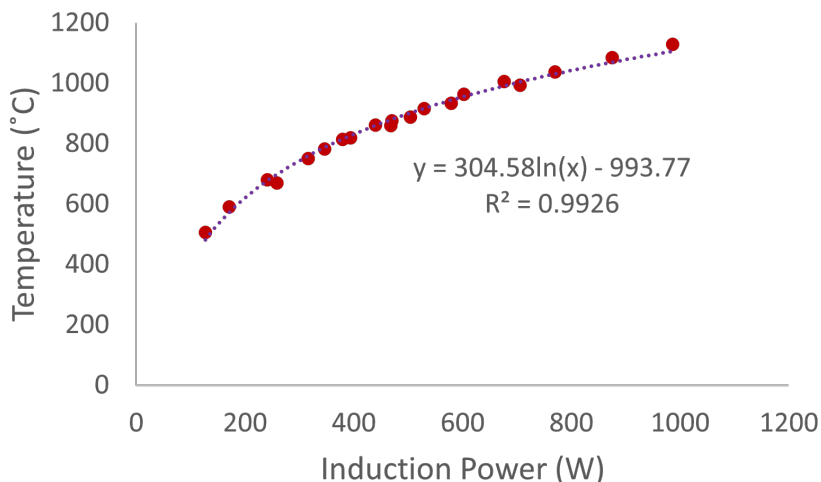


Figure 6.3: Temperature vs. induction power for the induction furnace.

molecules in air) is that positive argon pressure prevented backflow of air or oxygen into the jacketed section. Active protection of the graphite in this way improves the durability of the system and carries away the majority of substances which are "burned off" from the graphite in the first heating cycle and after long times between use of the furnace. After more than 50 hours in operation, the graphite workpiece used at the APS and Caltech was protected from oxidation using flowing argon and showed no visible signs of degradation.

6.3 Atmosphere control and incorporation of steam

Inspiration for incorporating steam was taken from the steam exposure furnaces used in the work of Opila⁷ and in steam cycling at NASA Glenn¹⁰. Those furnaces relied on different inlets for water and carrying gas. In this work, as in those references, water is dripped into quartz wool in an area of the furnace which is a few hundred degrees C. Using an induction coil ~40mm tall and centered around the X-ray window, when the hot section is at 1315-1320°C the area near the quartz wool is measured in the range of 350-400°C. There, the water heats until evaporation. The carrying gas, in this case oxygen, carries the water vapor and flows through the sample chamber over the sample(s). Other carrying gases have been used to study the dominant oxidants in oxidation experiments⁷. Use of a different carrying gas is compatible with this custom furnace, as well.

Flow rates for oxygen and water are set using the rates discussed by Opila⁷. Those rates account for the expansion of water vapor and oxygen and result in a given volume percentage of water vapor in the gas mixture at high temperature^{7,10}. The diameter of the tube discussed in Ref. [7] should be taken into account when setting gas flow rates using the custom furnace.

For example, the same face velocity as in the work of Opila can be achieved by adjusting the oxygen flow to account for the difference in cross-sectional area of the tube. Water flow can then be decreased by the same factor as oxygen to maintain the same volume percentage of water vapor as in that work⁷. In testing at Caltech, DI water flow rate was set to 6.6mL/h using a syringe pump to supply the water through the inlet port. Then, the room-temperature O₂ flow rate was tuned to 16.5cm³/min to result in 90 vol.% water vapor in the hot section. These values were also chosen to set a room-temperature face velocity of ~ 93 mm/min, so that room temperature gases would take approximately one minute to flow from the quartz wool to the sample. Heating gases are expected to expand and should therefore flow faster. Using the tabulated values of Opila⁷ and accounting for the the modifications made to O₂ and liquid H₂O flow rates, the flow rate at high temperature was determined to be 165cm³/min. However, since the overall length and hot section length of this induction furnace are shorter than those of a conventional tube furnace, and expanding gases may provide back pressure against additional O₂ and H₂O vapor flowing into the furnace, the actual flow rate around the sample is not fully quantified.

Table 6.1: H₂O and O₂ flow rates, from the work of Opila⁷ (marked *) and this work. H₂O liquid and O₂ flow rates determined the H₂O vapor and total flow rates.

H ₂ O content (vol%)	H ₂ O liquid flow rate (mL/h)	H ₂ O vapor flow rate (cm ³ /min)	Oxygen flow rate (cm ³ /min)	Total flow rate (cm ³ /min)
10*	4.2	95	860	955
25*	6.7	150	450	600
50*	11.1	250	250	500
70*	11.1	250	107	357
90*	20.0	450	50	500
90	6.6	148.5	16.5	165

The current iteration of the induction furnace does not incorporate control over the exhaust gases from the sample chamber. With the fluid flow rates discussed above, this was not an issue during sample exposures because there was no evidence of backfill of the sample chamber by air. One benefit of using a sample chamber of small diameter is that it is relatively simple to achieve face velocities preventing backflow without using excessive amounts of gas. An experimental opportunity for this furnace is that flow rates be tuned to achieve different effects, such as studying gas velocity in sample exposure, and take into account heating of the gas mixture prior to reaching the sample.

6.4 Sample positioning and manipulation

At the APS beamline, stage motors are used to manipulate sample position by translation along, and rotation around, the x (horizontal, normal to the beam path), y (vertical, normal to the beam path), and z (along the beam path) axes. Since biaxial stress measurements by WAXS are sensitive to the orientation of the sample, it is critical to build in range of motion in the *in-situ* apparatus design. This was achieved by choosing the largest inner diameter for the inner quartz tube which allowed for at least a few millimeter wall thickness of the cylindrical graphite workpiece. The outer diameter of the graphite was set by the inner and outer diameters of the outer quartz tube in the jacketed tubing setup, which was in turn determined by the diameter of available (pre-made) induction coils. However, custom induction coil sizes or geometries would allow for different quartz tubing sizes and therefore more or less sample range of motion. Allowable sample rotation about the x and z axes (normal to the vertical axis in Fig. 6.1) is also determined by the sample size and length of supporting rod inserted into the sample chamber tube. Rotational range of motion around these axes decreases with increasing insertion of the sample supporting rod into the sample chamber.

Sample positioning and manipulation is facilitated by leaving the bottom end of the sample chamber open. In testing at Caltech, it was observed using the gas flow rates discussed that there was no back-flow of air into the sample chamber which altered any observable features of the samples. This indicates that the face velocity of the flowing gases was sufficient to prevent backflow.

6.5 Applications

6.5.1 Annealing

The *in-situ* furnace was used at Caltech to anneal samples for short periods of time, for other chapters of this work. For $\text{Yb}_2\text{Si}_2\text{O}_7$ -based powders, each sample was placed into a capillary tube and held vertically using a drill chuck, which was raised and lowered using a benchtop scissor lift. With the capillary placed in the hot section, the temperature of the furnace was increased to 1315-1320°C for 30 minutes. One minute was added to the beginning of the 30-minute annealing time to allow for the furnace to reach the temperature based on the induction workhead setting. Since air exposure at high temperature posed no problems for the topcoat powders, the gas inlet ports for the sample chamber were left open and the powders were annealed in air. After annealing, the powders were then removed from the capillaries and stored for WAXS measurement at the APS.

For multilayer EBC/CMC samples, one sample each of baseline, 6A, and M2Y composition

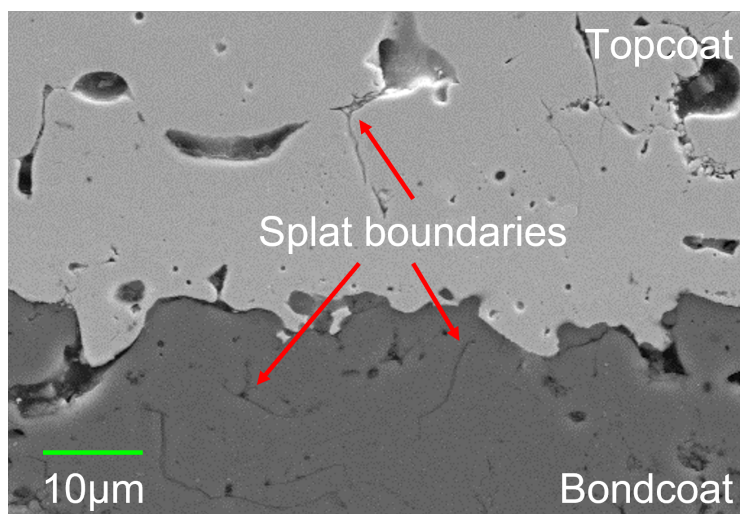


Figure 6.4: A baseline sample, annealed in flowing argon for 30 minutes using the custom induction furnace.

were annealed to assess the effects of annealing on microstructure (Chapter 2). For each composition, the sample was placed on a small quartz plate, which was balanced on a vertically oriented quartz tube and again held in place using a drill chuck. With the sample raised into the hot zone using the scissor lift, the temperature was increased to 1315-1320°C for 30 minutes (plus one minute to reach maximum temperature). Using the O₂ inlet, flowing argon gas was used to purge the air from the sample chamber and enable annealing in an inert environment. No TGO was visible in the annealed samples (Fig. 6.4), indicating that the argon flow successfully created a substantially inert environment. Similarly, a baseline sample sectioned for single-edge notched beam (SENB) testing (Chapter 5) was annealed using this method. Backflow of air into the sample chamber was not observed during these annealing runs, but larger-diameter tubing or slower gas flow could allow for backflow of air. This concern is addressed later in this chapter.

6.5.2 Steam cycling

Steam cycling was performed at Caltech on a baseline sample for 10 hours, using the flow rates for this furnace in Table 6.1. The high temperature for cycling was set to 1315-1320°C, and the low temperature was ~300°C. As in Ref. [10], the high temperature dwell was 60 minutes and the low temperature dwell was 20 minutes. One "hour" of steam cycling consisted of one high temperature dwell and one low temperature dwell.

As seen in Fig. 6.5, there is a notable TGO with some cracking at the topcoat-bondcoat interface. The TGO is approximately 2 μ m thick. The sample steam-cycled using the induction

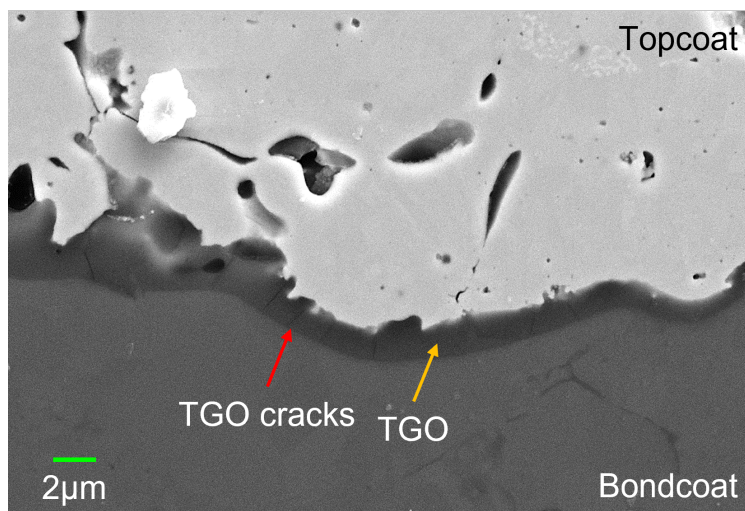


Figure 6.5: A baseline sample, steam cycled for 10 hours at Caltech using the custom induction furnace.

furnace was smaller than the samples steam-cycled by Kang Lee at NASA Glenn Research Center. Oxidant ingress through the uncoated sides of the sample could lead to accelerated oxidation, and TGO thicknesses require further investigation to quantify this effect.

6.5.3 High-temperature measurements at the APS

At APS beamline 1, heating experiments in air were used as a proof of concept for the heating and durability of the custom induction furnace, and to observe the effects (if any) of furnace materials and conditions on X-ray measurements. As-sprayed $\text{Yb}_2\text{Si}_2\text{O}_7$ -based topcoat powders were heated to the approximate maximum steam cycling temperature using the induction furnace to observe crystallization and thermal expansion using WAXS. As with powder annealing at Caltech, the topcoat powder of a given composition was loaded into a capillary and heated to high temperature (approximately 1300°C) in increments of approximately $25\text{-}50^\circ\text{C}$ above $\sim 600^\circ\text{C}$. The logarithmic dependence of temperature on induction power, shown in Fig. 6.3, was used to determine temperature based on power. After 3-5 minutes for each set temperature (based on induction power) to settle, a WAXS diffraction pattern was collected.

6.5.3.1 Heating and crystallization

On heating to high temperature in air, it was observed for each as-sprayed powder composition that crystallization of $\text{Yb}_2\text{Si}_2\text{O}_7$ occurred within a few minutes at approximately 1000°C (Fig. 6.7). Stolzenburg studied the crystallization of Yb_2SiO_5 and $\text{Yb}_2\text{Si}_2\text{O}_7$ after

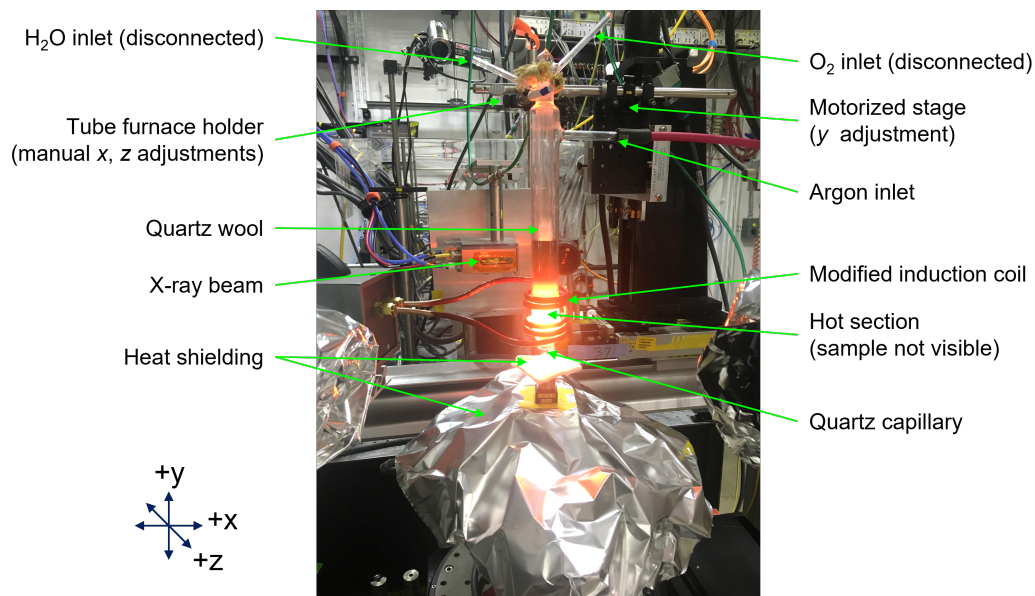


Figure 6.6: The custom induction furnace, in place and at high temperature ($1000^{\circ}\text{C}+$) at the APS Beamline 1-ID.

96 hours heat treatment in flowing air, noting that the Yb-silicates were mostly or entirely crystallized after this exposure¹¹. Powder WAXS studies using the induction furnace in this work indicate that crystallization takes place near 1000°C after only a few minutes. This observation provides important insight into the evolution of stresses in the multilayer samples during the transition from the as-sprayed to steam-cycled conditions. For example, any stress changes associated with crystallization of the topcoat can be assumed to occur within the first steam cycle to high temperature, rather than over the course of several cycles and many hours.

Additional observations of the 6A system provide insight into the behavior of the dopants in the $\text{Yb}_2\text{Si}_2\text{O}_7$ -based system while heating in air. Fig. 6.8 shows the products of the MATLAB fitting process for the $\text{Yb}_2\text{Si}_2\text{O}_7$ (200) peak in the baseline and 6A systems. Compared to the baseline peaks, which are readily fit using the MATLAB code (Fig. 6.8a and c), the peaks of 6A are not fit appropriately using the same fitting procedure and parameters upon the first heating cycle and prior to crystallization of the amorphous disilicate. There is an additional peak in the 6A pattern at this temperature, which is likely either Yb_2SiO_5 (211) or mullite (210). This is difficult to discern, as the d -spacings of these peaks are quite close: from the literature, $d_{\text{Yb}_2\text{Si}_2\text{O}_7}^{(200)} = 3.325\text{\AA}$, $d_{\text{Yb}_2\text{SiO}_5}^{(211)} = 3.326\text{\AA}$, $d_{\text{mullite}}^{(210)} = 3.399\text{\AA}$. Note that these additional peaks were not present in the 6A powder patterns at room temperature prior to heating and at low temperatures during and after the first heating cycle. Since heating and CTE was studied post-crystallization, the 6A peaks were not deconvolved for

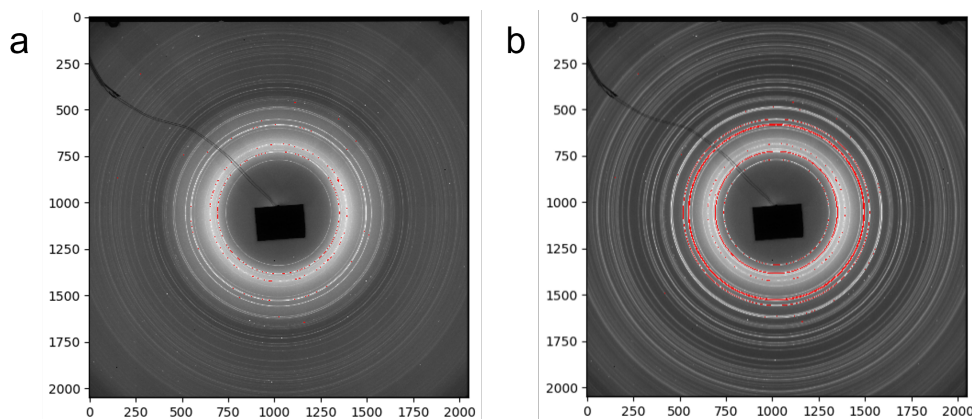


Figure 6.7: WAXS patterns from the baseline powder: (a) before crystallization (991°C) and (b) after crystallization (1030°C). Remaining amorphous background is from the quartz capillary and furnace tubing. Axis values are pixels on the 2D detectors. Red pixels represent higher intensity.

the phenomenon noted here. These peaks developed at temperatures below the maximum temperature ($\sim 1300^\circ\text{C}$) and after only a few minutes at each WAXS measurement temperature. This indicates that the dopants react rapidly with the constituents of the as-sprayed powder to form the secondary phases observed in Chapter 2.

The offset intensity for the fits is 1000; peak intensity is the value shown minus this offset. After crystallization of the $\text{Yb}_2\text{Si}_2\text{O}_7$ phase there was an intensity increase of $\sim 5\text{-}10\times$ for the disilicate phase peaks compared to the as-sprayed condition. After crystallization, due to increased disilicate peak intensity, low intensity of the secondary-phase peak, and nearby peak centers of the disilicate phase and the secondary phase at the location noted, the smaller peak could not be separated reliably from the disilicate peak after crystallization of 6A (Fig. 6.8d). The influence of the secondary peak on the disilicate peak center is minimal or nonexistent, and so the disilicate peak was fit singly after crystallization. For both the baseline and the dopant-modified $\text{Yb}_2\text{Si}_2\text{O}_7$ -based materials, calorimetry would allow determination of temperatures of secondary phase formation, $\text{Yb}_2\text{Si}_2\text{O}_7$ crystallization, and the relative kinetics of these behaviors.

6.5.3.2 Thermal expansion

Coefficients of thermal expansion were assessed for the powders on the cooling ramp from high temperature to room temperature so that the effects of crystallization would not complicate the analysis. Using the method described in Section 4.3.4 (and equation 4.22), the WAXS measurements were used to determine the lattice parameters for each combination of

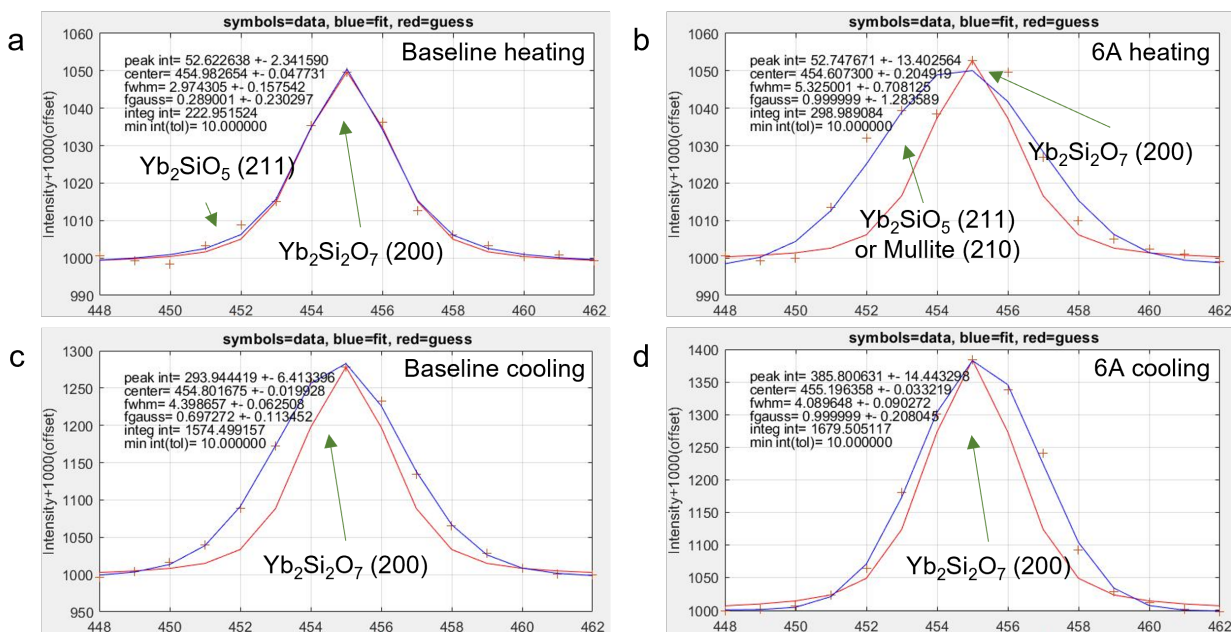


Figure 6.8: WAXS fitting of the $\text{Yb}_2\text{Si}_2\text{O}_7$ (200) peak in the baseline (a and c) and 6A (b and d) powders. With baseline and 6A at 915-920°C (a and b), additional peak intensity distorts fitting in 6A (b). After crystallization and upon cooling to $\sim 910^\circ\text{C}$, both baseline and 6A peaks are readily fit as single peaks (c and d).

composition and temperature. This included deconvolving the relevant overlapping diffraction rings and checking for agreement with Powder Diffraction File (PDF) data, both in absolute values at room temperatures and relative to nearby peaks at higher temperatures, to verify accurate peak fitting and identification. Lattice parameters were then used to calculate interplanar d -spacings. As discussed previously, this method was helpful in mitigating measurement errors associated with low-radius or single-index peaks in the diffraction pattern. The normalized expansion is plotted against temperature for the (001), (020), and (200) peaks of the baseline system. The (021) peak is included, as well, since that peak is the most prominent in the XRD pattern for $\text{Yb}_2\text{Si}_2\text{O}_7$ and is used for strain calculations in the remainder of this work. Linear fits in this work do not include the data points near 200°C. Additional furnace calibration is needed in that temperature range, since the temperature is very sensitive to induction power at lower temperatures.

As in Ref. [140], the thermal expansion in the primary directions is highest in the a parameter, or (200), and is lower in the b parameter, or (020), and lowest in the c parameter, or (001). This was shown in Ref. [140] for β -polymorph rare-earth disilicates, including $\text{Yb}_2\text{Si}_2\text{O}_7$, measured from powder samples from 303-1873K. The curvature observed in the present work appears more pronounced than in Ref. [140], although this is not quantified.

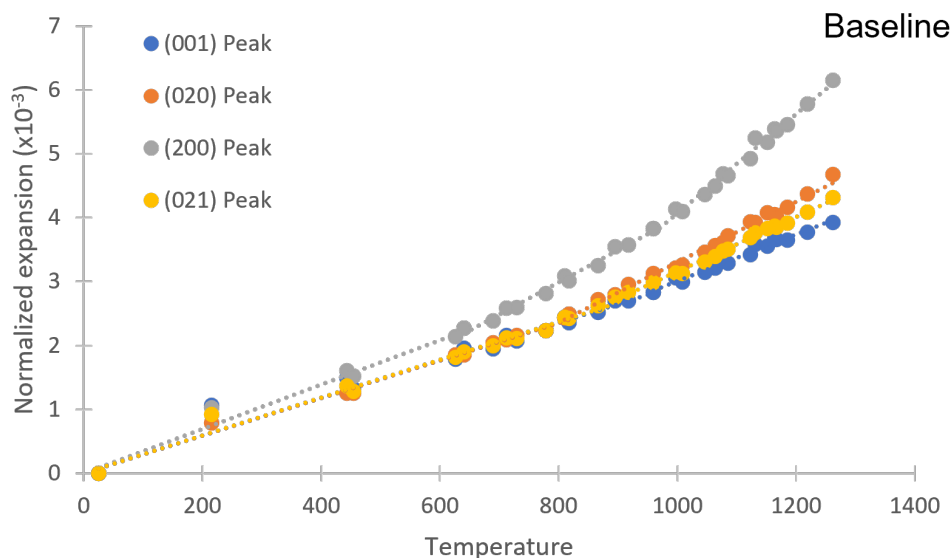


Figure 6.9: Normalized expansion vs. temperature for the baseline $\text{Yb}_2\text{Si}_2\text{O}_7$ powder.

The difference could result from the experimental details (transmission versus reflection geometries, for example). In both cases, the curvature observed could be related to anharmonic phonon effects on thermal expansion in the material. To the author’s knowledge, there is no widely available data on thermal expansion of $\text{Yb}_2\text{Si}_2\text{O}_7$ collected from single-crystal experiments. In the work of Stolzenburg et al., the (001), (020), and (200) planes were averaged to assess bulk thermal expansion^{11,99}; the same is done here, with the results tabulated for each composition. When the data are plotted for all temperatures measured, there is an increase in the slope of the curve at higher temperatures (greater than $\sim 900^\circ\text{C}$), as is common at elevated temperatures. To account for this, multiple fits were used for each peak. Two fits accounted for most behavior, except for the (200) peak which showed three separate temperature regimes of the normalized expansion. The average value for this intermediate temperature range is composed of the intermediate temperature value for (200) and the lower-temperature values for the other principal directions. Similar nonlinear behavior was shown in Stolzenburg et al.^{11,99}, although that data set included fewer measurements and only extended to 1000°C ; single linear fits were used for the data at the time.

Normalized expansion is plotted and CTEs are determined for the 6A and M2Y systems, as well (Fig. 6.10). The results for the baseline system, as well as 6A and M2Y, are reported in Table 6.2. The CTE values reported at the lower temperature range for all peaks of the baseline system are lower in this work than in the previous measurements^{11,99}. However, values of $3.6\text{-}4.5 \times 10^{-6} \text{ }^\circ\text{C}^{-1}$ have been reported in the literature for the CTE of $\text{Yb}_2\text{Si}_2\text{O}_7$ ¹⁴⁰⁻¹⁴², with

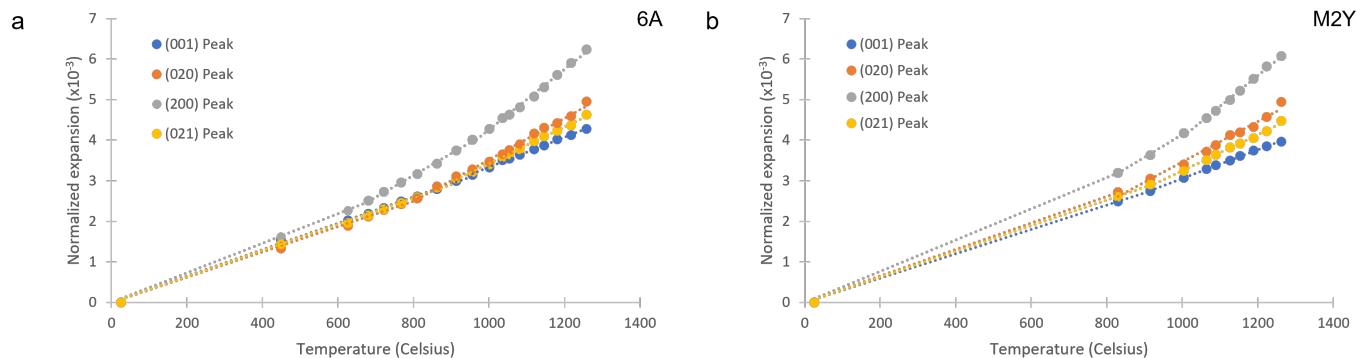


Figure 6.10: Normalized expansion vs. temperature for the 6A and M2Y $\text{Yb}_2\text{Si}_2\text{O}_7$ -based powders.

those of Stolzenburg et al.^{11,99} among the higher values. The average value of the baseline CTE (used as an approximate for the bulk) in the range $25\sim 950^\circ\text{C}$ is smaller than the value reported in Ref. [11]; above that temperature, the CTEs measured in this work are higher. It is likely that, with additional data points measured here, these provide a more accurate analysis of CTE. The larger number of data points in this study was enabled in part by the relative insensitivity of the custom induction furnace to high temperature ramp rates. With less time needed to produce temperature changes, and only $\sim 3\text{-}5$ minutes needed for temperature equilibration at each goal temperature, more measurements could be taken. Another significant benefit of the transmission diffraction setup is that, in this case, the sample position should change symmetrically about the center of mass of diffraction, meaning that the d -spacing values should not change due to the sample position changing with expansion. In contrast, with a reflection diffraction setup (as in laboratory diffraction), sample expansion and the increased surface height of the sample can result in pseudo-strain effects.

There is also a benefit to using the custom induction furnace from a materials design and engineering perspective. The differences between CTE values based on crystallographic reflections indicates that texturing of the $\text{Yb}_2\text{Si}_2\text{O}_7$ topcoat could be used to minimize thermal mismatch stresses arising in the multilayer materials. The stress profiles seen in Fig. 6.11 were produced using the CTEs from the (200) peak (grey) and the (001) peak (blue). CTEs for the relevant temperature ranges for each peak were used in the analytical model of Hsueh et al.¹⁰⁹. The thermal stress predictions are plotted as the sums of the thermal stresses for all the relevant temperature intervals. The change of CTE based on crystallographic orientation indicates that texturing the coating would allow for a tailorable CTE, thus minimizing the thermal stresses. Coating processing techniques which would produce crystallographic texture would need to be developed.

Table 6.2: Tabulated CTE data, from this work and that of Stolzenburg et al.^{11,99}. Average (\sim bulk) values are from the three principal directions and do not include (021). R^2 values marked * are only fit with two points.

	Stolzenburg et al. ^{11,99} $\times 10^{-6} \text{C}^{-1}$	25~900°C		~650-960°C		~900-1300°C	
		$\times 10^{-6} \text{C}^{-1}$	R^2	$\times 10^{-6} \text{C}^{-1}$	R^2	$\times 10^{-6} \text{C}^{-1}$	R^2
Baseline (001)	4.25	2.99	0.999	–	–	3.65	0.993
Baseline (020)	4.70	2.97	0.999	–	–	4.75	0.990
Baseline (200)	5.20	3.58	0.999	5.20	0.997	7.74	0.993
Baseline Average	4.7	3.18	–	3.72	–	5.38	–
Baseline (021)	–	3.00	0.999	–	–	4.29	0.995
6A (001)	–	3.26	1.00	–	–	3.69	0.998
6A (020)	–	3.12	0.999	–	–	5.13	0.995
6A (200)	–	3.65	0.999	5.39	0.997	7.41	0.995
6A Average	–	3.34	–	3.92	–	5.13	–
6A (021)	–	3.23	0.999	–	–	4.53	0.998
M2Y (001)	–	3.01	1.00*	–	–	3.53	0.999
M2Y (020)	–	3.27	0.999	–	–	4.99	0.986
M2Y (200)	–	3.85	0.999	5.61	0.998	7.58	0.997
M2Y Average	–	3.38	–	3.96	–	5.37	–
M2Y (021)	–	3.16	1.00*	–	–	4.44	0.996

It should be noted that due to the non-linearity of the coefficients of thermal expansion, the results from the analytical model are the summation of stresses from each linear segment over the full temperature range (1300 to 50°C). A more sophisticated model might account for multi-value CTEs more cohesively and could produce different stress values, although this effect is not quantified here.

6.6 Limitations and suggested improvements

It was observed, after extensive heating experiments, that a scale developed in the jacketed section of the custom furnace which obscured visibility of the samples. This did not interfere with the ability to position the tubing and samples using the tomography detector at the APS. However, since the scale could be either a different phase or some microstructural effect of the quartz tubing, a WAXS pattern was collected of just the induction furnace, with the X-ray beam passing through the four quartz walls and the scale in the jacketed section. As seen in Fig. 6.12, there is a contribution from the amorphous fused quartz phase but there is also a crystalline phase present. The peaks of the crystalline phase correspond to α -cristobalite. Two peaks are present for each peak position due to the diameter of the tubing, where the walls diffracting the photon beam are far enough apart along the beam path that they produce separate diffraction rings. As with the TGO of the multilayer

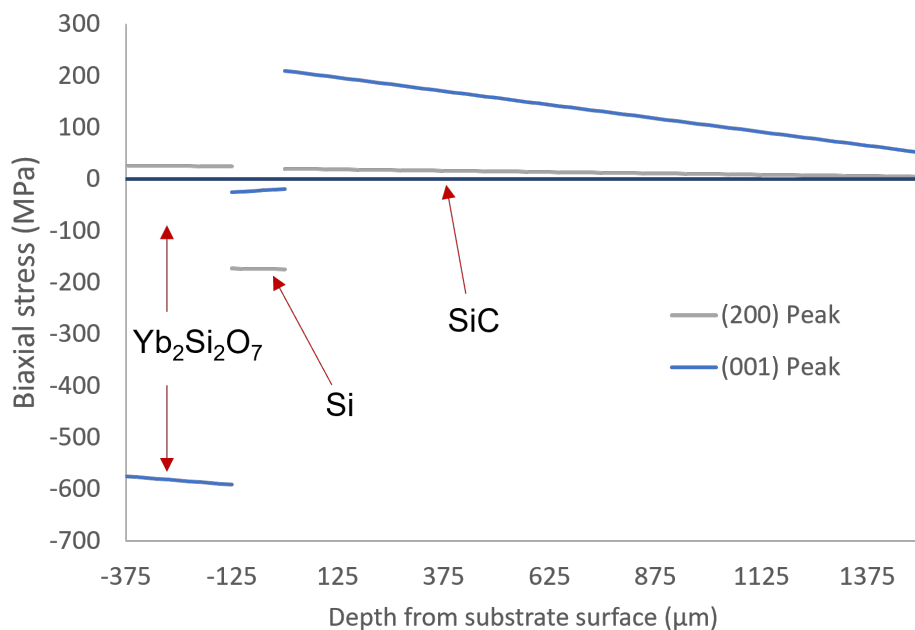


Figure 6.11: Calculated stresses, based on the model by Hsueh et al.¹⁰⁹, with CTEs for (200) and (001) peaks.

EBC/CMC samples, the presence of α -cristobalite indicates that β -cristobalite forms at high temperature, in this case from the quartz tubing, as opposed to thermal oxidation. It is unclear at this point how long the furnace can operate before the cristobalite scale, and related transformations between cristobalite structures, produce deleterious effects to the furnace performance. The cristobalite pattern will also obfuscate diffraction measurements of materials for which either cristobalite polymorph is the phase of interest. In the case of the EBC/CMC materials of this work, and the TGOs observed, this issue could be addressed by performing *in-situ* measurements early in the overall use of a new tube furnace (prior to significant scale development). Alternatively, and more likely, alterations to the furnace design which allow for more space between the graphite workpiece and the inner tube (where the scale develops) or a different tubing material (such as sapphire) may be needed for extensive oxidation studies involving a cristobalite oxide, where instead alumina peaks would need to be accounted for. For material systems not containing or developing cristobalite, the development of cristobalite on the furnace tubing may not be an issue and can simply be accounted for in the long-term use of the device.

In the event of backflow problems, using the same basic design as in Fig. 6.1, additional steps to prevent backflow which can reach the sample include increasing the face velocity of flowing gases, using a smaller diameter inner tube, and increasing the distance from the

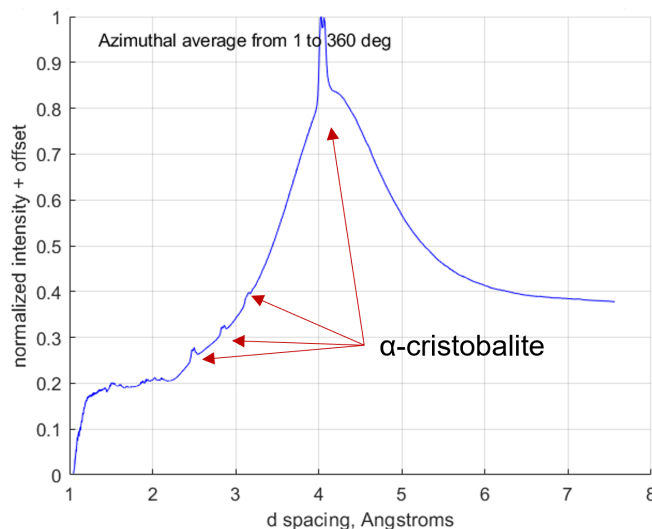


Figure 6.12: WAXS pattern from the empty induction tube furnace. Amorphous background from fused quartz and crystalline peaks from α -cristobalite indicate some devitrification of the tubing after extensive use.

sample position (hot section) to the exhaust end of the tube. Use of a larger diameter inner tube, to increase sample size or maneuverability, would require more gas flow to maintain face velocity and maintain minimal backflow. Additionally, including foil or quartz wool into or near the exhaust of the inner tube to help prevent any backflow. Lastly, implementing an active exhaust system, such as fans to provide negative pressure near the exhaust end of the inner tube, can aid in removing gases from the sample chamber and prevent backflow of air.

Overall, the potential for customization of the induction furnace allows for many different configurations. Induction coil and tubing dimensions can accommodate varying sample sizes and experiments, as well as arrangements for moving the coil and tubing separately from one another for ease of assembly. The variability afforded by the inlet ports allows for different flowing gases to be used, as demonstrated through annealing in flowing argon, or for the ports to be left unattached to gas flow so that heating experiments can be performed in air, as in the powder heating experiments at the APS. The susceptor material can also be changed. Specifically, if a simpler design without a jacketed tubing setup is needed, alloy or metallic susceptors can be used as long as melting and contamination are not a concern or are adequately addressed.

CONCLUSIONS AND SUGGESTIONS FOR FUTURE WORK

7.1 Summary and conclusions

7.1.1 Baseline

The baseline, unmodified $\text{Yb}_2\text{Si}_2\text{O}_7$ system served as the control for the studies in this work. Observations of microstructure verified the phase stability of the EBC topcoat, which retained residual Yb_2SiO_5 splats even after 1000 hours of steam cycling. Parabolic growth of the TGO in the baseline system occurred and was the thickest of the compositions studied at each steam cycling interval. Baseline system TGO thickness was approximately $14\mu\text{m}$ thick after 1000 hours of steam cycling. Extensive cracking in the TGO resulted from the transformation from high-temperature β -cristobalite to low-temperature α -cristobalite, which is accompanied by a $\sim 5\%$ volume reduction. Increasingly thick TGO and additional transformations between the cristobalite polymorphs resulted in both vertical cracking in the TGO and interface cracking between the TGO and the topcoat and substrate after 1000 hours of steam cycling. As discussed in Chapter 2, this is a critical failure mechanism for EBC systems.

The evolution of internal stresses measured in the baseline system were directly related to the microstructure and TGO growth observed. The coating stresses in the annealed condition were compressive, which was favorable for preventing through-thickness cracking. With progressive TGO growth and cracking, which served to relieve stresses, the topcoat stresses evolve from compressive to stress-free in 500 hours of steam cycling. After 1000 hours of steam cycling, tensile stresses were measured in the topcoat, possibly due to additional TGO growth which was accelerated at and near vertical TGO cracks, expanding the TGO and exerting some tensile force on the topcoat. Compressive internal stresses in the topcoat are useful for providing crack-closing forces and preventing through-thickness cracking. The change in the baseline topcoat from compressive to tensile internal stresses over 1000 hours of steam cycling shows that the baseline system develops an unfavorable internal stress state after 1000 hours of steam cycling, a far smaller duration than the 25,000 hours stated in Chapter 2 as the goal life span of EBC/CMC components⁸⁴.

Interface toughness of the baseline system was shown to decrease from the annealed state to the steam-cycled state, primarily due to the presence of the TGO. In the annealed state, where single-edge notched beam bending was used, interface toughness was measured to be

greater than $0.69\text{MPa}\sqrt{m}$. Notably, in the SENB test beam the topcoat-bondcoat interface did not fail despite the placement of the notch. Rather, the bondcoat-substrate failed and the load value provided a lower bound for the topcoat-bondcoat interface toughness. Using indentation methods, the maximum toughness of the interface between $\text{Yb}_2\text{Si}_2\text{O}_7$ and α -cristobalite TGO was estimated to be $\sim 0.45\text{MPa}\sqrt{m}$. These boundary estimates for the interface toughness values confirm that, as expected, the interface toughness degrades as TGO grows between the topcoat and bondcoat of these EBCs. Nanoindentation was chosen to avoid microstructural features from plasma-spraying, and SENB testing was chosen due to the difficulty of propagating cracks into annealed interfaces with nanoindentation. The remaining difficulties in sampling sufficient material (in indentation) and in sample machining (for notched beam bending) leave room to refine the methods for additional measurements. Due to the degradation of interface toughness, and the prevalence of cracking in the TGO and at its interfaces with the topcoat and bondcoat, the adhesion of the topcoat to the rest of the EBC system decreases over time, as anticipated.

In-situ heating experiments, at the Advanced Photon Source, were used to observe rapid crystallization of the $\text{Yb}_2\text{Si}_2\text{O}_7$ topcoat powders upon the first heating cycle after plasma-spray deposition. The crystallization took place after only a few minutes exposure to $\sim 1050^\circ\text{C}$ in air. *In-situ* heating was also used to assess thermal expansion and calculate CTE in more detail than has been discussed in the literature. When covering a larger temperature range than the work of Stolzenburg et al.^{11,99}, there were multiple temperature ranges observed, each of which is best fit by a different CTE. Further work is needed to determine the CTE in greater detail between room temperature and approximately 600°C .

Previous $\text{Yb}_2\text{Si}_2\text{O}_7$ studies indicated the disilicate performs well in terms of volatility in steam, reactions with contaminants (CMAS), and thermal expansion in heating experiments in air less than 100 hours long^{11,12,15}. The challenge of TGO-based failure in $\text{Yb}_2\text{Si}_2\text{O}_7$ EBCs, however, has been addressed more recently¹⁵. Due to extensive TGO growth and cracking, and the associated changes in internal stress and interface toughness, the baseline $\text{Yb}_2\text{Si}_2\text{O}_7$ EBC is not well suited to endure extensive exposures to steam at high temperatures.

7.1.2 Alumina-modified (6A)

The 6A, or alumina-modified, $\text{Yb}_2\text{Si}_2\text{O}_7$ -based system was observed to develop a very different microstructure than the baseline system with any heat treatments after plasma-spray deposition. Residual monosilicate present in the baseline topcoat disappeared from the 6A topcoat. Instead, precipitates which appeared in two-dimensional micrographs as needles were present in the 6A topcoat. There was additionally a Yb-Al silicate interfacial layer

present between the topcoat and bondcoat. It was suspected, here and by Lee et al.¹⁰³, that the 6A system has a delayed onset to TGO growth while the interfacial layer develops and some precipitates of Yb-Al silicate composition begin to migrate through the TGO and bondcoat. The interfacial layer is discontinuous after 100 hours of steam cycling and again after 1000 hours of steam cycling, and is at its thickest (a few μm) and most continuous after 500 hours of steam cycling. TGO thickness and parabolic growth rate were reduced dramatically compared to the baseline system, both by more than 80%. This improvement was attributed to the effects of dopants on the diffusion of oxidants through the TGO, which was not single-phase α -cristobalite but which instead contained both α and β -cristobalite as well as mullite. The β -cristobalite structure was stabilized by "stuffing" cations and aluminum substitutions in the cristobalite structure. Stabilized β -cristobalite would not have undergone the $\sim 5\%$ volume reduction from the transformation to α -cristobalite, and so cracking of any stabilized β -phase was less of a concern. Mullite has been used previously as a diffusion barrier in EBC/CMC systems¹³, and likely contributed to the reduction of TGO growth. The decrease of TGO thickness of the 6A system compared to the baseline system is promising.

The TGO in 6A, modified by dopants as well as Yb from the topcoat, impedes oxidant diffusion not only as a TGO typically does (leading to parabolic growth rates) but also by containing mullite, a common diffusion barrier material, and possibly through stabilized β -cristobalite. The stabilized β -cristobalite does not experience the $\sim 5\%$ volume contraction upon transformation to α -cristobalite, and therefore develops fewer cracks. Since cracks can act as oxidant diffusion pathways, less cracking can aid in limiting TGO growth. The other dopant effects in the 6A system, in particular the development of the interfacial layer described in Chapter 2, appear related to the limited TGO growth through the movement of dopant oxides or elements to the topcoat-bondcoat interface, where some dopants are incorporated into the TGO. The exact composition, or range of compositions, of the interfacial layer and the needle-like precipitates are currently unknown. The reduction of TGO growth in the 6A system is favorable compared to the baseline system. However, from a conservative viewpoint the unknown effects of the secondary phases appearing in the microstructure should receive more attention prior to implementation of a 6A-composition EBC system.

Internal stresses in the 6A system also differed from those of the baseline system. Compressive stresses were observed after annealing and 100 hours of steam cycling. A nearly stress-free state was observed after 500 hours of steam cycling. After 1000 hours of steam cycling, the topcoat had returned to a compressive internal stress state. The internal stresses were again related to microstructure, in this case the presence and prevalence of the interfa-

cial layer (thickest at 500 hours steam cycling) rather than changing due to cracking of the TGO. In addition to being thinner than in the baseline, the TGO in 6A showed much less cracking and therefore provided less stress relief in the system. While the internal stresses in most cases are compressive in the coating materials, the stress-free topcoat seen after 500 hours of steam cycling indicates that dopants effects in the system play a role in the biaxial stress state at this intermediate time. Additional steam cycling of this system would indicate if the compressive topcoat stresses remain well after 1000 hours of steam cycling, which is necessary to determine the suitability of the 6A topcoat as an EBC in terms of internal stresses.

In-situ heating and synchrotron measurements showed that secondary phases develop early in heating of the 6A topcoat material. Prior to full crystallization of the $\text{Yb}_2\text{Si}_2\text{O}_7$ structure, secondary phases were shown to crystallize. Upon crystallization of the disilicate phase, the secondary phase peaks near the disilicate peaks were essentially dominated by the disilicate peaks and were effectively no longer observed. Secondary phase peaks not close to disilicate peaks were still visible.

CTE assessments from the *in-situ* measurements of the 6A powder showed similar behavior to the baseline system, where thermal expansion is better described by multiple CTEs to describe different temperature regions. As with the baseline system, 6A showed a higher CTE at the high end of the temperature scale for which measurements were taken. Differences in the CTE values between the modified and baseline systems are likely related to dopant effects, in terms of substitutions and vacancies in the $\text{Yb}_2\text{Si}_2\text{O}_7$ structure, although the chemical effects on CTE are not quantified beyond the measurements taken. However, the CTEs of baseline and 6A are still within $0.2\text{-}0.25 \times 10^{-6} \text{C}^{-1}$. The similarity of CTE between 6A and baseline topcoat powders is promising. However, without a more complete understanding of the effects of the interfacial layer and needle-like precipitates on internal stresses, and how these features change over even longer steam-cycling intervals, the 6A system is not known well enough for use as a coating in use on CMC components.

7.1.3 Mullite+YAG-modified (M2Y)

Like the 6A EBC/CMC system, the M2Y system developed a different microstructure than the baseline. There was no monosilicate phase present in the M2Y topcoat after heating, although some minor secondary phases developed as a result of dopant additions to the disilicate. Unlike the 6A system, there was not an interfacial layer observed in the M2Y system. TGO thickness and growth rates in M2Y were (as in 6A) dramatically reduced compared to the baseline system, again by more than 80%. As in 6A, this was attributed to

dopant incorporation into the TGO, in which transmission X-ray diffraction showed traces of β cristobalite and mullite.

The microstructure of the M2Y system over steam cycling combined key favorable traits from the baseline and 6A systems. As in the baseline system, there does not appear to be a new precipitate phase visible by SEM in the topcoat. There also were no needle-like precipitates in the topcoat, which were present in the 6A topcoat. The reduction of TGO thickness and parabolic rate, by more than 80%, in the M2Y compared to baseline is very promising for the M2Y EBC. This reduction is attributed to the effects of Al, Yb, and Y dopants in the TGO, which both stabilize some β cristobalite and form some mullite in the TGO. Furthermore, the lack of dopants effects with unknown implications, such as the interfacial layer and needle-like precipitates, makes the M2Y microstructure somewhat more predictable than that of 6A.

Internal stresses in the M2Y system showed the greatest stability of the three compositions during the change from the annealed condition through 1000 hours of steam cycling. The coating internal stresses, which began as compressive in the annealed condition, remained compressive and of significant magnitude (150MPa+) for all heat and steam cycling treatments measured. As in 6A, the TGO of the M2Y system was quite thin compared to baseline and developed minimal cracking, and so there was minimal or no relief of topcoat compressive stresses. The compressive sign of the stresses in M2Y, and the stability of those stresses over time, are very promising for the durability of that system. From a design perspective, the stresses in the M2Y system, moreso than the baseline and 6A systems, are favorable for use in EBCs because, (1) the compressive stresses help to prevent through-thickness cracking and, (2) the EBC stresses do not change sign (as in the baseline) or go to nearly zero and then change back (as in 6A).

As with the baseline and 6A topcoat materials, thermal expansion of the M2Y system was found to be well-fit by multiple trendlines for different temperature regimes. The smaller number of measurements for the M2Y system could result in some error in the calculated CTE, making direct comparison between this CTE and those of the baseline and 6A systems difficult. Additional data points in the temperature ranges measured, as well as in lower temperature ranges, would help to more fully determine the CTE(s) of the M2Y system. From the data of this work, the CTE of M2Y is similar to that of the baseline system, as was 6A, which is useful from a CTE and thermal match/mismatch design perspective.

Following microstructure and internal stress analyses, the M2Y EBC system is the most favorable for component implementation of the three studied in this work. The dopant effects, which reduced TGO growth without developing significant secondary phase precipitates or

Table 7.1: Summarized results from this work.

	Baseline	6A	M2Y
TGO phase(s)	α -cristobalite	α -, β -cristobalite, Mullite	α -, β -cristobalite, Mullite
TGO parabolic rate ($\mu\text{m}^2/\text{hr}$)	0.1932	0.0043	0.0027
Topcoat stresses after 1000h	Tensile	Compressive	Compressive
CTE, ~ 25 - 900°C ($^\circ\text{C}^{-1}$)	3.18	3.34	3.38
CTE, ~ 900 - 1300°C ($^\circ\text{C}^{-1}$)	5.38	5.13	5.37

interfacial layers, accomplish the goal of addressing TGO-based failure and avoiding unknown dopant effects. Coating internal stresses, in the range of 150-250MPa from the annealed state through 1000 hours of steam cycling, are relatively stable over time and aid in preventing cracking. Interface toughness between the topcoat and bondcoat or topcoat and TGO will help to determine the effects of TGO thickness and of dopants on interface toughness in this system, to enhance the comparison to the baseline EBC.

7.2 Future work

There are numerous opportunities for future work on the materials and techniques presented in this work. Opportunities to understand the basic science and fundamental behaviors of the EBC/CMC systems can focus on the roles of chemical modifications on materials behavior. Refinement of the techniques used in this work, and the use of additional techniques described here, should additionally help to isolate certain material properties in order to understand their basic behavior. From the engineering perspective, the results of this work and of other suggestions for future work can be used to develop and validate better EBC/CMC systems in the current and future material generations. The large compositional space for dopant additions in EBC topcoats, implied by the range of behaviors described in Chapter 2, serves as an excellent platform to refine composition. Mechanical studies of the internal stresses and fracture toughness can be used in mechanical modeling and simulations for predictive purposes in understanding the design and durability of EBC/CMCs.

7.2.1 Microstructure and oxidation

As shown in this work and in the literature^{15,103}, dopants play a major role in the development of microstructure in the multilayer EBC/CMC systems, as well as in the growth of the bondcoat TGO. The development of precipitates in the 6A topcoat, and of the interfacial layer between the topcoat and the bondcoat, can be observed more closely using steam

cycling exposures shorter than 100 hours and at intervals between the steam cycling times used so far. Since some of the microstructural features are temporary, based on their appearance and disappearance over 1000 hours of steam cycling, a finer-grained approach to steam cycling would likely help to explain the time scales of the behavior noted. Further characterization would also help to understand the phase of the interfacial layer, which should aid in understanding the interactions between the dopants and the topcoat and bondcoat in the alumina-modified system. A ternary phase diagram of the $\text{Yb}_2\text{O}_3\text{-Al}_2\text{O}_3\text{-SiO}_2$ system would be very helpful in this effort but, as noted also by Richards et al.¹⁴³, that phase diagram is not yet well-described.

Given the differences in the dopant effects between the 6A and M2Y systems, and the fact that the M2Y system has a smaller mole percentage of dopant oxides than the 6A system, there is ample opportunity to explore dopant formulations for $\text{Yb}_2\text{Si}_2\text{O}_7$ -based (and other RE silicate-based) systems. For example, alterations to the 6A composition to include less alumina, may provide similar results to M2Y. Compositional explorations could identify ideal compositions, or ranges of compositions, for which the TGO growth and other microstructural effects are both sufficiently minimized, or for which microstructural effects due to dopants are found to be favorable as was the TGO growth reduction observed. The role of alumina, the common dopant in the modified systems, underscores the importance of that addition into the topcoats as a method for reducing TGO growth and serves as an excellent starting point for composition refinements.

TGO growth deserves much attention, as well, due to the ambiguity surrounding the effects of the EBC topcoat on silicon TGO growth in the unmodified system as well as the effects of dopants on oxidant diffusivity through the TGO. A control experiment, mimicking the work of Deal and Grove, should verify the conformation of the silica TGO as being cristobalite or another SiO_2 polymorph. Assurance of a cristobalite TGO, through that experiment or through additional steps to transform the TGO into cristobalite, will permit a reliable comparison of TGO growth rates on uncoated silicon versus silicon with an EBC topcoat to assess the effects of the EBC topcoat on TGO growth. Then, the effects of dopants can be assessed by more direct comparison of TGO growth rates between the baseline and dopant-modified EBC systems. Those results may then allow for a more sophisticated understanding of the specific effects of dopants on oxidant diffusivity. Alternatively, processing TGOs resembling those of the 6A and M2Y systems onto silicon substrates, and then performing either oxidation exposures or electrochemical impedance spectroscopy (EIS), should allow for an accurate study of oxidant diffusivity. One way to accomplish these studies may be to adhere the $\text{Yb}_2\text{Si}_2\text{O}_7$ -based topcoat materials to a silicon wafer, grow a thin TGO through

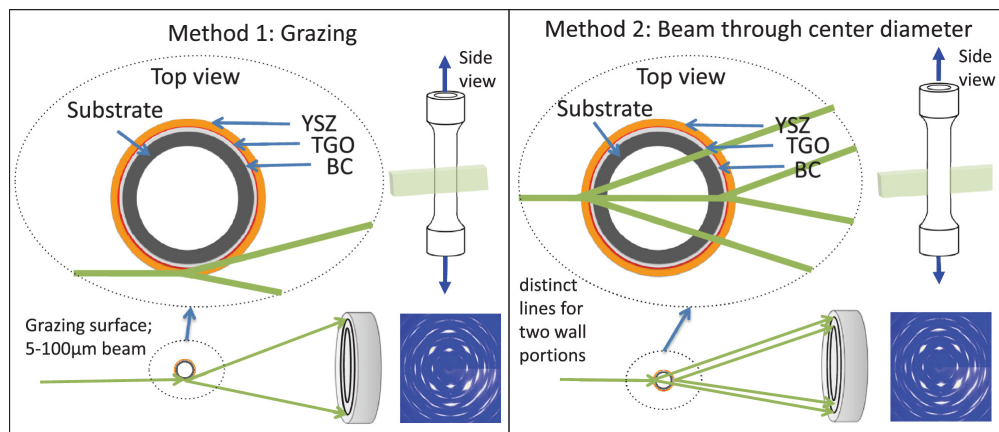


Figure 7.1: WAXS data collection on a cylindrical specimen. Figure reprinted from Siddiqui et al.¹⁰⁰ with publisher permission.

humid oxidation experiments, and delaminate the topcoat. Then, the classical diffusion experiments such as those of Deal and Grove⁶ and Opila⁷, or newer EIS techniques, can be implemented straightforwardly.

Lastly, microstructure can be used to influence the design of EBC coating layers. Electron-beam physical vapor deposition (EB-PVD) methods have been used to develop coatings with columnar structures with dendritic features⁵⁴. These microstructures can increase strain tolerance in order to minimize thermal mismatch stresses between the layers. Similarly, using detailed CTE data, coating orientations with favorable CTEs can be designed and deposited to minimize thermal mismatch between the layers.

7.2.2 Synchrotron experiments

Internal strain and stress measurements can be performed for different geometries than the flat coupons primarily discussed in this work. WAXS measurements were performed by Siddiqui et al. on cylindrical superalloy rods coated with a YSZ topcoat, a NiCoCrAlY bondcoat, and a Al_2O_3 TGO¹⁰⁰. Tangential, grazing-angle measurements from the outer cylinder walls and progressing through the layers, provided the radial and axial strains. WAXS measurements through the centers of the cylinders were used to determine circumferential strains and provided additional axial strain measurements¹⁰⁰.

Internal stress measurements of cylindrical geometries can be used to study EBC materials from multiple perspectives. As in the work of Siddiqui et al., the use of hollow cylinders allows for a thermal gradient to be applied across the layer thicknesses of the materials (Fig. 7.1)¹⁰⁰. While CMCs and EBCs are designed such that active cooling are not (or should not be) necessary, thermal gradients still occur during rapid heating and cooling of

large components. In addition, until current-generation EBC silicon bondcoats are replaced with materials of higher melting temperature, active cooling may be needed in the interim to prevent bondcoat melting. This provides motivation to study the effects of thermal gradients on internal stresses.

Synchrotron studies using cylindrical samples can also provide insight into the stress states of EBC/CMC materials near the leading and trailing edges of the turbine blades. The stresses developed in high-curvature areas, such as these edges are not likely to resemble those of the flat areas mimicked by the coupon-based samples measured in Chapter 4 of this work. By characterizing internal stresses in geometries resembling additional engine component areas, a more complete picture will emerge of stresses in the entire material systems. The cylindrical configuration additionally constrains oxidant ingress to migration through the EBC layers, which was only assumed to be the case in flat, coupon-based samples.

One benefit of the coupon-based samples is lost in cylindrical samples, though, and that is the clear distinction between layers (excepting overlaps due to interface roughness, etc.). Internal stress analysis for cylindrical samples must take into account stresses at multiple layer depths for each X-ray beam position except for the exact tangent of the cylinder. Because of this, cylindrical stress analysis will require additional analytical steps for each depth position from topcoat to substrate.

7.2.3 Interface toughness

Despite the advantages of nanoindentation compared to microindentation for EBC/CMC materials, nanoindentation toughness methods are still subject to microstructural challenges in terms of finding ample sites near interfaces for placing indentations. The current work required an economical use of samples, due to the time-intensive nature of steam-cycling materials for many hundreds of hours. Many more samples to use in testing would help to determine if the cracking behavior near and at interfaces are universal in steam-cycled baseline EBC/CMCs with TGOs. Improved sampling can also be facilitated by processing "model" samples, with interfaces of low roughness and layers with minimal porosity and no splat boundaries or other microstructural features which can interfere with indentation. These samples should be processed using non-plasma spray methods, such as slurry coating, sputtering, etc. to avoid the microstructure resulting from plasma-spray deposition. While such "model" samples would not benefit from the strain tolerance (in the layers) and mechanical interlocking (at interfaces) enjoyed by plasma-sprayed materials, they would more readily facilitate the measurement of intrinsic properties. In terms of the analytical method of He and Hutchinson, a more complete accounting of the effects of internal stresses, angled

crack-interface impingement, and curvature due to interface roughness would enhance the ability to measure toughness by this method. A proper accounting of internal stresses near and at high-curvature areas of the TGO, as mentioned earlier from the work of Evans et al.⁸⁸ would be required for a complete description of the effects of indentation cracking in these materials. The extent of such an effort requires extensive solid-mechanics analysis and therefore is not appropriate for the present work.

For single-edge notched beam testing, the method can be improved at the macroscale with more sophisticated machining capabilities. A longer notch at the topcoat-bondcoat interface may force cracking at that interface rather than at the bondcoat-substrate interface of the annealed baseline material. However, machining a deeper notch into the hard ceramic materials comprising the EBC/CMC system would require either ultra-sharp implements or a very thin wafering saw. One additional challenge is that, with interface roughness as large as tens of microns in some cases, a notch straight across a beam bending sample may not always lie directly at the layer interface. This is an additional opportunity to use the "model" materials mentioned above in mechanical testing.

The beam bending experiments could also be implemented at the micro/nano-scale, as in the work of Tertuliano et al.¹⁴⁴. In that work, a three-point bend fixture was developed for in-situ bending of micron-sized samples with the load applied using a diamond nanoindentation tip machined to a wedge shape for loading (Fig. 7.2). The same geometry can be used to measure fracture toughness in EBC/CMCs, although in three-point bending the maximum stress occurs directly under the loading wedge. Since the multilayer materials may result in some difficulties in loading the sample symmetrically, machining a nanoindentation tip into a double-wedge tip, rather than a single-wedge tip, would allow for four-point bending. The maximum load in that case is evenly distributed between the loading pins and the setup can be less sensitive to exact placement of the interface at the center of a single loading wedge. The samples for such a test can be fabricated using focused ion beam (FIB) machining. The opportunity of this test at the small scale is enabled the small size of the bend beam, which should allow for beams to be fabricated with nearly ideal (or at least mostly controllable) interface orientation with respect to the beam dimensions. The small size scale can also be used to eliminate the effects of mechanical interlocking due to interface roughness. Finally, many more samples can be fabricated for micron-sized sample testing from a single coupon of EBC/CMC than can be fabricated for macroscale testing.

Successful interface toughness testing methods, among the techniques used in this work and suggested for further exploration, should be applied to additional samples in the baseline system. In particular, baseline samples steam-cycled for less than 100 hours should be tested,

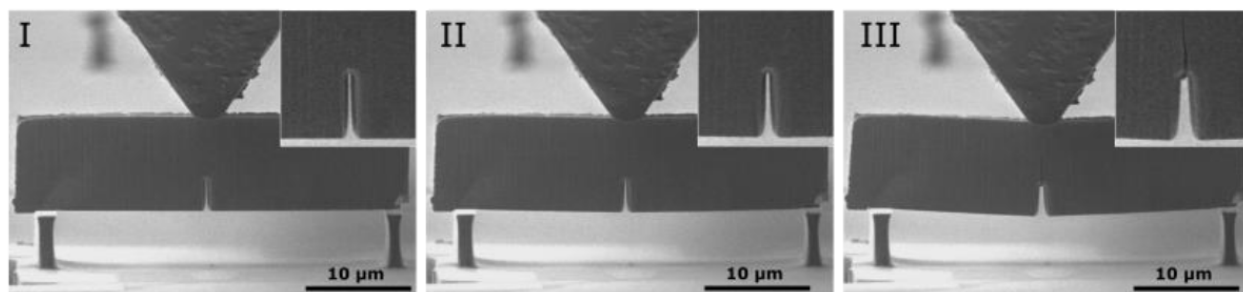


Figure 7.2: Nano/micro-scale three-point bend setup. Figure reprinted from Tertuliano et al.¹⁴⁵ with publisher permission.

in order to identify a cross-over point or transition TGO thickness (or range) from that of the annealed state to that of the post-steam cycling state. These methods can also be applied to the 6A and M2Y compositions to assess interface toughness in the dopant-modified systems. While interface toughness measurements in this work focused on the baseline system to explore the effect(s) of TGO thickness on interface toughness, the microstructural features and TGO modifications observed in Chapter 2 in 6A and M2Y imply different interface behavior than those observed in the baseline system. Interface toughness measurements can also be applied to next-generation EBC/CMC materials, with the work on the current-generation materials serving as the technical development and background work to support measurements in future multilayer systems.

7.2.4 Induction furnace and *in-situ* experiments

The motivation for developing the custom induction furnace was to perform *in-situ* oxidation testing of multilayer EBC/CMC materials at the synchrotron beamline. Steam cycling at Caltech and high-temperature measurements at the APS were both verified for this device. However, steam cycling and synchrotron measurements were not able to be combined in this work because of safety and scheduling constraints imposed due to the COVID-19 pandemic. Full implementation of steam cycling in the synchrotron beamline, using this furnace and either EBC/CMC samples or a similarly appropriate system, will complete the primary aim of this part of the work.

As next-generation EBCs and bondcoats are developed to permit increasing engine temperatures, *in-situ* experiments will have to reach the same high temperatures. The quartz tubing used for the custom induction furnace was observed to maintain its structure up to 1500–1600°C. As thermal and/or steam cycling reaches this temperature range, different tubing materials will be required for the furnace. Sapphire tubing, for example, would allow for furnace operation at temperatures near 2000°C.

For quartz tubing, the cristobalite scale observed and measured by WAXS must be accounted for as *in-situ* temperatures increase. Since β -cristobalite is the stable silica polymorph at high temperature, the conversion of fused silica to cristobalite should accelerate with increasing temperature. When the results of a given experiment are not obfuscated by the presence of cristobalite, the devitrification of the tubing will likely not be an issue unless the tubing fails, likely due to cracking from the transformation from β -cristobalite to α -cristobalite during steam cycling or other cooling. If cristobalite structure does interfere with experimental results, such as synchrotron measurements of cristobalite-bearing materials, then the tube furnace design will have to be altered to minimized cristobalite growth or new tubes will be required for experiments, on which there is no initial cristobalite scale.

As discussed in Chapter 6, the custom induction furnace permitted detailed measurements of CTE for the powders of $\text{Yb}_2\text{Si}_2\text{O}_7$ -based baseline, 6A, and M2Y composition. This information is useful for the design and engineering of coating materials, and texturing can potentially aid in minimizing thermal mismatch stresses. Further exploration of this concept can follow the work of Zimmerman et al. on texturing and thermal mismatch stresses in bulk Fe_2TiO_5 , where X-ray diffraction and pole figure measurements were used to assess crystallographic texture while microscopy was used to assess morphological texture¹⁴⁶. $\text{Yb}_2\text{Si}_2\text{O}_7$ does not show the same magnetic response as the Fe_2TiO_5 ¹⁴⁶, and so different processing methods would need to be used on the system at hand to produce crystallographic texturing. From the perspective of the custom furnace, the opportunity presented for materials design underscores the capabilities of rapid and accurate measurements enabled by the furnace. Measurement of stresses over a range of temperatures, enabled by rapid temperature changes and fast-sweep WAXS measurement methods at the synchrotron, will provide for detailed descriptions of stresses as they develop in the materials. This concept can be applied at various stages of bondcoat oxidation, as well, in order to expand the understanding of stresses along with TGO growth.

BIBLIOGRAPHY

1. Grondahl, C. M. & Tsuchiya, T. Performance Benefit Assessment of Ceramic Components in an MS9001FA Gas Turbine. *Journal of Engineering for Gas Turbines and Power* **123**, 513–519. ISSN: 0742-4795, 1528-8919. <https://asmedigitalcollection.asme.org/gasturbinespower/article/123/3/513/461365/Performance-Benefit-Assessment-of-Ceramic> (2021) (July 1, 2001).
2. *OST_R | BTS | Transtats* <https://www.transtats.bts.gov/fuel.asp?pn=1> (2022).
3. *FAA Aerospace Forecasts* Last Modified: 2022-03-24T15:10:36-0400. https://www.faa.gov/data_research/aviation/aerospace_forecasts/ (2022).
4. *Energy Content in common Energy Sources* https://www.engineeringtoolbox.com/energy-content-d_868.html (2022).
5. *U.S. energy facts explained - consumption and production - U.S. Energy Information Administration (EIA)* <https://www.eia.gov/energyexplained/us-energy-facts/> (2022).
6. Deal, B. E. & Grove, A. S. General Relationship for the Thermal Oxidation of Silicon. *Journal of Applied Physics* **36**, 3770–3778. ISSN: 0021-8979, 1089-7550. <http://aip.scitation.org/doi/10.1063/1.1713945> (2021) (Dec. 1965).
7. Opila, E. J., Smialek, J. L., Robinson, R. C., Fox, D. S. & Jacobson, N. S. SiC Recession Caused by SiO₂ Scale Volatility under Combustion Conditions: II, Thermodynamics and Gaseous-Diffusion Model. *Journal of the American Ceramic Society* **82**, 1826–1834. ISSN: 00027820, 15512916. <https://onlinelibrary.wiley.com/doi/10.1111/j.1151-2916.1999.tb02005.x> (2021) (July 1999).
8. More, K. L. *et al.* Exposure of Ceramics and Ceramic Matrix Composites in Simulated and Actual Combustor Environments. *Journal of Engineering for Gas Turbines and Power* **122**, 212–218 (2000).
9. Lee, K. Current status of environmental barrier coatings for Si-Based ceramics. *Surface and Coatings Technology* **133-134**, 1–7. ISSN: 02578972. <https://linkinghub.elsevier.com/retrieve/pii/S0257897200008896> (2022) (Nov. 2000).
10. Lee, K. N. *et al.* Upper Temperature Limit of Environmental Barrier Coatings Based on Mullite and BSAS. *Journal of the American Ceramic Society* **86**, 1299–1306. ISSN: 00027820, 15512916. <https://onlinelibrary.wiley.com/doi/10.1111/j.1151-2916.2003.tb03466.x> (2021) (Aug. 2003).
11. Stolzenburg, F. *Residual Stresses and Phase Transformations in Ytterbium Silicate Environmental Barrier Coatings* PhD thesis (Northwestern University, Evanston, IL, Dec. 2013). 203 pp.

12. Stolzenburg, F., Johnson, M., Lee, K., Jacobson, N. & Faber, K. The interaction of calcium–magnesium–aluminosilicate with ytterbium silicate environmental barrier materials. *Surface and Coatings Technology* **284**, 44–50. ISSN: 02578972. <https://linkinghub.elsevier.com/retrieve/pii/S0257897215005216> (2021) (Dec. 2015).
13. Stolzenburg, F. *et al.* The influence of calcium–magnesium–aluminosilicate deposits on internal stresses in Yb₂Si₂O₇ multilayer environmental barrier coatings. *Acta Materialia* **105**, 189–198. ISSN: 13596454. <https://linkinghub.elsevier.com/retrieve/pii/S1359645415301245> (2021) (Feb. 2016).
14. Schlichting, J. Oxygen transport through glass layers formed by a gel process. *Journal of Non-Crystalline Solids* **63**, 173–181. ISSN: 00223093. <https://linkinghub.elsevier.com/retrieve/pii/002230938490396X> (2021) (Feb. 1984).
15. Lee, K. N. Yb₂Si₂O₇ Environmental barrier coatings with reduced bond coat oxidation rates via chemical modifications for long life. *Journal of the American Ceramic Society* **102**, 1507–1521. ISSN: 00027820. <https://onlinelibrary.wiley.com/doi/10.1111/jace.15978> (2021) (Mar. 2019).
16. Padture, N. P. Thermal Barrier Coatings for Gas-Turbine Engine Applications. *Science* **296**, 280–284. ISSN: 00368075, 10959203. <https://www.sciencemag.org/lookup/doi/10.1126/science.1068609> (2021) (Apr. 12, 2002).
17. Levi, C. G., Hutchinson, J. W., Vidal-Sétif, M.-H. & Johnson, C. A. Environmental degradation of thermal-barrier coatings by molten deposits. *MRS Bulletin* **37**, 932–941. ISSN: 0883-7694, 1938-1425. <http://link.springer.com/10.1557/mrs.2012.230> (2021) (Oct. 2012).
18. Kingery, W. D., Bowen, H. K. & Uhlmann, D. R. *Introduction to Ceramics* 2nd. 1056 pp. ISBN: 978-0-471-47860-7 (John Wiley & Sons, Inc., New York, NY, May 1976).
19. Schmidt, S. *et al.* Advanced ceramic matrix composite materials for current and future propulsion technology applications. *Acta Astronautica* **55**, 409–420. ISSN: 00945765. <https://linkinghub.elsevier.com/retrieve/pii/S0094576504001626> (2021) (Aug. 2004).
20. Rosso, M. Ceramic and metal matrix composites: Routes and properties. *Journal of Materials Processing Technology* **175**, 364–375. ISSN: 09240136. <https://linkinghub.elsevier.com/retrieve/pii/S092401360500419X> (2022) (June 2006).
21. Dressler, W. & Riedel, R. Progress in Silicon-Based Non-Oxide Structural Ceramics. *International Journal of Refractory Metals and Hard Materials* **15**, 13–47 (1997).
22. Shackelford, J. F. & Alexander, W. *CRC Materials Science and Engineering Handbook* 3rd. ISBN: 0-8493-2696-6 (CRC Press, Boca Raton, FL, 2001).
23. *Inconel 718* <https://www.espimetals.com/index.php/technical-data/91-inconel-718> (2022).
24. Callister, W. D. & Rethwisch, D. G. *Materials science and engineering: an introduction* 9th edition. 960 pp. ISBN: 978-1-118-32457-8 (Wiley, Hoboken, NJ, 2014).

25. *Aluminum 2024-T3* <http://www.matweb.com/search/DataSheet.aspx?MatGUID=57483b4d782940faaf12964a1821fb61&ckck=1> (2022).
26. *Titanium Ti-6Al-4V (Grade 5), Annealed Bar* <http://www.matweb.com/search/DataSheet.aspx?MatGUID=10d463eb3d3d4ff48fc57e0ad1037434> (2022).
27. *AISI 4340 Alloy Steel (UNS G43400)* AZoM.com. Section: Materials Article. <https://www.azom.com/article.aspx?ArticleID=6772> (2022).
28. Xu, Y., Cheng, L., Zhang, L., Yin, X. & Yin, H. High performance 3D textile Hi-Nicalon SiC/SiC composites by chemical vapor infiltration. *Ceramics International* **27**, 565–570. ISSN: 02728842. <https://linkinghub.elsevier.com/retrieve/pii/S0272884201000025> (2021) (Jan. 2001).
29. Šajgalik, P., Dusza, J. & Hoffmann, M. J. Relationship between Microstructure, Toughening Mechanisms, and Fracture Toughness of Reinforced Silicon Nitride Ceramics. *Journal of the American Ceramic Society* **78**, 2619–2624. ISSN: 00027820. <https://onlinelibrary.wiley.com/doi/10.1111/j.1151-2916.1995.tb08031.x> (2021) (Oct. 1995).
30. Gibson, I. R., Dransfield, G. P. & Gibson, I. R. Sinterability of commercial 8 mol% yttria-stabilized zirconia powders and the effect of sintered density on the ionic conductivity. *Journal of Materials Science* **33**, 4297–4305. ISSN: 0022-2461. <http://link.springer.com/10.1023/A:1004435504482> (2022) (Sept. 1998).
31. Sakuma, T., Yoshizawa, Y.-I. & Suto, H. The microstructure and mechanical properties of yttria-stabilized zirconia prepared by arc-melting. *Journal of Materials Science* **20**, 2399–2407. ISSN: 0022-2461, 1573-4803. <http://link.springer.com/10.1007/BF00556069> (2022) (July 1985).
32. *Zirconium Oxide, Zirconia, ZrO 2* <http://www.matweb.com/search/datasheet.aspx?MatGUID=0742ddaddf80467fb6532e025c694e89&ckck=1> (2022).
33. Chantikul, P., Anstis, G. R., Lawn, B. R. & Marshall, D. B. A Critical Evaluation of Indentation Techniques for Measuring Fracture Toughness: II, Strength Method. *Journal of the American Ceramic Society* **64**, 539–543. ISSN: 0002-7820, 1551-2916. <https://onlinelibrary.wiley.com/doi/10.1111/j.1151-2916.1981.tb10321.x> (2021) (Sept. 1981).
34. Chantikul, P., Bennison, S. J. & Lawn, B. R. Role of Grain Size in the Strength and R-Curve Properties of Alumina. *Journal of the American Ceramic Society* **73**, 2419–2427. ISSN: 0002-7820, 1551-2916. <https://onlinelibrary.wiley.com/doi/10.1111/j.1151-2916.1990.tb07607.x> (2022) (Aug. 1990).
35. Patnaik, P. *Handbook of inorganic chemicals* 1086 pp. ISBN: 978-0-07-049439-8 (McGraw-Hill, New York, 2003).
36. Jorgensen, P. J. Effect of an Electric Field on Silicon Oxidation. *The Journal of Chemical Physics* **37**, 874–877. ISSN: 0021-9606, 1089-7690. <http://aip.scitation.org/doi/10.1063/1.1733177> (2022) (Aug. 15, 1962).

37. Opila, E. J. & Hann, R. E. Paralineer Oxidation of CVD SiC in Water Vapor. *Journal of the American Ceramic Society* **80**, 197–205. ISSN: 00027820. <https://onlinelibrary.wiley.com/doi/10.1111/j.1151-2916.1997.tb02810.x> (2022) (Jan. 1997).
38. Motzfeldt, K. On the Rates of Oxidation of Silicon and of Silicon Carbide in Oxygen, and Correlation with Permeability of Silica Glass. *Acta Chemica Scandinavica* **18**, 1596–1606 (1964).
39. Zheng, Z., Tressler, R. E. & Spear, K. E. Oxidation of Single-Crystal Silicon Carbide: Part II . Kinetic Model. *Journal of The Electrochemical Society* **137**, 2812–2816. ISSN: 0013-4651, 1945-7111. <https://iopscience.iop.org/article/10.1149/1.2087080> (2022) (Sept. 1, 1990).
40. Luthra, K. L. Some New Perspectives on Oxidation of Silicon Carbide and Silicon Nitride. *Journal of the American Ceramic Society* **74**, 1095–1103. ISSN: 0002-7820, 1551-2916. <https://onlinelibrary.wiley.com/doi/10.1111/j.1151-2916.1991.tb04348.x> (2022) (May 1991).
41. Costello, J. A. & Tressler, R. E. Oxidation Kinetics of Silicon Carbide Crystals and Ceramics: I, In Dry Oxygen. *Journal of the American Ceramic Society* **69**, 674–681. ISSN: 0002-7820, 1551-2916. <https://onlinelibrary.wiley.com/doi/10.1111/j.1151-2916.1986.tb07470.x> (2022) (Sept. 1986).
42. Opila, E. J. Variation of the Oxidation Rate of Silicon Carbide with Water-Vapor Pressure. *Journal of the American Ceramic Society* **82**, 625–636. ISSN: 00027820, 15512916. <https://onlinelibrary.wiley.com/doi/10.1111/j.1151-2916.1999.tb01810.x> (2022) (1999).
43. Wilson, M. & Opila, E. A Review of SiC Fiber Oxidation with a New Study of Hi-Nicalon SiC Fiber Oxidation: A Review of SiC Fiber Oxidation... *Advanced Engineering Materials* **18**, 1698–1709. ISSN: 14381656. <https://onlinelibrary.wiley.com/doi/10.1002/adem.201600166> (2021) (Oct. 2016).
44. Opila, E. J. & Boyd, M. K. Oxidation of SiC Fiber-Reinforced SiC Matrix Composites with a BN Interphase. *Materials Science Forum* **696**, 342–347. ISSN: 1662-9752. <https://www.scientific.net/MSF.696.342> (2022) (Sept. 2011).
45. More, K. L., Tortorelli, P. F., Ferber, M. K. & Keiser, J. R. Observations of Accelerated Silicon Carbide Recession by Oxidation at High Water-Vapor Pressures. *Journal of the American Ceramic Society* **83**, 211–13. ISSN: 00027820, 15512916. <https://onlinelibrary.wiley.com/doi/10.1111/j.1151-2916.2000.tb01172.x> (2022) (Jan. 2000).
46. Opila, E. J. Oxidation and Volatilization of Silica Formers in Water Vapor. *Journal of the American Ceramic Society* **86**, 1238–1248. ISSN: 00027820, 15512916. <https://onlinelibrary.wiley.com/doi/10.1111/j.1151-2916.2003.tb03459.x> (2022) (Aug. 2003).

47. Miller, R., Levine, S. & Hodge, P. *Thermal Barrier Coatings for Superalloys in Superalloys 1980 (Fourth International Symposium)* Superalloys (TMS, 1980), 473–480. ISBN: 978-0-87170-102-2. http://www.tms.org/Superalloys/10.7449/1980/Superalloys_1980_473_480.pdf (2022).
48. Hodge, P. E., Stecura, S., Gedwill, M. A., Zaplatynsky, I. & Levine, S. R. Thermal barrier coatings: Burner rig hot corrosion test results. *Journal of Materials for Energy Systems* **1**, 47–58. ISSN: 0162-9719. <http://link.springer.com/10.1007/BF02833361> (2022) (Mar. 1980).
49. Miller, R. A. & Lowell, C. E. Failure mechanisms of thermal barrier coatings exposed to elevated temperatures. *Thin Solid Films* **95**, 265–273. ISSN: 00406090. <https://linkinghub.elsevier.com/retrieve/pii/0040609082900190> (2022) (Sept. 1982).
50. Hasselman, D. P. H. *et al.* Thermal Diffusivity and Conductivity of Dense Polycrystalline ZrO₂ Ceramics: A Survey. *American Ceramic Society Bulletin* **66**, 8 (1987).
51. Stott, F., Taylor, R. & de Wet, D. *The effects of molten silicate deposits on the stability of thermal barrier coatings for turbine applications at very high temperatures in Proceedings of Advanced Materials* International Society for the Advancement of Material and Process Engineering (SAMPE) Metals and Metals Processing Conference (Toronto, Canada, 1992), M92–M101. ISBN: 0-938994-66-2.
52. Klemens, P. G. & Tewordt, L. Reduction of the Lattice Thermal Conductivity of Superconductors due to Point Defects. *Reviews of Modern Physics* **36**, 118–120. ISSN: 0034-6861. <https://link.aps.org/doi/10.1103/RevModPhys.36.118> (2022) (Jan. 1, 1964).
53. Rahmel, A. High temperature corrosion. Von P. Kofstad. Elsevier Applied Science Publishers Ltd., London - New York, 1988. 558 S., zahlr. Abb. u. Tab., Preis: £ 68.00. *Materials and Corrosion/Werkstoffe und Korrosion* **39**, 354–354. ISSN: 0947-5117, 1521-4176. <https://onlinelibrary.wiley.com/doi/10.1002/maco.19880390713> (2022) (July 1988).
54. Schmitt, M. P., Harder, B. J. & Wolfe, D. E. Process-structure-property relations for the erosion durability of plasma spray-physical vapor deposition (PS-PVD) thermal barrier coatings. *Surface and Coatings Technology* **297**, 11–18. ISSN: 02578972. <https://linkinghub.elsevier.com/retrieve/pii/S025789721630278X> (2022) (July 2016).
55. Ridley, M., Gaskins, J., Hopkins, P. & Opila, E. Tailoring thermal properties of multi-component rare earth monosilicates. *Acta Materialia* **195**, 698–707. ISSN: 13596454. <https://linkinghub.elsevier.com/retrieve/pii/S1359645420304365> (2022) (Aug. 2020).
56. Lee, K. N., Jacobson, N. S. & Miller, R. A. Refractory Oxide Coatings on SiC Ceramics. *MRS Bulletin* **19**, 35–38. ISSN: 0883-7694, 1938-1425. <http://link.springer.com/10.1557/S088376940004820X> (2022) (Oct. 1994).

57. Shah, A. R., Brewer, D. N. & Murthy, P. L. N. Life Prediction Issues in Thermal/Environmental Barrier Coatings in Ceramic Matrix Composites. *National Aeronautics and Space Administration*, 20 (2001).
58. Lee, K. N. & van Roode, M. Environmental barrier coatings enhance performance of SiC/SiC ceramic matrix composites. *American Ceramic Society Bulletin* **98**, 8 (2019).
59. Harder, B. J., Almer, J. D., Weyant, C. M., Lee, K. N. & Faber, K. T. Residual Stress Analysis of Multilayer Environmental Barrier Coatings. *Journal of the American Ceramic Society* **92**, 452–459. ISSN: 00027820, 15512916. <https://onlinelibrary.wiley.com/doi/10.1111/j.1551-2916.2008.02888.x> (2021) (Feb. 2009).
60. Steibel, J. Ceramic matrix composites taking flight at GE Aviation. *Am. Ceram. Soc. Bull* **98**, 30–33 (2019).
61. *Plasma Spraying* <http://www.amphardchrome.co.uk/plasma-spraying.php> (2022).
62. Price, J., van Roode, M. & Stala, C. Ceramic Oxide-Coated Silicon Carbide for High Temperature Corrosive Environments. *Key Engineering Materials* **72-74**, 71–84. ISSN: 1662-9795. <https://www.scientific.net/KEM.72-74.71> (2022) (Jan. 1992).
63. Lee, K. N. Key Durability Issues With Mullite-Based Environmental Barrier Coatings for Si-Based Ceramics. *Journal of Engineering for Gas Turbines and Power* **122**, 632–636. ISSN: 0742-4795, 1528-8919. <https://asmedigitalcollection.asme.org/gasturbinespower/article/122/4/632/463324/Key-Durability-Issues-With-MulliteBased> (2021) (Oct. 1, 2000).
64. Lee, K. N. & Miller, R. A. Development and environmental durability of mullite and mullite/YSZ dual layer coatings for SiC and Si₃N₄ ceramics. *Surface and Coatings Technology* **86-87**, 142–148. ISSN: 02578972. <https://linkinghub.elsevier.com/retrieve/pii/S0257897296030745> (2022) (Dec. 1996).
65. *Advances in ceramic-matrix composites IV* (eds Bansal, N. P., Singh, J. P. & Society, A. C.) *Ceramic transactions* **v. 96**. Meeting Name: Ceramic-Matrix Composites Symposium OCLC: ocm41462823 (American Ceramic Society, Westerville, Ohio, 1999). 465 pp. ISBN: 978-1-57498-059-2.
66. Lee, K. N., Fox, D. S. & Bansal, N. P. Rare earth silicate environmental barrier coatings for SiC/SiC composites and Si₃N₄ ceramics. *Journal of the European Ceramic Society* **25**, 1705–1715. ISSN: 09552219. <https://linkinghub.elsevier.com/retrieve/pii/S095522190400531X> (2021) (Jan. 2005).
67. Lee, K. N. & King, D. *Degradation of Environmental Barrier Coatings (EBC) Due to Chemical and Thermal Expansion Incompatibility* in. Electrochemical Society Meeting (Washington D.C., 2001), 12.
68. Harder, B. J., Almer, J., Lee, K. N. & Faber, K. T. *In situ* stress analysis of multilayer environmental barrier coatings. *Powder Diffraction* **24**, 94–98. ISSN: 0885-7156, 1945-7413. https://www.cambridge.org/core/product/identifier/S088571560001172/type/journal_article (2021) (June 2009).

69. Harder, B. & Faber, K. Transformation kinetics in plasma-sprayed barium- and strontium-doped aluminosilicate (BSAS). *Scripta Materialia* **62**, 282–285. ISSN: 13596462. <https://linkinghub.elsevier.com/retrieve/pii/S1359646209007313> (2022) (Mar. 2010).
70. Costa, G. C. & Jacobson, N. S. Mass spectrometric measurements of the silica activity in the Yb₂O₃–SiO₂ system and implications to assess the degradation of silicate-based coatings in combustion environments. *Journal of the European Ceramic Society* **35**, 4259–4267. ISSN: 09552219. <https://linkinghub.elsevier.com/retrieve/pii/S0955221915300649> (2021) (Dec. 2015).
71. *REE - Rare Earth Elements - Metals, Minerals, Mining, Uses* <https://geology.com/articles/rare-earth-elements/> (2022).
72. Gambogi, J. *U.S. Geological Survey, Mineral Commodity Summaries, January 2021* (United States Geological Survey, Jan. 2021), 2. <https://pubs.usgs.gov/periodicals/mcs2021/mcs2021-rare-earths.pdf>.
73. Survey, U. S. G. *ree-trends.pdf* <https://s3-us-west-2.amazonaws.com/prd-wret/assets/palladium/production/mineral-pubs/rare-earth/ree-trends.pdf> (2022).
74. Ridley, M. J. & Opila, E. J. Thermomechanical and thermochemical stability of HfSiO₄ for environmental barrier coating applications. *Journal of the American Ceramic Society* **104**, 3593–3602. ISSN: 0002-7820, 1551-2916. <https://onlinelibrary.wiley.com/doi/10.1111/jace.17729> (2022) (July 2021).
75. Ridley, M. & Opila, E. Thermochemical stability and microstructural evolution of Yb₂Si₂O₇ in high-velocity high-temperature water vapor. *Journal of the European Ceramic Society* **41**, 3141–3149. ISSN: 09552219. <https://linkinghub.elsevier.com/retrieve/pii/S0955221920304386> (2022) (May 2021).
76. Lepple, M. *et al.* Thermochemistry and phase stability of the polymorphs of yttrium tantalate, YTaO₄. *Journal of the European Ceramic Society* **41**, 1629–1638. ISSN: 09552219. <https://linkinghub.elsevier.com/retrieve/pii/S0955221920308529> (2022) (Feb. 2021).
77. Jackson, R. W., Zaleski, E. M., Hazel, B. T., Begley, M. R. & Levi, C. G. Response of molten silicate infiltrated Gd₂Zr₂O₇ thermal barrier coatings to temperature gradients. *Acta Materialia* **132**, 538–549. ISSN: 13596454. <https://linkinghub.elsevier.com/retrieve/pii/S135964541730280X> (2022) (June 2017).
78. Holgate, C. S., Seward, G. G., Ericks, A. R., Poerschke, D. L. & Levi, C. G. Dissolution and diffusion kinetics of yttria-stabilized zirconia into molten silicates. *Journal of the European Ceramic Society* **41**, 1984–1994. ISSN: 09552219. <https://linkinghub.elsevier.com/retrieve/pii/S0955221920308694> (2022) (Mar. 2021).
79. Summers, W. D. *et al.* Roles of composition and temperature in silicate deposit-induced recession of yttrium disilicate. *Acta Materialia* **160**, 34–46. ISSN: 13596454. <https://linkinghub.elsevier.com/retrieve/pii/S1359645418306803> (2022) (Nov. 2018).

80. Zhao, H., Richards, B. T., Levi, C. G. & Wadley, H. N. Molten silicate reactions with plasma sprayed ytterbium silicate coatings. *Surface and Coatings Technology* **288**, 151–162. ISSN: 02578972. <https://linkinghub.elsevier.com/retrieve/pii/S0257897215304801> (2022) (Feb. 2016).
81. Grant, K. M., Krämer, S., Seward, G. G. E. & Levi, C. G. Calcium-Magnesium Alumino-Silicate Interaction with Yttrium Monosilicate Environmental Barrier Coatings: YMS Interaction with YMS EBCs. *Journal of the American Ceramic Society* **93**, 3504–3511. ISSN: 00027820. <https://onlinelibrary.wiley.com/doi/10.1111/j.1551-2916.2010.03916.x> (2022) (Oct. 2010).
82. Harder, B. J., Ramirez-Rico, J., Almer, J. D., Lee, K. N. & Faber, K. T. Chemical and Mechanical Consequences of Environmental Barrier Coating Exposure to Calcium-Magnesium-Aluminosilicate: Chemical and Mechanical Consequences of EBC Exposure to CMAS. *Journal of the American Ceramic Society* **94**, s178–s185. ISSN: 00027820. <https://onlinelibrary.wiley.com/doi/10.1111/j.1551-2916.2011.04448.x> (2021) (June 2011).
83. Harder, B. J., Zhu, D., Schmitt, M. P. & Wolfe, D. E. *High Temperature Multilayer Environmental Barrier Coatings Deposited Via Plasma Spray-Physical Vapor Deposition* Materials Science and Technology. Pittsburgh, PA, Oct. 12, 2014. <https://ntrs.nasa.gov/api/citations/20150000326/downloads/20150000326.pdf>.
84. Lipiak, G., Bussmann, S., Steinwachs, C. & Lüttenberg, A. *Lifetime Extension for SIEMENS Gas Turbines* 2006.
85. Lee, E. Y. Diffusional Interactions and Reactions between a Partially Stabilized Zirconia Thermal Barrier Coating and the NiCrAlY Bond Coat, 7.
86. Borom, M. P., Johnson, C. A. & Peluso, L. A. Role of environmental deposits and operating surface temperature in spallation of air plasma sprayed thermal barrier coatings, 11.
87. Krämer, S., Yang, J., Levi, C. G. & Johnson, C. A. Thermochemical Interaction of Thermal Barrier Coatings with Molten CaO-MgO-Al₂O₃-SiO₂ (CMAS) Deposits. *Journal of the American Ceramic Society* **89**, 3167–3175. ISSN: 0002-7820, 1551-2916. <https://onlinelibrary.wiley.com/doi/10.1111/j.1551-2916.2006.01209.x> (2022) (Oct. 2006).
88. Evans, A., Mumm, D., Hutchinson, J., Meier, G. & Pettit, F. Mechanisms controlling the durability of thermal barrier coatings. *Progress in Materials Science* **46**, 505–553. ISSN: 00796425. <https://linkinghub.elsevier.com/retrieve/pii/S0079642500000207> (2021) (Jan. 2001).
89. Schlichting, K., Padture, N., Jordan, E. & Gell, M. Failure modes in plasma-sprayed thermal barrier coatings. *Materials Science and Engineering: A* **342**, 120–130. ISSN: 09215093. <https://linkinghub.elsevier.com/retrieve/pii/S0921509302002514> (2022) (Feb. 2003).

90. Lipkin, D. M. & Clarke, D. R. Measurement of the stress in oxide scales formed by oxidation of alumina-forming alloys. *Oxidation of Metals* **45**, 267–280. ISSN: 0030-770X, 1573-4889. <http://link.springer.com/10.1007/BF01046985> (2022) (Apr. 1996).
91. Wang, Y., Sohn, Y., Fan, Y., Zhang, L. & An, L. Oxygen Diffusion Through Al-Doped Amorphous SiO₂. *Journal of Phase Equilibria & Diffusion* **27**, 671–675. ISSN: 15477037, 00000000. <http://openurl.ingenta.com/content/xref?genre=article&issn=1547-7037&volume=27&issue=6&spage=671> (2022) (Dec. 1, 2006).
92. Lu, Y., Luo, L., Liu, J., Zhu, C. & Wang, Y. Failure Mechanism Associated with the Thermally Grown Silica Scale in Environmental Barrier Coated C/SiC Composites. *Journal of the American Ceramic Society* **99** (ed Jacobson, N.) 2713–2719. ISSN: 00027820. <https://onlinelibrary.wiley.com/doi/10.1111/jace.14273> (2022) (Aug. 2016).
93. Zhang, X. *et al.* Oxidation and thermal shock resistant properties of Al-modified environmental barrier coating on SiCf/SiC composites. *Ceramics International* **43**, 13075–13082. ISSN: 02728842. <https://linkinghub.elsevier.com/retrieve/pii/S0272884217313810> (2022) (Nov. 2017).
94. Lee, K. N., Eldridge, J. I. & Robinson, R. C. Residual Stresses and Their Effects on the Durability of Environmental Barrier Coatings for SiC Ceramics. *Journal of the American Ceramic Society* **88**, 3483–3488. ISSN: 0002-7820, 1551-2916. <https://onlinelibrary.wiley.com/doi/10.1111/j.1551-2916.2005.00640.x> (2021) (Dec. 2005).
95. Weyant, C. M., Faber, K. T., Almer, J. D. & Guiheen, J. V. Residual Stress and Microstructural Evolution in Environmental Barrier Coatings of Tantalum Oxide Alloyed with Aluminum Oxide and Lanthanum Oxide. *Journal of the American Ceramic Society* **89**, 971–978. ISSN: 0002-7820, 1551-2916. <https://onlinelibrary.wiley.com/doi/10.1111/j.1551-2916.2005.00830.x> (2021) (Mar. 2006).
96. Withers, P. & Bhadeshia, H. Residual stress. Part 1 – Measurement techniques. *Materials Science and Technology* **17**, 355–365. ISSN: 0267-0836, 1743-2847. <http://www.tandfonline.com/doi/full/10.1179/026708301101509980> (2022) (Apr. 2001).
97. Weyant, C. M., Faber, K. T., Almer, J. D. & Guiheen, J. V. Residual Stress and Microstructural Evolution in Tantalum Oxide Coatings on Silicon Nitride: Residual Stress and Microstructure in Tantalum Oxide Coatings. *Journal of the American Ceramic Society* **88**, 2169–2176. ISSN: 00027820, 15512916. <https://onlinelibrary.wiley.com/doi/10.1111/j.1551-2916.2005.00396.x> (2021) (June 1, 2005).
98. Weyant, C., Almer, J. & Faber, K. Through-thickness determination of phase composition and residual stresses in thermal barrier coatings using high-energy X-rays. *Acta Materialia* **58**, 943–951. ISSN: 13596454. <https://linkinghub.elsevier.com/retrieve/pii/S1359645409006892> (2021) (Feb. 2010).

99. Stolzenburg, F., Almer, J., Lee, K. N., Harder, B. J. & Faber, K. T. *Stresses in Ytterbium Silicate Multilayer Environmental Barrier Coatings* in. Denver X-ray Conference (Denver, CO, 2011), 11. <https://resolver.caltech.edu/CaltechAUTHORS:20140912-093131896>.
100. Siddiqui, S. F. *et al.* Synchrotron X-ray measurement techniques for thermal barrier coated cylindrical samples under thermal gradients. *Review of Scientific Instruments* **84**, 083904. ISSN: 0034-6748, 1089-7623. <http://aip.scitation.org/doi/10.1063/1.4817543> (2021) (Aug. 2013).
101. Richards, B. T., Begley, M. R. & Wadley, H. N. Mechanisms of Ytterbium Monosilicate/Mullite/Silicon Coating Failure During Thermal Cycling in Water Vapor. *Journal of the American Ceramic Society* **98** (ed Smialek, J. L.) 4066–4075. ISSN: 0002-7820, 1551-2916. <https://onlinelibrary.wiley.com/doi/10.1111/jace.13792> (2021) (Dec. 2015).
102. Shannon, R. D. Revised effective ionic radii and systematic studies of interatomic distances in halides and chalcogenides. *Acta Crystallographica Section A* **32**, 751–767. ISSN: 0567-7394. <http://scripts.iucr.org/cgi-bin/paper?S0567739476001551> (2022) (Sept. 1, 1976).
103. Lee, K., Garg, A. & Jennings, W. Effects of the chemistry of coating and substrate on the steam oxidation kinetics of environmental barrier coatings for ceramic matrix composites. *Journal of the European Ceramic Society* **41**, 5675–5685. ISSN: 09552219. <https://linkinghub.elsevier.com/retrieve/pii/S0955221921002909> (2022) (Sept. 2021).
104. Aumento, F. Stability, lattice parameters, and thermal expansion of beta-cristobalite. *American Mineralogist* **51**, 1167–1176. ISSN: 0003-004X. (2022) (July 1, 1966).
105. Thomas, E. S. *et al.* Further Investigation of the Stabilization of beta-Cristobalite. *Journal of the American Ceramic Society* **77**, 49–56. ISSN: 0002-7820, 1551-2916. <https://onlinelibrary.wiley.com/doi/10.1111/j.1151-2916.1994.tb06956.x> (2022) (Jan. 1994).
106. R. C. Breneman. Hysteresis upon Repeated Cycling through the Beta-Alpha Cristobalite Transformation. <https://doi.org/10.4416/JCST2014-00048> (2022) (2015).
107. Richards, B. T., Sehr, S., de Franqueville, F., Begley, M. R. & Wadley, H. N. Fracture mechanisms of ytterbium monosilicate environmental barrier coatings during cyclic thermal exposure. *Acta Materialia* **103**, 448–460. ISSN: 13596454. <https://linkinghub.elsevier.com/retrieve/pii/S1359645415300197> (2021) (Jan. 2016).
108. Rodríguez-Viejo, J., Sibieude, F., Clavaguera-Mora, M. T. & Monty, C. ¹⁸O diffusion through amorphous SiO₂ and cristobalite. *Applied Physics Letters* **63**, 1906–1908. ISSN: 0003-6951, 1077-3118. <http://aip.scitation.org/doi/10.1063/1.110644> (2022) (Oct. 4, 1993).

109. Hsueh, C. H., De Jonghe, L. C. & Lee, C. S. Modeling of Thermal Stresses in Joining Two Layers with Multi- and Graded Interlayers. *Journal of the American Ceramic Society* **89**, 251–257. ISSN: 0002-7820, 1551-2916. <https://onlinelibrary.wiley.com/doi/10.1111/j.1551-2916.2005.00658.x> (2021) (Jan. 2006).
110. *Properties of crystalline silicon* (eds Hull, R. & of Electrical Engineers, I.) *EMIS datareviews series* **20** (INSPEC, London, 1999). 1016 pp. ISBN: 978-0-85296-933-5.
111. Pabst, W. & Gregorová, E. Elastic Properties of Silica Polymorphs – A Review, 18 (2013).
112. Vook, R. W. & Witt, F. Thermally Induced Strains in Evaporated Films. *Journal of Applied Physics* **36**, 2169–2171. ISSN: 0021-8979, 1089-7550. <http://aip.scitation.org/doi/10.1063/1.1714442> (2022) (July 1965).
113. He, B. B. *Two-dimensional x-ray diffraction* OCLC: ocn303927987. 426 pp. ISBN: 978-0-470-22722-0 (Wiley, Hoboken, N.J, 2009).
114. Seltzer, S. *Tables of X-Ray Mass Attenuation Coefficients and Mass Energy-Absorption Coefficients, NIST Standard Reference Database 126* Type: dataset. 1995. <http://www.nist.gov/pml/data/xraycoef/index.cfm> (2022).
115. Almer, J. D. & Winholtz, R. A. *Springer handbook of experimental solid mechanics* OCLC: ocn213479617. 1097 pp. ISBN: 978-0-387-26883-5 (Springer, Berlin, 2008).
116. Fauchais, P. Understanding plasma spraying. *Journal of Physics D: Applied Physics* **37**, R86–R108. ISSN: 0022-3727, 1361-6463. <https://iopscience.iop.org/article/10.1088/0022-3727/37/9/R02> (2022) (May 7, 2004).
117. Momma, K. & Izumi, F. *VESTA 3* for three-dimensional visualization of crystal, volumetric and morphology data. *Journal of Applied Crystallography* **44**, 1272–1276. ISSN: 0021-8898. <http://scripts.iucr.org/cgi-bin/paper?S0021889811038970> (2022) (Dec. 1, 2011).
118. Ming-Yuan, H. & Hutchinson, J. W. Crack deflection at an interface between dissimilar elastic materials. *International Journal of Solids and Structures* **25**, 1053–1067. ISSN: 00207683. <https://linkinghub.elsevier.com/retrieve/pii/0020768389900218> (2021) (1989).
119. Bhattacharya, A. K., Petrovic, J. J. & Danforth, S. C. Indentation Method for Determining the Macroscopic Fracture Energy of Brittle Bimaterial Interfaces. *Journal of the American Ceramic Society* **75**, 413–417. ISSN: 0002-7820, 1551-2916. <https://onlinelibrary.wiley.com/doi/10.1111/j.1151-2916.1992.tb08195.x> (2021) (Feb. 1992).
120. He, M. Y., Evans, A. G. & Hutchinson, J. W. Crack deflection at an interface between dissimilar elastic materials: Role of residual stresses. *International Journal of Solids and Structures* **31**, 3443–3455. ISSN: 00207683. <https://linkinghub.elsevier.com/retrieve/pii/0020768394900256> (2021) (Dec. 1994).

121. Palmqvist, S. Rißbildungsarbeit bei Vickers-Eindrücken als Maß für die Zähigkeit von Hartmetallen. *Archiv für das Eisenhüttenwesen* **33**, 629–634. ISSN: 00038962. <https://onlinelibrary.wiley.com/doi/10.1002/srin.196203379> (2022) (Sept. 1962).
122. Anstis, G., Chantikul, P., Lawn, B. & Marshall, D. A Critical Evaluation of Indentation Techniques for Measuring Fracture Toughness: I, Direct Crack Measurements. *Journal of the American Ceramic Society* **64**, 533–538. ISSN: 0002-7820, 1551-2916. <https://onlinelibrary.wiley.com/doi/10.1111/j.1151-2916.1981.tb10320.x> (2021) (Sept. 1981).
123. Lawn, B. R., Evans, A. G. & Marshall, D. B. Elastic/Plastic Indentation Damage in Ceramics: The Median/Radial Crack System. *Journal of the American Ceramic Society* **63**, 574–581. ISSN: 0002-7820, 1551-2916. <https://onlinelibrary.wiley.com/doi/10.1111/j.1151-2916.1980.tb10768.x> (2022) (Sept. 1980).
124. *Knoop Hardness Testing Method* Buehler, an ITW Company. <https://www.buehler.com/knoop-hardness-testing.php> (2022).
125. Glinicki, M. A. & Zielinski, M. Depth-sensing indentation method for evaluation of efficiency of secondary cementitious materials. *Cement and Concrete Research* **34**, 721–724. ISSN: 00088846. <https://linkinghub.elsevier.com/retrieve/pii/S0008884603003715> (2022) (Apr. 2004).
126. Marshall, D. B., Noma, T. & Evans, A. G. A Simple Method for Determining Elastic-Modulus-to-Hardness Ratios using Knoop Indentation Measurements. *Journal of the American Ceramic Society* **65**, c175–c176. ISSN: 0002-7820, 1551-2916. <https://onlinelibrary.wiley.com/doi/10.1111/j.1151-2916.1982.tb10357.x> (2021) (Oct. 1982).
127. Scholz, T., Schneider, G. A., Muñoz-Saldaña, J. & Swain, M. V. Fracture toughness from submicron derived indentation cracks. *Applied Physics Letters* **84**, 3055–3057. ISSN: 0003-6951, 1077-3118. <http://aip.scitation.org/doi/10.1063/1.1711164> (2022) (Apr. 19, 2004).
128. Bor, B., Giuntini, D., Domènech, B., Swain, M. V. & Schneider, G. A. Nanoindentation-based study of the mechanical behavior of bulk supercrystalline ceramic-organic nanocomposites. *Journal of the European Ceramic Society* **39**, 3247–3256. ISSN: 09552219. <https://linkinghub.elsevier.com/retrieve/pii/S0955221919302122> (2022) (Aug. 2019).
129. *SURFACE Nanolab ...always one step ahead* <https://www.surface-tec.com/nanotips.php> (2022).
130. Harding, D. S., Oliver, W. C. & Pharr, G. M. Cracking During Nanoindentation and its Use in the Measurement of Fracture Toughness. *MRS Proceedings* **356**, 663. ISSN: 0272-9172, 1946-4274. <http://link.springer.com/10.1557/PROC-356-663> (2022) (1994).

131. Lee, J., Gao, Y., Johanns, K. & Pharr, G. Cohesive interface simulations of indentation cracking as a fracture toughness measurement method for brittle materials. *Acta Materialia* **60**, 5448–5467. ISSN: 13596454. <https://linkinghub.elsevier.com/retrieve/pii/S1359645412004594> (2022) (Sept. 2012).
132. Sebastiani, M., Johanns, K., Herbert, E. & Pharr, G. Measurement of fracture toughness by nanoindentation methods: Recent advances and future challenges. *Current Opinion in Solid State and Materials Science* **19**, 324–333. ISSN: 13590286. <https://linkinghub.elsevier.com/retrieve/pii/S1359028615000285> (2022) (Dec. 2015).
133. Bruns, S., Petho, L., Minnert, C., Michler, J. & Durst, K. Fracture toughness determination of fused silica by cube corner indentation cracking and pillar splitting. *Materials & Design* **186**, 108311. ISSN: 02641275. <https://linkinghub.elsevier.com/retrieve/pii/S026412751930749X> (2022) (Jan. 2020).
134. Laugier, M. T. New formula for indentation toughness in ceramics. *Journal of Materials Science Letters* **6**, 355–356. ISSN: 0261-8028, 1573-4811. <http://link.springer.com/10.1007/BF01729352> (2022) (Mar. 1987).
135. Cuadrado, N., Casellas, D., Anglada, M. & Jiménez-Piqué, E. Evaluation of fracture toughness of small volumes by means of cube-corner nanoindentation. *Scripta Materialia* **66**, 670–673. ISSN: 13596462. <https://linkinghub.elsevier.com/retrieve/pii/S1359646212000504> (2022) (May 2012).
136. Oliver, W. & Pharr, G. An improved technique for determining hardness and elastic modulus using load and displacement sensing indentation experiments. *Journal of Materials Research* **7**, 1564–1583. ISSN: 0884-2914, 2044-5326. <http://link.springer.com/10.1557/JMR.1992.1564> (2022) (June 1992).
137. Tsui, Y., Doyle, C. & Clyne, T. Plasma sprayed hydroxyapatite coatings on titanium substrates Part 1: Mechanical properties and residual stress levels. *Biomaterials* **19**, 2015–2029. ISSN: 01429612. <https://linkinghub.elsevier.com/retrieve/pii/S0142961298001033> (2022) (Nov. 1998).
138. Kleer, G., Schonholz, R. & Doll, W. Interface crack resistance of zirconia-based thermal barrier coatings [TBC's]. **329** (1991).
139. Richards, B. T., Zhu, D., Ghosn, L. J. & Wadley, H. N. in *Ceramic Engineering and Science Proceedings* (eds Kriven, W. M., Wang, J., Zhu, D. & Fischer, T.) 219–237 (John Wiley & Sons, Inc., Hoboken, NJ, USA, Dec. 25, 2015). ISBN: 978-1-119-21174-7. <https://onlinelibrary.wiley.com/doi/10.1002/9781119211747.ch18> (2021).
140. Fernández-Carrión, A. J., Allix, M. & Becerro, A. I. Thermal Expansion of Rare-Earth Pyrosilicates. *Journal of the American Ceramic Society* **96** (ed White, M.) 2298–2305. ISSN: 00027820. <https://onlinelibrary.wiley.com/doi/10.1111/jace.12388> (2022) (July 2013).

141. Xu, Y., Hu, X., Xu, F. & Li, K. Rare earth silicate environmental barrier coatings: Present status and prospective. *Ceramics International* **43**, 5847–5855. ISSN: 02728842. <https://linkinghub.elsevier.com/retrieve/pii/S027288421730175X> (2021) (June 2017).
142. Kane, K. A. *et al.* Steam oxidation of ytterbium disilicate environmental barrier coatings with and without a silicon bond coat. *Journal of the American Ceramic Society* **104**, 2285–2300. ISSN: 0002-7820, 1551-2916. <https://onlinelibrary.wiley.com/doi/10.1111/jace.17650> (2022) (May 2021).
143. Richards, B. T. *et al.* Response of ytterbium disilicate–silicon environmental barrier coatings to thermal cycling in water vapor. *Acta Materialia* **106**, 1–14. ISSN: 13596454. <https://linkinghub.elsevier.com/retrieve/pii/S1359645415301592> (2021) (Mar. 2016).
144. Tertuliano, O. A. & Greer, J. R. The nanocomposite nature of bone drives its strength and damage resistance. *Nature Materials* **15**, 1195–1202. ISSN: 1476-1122, 1476-4660. <http://www.nature.com/articles/nmat4719> (2022) (Nov. 2016).
145. Tertuliano, O. A., Edwards, B. W., Meza, L. R., Deshpande, V. S. & Greer, J. R. Nanofibril-mediated fracture resistance of bone. *Bioinspiration & Biomimetics* **16**, 035001. ISSN: 1748-3182, 1748-3190. <https://iopscience.iop.org/article/10.1088/1748-3190/abdd9d> (2022) (May 1, 2021).
146. Zimmerman, M. H., Faber, K. T., Fuller, E. R., Kruger, K. L. & Bowman, K. J. Texture Assessment of Magnetically Processed Iron Titanate. *Journal of the American Ceramic Society* **79**, 1389–1393. ISSN: 0002-7820, 1551-2916. <https://onlinelibrary.wiley.com/doi/10.1111/j.1151-2916.1996.tb08600.x> (2022) (May 1996).